Multi-scale remote sensing methods for an improved understanding of forest decline in the Zagros Forest area

Abstract

Forests play a crucial role in providing ecosystem services such as fodder and fuelwood, as well as preventing erosion and regulating climate. However, forests are currently facing rapid decline in many parts of the world, which has far-reaching impacts on both the environment and society. While deforestation receives considerable attention in the literature, there is a need to delve deeper into understanding and managing forest decline, particularly in arid and semi-arid regions. These regions, with their delicate ecosystems associated with challenges related to intense and long-lasting droughts, require special focus. This thesis seeks to enhance our comprehension of forest decline in arid and semi-arid regions by applying remote sensing (RS) techniques. It also aims to address the potential challenges that RS may encounter in these ecosystems.

The overall thesis is divided into three studies each dealing with a specific aspect of forest decline analysis. Due to the crucial importance of accurate forest cover (FC) mapping as a basic prerequisite for detecting and understanding forest decline, the first study was centered on developing a work-flow for the precise estimation of woody canopy cover across the expansive semi-arid Zagros mountain area exceeding 500,000 km^2, for which no representative FC map existed. The study sought to address the challenge of accurately characterizing woody canopy presence, which tends to be underestimated in arid and semi-arid regions by existing global mapping approaches. To address this, the study introduced a comprehensive remote-sensing workflow that combines multi-year Sentinel-2 (S2) data sourced from the Google Earth Engine and very high-resolution (VHR) imagery archives from Google® and Bing®. Several random forest (RF) models were trained and evaluated across different spatial resolutions to test the effect of spatial grain on mapping outputs, with the model featuring a 40-m spatial resolution emerging as the most effective. This model established robust associations between the reference dataset and woody canopy density estimates derived from S2 imagery, yielding a median coefficient of determination (R^2) and root mean square error (RMSE) of 0.67 and 0.11, respectively. The workflow developed in this study is likely transportable to other arid and semi-arid regions, providing a resource-efficient workflow for woody canopy cover estimation and mapping.

In the second study, the focal point was the detection and mapping of forest decline through the use of time series data and statistical trend analysis. This study, conducted within a smaller segment of the Zagros region (covering 3500 km^2), employed three distinct approaches (i.e., RF, anomaly detection, and Sen´s Slope) based on Landsat time series (between 1986 and 2021) to differentiate between non-declining and declining forest patches. Among these three approaches, the RF classification method exhibited the highest accuracy and kappa values of ca. 0.75 and 0.50, respectively. The anomaly detection approach displayed overall accuracy and kappa values of 0.65 and 0.30, while Sen's slope approach demonstrated accuracy and kappa values of 0.64 and 0.30, respectively. Interestingly, the outcomes of the RF classification proved to be relatively independent of the Landsat data acquisition timing, suggesting that

Abstract

environmental variables may have played a more significant role in distinguishing between declining and non-declining regions than the spectral characteristics of the trees as observed remotely. Based on the results of this study, it can be inferred that detecting declining forest areas in arid and semi-arid regions using Landsat data poses a notable challenge, primarily due to the weak vegetation signals caused by the sparse and patchy canopy cover against a bright soil background. We assume that this is one of the key obstacles to detecting the subtle degradation signals. This study underscored the potential hurdles to forest decline detection via RS in arid and semi-arid regions and highlighted the need for the incorporation of additional environmental variables to overcome these limitations.

In the final study of this thesis, the main aim was to gain insights into the underlying factors that contribute to the decline of individual trees and tree groups (encompassing five individual trees). This investigation delves into the issue of tree and forest decline in Zagros forests, taking a set of relevant environmental variables such as slope and precipitation, as well as tree characteristics like diameter at breast height (DBH) and tree height (H) into account. Field data was collected from part of the Zagros forests covering an area of 165 km^2, and was combined with environmental data from publicly accessible databases. Relationships between tree decline and environmental factors were analyzed through the application of generalized additive models (GAMs). The results shed light on the significance of specific environmental factors, such as slope and the Bioclimate-16 variable (representing precipitation during the wettest quarter), in influencing individual tree decline across various decline categories (i.e., non-declining, slightly declining, moderately declining, and severely declining) (p-values of 0.009 and 0.02 for slope and Bioclimate-16, respectively). The optimal multivariate model for assessing tree group decline incorporates variables such as slope, soil organic carbon (SOC), and silt, with SOC emerging as the predominant factor (p-value = 0.04). Notably, no significant correlation between forest decline and tree characteristics (especially tree height) was discerned. To ensure the model's robustness, potential spatial autocorrelation was assessed using the Moran´s I test. Additionally, a spectral analysis of bare soil in areas experiencing decline compared to non-declining regions consistently revealed diminished reflectance values across ten S2 bands, with VNIR-3, SWIR-2, red, green, and blue bands that consistently exhibited strong significance (confirmed through the Wilcoxon test) in all seasons except winter. These reduced reflectance values may signify that forests growing on soils with larger grain size (i.e., a higher proportion of sand) and/or higher organic carbon content may exhibit a higher susceptibility to tree decline. This study significantly contributes to our comprehension of the environmental factors associated with forest decline in semi-arid forests, which also underscores the potential utility of the spectral characteristics of bare soil in sparsely covered arid and semi-arid forests for predicting the likelihood of tree and forest decline.

In summary, this thesis highlighted the unreliability of certain global FC products in arid and semi-arid regions. It meticulously mapped the woody cover across the entire Zagros forest solely using RS data, offering a versatile workflow that is applicable to various ecosystems, especially those in arid and semi-arid regions worldwide. The research further examined the RS-based separability of both declining and non-declining forest areas in the Zagros and revealed substantial challenges associated with using RS for detecting forest decline in sparsely

Abstract

vegetated arid and semi-arid landscapes. Ultimately, this study made a significant contribution to the understanding of tree and forest decline in the semi-arid Zagros forests, by identifying a set of environmental factors that differed between declining and non-declining areas. The outcomes of this thesis are aimed to call for more international attention and support subsequent studies on the complex forest decline phenomenon within the fragile Zagros ecosystems and beyond.

Zusammenfassung

Wälder spielen eine entscheidende Rolle bei der Bereitstellung von Ökosystemleistungen wie Futter und Brennholz sowie beim Schutz vor Erosion und bei der Regulierung des Klimas. In vielen Teilen der Welt gibt es jedoch einen raschen Rückgang von Wald , was weitreichende Auswirkungen auf Umwelt und Gesellschaft hat. Während der Entwaldung in der einschlägigen Literatur große Aufmerksamkeit gewidmet wird, besteht die Notwendigkeit, auch das Verständnis von Waldrückgang zu vertiefen und Methoden zum Umgang damit zu erarbeiten, insbesondere in semi-ariden Regionen. Diese Gebiete mit ihren empfindlichen Ökosystemen, welche mit den Herausforderungen intensiver und lang anhaltender Dürreperioden konfrontiert sind, erfordern besondere Aufmerksamkeit. Diese Arbeit soll das Verständnis des Waldrückgangs in semi-ariden Regionen durch die Anwendung von Fernerkundungstechniken verbessern. Sie zielt auch darauf ab, die potenziellen Herausforderungen bei der Anwendung von Fernerkundung in diesen Ökosystemen anzugehen.

Die Arbeit wurde in drei Studien unterteilt, die sich jeweils mit einem bestimmten Aspekt der Analyse des Waldrückgangs befassen. Da eine genaue Kartierung der Waldbedeckung die Grundvoraussetzung für die Erkennung und das Verständnis des Waldrückgangs ist, konzentrierte sich die erste Studie auf die Entwicklung eines Arbeitsablaufs für die präzise Schätzung der Waldbedeckung im ausgedehnten semi-ariden Zagros-Gebiet, das eine Fläche von mehr als 500.000 km² einnimmt und für das zuvor keine repräsentative Waldbedeckungskarte existierte. Ziel der Studie war es, das Vorhandensein von Gehölzen genau zu charakterisieren, da dieses in semi-ariden Regionen durch bereits existierende globale Kartierungsansätze tendenziell unterschätzt wird. Um dies zu erreichen, wurde ein umfassender Fernerkundungs-Workflow eingeführt, der von Google Earth Engine bezogene Sentinel-2-Daten (S2) mehrerer Jahre mit sehr hoch auflösenden Bild-Datensätzen von Google® und Bing® kombiniert. Mehrere Random-Forest-Modelle wurden für verschiedene räumliche Auflösungen trainiert und evaluiert, um die Auswirkungen der räumlichen Ausflösung auf die Kartierungsergebnisse zu untersuchen, wobei sich das Modell mit einer Auflösung von 40 Metern als das effektivste herausstellte. Dieses Modell stellte robuste Beziehungen zwischen dem Referenzdatensatz und den aus S2-Bildern abgeleiteten Schätzungen der Gehölzbedeckung her und erreichte einen mittleren Bestimmtheitsgrad (R^2) von 0,67 und einen mittleren quadratischen Fehler (RMSE) von 0,11.

Der in dieser Studie entwickelte Arbeitsablauf ermöglicht eine ressourceneffiziente Schätzung und Kartierung der Gehölzbedeckung. Es ist anzunehmen, dass er auch auf andere semi-aride Regionen übertragbar ist.

In der zweiten Studie lag der Schwerpunkt auf der Erkennung und Kartierung des Waldrückgangs durch die Verwendung von Zeitreihen und statistische Trendanalysen. In dieser Studie, die in einem kleineren Segment (3500 km²) der Zagros-Region durchgeführt wurde, wurden drei verschiedene Ansätze (Random Forest (RF), Anomalie-Erkennung und

Zusammenfassung

Sen's Slope) verwendet, um auf der Grundlage von Landsat-Zeitreihen von 1986 bis 2021 zwischen Flächen mit und ohne Waldrückgang zu unterscheiden. Unter diesen drei Ansätzen wies die RF-Klassifizierungsmethode die höchste Genauigkeit und den höchsten Kappa-Wert von 0,75 bzw. 0,50 auf. Der Ansatz zur Erkennung von Anomalien wies eine Gesamtgenauigkeit von 0,65 und einen Kappa-Wert von 0,30 auf, während der Sen's Slope-Ansatz eine Genauigkeit von 0,64 und einen Kappa-Wert von 0,30 zeigte. Interessanterweise erwiesen sich die Ergebnisse der RF-Klassifizierung als relativ unabhängig vom Zeitpunkt der Landsat-Datenerfassung, was darauf hindeutet, dass Umweltvariablen bei der Unterscheidung zwischen Regionen mit rückläufiger und nicht rückläufiger Gehölzbedeckung eine wichtigere Rolle gespielt haben könnten als die mittels Fernerkundung beobachteten spektralen Merkmale der Gehölze. Aus den Ergebnissen dieser Studie lässt sich ableiten, dass die Erkennung abnehmender Waldflächen in semi-ariden Regionen mit Hilfe von Landsat-Daten eine besondere Herausforderung darstellt, vor allem aufgrund der schwachen Vegetationssignale, die durch die spärliche und lückenhafte Vegetationsbedeckung vor einem hellen Bodenhintergrund verursacht werden. Wir gehen davon aus, dass dies eines der größten Hindernisse für die Erkennung der subtilen Degradationssignale ist. Diese Studie unterstreicht die potenziellen Hürden für die Erkennung des Waldsrückgangs mittels Fernerkundung in semi-ariden Regionen und verdeutlicht die Notwendigkeit, zur Überwindung dieser Einschränkungen zusätzliche Umweltvariablen mit einzubeziehen.

In der abschließenden Studie dieser Arbeit ging es darum, Einblicke in die zugrunde liegenden Faktoren zu gewinnen, die zum Rückgang einzelner Bäume und Baumgruppen (fünf Einzelbäume umfassend) beitragen. Diese Untersuchung befasst sich unter Berücksichtigung von Umweltvariablen wie Hangneigung und Niederschlag sowie Baummerkmalen wie Brusthöhendurchmesser und Baumhöhe mit dem Rückgang von Bäumen und Wäldern in der Zagros-Region. Die Felddaten wurden in einem Teil der Zagros-Wälder auf einer Fläche von 165 km² gesammelt und mit Umweltdaten aus öffentlich zugänglichen Datenbanken kombiniert. Die Beziehungen zwischen dem Rückgang der Bäume und den Umweltfaktoren wurden mit Hilfe generalisierter additiver Modelle (GAMs) analysiert. Die Ergebnisse geben Aufschluss über die Bedeutung spezifischer Umweltfaktoren, wie z. B. die Hangneigung und die Bioclim-16-Variable (Niederschlag während des feuchtesten Quartals), für den Rückgang einzelner Bäume in verschiedenen Rückgangskategorien, d. h. nicht abnehmend, leicht abnehmend, mäßig abnehmend und stark abnehmend (p-Werte von 0,009 für Hangneigung und 0,02 für Bioclim-16). Das beste multivariate Modell zur Bewertung des Rückgangs von Baumgruppen umfasst Variablen wie Hangneigung, organischer Kohlenstoff im Boden (SOC) und Schluff, wobei sich der SOC als wichtigster Faktor herausstellte (p-Wert = 0,04). Bemerkenswert ist, dass kein signifikanter Zusammenhang zwischen dem Waldrückgang und den Baummerkmalen, insbesondere der Baumhöhe, festgestellt werden konnte. Um die Robustheit des Modells zu gewährleisten, wurde eine mögliche räumliche Autokorrelation mit dem Moran's I-Test untersucht. Darüber hinaus ergab eine Spektralanalyse des blanken Bodens in Gebieten mit rückläufiger Entwicklung im Vergleich zu Regionen ohne rückläufige Entwicklung durchgängig verringerte Reflexionswerte in zehn S2-Bändern, wobei VNIR-3, SWIR-2, rote, grüne und blaue Bänder in allen Jahreszeiten außer im Winter durchgängig eine

Zusammenfassung

hohe Signifikanz aufwiesen (bestätigt durch den Wilcoxon-Test). Diese geringeren Reflexionswerte könnten darauf hindeuten, dass Wälder, die auf Böden mit größerer Korngröße (d. h. einem höheren Sandanteil) und/oder höherem Gehalt an organischem Kohlenstoff wachsen, anfälliger für Baumrückgang sind. Diese Studie leistet einen wichtigen Beitrag zum Verständnis der Umweltfaktoren, die mit dem Waldrückgang in semi-ariden Wäldern in Verbindung stehen, und unterstreicht den potenziellen Nutzen der spektralen Eigenschaften von blankem Boden in spärlich bewachsenen semi-ariden Wäldern für die Vorhersage der Wahrscheinlichkeit von Baum- und Waldrückgang.

Zusammenfassend lässt sich sagen, dass diese Arbeit die Unzuverlässigkeit bestimmter globaler Waldbedeckungsprodukte in semi-ariden Regionen aufzeigt. Die Gehölzbedeckung des gesamten Zagros-Waldes wurde ausschließlich mit Fernerkundungsdaten kartiert und ein vielseitig einsetzbarer Arbeitsablauf entwickelt, der auf verschiedene Ökosysteme anwendbar ist, insbesondere in semi-ariden Regionen weltweit. Es wurde ferner die fernerkundungsbasierte Trennbarkeit von rückläufigen und nicht rückläufigen Waldgebieten in der Zagros-Region untersucht und gezeigt, dass der Einsatz von Fernerkundung zur Erkennung des Waldrückgangs in spärlich bewachsenen semi-ariden Landschaften mit erheblichen Herausforderungen verbunden ist. Letztendlich leistete diese Studie einen wichtigen Beitrag zum Verständnis des Rückgangs von Bäumen und Wäldern in den semi-ariden Zagros-Wäldern, indem sie eine Reihe von Umweltfaktoren identifizierte, die sich zwischen Gebieten mit und ohne Rückgang unterscheiden. Die Ergebnisse dieser Arbeit sollen zu mehr internationaler Aufmerksamkeit aufrufen und weitere Studien zu diesem komplexen Phänomen in den fragilen Zagros-Ökosystemen und darüber hinaus unterstützen.

Contents

Contents

Contents

List of Figures

List of Figures

List of Figures

List of Tables

1. Introduction

1.1. Importance of forests and forest decline

Forests hold immense value fby providing essential ecosystem goods and services. These services encompass resources like fodder, fuelwood, timber, medicinal plants, and herbs. Furthermore, forests play a vital role in maintaining soil stability, mitigating climate change, conserving water, and preventing erosion and desertification (Waroux and Lambin, 2012). They also play a crucial role in addressing a variety of pressing sustainability and social-ecological challenges, including the loss of biodiversity (Estoque et al., 2022). However, forests are declining rapidly in many regions of the world (Kuuluvainen et al., 2021). Approximately 2 billion hectares of the Earth's forests have been subject to degradation, making forest decline a recognized international problem with environmental, social, and economic repercussions beyond the geographical borders. The negative consequences of decline do not only affect ecosystems (i.e., forest function and structure) (Wang et al., 2020; Vásquez-Grandón et al., 2018) but also the society. This has the potential to negatively impact millions of people who rely, either entirely or partially, on the benefits and resources that forests provide at local, regional, and global levels (Vásquez-Grandón et al., 2018). This impact extends to the vital ecosystem services that forests provide (Waroux and Lambin, 2012). Even though forest decline is a crucial topic, a tendency to focus on deforestation persists within the literature (e.g., Caballero et al., 2023; Jin et al., 2016), particularly in arid and semi-arid regions. The term forest decline refers to a "reduction of the capacity of a forest to provide goods and services" (Simula, 2009), while deforestation is "the permanent conversion of forests to alternative land cover types" (Hoekman et al., 2020). Whereas there is still a considerable research background on forest decline within tropical forests (e.g., Hoekman et al., 2020), temperate forests (e.g., Sáenz-Romero et al., 2020), and boreal forests (e.g., Kuuluvainen et al., 2021; Sánchez-Pinillos et al., 2021), there is a noticeable dearth of attention paid to the forest decline in arid and semi-arid regions (e.g., Ghasemi et al., 2023; le Polain de Waroux et al., 2012). It is, therefore, essential to map, and understand the forest decline for better forest management, particularly in arid and semi-arid regions with fragile ecosystems (Andrews et al., 2020; Anderegg et al., 2012) with periodic droughts, extreme heat, and overexploitation of scarce resources (i.e., water) (Malagnoux et al., 2007).

1.2. Plants' responses to stress

In order to monitor forest decline, it is crucial to understand the structural and physiological responses of plants to stress (Pontius et al., 2020). Plants have mechanisms for adapting to environmental pressures such as water scarcity, but when these conditions exceed what is average for them, it can be hazardous to their health. One of the mechanisms plants use to cope with stress is the development of protective pigments in leaves (Pontius et al., 2020). By

capturing changes in canopy color, imagery can indicate the health status of trees (Windrim et al., 2020; Makinde and Salami, 2013). Another mechanism trees use to cope with stress is leaf orientation. The angle between the leaf normal and the zenith is a significant leaf trait associated with light interception, photosynthesis, energy balance, and competition among individual plants. Adjusting leaf angles can be a strategic response to variability in light, heat, or water conditions (Yang et al., 2023). Many trees exhibit the ability to rapidly change their leaf configurations in response to environmental stresses (Briglia et al., 2020). Tree leaf senescence, which involves cellular structural, metabolic, and gene expression changes, is another example of an adaptive mechanism. The senescence of leaves can be accelerated or postponed by environmental factors such as light, temperature, and water status (Zhao et al., 2022a). Generally, higher temperatures delay senescence, while drought accelerates it, with variations among species. That is, warm weather and drought have opposing effects on senescence timing, as Estiarte and Penuelas (2015) noted. Prolonged senescence can extend chloroplast lifespan, boost photosynthesis, and enhance source strength (Zhao et al., 2022a). Additionally, early senescence due to heat stress can improve heat tolerance, as observed by He et al. (2021). These adaptability strategies of trees are called plasticity (Zheng et al., 2023). However, prolonged exposure to stressful situations causes trees to decline (Hosseini et al., 2017).

1.3. Definition of forest decline

Until now, there has been no universally accepted definition of "forest decline," and it continues to be extremely difficult to establish a clear and practical definition (Vásquez-Grandón et al., 2018). Several definitions have been introduced with one already provided in section 1.1 However, there is still some disagreement as to what exactly constitutes forest decline (Ciesla and Donaubauer, 1994). These disagreements are influenced by the goals and management intentions of global organizations, countries, and researchers. These diverse viewpoints have given rise to various distinct definitions of forest decline, with each definition highlighting different aspects such as forest structure, biomass, biodiversity, and ecosystem services (ES) (Delgado-Aguilar et al., 2019). For instance, Tejaswi (2007) defines forest decline as "a process that results in temporary or permanent deterioration in tree crown cover or species composition while the intact canopy cover remains above 10%" (this percentage may differ according to different climate zones and ecosystem types). Studies like Ciesla and Donaubauer (1994) described forest decline as an episodic event characterized by an early, progressive loss of vigor and health of trees or stands over a period in the absence of evidence of a single, clearly identified causative factor, such as a physical disturbance or attack by an aggressive disease or pest. The terms "forest dieback", "forest decline", "stand-level dieback", "canopy level dieback", or in German, "Waldsterben", or "Waldschäden" have been used with varying degrees of interchangeability to describe this problem (Ciesla and Donaubauer, 1994). Depending on the definition, forest decline is identified by symptoms such as stunted growth, early autumnal leaf coloring, yellowing, foliage loss, twig die-off, and an increased presence and pathogenicity of fungi that decay roots. Another characteristic of forest decline is that it

progresses differently among trees within the same stand. While some may exhibit only slight symptoms, others may be in an intermediate condition, and still others may be dead. In Romania, for example, oak decline was identified by a reduction in annual shoot growth, smaller leaf size, as well as yellowing, wilting, and leaf loss (Ciesla and Donaubauer, 1994). In this thesis, forest decline refers primarily to the temporary or permanent deterioration of tree cover, with a particular focus on the Persian Oak or Brant's oak.

1.4. Forest decline in arid and semi-arid areas

Arid and semi-arid regions have experienced significant decline processes in the last few decades (le Polain de Waroux et al., 2012) (see Figure 1.1 for the global distribution of these regions). Deforestation in these areas has been extensively studied, but the problem of forest decline has received less attention (Vásquez-Grandón et al. 2018). Studying forest decline requires long-term data collection and analysis to understand gradual changes (Vásquez-Grandón et al., 2018). This can be resource-intensive and demanding in terms of time and funding. Also, a significant limitation in comprehending forest decline processes relates to the frequently restricted availability of field datasets. Collecting data on forest decline necessitates labor-intensive and time-consuming field campaigns, which are particularly challenging due to the forest's wide geographic extent. Furthermore, certain regions may be difficult to assess because of restricted accessibility, for example, when quantifying forests on exceedingly steep inclines in remote zones with inadequately maintained or insufficient road systems (Diao et al., 2020; Lausch et al., 2016). Forest decline is often the result of multiple stressors (i.e., biotic and abiotic factors) acting simultaneously (Hosseini et al., 2017). Isolating the individual contributions of each stressor is challenging, and understanding the interactions between these factors requires interdisciplinary research.

In line with the above stated, forest decline in arid and semi-arid ecosystems presents significant ecological and environmental challenges due to the unique challenges faced by these regions, including water scarcity, fragile ecosystems, local livelihoods closely depending on the forest, and unique biodiversity (Andrews et al., 2020; Malagnoux et al., 2007). More than one billion people residing in arid and semi-arid climates rely on these forests to provide ES (le Polain de Waroux et al., 2012), making their decline particularly significant. To address these challenges, this thesis explores the capability of multi-scale remote sensing (RS) techniques to improve our understanding of forest decline in this specific context.
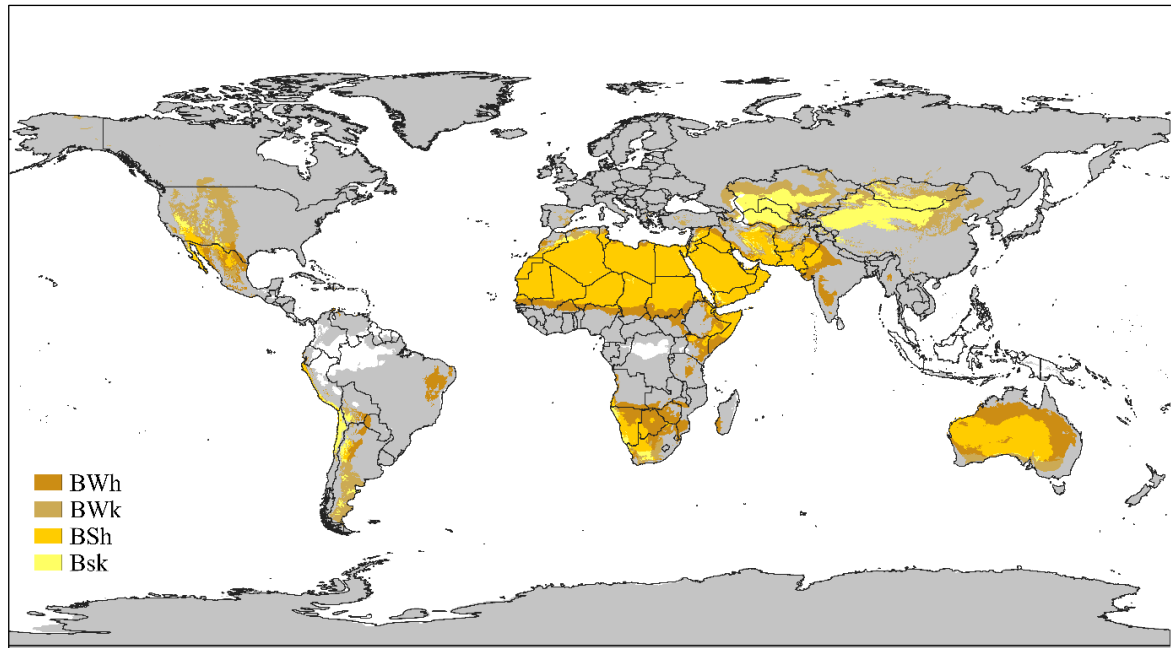
Figure 1.1 Global Distribution of arid and semi-arid climates according to the Köppen-Geiger Classification. The map uses different colors to depict arid regions (BWh and BWk) and semi-arid regions (BSh and BSk). The source of data used for this map is Beck et al. (2018).

1.5. Forest decline drivers in arid and semi-arid areas

Climate models concur that as temperatures rise during the 21st century, numerous arid and semi-arid areas will face more frequent, severe, and prolonged droughts (Anderegg et al., 2012). This will result in reduced overall soil moisture, heightened stress for trees due to drought, increased vulnerability to insect and disease outbreaks, and an elevated risk of wildfires (Andrews et al., 2020). Forest decline results from a complex interplay of biotic and abiotic factors. Climate change-related weather extremes like droughts are a major contributor to tree mortality and forest decline (Hosseini et al., 2017; Sulla-Menashe et al., 2014; Waroux and Lambin, 2012; Peñuelas and Sardans, 2021), particularly in arid and semi-arid regions. Moreover, overexploitation, pollution, wildfires (Sasaki and Putz, 2009), uncontrolled grazing, logging, insect damage, and pathogens exacerbate drought-induced stress (Sánchez-Pinillos et al., 2021). There is no single answer to the question of what factors contribute to forest decline processes. The influence of environmental factors on forest and tree decline, (Clatterbuck, 2006), must be examined in conjunction with local conditions and the historical progression of the phenomenon (Bałazy et al., 2019). In this context, it is important to acknowledge that forest decline represents a multifaceted phenomenon necessitating a comprehensive examination of the contributing factors. While the complexities inherent in this phenomenon are duly recognized, this thesis is dedicated to the systematic exploration of these driving factors. It should be noted that the exact characteristics of these drivers continue to be the subject of ongoing research, which plays an integral role in the research inquiries posed within the context of this thesis.

1.6. The showcased ecosystem: the semi-arid Zagros forests

The Zagros forests cover approximately 20% of Iran's western land region (see Figure 1.2). The elevation in the Zagros Mountains varies widely, ranging from 200 to 4,409 m above sea level. Annual precipitation varies across the region from 250 to 800 mm. Mean annual temperatures also differ across the expanse, measuring 11°C in the northwest and 25°C in the southwest. The soil composition mainly results from limestone origins and is characterized by a pH range of 7.0 to 8.5 (Sagheb Talebi et al., 2014). The summers in Zagros are long and very hot, with low humidity. As one moves from southwest to southeast, there is a gradual increase in the mean annual temperature, along with a change in the temperature range (Sagheb Talebi et al., 2014). Brant's Oak (*Quercus brantii* var. persica) is the most common tree species in the area, interspersed with *Quercus infectoria* (G. Olivier), *Quercus libani* (G. Olivier), *Pistacia atlantica* (Desf., Wild Pistachio), *Acer monspessulanum* (L.), *Crategus* spp., *Amygdalus* spp., and *Pyrus* spp. (Erfanifard et al., 2014).
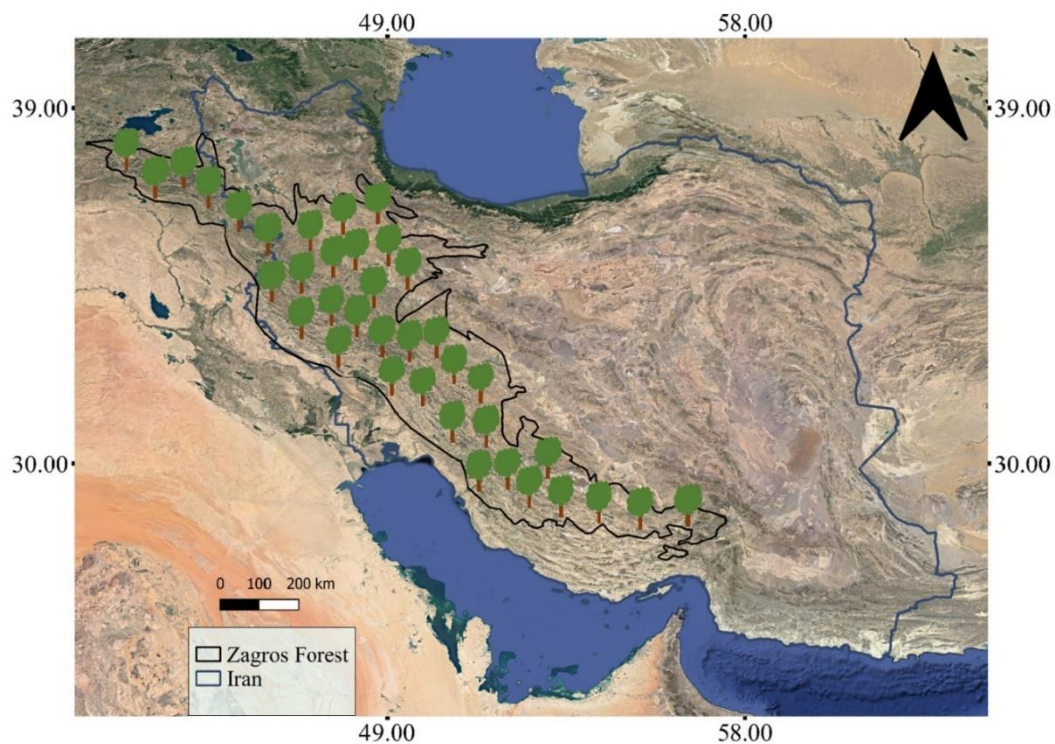
Figure 1.2 Zagros Forest locations over Iran

The Zagros Mountains cover more than 5 million hectares and comprise 40% of Iran's total forest area. They have been negatively affected by extreme weather conditions and wildfires, making them more susceptible to forest insects and pathogens. Over the past few decades, Zagros forests have been facing severe oak dieback (see Figure 1.3). The study of forest decline in the Zagros ecosystem is still in its early stages. There is still a lack of understanding of which regions are affected, and it is crucial to understand the main drivers of forest decline (i.e., topography, climate, soil) in those regions (Moradi et al., 2021).

Figure 1.3 Examples of the occurrence of tree decline in the Zagros (photos taken by Elham Shafeian from sites located in the central Zagros zone, September 2021).

1.7. Woody/Forest cover dynamics in arid and semi-arid areas

A thorough examination of woody or forest cover (FC) in the study region is vital for a comprehensive understanding of deforestation and forest decline (Wang and Cochrane, 2005). FC has been identified as a crucial tool for detecting and comprehending forest decline (Ghanbari Motlagh and Kiadaliri, 2021; Yang et al., 2017; Hosseini et al., 2017; Gonsamo et al., 2013). FC refers to the amount of land covered by the vertical projection of tree canopies relative to the total area. Precise FC mapping is crucial for estimating carbon stocks, biomass, and as contribution to global change research (Ye et al., 2014). Changes in FC have significant impacts on ecosystem services, biodiversity, climate change feedback, and human well-being (Kuemmerle et al., 2009; Huang et al., 2008). FC change, especially a reduction, may indicate a decline or excessive use in forest and woodland areas, suggesting deforestation (Wang and Cochrane, 2005). Evaluating the precision of official forestry data and comprehending trends in FC pose challenges in numerous regions around the world. The field-based mapping of FC changes in mountainous and semi-arid regions is a time-consuming and complex task which partly explains why comprehensive forest change maps for these regions are scarce. RS methods are essential to overcome this challenge and provide more accurate estimations (Kuemmerle et al., 2009).

1.8. The role of RS in the study of forest decline

RS techniques, such as those used in this thesis, have been applied in various studies to detect forest decline in arid and semi-arid regions (e.g., Ghasemi et al., 2023; Ghasemi et al., 2022; Karami et al., 2018). Unlike costly and time-intensive ground-based methods for monitoring tree mortality and forest decline in forest ecosystems (Sherwood et al., 2021), RS offers a practical alternative for analyzing forest changes across extensive areas (Iverson et al., 1989). RS involves the use of devices to collect information about objects or areas without direct contact. Different materials interact uniquely with sunlight through the processes of reflection, absorption, or transmission at distinct wavelengths, creating identifiable spectral signatures (Lanfri, 2010). Changes in tree and foliage morphology due to stress can be discerned using remote sensors, by comparing scenes before and after the decline phenomenon. Studies by Senf et al. (2020), Wang et al. (2020), and Iverson et al. (1989) have demonstrated the effectiveness of this method. Repeated analysis enables efficient monitoring of vegetation health, using for example greenness information (Iverson et al., 1989).

Although each plant species has unique spectral features, there are common variations in spectral responses to stress (Pontius et al., 2020). Healthy green vegetation preferentially absorbs red and blue light wavelengths for use in photosynthesis. Greenlight (wavelength 545–565 nm), however, is mostly reflected, leading to the green appearance of healthy photosynthetically active biomass (Iverson et al., 1989; Wahbi et al., 2018). Stress-induced changes in leaf chemistry and physiology can be detected in the blue (480–520 nm) and red (600–680 nm) regions through changed chlorophyll absorption (Pontius et al., 2020). Shortwave infrared (SWIR bands; 1550–1750 nm) bands are sensitive to soil moisture and vegetation water stress (Yao et al., 2018). Masaitis et al. (2012) found a robust correlation between the spectral reflectance properties of trees and their stress status. They also confirmed that stress detection in some tree species is most sensitive to the red-edge spectral zone. Meiforth et al. (2020) demonstrated that a combination of six spectral bands in the visible and near-infrared (VNIR) range (550–970 nm) from hyperspectral images is sufficient to capture the complete range of canopy stress symptoms in kauri trees in New Zealand. Darvishi Boloorani et al. (2020) investigated the spectral characteristics of two-year-old Persian oak seedlings experiencing simultaneous water deficiency and dust storm stress. The spectral values of samples allowed for the successful identification of stressed samples and the type of stress at both leaf and canopy levels. The principles and changes in the spectral characteristics of vegetation under stress are used in this thesis to detect, map, and study tree and forest decline in the Zagros semi-arid forest.
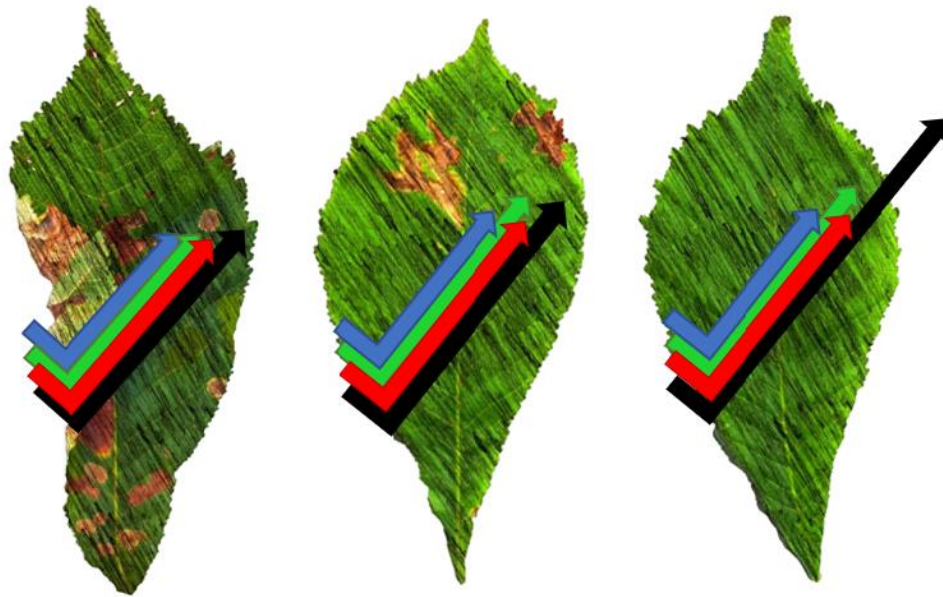
Figure 1.4 Different spectral reflectance patterns exist between almost dead, stressed, and healthy leaves (illustrated here with *Aesculus hippocastanum*, at leaf level from left to right) (photos taken and edited by Elham Shafeian). The healthy plant displays high absorption of visible light (RGB) and significant reflection of near-infrared light (black arrow), whereas the sparse or unhealthy vegetation shows high absorption of visible light and decreased reflection of near-infrared light (Pontius et al., 2020).

One common methodical approach to examining vegetation's health status in RS is to apply spectral indices. In RS, a spectral index is a mathematical expression or formula that extracts specific data about the surface being seen from the reflectance values of various bands or wavelengths of electromagnetic light. These indices are useful for a number of purposes, including the classification of land cover (LC), determining the health of the vegetation, and monitoring the environment (Farella et al., 2022). Vegetation mapping and monitoring often use spectral vegetation indices (VIs) to assess forest decline over large regions (Xie et al., 2008; Moreno-Fernández et al., 2021). Various VIs have been developed to detect changes in vegetation using RS data, with certain indices designed specifically for arid and semi-arid environments. These indices are effective for monitoring changes in vegetation cover and are derived from land surface reflectance. However, there are some limitations to using spectral indices in semi-arid environments that will be discussed later.

Using RS-based time series analysis is a reliable method for uncovering changes on the Earth's surface and quantifying their magnitude over a designated monitoring period (Griffiths and Hostert, 2015). To effectively monitor and quantify changes and trends in vegetation, long-term and consistent satellite data records are essential. Time-series methods provide a structured approach that enables the assessment of alterations in FC over time with greater detail. Moreover, they allow the identification and measurement of long-term trends related to gradual changes in the canopy (Griffiths and Hostert, 2015). RS time series data can be based on raw digital numbers or variables derived from the original data. Such variables include geophysical variables such as top-of-the-atmosphere reflectance and land surface temperature, as well as spectral indices like the Normalized Difference Vegetation Index (NDVI). Both

kinds of variables can be utilized to establish long-term time series and analyze them with respect to different statistical parameters. In forest monitoring, the primary goal of using RS and time series data is to understand how forests are changing over time (see Figure 1.5 as an example). This is accomplished by analyzing the changes in selected measures across various periods that are indicative of significant alterations within the forest (Kuenzer et al., 2015). In recent years, various methodologies have been developed to map forest dynamics and changes using a time series of multispectral optical satellite data (see next section), including MODIS, Landsat, and S2 (Francini and Chirici, 2022; Rodman et al., 2021; Wang et al., 2020; Lima et al., 2019; Sulla-Menashe et al., 2014). The combination of increased access, improved availability of algorithms and computer code and more powerful hardware and software has led to significant growth of the RS community applying time series approaches. Among these approaches, Landsat time series have been particularly recognized as a valuable data source for monitoring and assessing forest decline and disturbances, as well as providing continuous reports on forest dynamics and changes. This is due to their free accessibility, relatively high spatial resolution, and long and consistent acquisition record, making them readily available for analysis (Dutrieux et al., 2015; Zhu et al., 2020; Diao et al., 2020; Senf et al., 2020; Giannetti et al., 2020; Rodman et al., 2021).
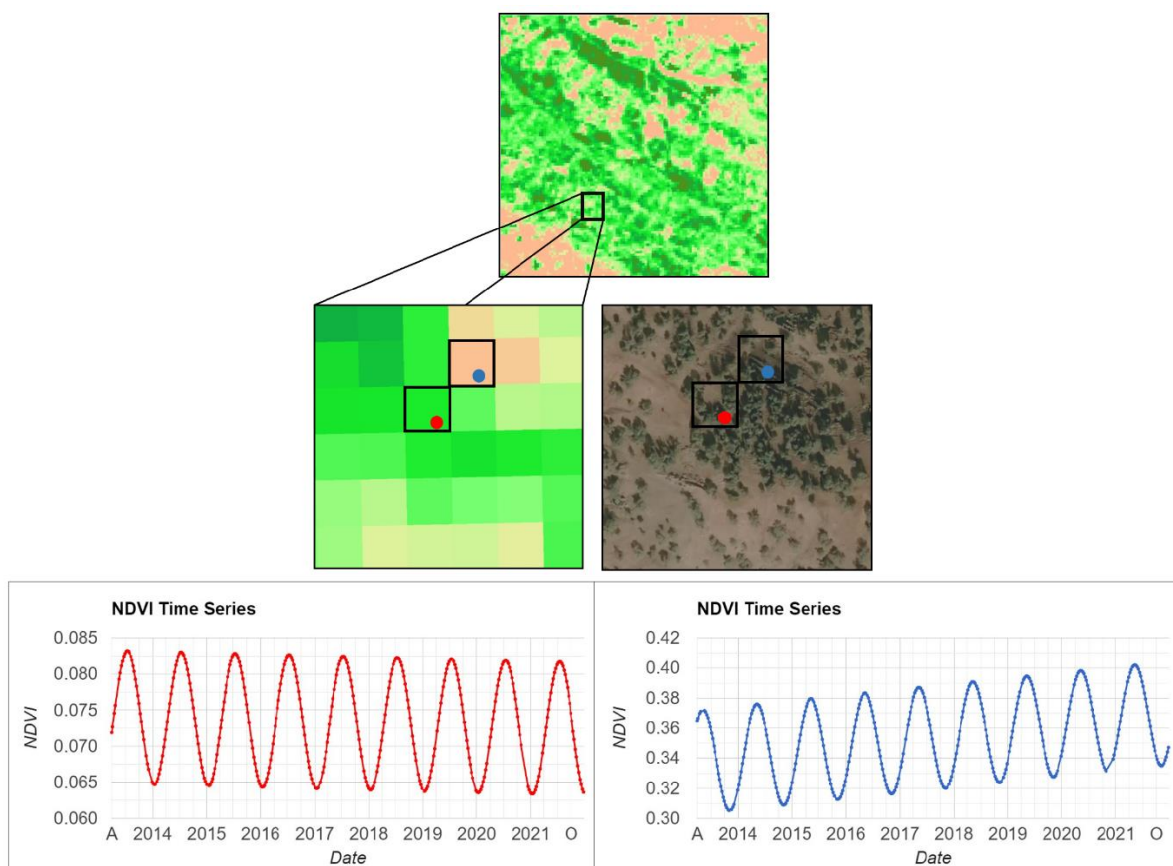
Figure 1.5 Time series of a tree group with an increasing vegetation signal (blue) and a decreasing vegetation signal (red) using a Landsat-8 NDVI time series in part of the study area (the green colors in the map represent higher NDVI values and therefore higher vegetation vitality, and the yellow and pink colors represent lower NDVI values and lower vegetation vitality).

Time-series algorithms for detecting FC change and disturbances over time, include for example Continuous Change Detection and Classification (CCDC; Zhu and Woodcock, 2014), Landsat-based Trends in Disturbance and Recovery Detection (LandTrendr; Kennedy et al., 2010), and Breaks for Additive Season and Trend (BFAST; Verbesselt et al., 2010). However, these algorithms are more advantageous for monitoring large-scale forest changes or deforestation than assessing minor changes induced by forest decline and tree mortality (Zhu et al., 2020; Kennedy et al., 2018; Lausch et al., 2016). For example, the CCDC algorithm demonstrates high spatial and temporal accuracy for detecting various LC changes but performs poorly in identifying forest disturbances with relatively minor change magnitudes (Zhu et al., 2020). LandTrendr utilizes Landsat time-series stacks and temporal segmentation to identify significant characteristics related to discrete and gradual trends (Pasquarella et al., 2022). However, it has limited application in arid and semi-arid regions. On the other hand, the BFAST algorithm, following a similar principle as LandTrendr, excels at detecting abrupt changes, not gradual ones like forest decline (Watts and Laffan et al., 2014). Due to the mentioned drawbacks of these algorithms, we employed alternative time series approaches such as Sen's slope and anomaly analysis in this thesis. The implementation of these methods will be explained in depth in Chapter 3.

1.9. Employed RS sensors: spatial and temporal resolutions

A sensor, such as a digital camera, acts as a tool for detecting and recording electromagnetic radiation that comes from the surface or atmosphere of the Earth. This radiation can include visible light, infrared, or microwave wavelengths. In typical passive optical sensors, this radiation information is stored in the form of images composed of pixels with each pixel representing one cell of the sensor chip. Spatial resolution is the measure of detail within the collected images, typically indicated by pixel size, that is the area that is represented by one pixel in the final image (e.g., 30 m pixel size represents a 30 m by 30 m area) (Lillesand et al., 2008). RS sensors are categorized into passive sensors, which measure reflected energy emitted typically by the sun, and active sensors, which emit their own radiation. This thesis focuses on passive satellite imagery, particularly Sentinel-2 (S2) and Landsat multispectral imagery.

Choosing the appropriate RS sensor is vital for any applied RS study and should take into account the mapping goals, image expenses, climate and atmospheric conditions, and the associated technical challenges for image interpretation (Xie et al., 2008). Multispectral satellite images are advantageous because of their ability to provide extensive spatial coverage and comparably high temporal resolution. Figure 1.6 showcases the sensors employed in this study, including their temporal and spatial resolutions. Details regarding the sensors' resolutions can be found in Table 1.1 to Table 1.4. All RS data employed in the thesis is freely accessible and downloadable for example from the Google Earth Engine (GEE) platform.

1.9.1. S2

Multispectral sensors can struggle to detect early decline symptoms in individual trees due to limitations in spectral, spatial, and temporal resolution (Pontius et al., 2020). However, the

launch of the European Space Agency's S2 (A and B) multispectral sensor showed promise in detecting spectral changes related to forest decline problems (Pontius et al., 2020). The S2 mission includes two polar-orbiting satellites with a 5-day constellation revisit interval and a 10-day individual satellite revisit interval. Detailed spectral band information is available in Table 1.1 (Pontius et al., 2020). In the first study, S2 data were utilized for FC mapping (see Chapter 2). Additionally, in the third study, the S2 spectral values of bare soil surrounding healthy and declining trees of the field-sampled plots were analyzed (see Chapter 4).

Table 1.1 S2 band information

S2 Spectral Band	Wavelength (nm)	Spatial Resolution (m)
B1 - Ultra Blue (Coastal and Aerosol)	433-453	60
B2 - Blue	458-523	10
B3 - Green	543-578	10
B4 - Red	650-680	10
B5 - Visible and Near Infrared (VNIR)	698-713	20
B6- Visible and Near Infrared (VNIR)	733-748	20
B7 - Visible and Near Infrared (VNIR)	773-793	20
B8 - Visible and Near Infrared (VNIR)	785-900	10
B8a - Near Infrared Narrow (NIRn)	855-875	20
B9 – Water Vapor	935-955	60
B10 - Short Wave Infrared (Cirrus)	1360-1390	60
B11 - Short Wave Infrared (SWIR1)	1565-1655	20
B12 - Short Wave Infrared (SWIR2)	2100-2280	20

1.9.2. Landsat

The Landsat family of sensors offers a vast array of data, which is particularly valuable for examining changes in forests on both regional and global scales, as noted by Xie et al. (2008). These sensors have undergone various upgrades since their initial launch in 1972. The multispectral bands in Landsat 4, 5, 7, and 8 provide a spatial resolution of 30 m and a temporal resolution of 16 days, as described by Lillesand et al. (2008). In the second part of this thesis, we utilized Landsat's time series data spanning from 1986 to 2021 to identify and map forest decline using various methodologies (a comprehensive explanation of these methods will be provided in Chapter 2). Further detailed information regarding the Landsat sensors employed in this study can be found in Table 1.2 to Table 1.4.

Table 1.2 Landsat-4 and -5 band information

Landsat-4 and 5 Spectral Band	Wavelength (nm)	Spatial Resolution (m)
Band 1 - Blue	450- 520	30
Band 2 - Green	520-600	30
Band 3 - Red	630-690	30
Band 4 - Near Infrared (NIR)	760-900	30
Band 5 - Near Infrared (NIR)	1550 - 1750	30
Band 6 - Thermal	1040 - 1250	120
Band 7 - Mid-Infrared	2080 - 2350	30

Table 1.3 Landsat-7 band information

Landsat-7 Spectral Band	Wavelength (nm)	Spatial Resolution (m)
Band 1 - Blue	450-520	30
Band 2 - Green	520-600	30
Band 3 - Red	630-690	30
Band 4 - Near Infrared (NIR)	770-900	30
Band 5 - Shortwave Infrared (SWIR) 1	1550-1750	30
Band 6 - Thermal	1040-1250	60
Band 7 - Shortwave Infrared (SWIR) 2	2090-2350	30
Band 8 – Panchromatic	520-900	15

Table 1.4 Landsat-8 band information

Landsat-8 Spectral Band	Wavelength (nm)	Spatial Resolution (m)
Band 1 - Coastal aerosol	430-450	30
Band 2 - Blue	450-510	30
Band 3 - Green	530-590	30
Band 4 - Red	640-670	30
Band 5 - Near Infrared (NIR)	850-880	30
Band 6 - Shortwave Infrared (SWIR) 1	1570-1650	30
Band 7 - Shortwave Infrared (SWIR) 2	2110-2290	30
Band 8 - Panchromatic	500-680	15
Band 9 - Cirrus	1360-1380	30
Band 10 - Thermal Infrared (TIRS) 1	1060-1119	100
Band 11 - Thermal Infrared (TIRS) 2	1150-1251	100
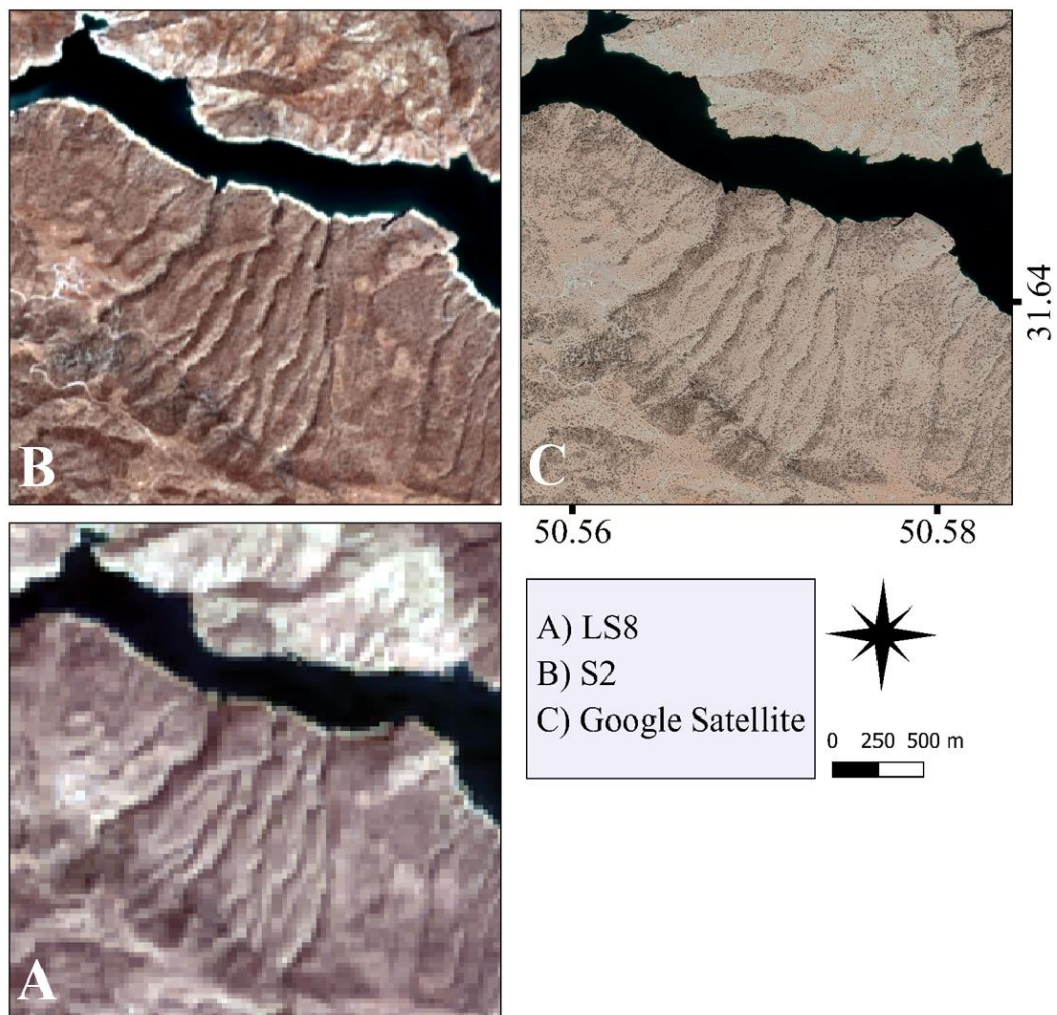
Figure 1.6 Part of the study area: RS datasets with varying spatial resolutions utilized in this thesis from bottom left to top right: (A) Landsat-8; (B) S2, and (C) VHR Google Satellite images

1.10. Research gaps in studying arid and semi-arid FC and forest decline using RS

1.10.1. Reliability of global FC products

The assessment of FC using satellite imagery has received comparatively less attention within arid and semi-arid regions (Soleimannejad et al., 2018; Yang et al., 2012). In contrast, earlier studies tend to concentrate on temperate ecosystems (e.g., Heckel et al., 2020), boreal regions (e.g., Korhonen et al., 2017), and tropical forests (e.g., Waśniewski et al., 2020). Conducting consistent ecosystem-wide assessments of FC across expansive geographical areas is challenging to achieve solely through field campaigns. As a result, many research efforts have merged field data with RS information to tackle this issue (e.g., Wagenseil and Samimi, 2007) or, alternatively, collected data solely using high-resolution aerial surveys, unmanned aircraft, or satellites (e.g., Fassnacht et al., 2021; Ludwig et al., 2019; Kattenborn et al., 2019). In the context of forest RS, tropical, temperate, and boreal forests set themselves apart from arid and

semi-arid ecosystems that exhibit a specific pattern of scattered tree occurrences. The resulting discontinuous crown cover leads to unique structural and spectral characteristics which differ from the mostly continuous FC in temperate, tropical, and boreal forests. The canopies of arid and semi-arid forests, characterized by a patchy and often sparse nature, also form a strong contrast with the bright soil background (Abdollahnejad et al., 2019). This contrast notably impacts the relationship between the FC and the satellite signal that is observed. These variations in spectral characteristics might be a key reason for the limited reliability of global FC products in these regions (Cunningham et al., 2019). Notably, underestimations of FC are commonly observed in these ecosystems (Friedl et al., 2002; Bastin et al., 2017; Cunningham et al., 2019). This scenario can create issues because global FC products are commonly used in environmental modeling and the planning of forest restoration and afforestation efforts, as well as forest decline studies. However, they are rarely thoroughly validated on a global scale (Fagan 2020). The issue with the accuracy of global products becomes evident (also mentioned by Bai 2010) in examples like Figure 1.7, where regions densely covered with trees are inaccurately portrayed as largely free of forests in two global FC products: the Hansen Global Forest Change Map 2000–2014 and the Global TanDEM-X Forest/Non-Forest Map by DLR. These two products indicate that most areas in the Zagros region have less than 10 percent woody vegetation or forests, even though in reality, there are locations where these forests have cover values ranging from 60 to 80 percent (Sagheb-Talebi et al., 2014). Therefore, a proper workflow to determine FC in arid and semi-arid patchy forests like Zagros is still missing.
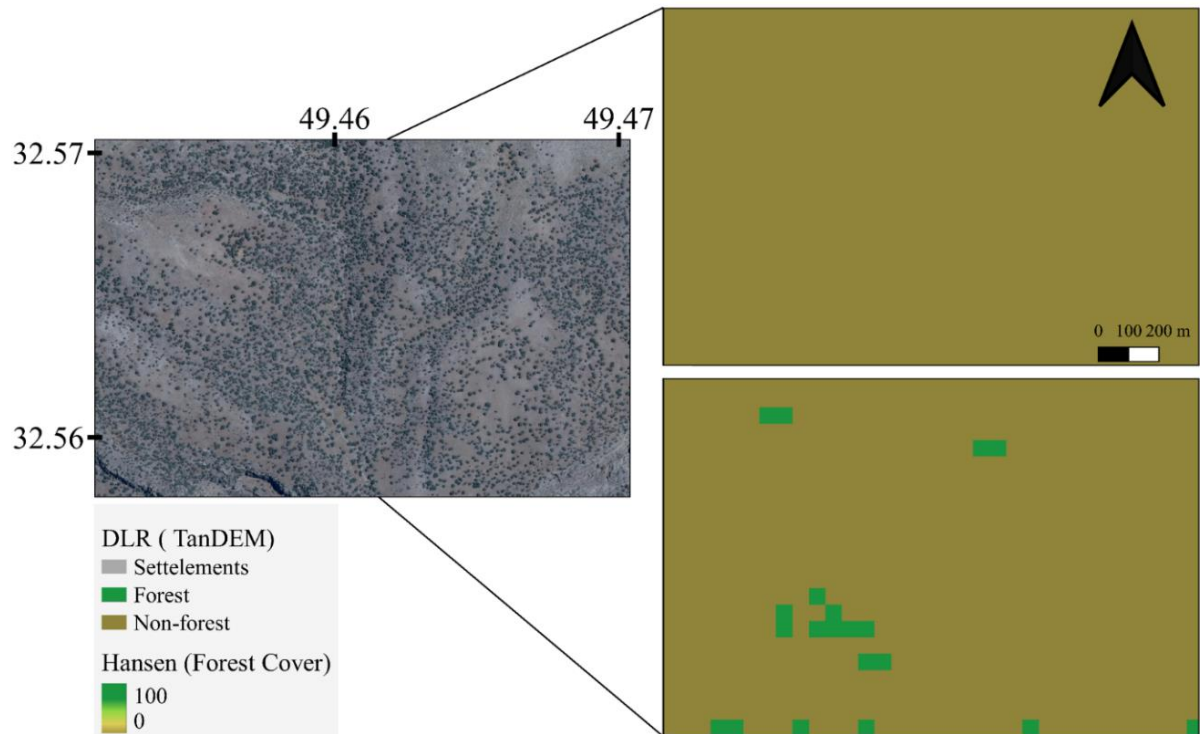
Figure 1.7 A Google satellite view of a small area of the Zagros region is in the left panel. The Hansen Treecover 2000 layer from the global FC product is shown in the upper right quadrant. Even though the high-resolution images show a significant amount of woody cover in this location of the Zagros area, the Hansen FC data suggests no coverage across the area. The DLR TanDEM-X Forest/Non-Forest

(FNF) product for the same area is shown in the lower right panel. Most of the zoomed-in area is categorized as non-forest (EPSG 4326).

1.10.2. Forest decline mapping and understanding

Another issue with using RS to detect forest decline is that it can only detect symptoms of decline that are visible and occur in large enough areas to be seen by the sensor, as noted by Pontius et al. in 2020. Subtle spectral signals related to degradation or decline are difficult to detect (Hoekman et al., 2020). Forest disturbance caused by abrupt and discrete disturbances (i.e., wildfire or timber harvest) is easier to spot than forest decline caused by gradual disturbances that last several years. As a result, there have been relatively few studies focusing on the detection and mapping of forest decline, particularly in arid and semi-arid regions.

The few existing studies for the Zagros region have concentrated on mapping and monitoring forest decline (e.g., Ghasemi et al., 2023; Ghasemi et al., 2022; Karami et al., 2018). On the other hand, investigations into the causes and interconnections of potentially related variables responsible for this decline are still sparse and only very limited studies exist (Moradi et al., 2021). Therefore, more driver analyses examining forest decline in arid and semi-arid forests are still urgently needed.

1.11. Research objectives

1. The objective of the first study in this thesis is to develop a workflow for estimating woody coverage in an extensive semi-arid region covering over 5,000,000 hectares using readily available S2 satellite data. Additionally, as a secondary aim, we investigate the impact of different spatial grains on the accuracy of the model.

2. The second study is focused on assessing the efficiency of established techniques, including random forest (RF), anomaly detection, and Sen's slope analysis, in the detection and mapping of forest decline within a portion of the semi-arid Zagros forests, covering an area of approximately 350,000 hectares. This evaluation is based on the analysis of Landsat time series data spanning from 1986 to 2021.

3. The third study, covering an area of approximately 165 km², seeks to examine the environmental factors and tree attributes contributing to the decline of mountainous, patchy, semi-arid Zagros forests. It aims to understand the impact of factors like topography, FC, DBH (diameter at breast height), and other relevant variables on the varying levels of tree and forest decline, including healthy, mildly declining, moderately declining, and severely declining conditions. The objective is to enhance our comprehension of the forest decline phenomenon by analyzing the associations between different patterns of decline and potential contributing factors.

1.12. Thesis roadmap and structure

The first chapter, "Introduction", has supplied a synopsis of this thesis, including its research gaps, motivations, and definitions of key terms. Chapter 2 depicts the first study published in the scientific journal "International Journal of Applied Earth Observation and Geo-information", which uses S2 and high-resolution data to produce a woody cover map for the entire Zagros forests at various spatial grains. This chapter also the description of a workflow to create a comprehensive LC map of the study area.

Chapter 3 presents the second study on forest decline detection published in the "European Journal of Remote Sensing". This study is focused on detecting and mapping forest decline within a portion of the Zagros Forest, utilizing three time-series approaches: RF, anomaly analysis, and Sen's slope. Landsat satellite time series data spanning 36 years is employed for this purpose. Chapter 4 presents the third study submitted to "Forestry: An International Journal of Forest Research". This study is focused on understanding forest decline within a 165 km^2 portion of the Zagros Forest. Environmental factors, such as topography, FC, etc., are studied alongside tree characteristics, including DBH. Finally, Chapter 5, Synthesis and Outlook, concludes the thesis by summarizing the key findings and addressing the challenges encountered. This chapter also lays the foundation for future research through thought-provoking recommendations.

1.13. List of papers

1. **Shafeian**, **E**., Fassnacht, F.E., and Latifi, H., 2021. Mapping fractional woody cover in an extensive semi-arid woodland area at different spatial grains with Sentinel-2 and very high-resolution data, International Journal of Applied Earth Observation and Geo-Information, 105, 102621; DOI: 1016/j.jag.2021.102621.
2. **Shafeian**, **E**., Fassnacht, F.E., and Latifi, H., 2023. Detecting semi-arid forest decline using Landsat time series, European Journal of Remote Sensing, 56(1); DOI: 10.1080/22797254.2023.2260549.
3. **Shafeian**, **E**., Ewald, M., Latifi, H., Fassnacht, F.E., 2023. Unveiling the main drivers of tree decline in Zagros semi-arid Forests, Forestry: An International Journal of Forest Research, (submitted).

1.14. Summary of the author's contribution

The research papers were prepared in collaboration with several co-authors. All manuscripts were originally drafted by me and subsequently revised by the co-authors. Apart from writing, I was involved in the study design and conducted the fieldwork with the help of my co-authors (and others). I performed the data processing and analysis, stimulated by the ideas of the co-authors. Finally, the results were discussed and interpreted in collaboration with the co-authors.

2. Mapping fractional woody cover in an extensive semi-arid woodland area at different spatial grains with Sentinel-2 and very high-resolution data

Elham Shafeian, Fabian Ewald Fassnacht, Hooman Latifi

Abstract

Woody canopy cover is an essential variable to characterize and monitor vegetation health, carbon accumulation, and land-atmosphere exchange processes. RS-based global woody and FC maps are available, but with varying qualities. In arid and semi-arid areas, existing global products often underestimate the presence of woody cover due to the sparse woody cover and bright soil background. Case studies on smaller regions have shown that a combination of collected field data and medium-to-high-resolution free satellite data (e.g., Landsat or S2) can provide woody cover estimates with practically sufficient accuracy. However, earlier studies focused on comparably small regions and relied on costly field data. Here, we present a fully RS-based workflow to derive woody cover estimates over an area covering more than 0.5 million km^2. The workflow is showcased over the Zagros Mountains, a semi-arid mountain range covering western Iran, the northeast of Iraq, and a smaller fraction of southeast Turkey. We use the Google Earth Engine to create homogeneous S2 mosaics of the region using data from several years. These data are combined with reference woody cover values derived by a semi-automatic procedure from Google® and Bing® very high resolution (VHR) imagery. Several RF models at different spatial grains were trained and validated at each grain with iterative splits of the reference data into training and validation sets (100 repetitions). The best results (considering the trade-off between model performance and spatial detail) were obtained for the model with a 40-m spatial grain, which showed stable relationships between the VHR-derived reference data and the S2-based estimates of woody cover density. The model resulted in median values of the R^2 and RMSE of 0.67 and 0.11, respectively. Our workflow is potentially also applicable to other arid and semi-arid regions and can contribute to improving currently available global woody cover products, which often perform poorly in semi-arid and arid regions. Comparisons between our woody cover products and common global woody or FC products indicate the clear superiority of our approach. In future studies, these results may be further improved by taking into account regional differences in the drivers of woody cover patterns along the environmental gradient of the Zagros area.

2.1. Introduction

Woody vegetation canopy cover (hereafter termed woody cover) is one of the most commonly used structural parameters to describe forest and woodland ecosystems and is an essential biodiversity variable under the class of ecosystem structure (Jongman et al., 2017). Woody cover is defined as the fraction of land that is covered by the vertical projection of trees' and shrubs' canopies relative to the entire area (Gonsamo et al., 2013; Yang et al., 2017). The woody cover is also an important input parameter to describe biosphere-atmosphere exchange processes such as evapotranspiration (Villegas et al., 2015). Further, woody cover can be used to describe the current state of an ecosystem: reductions in woody cover may indicate decline or overexploitation processes in forest and woodland areas (e.g., Wang and Cochrane, 2005), with corresponding losses in biomass and, hence, sequestered carbon. Increases in woody cover may indicate reduced anthropogenic pressure, for example, due to land-use changes (e.g., Baumann et al., 2012) or climate-change-induced encroachment of woody species in temperature- or, in some cases, precipitation-limited ecosystems (e.g., García Criado et al., 2020). In dryland ecosystems, an increase in woody cover may indicate unfavorable shrub encroachment processes, which may fragment habitats and endanger biodiversity (e.g., Yang and Crews, 2019). Regular monitoring of woody cover at the ecosystem level over large geographical areas is hardly feasible with terrestrial surveys alone. Hence, numerous studies have combined field data with RS data (e.g., Wagenseil and Samimi, 2007) or directly used remote sensing approaches to map forest or woody cover (e.g., Yang and Crews, 2019; Zhang et al., 2019; Nagelkirk and Dahlin, 2020). Woody cover over local to regional extents has, for example, been estimated from airborne RS data, including aerial photographs (e.g., Fadaei et al., 2010; López et al., 2016) and laser scanning data (e.g., Andersen et al., 2005; Lee and Lucas, 2007). While these approaches typically provide realistic woody cover estimates, these data are often restricted in their spatial coverage due to quite high costs and thus may not be available for some parts of the Earth. Therefore, other studies examined freely available satellite data to estimate forest and woody cover using data from sensors such as Landsat TM (Rikimaru et al., 2002; Nandy et al., 2003; Deka et al., 2012), Landsat ETM+ (Deka et al., 2012; Joshi et al., 2006), Landsat 8-OLI (Korhonen, 2017), and S2 (e.g., Korhonen et al., 2017; Zhang et al., 2019). As summarized by Yang et al. (2017), most of these studies applied one of three methodical approaches to estimate woody cover. These include pixel-wise and spectral unmixing, physically-based modeling, and empirical modeling approaches.

In contrast to empirical methods, the spectral unmixing method does not necessarily involve field-based measurements, as all required information can be derived directly from the image being unmixed (Nagelkirk and Dahlin, 2020). The basic principle of pixel-wise spectral unmixing follows the assumption that the spectrum of each pixel is a (linear) mixture of the spectra of a limited number of so-called endmembers. Each endmember represents the spectral properties of one of the "pure" LC classes typically occurring in the region (e.g., soil, woody vegetation, rocks).

Comparing the spectrum measured for an individual pixel against the mixed spectra of the end members then allows us to estimate the percentage cover of each of the corresponding LC classes in the pixel. In a recent study in the presence of field data, spectral unmixing outperformed linear regression for mapping woody cover in a savannah environment, while RF outperformed the unmixing approach (Nagelkirk and Dahlin, 2020). The selection of endmembers was stated to be challenging in semi-arid regions due to the varying spectral properties of vegetation and soil over time and space (Nagelkirk and Dahlin, 2020).

The inversion of physically-based models, which simulate the physical relationships between vegetation canopies' spectral reflectance and a set of parameters including leaf and canopy traits, soil properties, and view-geometry parameters, has also been used to estimate fractional vegetation cover (FVC), a variable related to woody cover (Baret et al., 2007; Yang et al., 2017). Direct inversion of these models is usually difficult due to the complexity of the physical models, which often require the definition of numerous parameters while the corresponding data are limited. The comparably heterogeneous horizontal vegetation structure of semi-arid woodlands may also not match the key assumptions of some radiative transfer models. For example, the SAIL model assumes a horizontally homogeneous canopy (Verhoef 1984), which cannot be assumed for most semi-arid woodlands at the spatial scale of Landsat or S2. Hence, most studies and data products that follow a physical modeling approach to estimate variables related to vegetation cover are based on coarse-resolution data. Using coarse-resolution data, some generalizations can be made concerning the parameters required for the inversion procedure, and the assumption of a homogeneous canopy cover may become acceptable. For example, Yang et al. (2017) mention products based on MODIS and MERIS data, and Baret et al. (2007) used the PROSAIL model to estimate FVC from VEGETATION data at approximately 1.15 km spatial resolution. Contrarily, studies applying physically-based models to estimate vegetation cover at finer resolution are lacking, most likely due to the restrictions outlined above.

Finally, the presumably most common and straightforward approach to estimating woody cover is via empirical models, in which a statistical relationship between vegetation cover and remotely sensed spectral information is established (Yang et al., 2017). Many earlier studies combined woody cover reference values obtained from field data or very high spatial resolution imagery (VHR) with moderate to high spatial resolution satellite data (e.g., Wagenseil and Samimi, 2007; Bucini et al., 2009) via statistical or machine learning models (e.g., Wingate et al., 2019; Liao et al., 2020; Anchang et al., 2020). Machine learning models are often applied because of their computational efficiency and robustness against noisy data, as well as their ability to estimate multivariate nonlinear relationships (Yang et al., 2017). A general key limitation of empirical models is their commonly observed restriction to the environmental conditions under which they were established (Schlerf and Atzberger, 2006). As a result, empirical models often cannot be extrapolated to new conditions that were not covered in their calibration data (Twery and Weiskittel, 2013). Calibration data, in turn, are typically constrained by the availability of field or other reference datasets. On the other hand, empirical models need only basic inputs, are simple

to implement, and often perform better than physical models and spectral unmixing approaches within a limited data space or study area. Hence, they are a viable option if the corresponding reference data demands can be met. This high data demand for empirical models has become less problematic over the last few years. Numerous new satellite sensors deliver continuous streams of satellite data, with some of the data being available free of charge (Turner et al., 2015). Also, corresponding reference data have become increasingly available through data sharing and direct derivation from VHR imagery collected by aerial surveys, unmanned aerial systems, or satellites (e.g., Ludwig et al., 2019; Kattenborn et al., 2019; Fassnacht et al., 2021). In summary, empirical models have shown to work well if sufficient reference data are available, i.e., the advantages of empirical models over physical models and unmixing approaches may prevail if large amounts of reference data can be obtained at a low cost.

Independent from the applied methodology, earlier studies examining workflows to estimate woody cover tend to focus on temperate (e.g., Heckel et al., 2020), boreal (e.g., Korhonen et al., 2017), and tropical forests (e.g., Waśniewski et al., 2020). Contrarily, the estimation of woody cover from satellite imagery has been less frequently examined in arid and semi-arid regions (Soleimannejad et al., 2018; Yang et al., 2012). In the context of RS, such regions differ from tropical, temperate, and boreal forests in both their structural and spectral properties. Dryland ecosystems like the woodlands found in the semi-Mediterranean Zagros area on which we focus in this study are associated with patchy occurrences of trees and a corresponding discontinuous crown cover. In Zagros, these patterns are a result of the joint effects of a longstanding land use history and climatic conditions. These patchy and often sparse canopies typically build a strong contrast to the bright soil background (Abdollahnejad et al., 2019), which notably affects the relationship between woody cover and the observed satellite signal.

Depending on the exact location and season in which RS data are acquired, herbaceous vegetation may additionally have a notable influence on the spectral signal (Rautiainen and Heiskanen, 2013; Rautiainen et al., 2011). In arid and semi-arid regions, vegetation growth is mostly limited by water availability; thus, vegetation phenology displays pronounced seasonal trends following the precipitation patterns (wet and dry seasons) of the region (Wagenseil, Samimi, 2007). Hence, previous studies suggested that applying multi-temporal intra-annual data can be useful for mapping woody cover in arid and semi-arid regions (Zandler et al., 2015; Wingate et al., 2019; Ludwig et al., 2019). It has also been observed that spectral bands in the visual and near-infrared regions often show a greater contrast between soil and woody vegetation during the dry season due to the lack of herbaceous vegetation (Ludwig et al., 2019). These differences in the spectral properties of arid and semi-arid woodland forests as compared to boreal, temperate, and tropical forests may be one important reason why global FC products often perform poorly in arid and semi-arid regions (Cunningham et al., 2019). In particular, underestimations of woody cover are common in these ecosystems (Friedl et al., 2002; Bastin et al., 2017; Cunningham et al., 2019). This can be problematic as these global FC products are often used as input to environmental modeling studies and for the planning of forest restoration and afforestation measures but are rarely

scientifically evaluated in these studies (Fagan, 2020). Inaccuracies in these products may also affect future decision-making, especially in regions that are associated with data scarcity (Cunningham et al., 2019). This local quality issue of global products is shown, for example, in Figure 2.1, where areas densely stocked with trees are depicted as mostly unforested in two global FC products (i.e., the Hansen Global Forest Change map 2000–2014 and the Global TanDEM-X Forest/Non-Forest Map by DLR). These two products show less than 5 percent woody vegetation or forests in most parts of the Zagros area, although in reality there are some areas in which these woodlands have cover values of up to 80–90 percent (Sagheb-Talebi et al., 2014). It has to be mentioned, though, that, for example, the Hansen global FC product is estimated for trees with heights greater than 5 m. These tree heights are not achieved in all areas of Zagros; however, a comparably large fraction of the oak forests of the region have notably higher trees. This is only one example that shows that the accurate quantification of woody cover from satellite imagery over dryland ecosystems with sparse vegetation cover (Soleimannejad et al., 2018; Yang et al., 2012) and often limited amounts of field reference data (Bai, 2010) still remains a challenge.
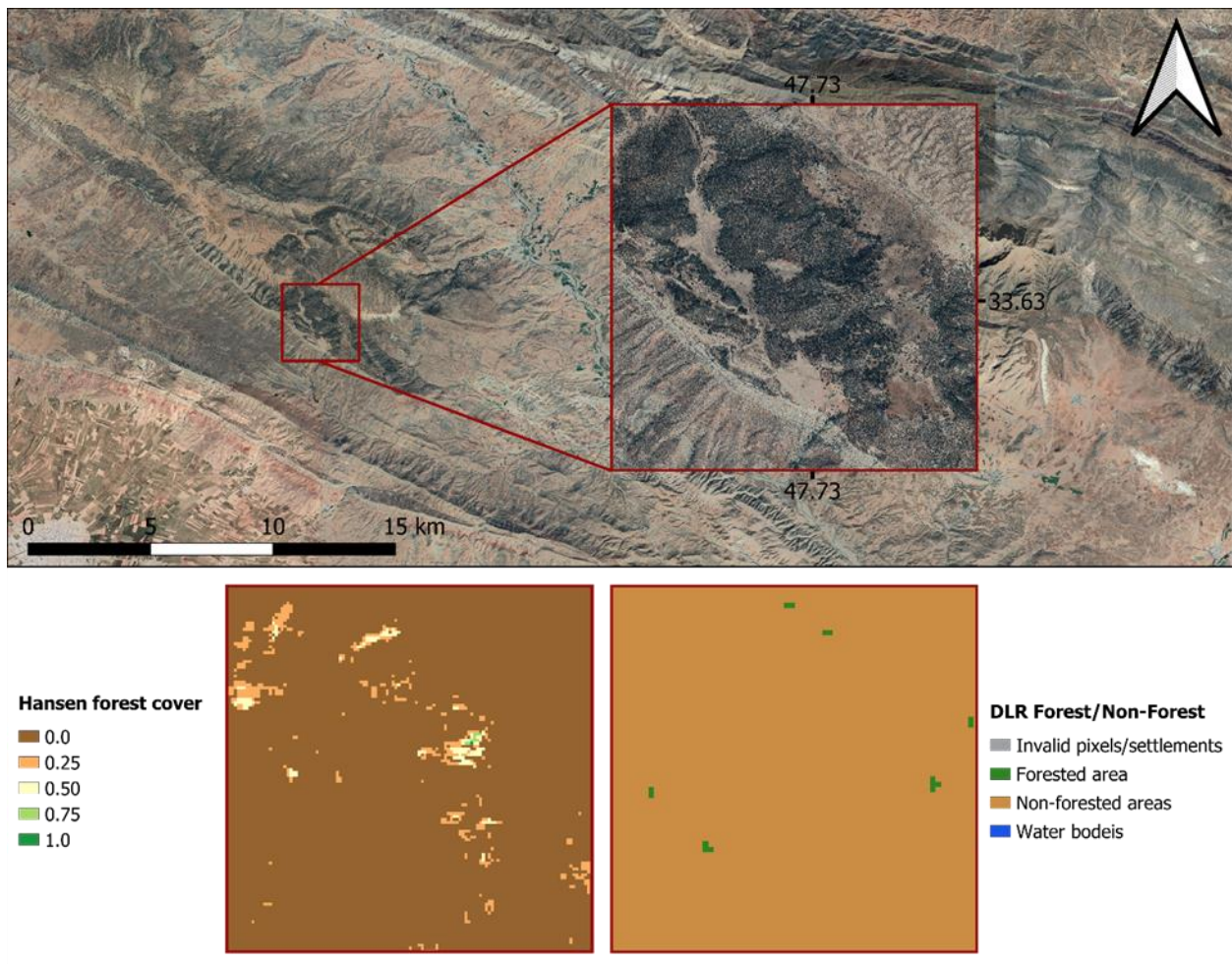
Figure 2.1 The top panel shows a VHR Google satellite image of a small area in Zagros. The bottom left panel shows the Hansen treecover2000 layer of the global FC product. In this area of Zagros, the Hansen FC is very low in most parts even though the VHR images show a very high woody cover; in the bottom right panel, the DLR TanDEM-X Forest/Non-Forest (FNF) product for the same area is depicted. Almost the whole area is classified as non-forest as well. (The comparison of this area with the results of our woody cover map, is also shown in the Supplementary Material I). All images are projected in the geographic coordinate system (EPSG 4326).

This challenge has been widely discussed in several recent studies. For example, Fagan (2020) shows that relying on current global FC products may lead to a wide overestimation of the afforestation potential in dryland regions as the actual FC is notably underestimated. Bastin et al. (2017) show in a study based on an extensive dataset of photo-interpreted forest and woodland plots in drylands (using VHR imagery available on Google Earth) that the actual tree cover of global drylands may be 40–47% higher than reported by global tree cover products. A more general discussion of the challenges of RS approaches in dryland ecosystems can be found in the recent review of Smith et al. (2019).

In this study, we focus on the "Zagros Forests," which spread over a semi-arid mountain range covering western Iran, the northeast of Iraq, and a smaller fraction of southeast Turkey. Baseline information is generally sparse in this enormous area (about 5.5 million ha), and obtaining a woody cover map at a fine spatial grain is an important contribution to characterizing the forest structure of this vast area. Furthermore, information on woody cover is an important prerequisite for subsequent forest decline analyses from satellite time series, as the comparably large influence of the soil background has to be accounted for (Soleimannejad et al., 2018; Yang et al., 2012). To our knowledge, no study so far has estimated the woody cover of the entire Zagros Forests. Previous studies only examined a smaller subset of the Zagros area (e.g., Darvishsefat and Saroei, 2003; Ahmadi Sani et al., 2007; Abdollahi et al., 2010; Shahvali Kouhshour et al., 2012; Mirzaeizadeh et al., 2015).

The objective of this study is to develop a workflow to derive woody cover estimates across a very large semi-arid area based on freely available S2 satellite data. As a sub-objective, we additionally examine how the spatial grain of the analysis affects the model quality. The latter is interesting for at least two reasons: 1. we expect that at the spatial grain of S2, the patchy occurrence of trees and shrubs may complicate the accurate estimation of woody cover, and switching to slightly coarser spatial grains may improve the model's performance. 2. A slightly coarser grain may additionally reduce the variability introduced by sub-pixel spatial shifts between reference data and S2 data. The presented workflow is potentially also applicable to other arid and semi-arid forest and woodland areas and can contribute to improving currently available global FC products, which often perform poorly across areas dominated by sparse woody vegetation on bright background soil.

2.2. Materials and Methods

2.2.1. Study Area

Our study area includes the entire Zagros Forests, covering more than 5.5 million ha across a length of approximately 1300 km (Khabazi, 2020; Rahimi et al., 2020). A third of the total population of Iran lives in this region (Pourmoghadam et al., 2013). The Zagros area encompasses more than 42 percent of Iran's forests. The area spreads from the southern part of West Azerbaijan Province to the Fars Province (Mahdavi et al., 2014) and expands to neighboring countries (northern Iraq and southeastern Turkey) (

Figure **2.2**). The climate in the Zagros area is semi-arid, with a mean annual precipitation of 250 to 800 mm and a mean annual temperature of 9 to 25 °C (Attarod et al., 2016). The woodlands in Zagros are associated with patchy occurrences of trees and a corresponding discontinuous crown cover. The most dominant and frequent tree species include Brant´s Oak (*Quercus brantii* var. persica), which is partly mixed with *Quercus infectoria* G.Olivier, *Quercus libani* G.Olivier, wild pistachio (*Pistacia atlantica* Desf.), *Acer monspessulanum* L., *Crategus* spp., *Amygdalus* spp., and *Pyrus* spp. (Erfanifard et al., 2014). The prevailing mixtures depend on multiple site factors along the latitudinal gradient. The Zagros Forests play an important role in maintaining endemic vegetation and wildlife habitats, providing forage and shelter for nomadic and rural populations and their cattle, as well as non-wood forest products like natural gum, oak seeds, and oak gall (Jazirei, Ebrahimi-Rostaghi, 2003; Sagheb-Talebi et al., 2014). Over the last decades, the Zagros area has been deeply affected by environmental and political processes such as the occurrence of weather extremes, the 8-year Iran-Iraq war (1980–1988), and the still ongoing oak dieback (Alibakhshi et al., 2019; Arsalani et al., 2018), which have all contributed to the decline of the ecosystems in Zagros.
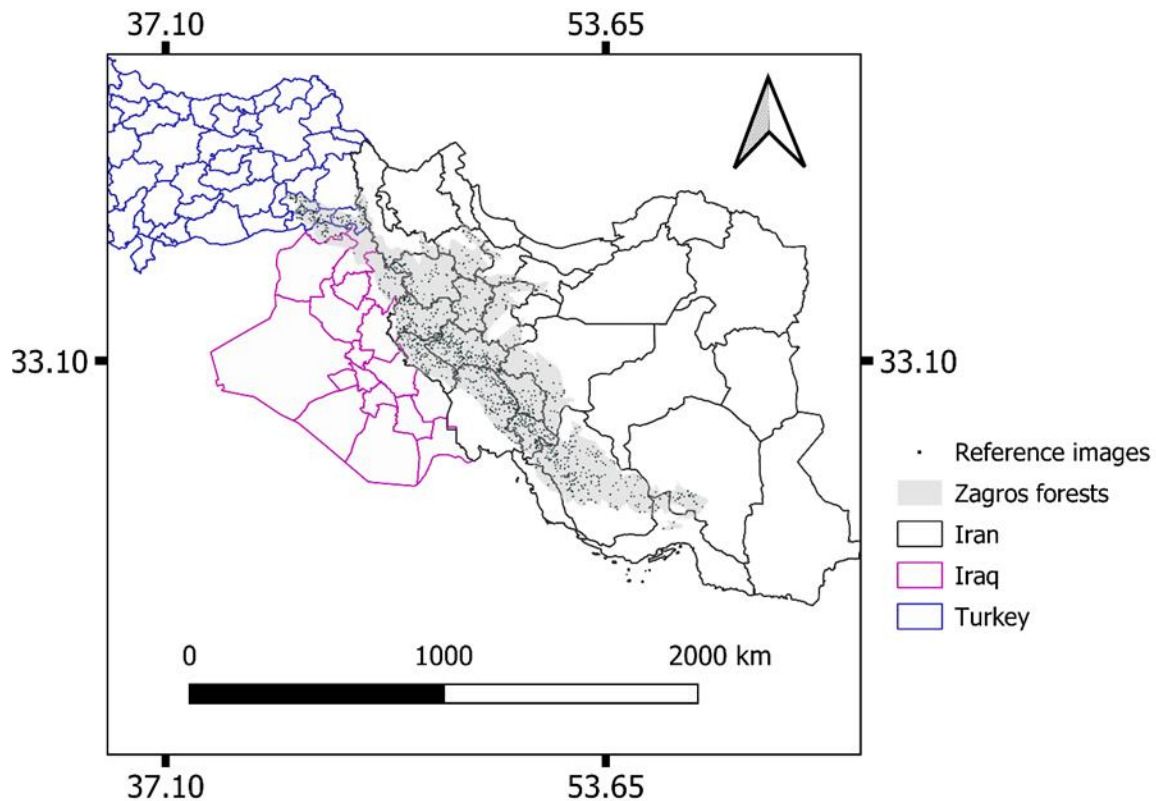
Figure 2.2 Location of the Zagros study area. The small black dots indicate the location of the reference images. The colored polygons show the provinces of the three countries comprising parts of the Zagros area.

2.2.2. RS data

This research is based on two main data sources: multispectral S2 satellite data and VHR satellite images from Google Earth and Bing.

2.2.2.1. Reference data preparation for woody cover estimation

A large woody cover reference data set was collected using VHR Google Earth and Bing imagery. The most recent acquisition dates for VHR imagery were 2015 and 2016, and the spatial resolution of Google Earth and Bing imagery ranges from 15 m to 15 cm. In this study, we did not use images with less than 1.5 m spatial resolution to reduce uncertainty in the reference dataset. To compose our reference dataset, a total of 8000 points were randomly sampled inside the Zagros area, and a square buffer with a 200×200 m area was generated around each point. To create these buffers, we used the gBuffer function available in the rgeos library (Bivand et al., 2018) in R (R Development Core Team, 2021). Then, the corresponding Google Earth and Bing images were visually screened in QGIS to allocate the Google and Bing images at each location to one of the

three classes ("wooded area =1", "no wooded area = 0," and "non-interpretable area" = 99) according to the area within each buffer. The non-interpretable areas mostly referred to image scenes of low quality (e.g., coarse spatial resolution, blurry images, images dominated by dark shadows) in which the woody cover could not clearly be identified. Non-interpretable areas were excluded, and the remaining images (in total, 1270 images) formed the basis of our reference dataset. The reference samples were well distributed over the entire Zagros area (
Figure **2.2**) and had an average distance of approximately 8.8 km from each other.

All the selected reference images were saved as geo-located screenshots in QGIS and cropped to the size of the squared buffers of 200 × 200 m. Then, a semi-automatic threshold-based approach was applied in R using raster and Rgdal libraries to prepare a binary dataset indicating the presence and absence of woody cover in each pixel of the high-resolution reference images. For this, we systematically applied several thresholds (typically ranging from 50 to 150 while the radiometric resolution of the screenshots was 8 bits with values from 0 to 255) to the blue channel of the RGB images until the resulting binary image agreed well with the visual impression of the woody cover's presence. Due to the very dark appearance of the woody vegetation in front of the bright soil background, this procedure was straightforward and reliable. This procedure resulted in high-resolution binary images indicating areas of woody cover and bare soil (
Figure **2.3**). From these images, the fractional woody cover in percent could be easily obtained for any subset of the high-resolution reference image by dividing the number of woody cover pixels by the total number of pixels. For each RF model (see
Figure **2.3**), we automatically produced the woody cover reference values from the high-resolution binary reference images by overlapping them with a polygon or vector file corresponding to the pixel size and selected grain of S2, as suggested by previous studies (e.g., Higginbottom et al., 2018). All reference images can be accessed via a link provided in Supplementary Material I.
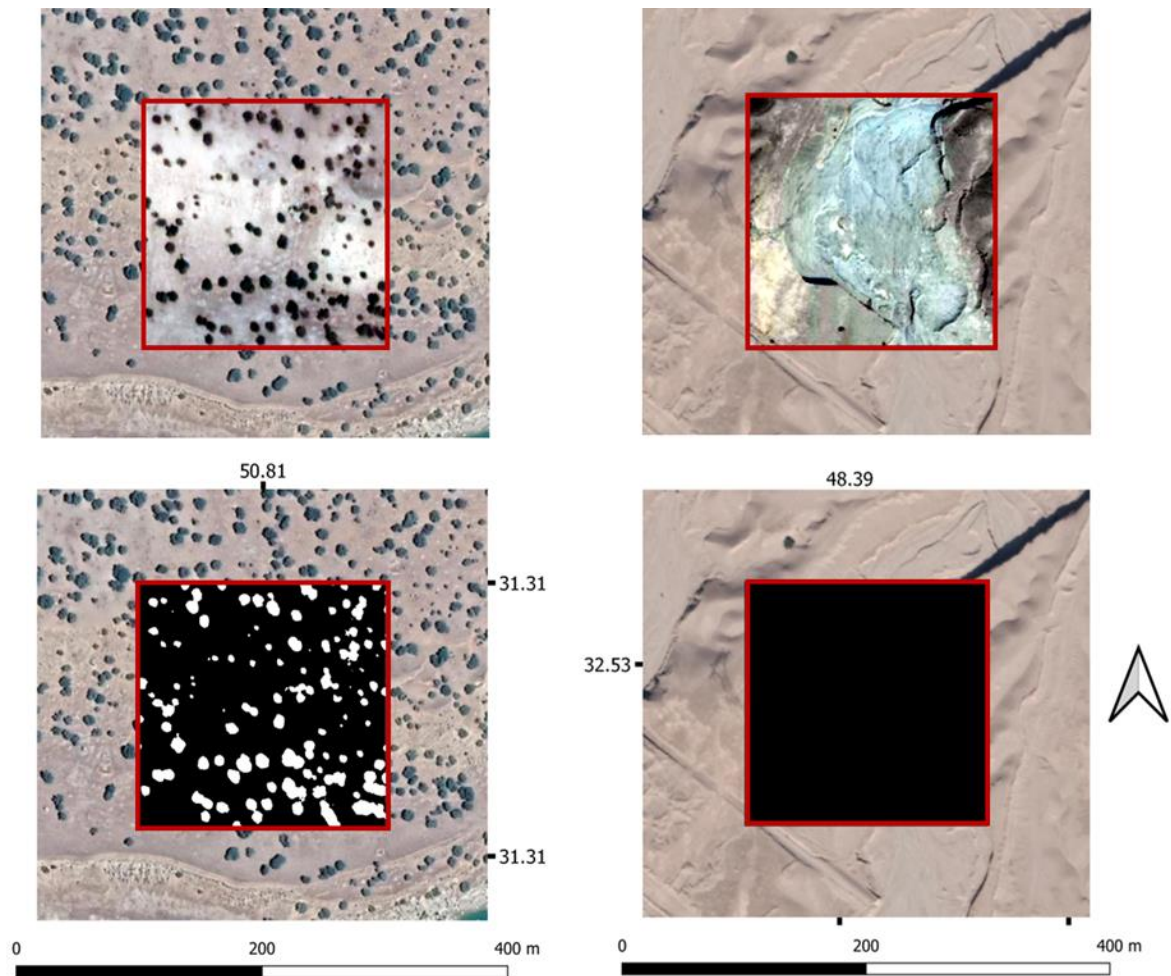
Figure 2.3 Preparation of the binary reference images for a wooded area (left panels) and a non-wooded area/bare soil (right panels) based on a simple threshold-based procedure.

2.2.2.2. Preparation of S2 mosaics and predictor variables

We applied S2 surface reflection imagery available in the GEE platform (https:/earthengine.google.org/) data catalog. A detailed description of this data product and the applied radiometric, geometric, and atmospheric corrections can be found on the GEE webpage: (https://developers.google.com/earth-engine/datasets/catalog/COPERNICUS_S2_SR, last access October 11, 2021).

These data have a 5-day temporal resolution. For creating cloud-free mosaics, we first defined a filter to only consider S2 images with a maximum cloud cover of 30%. Then, from all remaining images acquired in the time period between 2018 and 2020 and during the summer months (June–September), we calculated a composite mosaic image directly in the GEE. We did this by first using the quality assessment band (QA60) to eliminate cloud and cloud shadow-affected pixels for each of the S2 scenes (Gao et al. 2017; Zhang et al. 2020). Then we calculated the median reflectance value for each pixel and band from the remaining cloud-free image stack, which

26

resulted in a cloud-free, high-quality mosaic. A visual screening of the mosaic showed that no recognizable data artifacts were present. In our preliminary analyses, we also examined the potential benefits of adding S2 mosaics from other seasons, but these did not improve the results. For the sake of parsimony, we focused on the summer mosaics only.

In addition to the 10 S2 bands with 10- and 20-m resolutions, we calculated the NDVI and the reduced simple ratio (RSR) index. We included the RSR as it was found to decrease background effects in areas with open canopy cover in earlier studies (e.g., Brown et al., 2000; Zhu et al., 2010). Furthermore, a binary vegetation layer predictor variable was produced by applying a threshold of 0.17 to the S2 NDVI image, which resulted in a binary image of vegetated and non-vegetated areas. Then, the fraction of vegetation pixels at 10 m pixel size within the reference areas was determined and used as a predictor variable. The relatively low threshold was selected due to generally lower NDVI values in semi-arid regions such as the Zagros Forests (Eskandari et al., 2020). To account for potential influences of the large environmental gradient covered by the Zagros area on the relationship between RS data and woody cover, we also included Bioclim variables (BIO12 = annual precipitation, BIO15 = precipitation seasonality (coefficient of variation), BIO16 = precipitation of the wettest quarter, and BIO17 = precipitation of the driest quarter) from the GEE data catalog in our woody cover models. Furthermore, we calculated gray-level co-occurrence texture metrics (GLCM) using the NIR band (Band 8) of S2 and the NDVI to also consider the spatial context (Wood et al., 2012). GLCM texture variables were previously stated to be a strong proxy for vegetation structure (Wood et al., 2012) and were found to be beneficial for vegetation-related RS analyses in many earlier studies (e.g., Coburn and Roberts, 2004; Dobrowski et al., 2008). We calculated texture metrics in the GEE for neighborhoods of 3 × 3 and 5 × 5 pixels using the "glcmTexture " function and selected the metrics entropy, contrast, similarity/dissimilarity, correlation, and variance. The selection of metrics was based on the recommendations of Deur et al. (2020).

2.2.3. Methods

The methodical workflow for the study is summarized in Figure 2.4 and explained in more detail below. The GEE codes applied in this study can be found in Supplementary Material I.
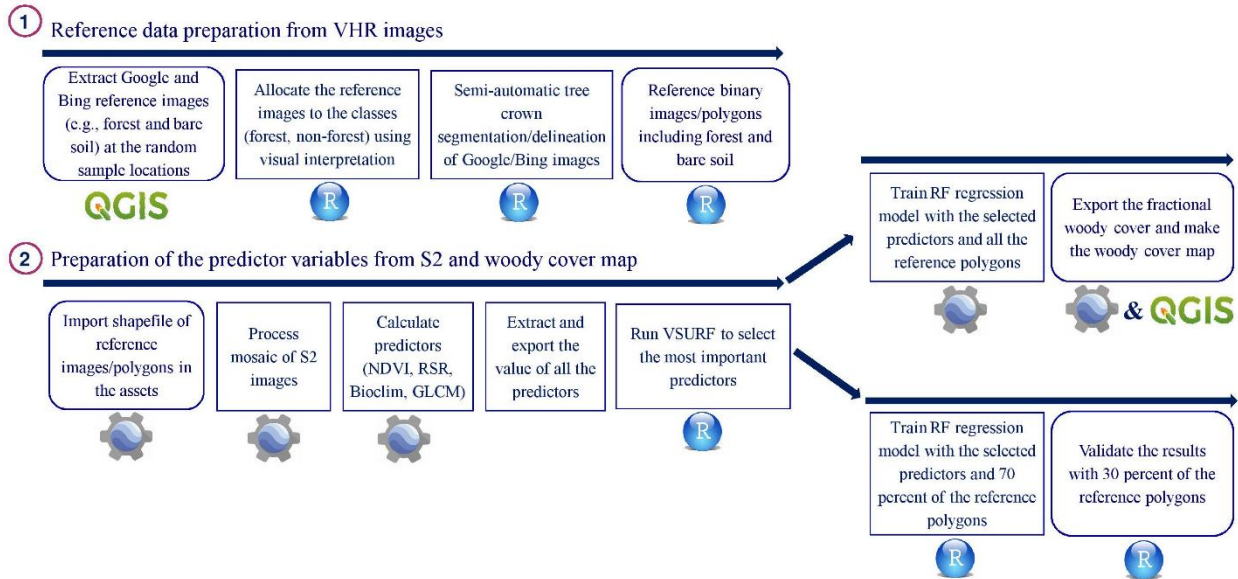
Figure 2.4 The applied workflow for woody cover mapping, the arrows represent the direction of the process.

2.2.3.1. RF Algorithm

We used the decision-tree ensemble method (RF) (Breiman 2001) to map the canopy cover and LC of the study area. For a summary of some earlier applications of RF in the context of RS, we refer to Belgiu and Drăguţ (2016). The benefits of RF over traditional classification and regression methods include its ability to manage numerous input variables, to run effectively on large datasets, to be less susceptible to noisy input data and outliers, and to be hardly prone to overfitting (Mellor et al., 2015; Gislason et al., 2006). RF is directly available in the GEE (Gaffarian et al., 2020). The availability of RF in GEE is particularly valuable as image processing on local computers would require a lot of memory, a long processing time, and a lot of storage space for our extensive study area.

2.2.3.2. Variable selection, modeling and multi-scale analysis

RF models were trained to predict the woody cover reference values using the 40 predictor variables described above and listed in Supplementary Material I. We ran multiple RF models trained at different spatial grains. We started with the original S2 resolution of 10 m and then reduced the resolution by 10 m steps. In the case of the model with 10 m resolution, we resampled the 20 m bands of S2 to 10 m in the GEE. This resulted in datasets with a pixel size of 10, 20, 30, 40,... up to 120 m. We ran RF models separately for each spatial grain. For each model, we automatically produced the woody cover reference values from the high-resolution woody cover-delineated RGB reference images by overlapping them with a polygon or vector file corresponding to the S2 pixel size of the current model and then counting the number of pixels in the high-resolution binary reference images that were assigned to the woody cover class. The corresponding

fractional woody cover values were attached to the reference polygons. This step was conducted in R using the raster and rgdal packages. After obtaining the reference values, the polygon vector file was imported into GEE. Then, the mean values of all predictor variables for the pixels covered by the polygons were obtained and exported as a CSV file using GEE. The extracted values were then imported into R to run a feature selection using the "three-step variable selection using random forests" (VSURF) package (Genuer et al., 2015). The VSURF method is based on the RF model and is designed to manage high-dimensional data. The VSURF package is highly scalable and can be used to select features in both regression and supervised classification problems. To perform VSURF, the first step is to exclude all non-essential variables from the dataset. The second step is to pick all variables that are correlated to the response and contribute to a good model's performance. For prediction purposes, the third step refines the collection by removing redundancy in the range of variables chosen in the second step (Genuer et al., 2015). The selected predictor variables for each spatial grain are reported in Table 2.1.

Using the VSURF-selected predictors, we then trained an RF model (ee.Classifier.smileRandomForest function with 500 trees) to predict woody cover across the entire Zagros area. This part of the analysis was again conducted in GEE. For model training in GEE, we used all available reference data to maximize the information content in the model used to create the prediction map of woody cover density. To further validate our models, we ran additional RF models in R by iteratively splitting the whole reference data set into 70% training and 30% validation samples. Optimal mtry parameters for the models in R were selected using the tuneRF function of the randomForest package. The tuneRF function was run with the following settings: ntreeTry = 50, stepFactor = 2, improve = 0.05, trace = TRUE, and doBest = TRUE. For the tuned models, we calculated RMSE and R^2 values based on the validation samples for each of the 100 model runs.

2.2.3.3. LC

Our woody cover predictions were created for the entire Zagros area, which also includes non-forested areas. Hence, a LC map was required to exclude other LC classes such as built-up, water, and agricultural areas. A recent country-wide LC map of Iran is available (Ghorbanian et al., 2020), and some other local products were provided by the provincial branches of the Research Institute of Forests and Rangelands, yet they are based on varied datasets and unclear methodology. Initial visual interpretation of those maps showed that they did not appropriately depict the wooded areas in our study region. Almost the entire woodland area in Zagros is classified as rangeland in the corresponding products (e.g., Ghorbanian et al., 2020), but other LC types were also misclassified in the available maps. Hence, a more suitable LC product was produced within this study. For this, we first prepared S2 mosaics following the workflow described above but containing all seasons. Using images of different seasons may improve the LC classification results, especially when classifying agricultural areas (Wingate et al., 2019; Zandler et al., 2015). Thus, we used mosaics based on the S2 images of the last three years, including the spring (March, April, and May),

summer (June, July, and August), and fall (September, October, and November) seasons. We excluded winter as the corresponding mosaics were more frequently affected by data artifacts from clouds and snow. For each season, we calculated a gray-scale image from the S2 image using Equation 1. Texture variables for each of these grayscale images were calculated using the glcmTexture function in GEE. We used a neighborhood size of 2 and a kernel size of 3×3, and all 21 available texture metrics were used as predictors (e.g., entropy, contrast, asimilarity, correlation, etc.).

$$\text{Grey Scale Image} = 0.3 \times S2\,\text{Band}\,8 + 0.59 \times S2\,\text{Band}\,4 + 0.11 \times S2\,\text{Band}\,3 \qquad (2.1)$$

We further used additional vegetation indices (e.g., Soil Adjusted Vegetation Index (SAVI), Normalized Difference Tillage Index (NDTI), introduced by Deventer et al. (1997), Enhanced Vegetation Index (EVI), SRTM digital elevation data (Farr et al., 2007), and predictor variables from Sentinel-1 (S1) images). We used S1 C-band Ground Range Detected SAR data from GEE (ImageCollection ID: COPERNICUS/S1 GRD) at 10 m pixel size for the spring (March, April, and May), summer (June, July, and August), and fall (September, October, and November) seasons between 2018 and 2020. To construct a homogeneous subset of S1 data, metadata properties were used to filter the S1 data collection with the following settings: polarization of the transmitter and receiver: ['VV', 'VH'], instrument mode of "IW" (interferometric wide swath and orbit properties pass: "DESCENDING"). Then we calculated a composite mosaic image directly in the GEE, obtaining median-backscatter values for each pixel.

We defined seven LC classes for the supervised classification, including built-up, plantations (orchards), agriculture, water, wooded areas, rangeland, and bare soil. We collected approximately 1,000 reference data points per class via visual interpretation of high-resolution Google and Bing imagery in GEE. 70 percent of these points were used to train an RF model in classification mode to classify the stacked image for the entire Zagros area. Point-based training for RF classifiers was stated to result in more accurate classification compared to polygon-based training (Corcoran et al., 2015). We used an equal number of training points for each class since RF tends to assign more pixels to the classes with a larger number of training points (e.g., Latifi et al., 2015). Analogously to the woody cover models, we used the VSURF package to select the most important predictors to improve the model. In the final model, 25 important variables were selected by VSURF (see Supplementary Material I). Then, after adding the important variables, we ran the model by splitting the whole reference data set into 70% training and 30% validation samples to create the prediction map. We ran additional RF models to validate our model by iteratively splitting the whole reference data set into 70% training and 30% validation samples, following the same approach outlined above for the woody cover models. We calculated confusion matrices from the 100 iterations and reported the accuracy of the classification via overall accuracy, kappa, and class-specific accuracies (sensitivity, specificity, and balanced accuracy).

2.2.3.4. Woody cover histogram

As a final step, we created 25,000 random points across the entire Zagros area, and at the location of each random point, we extracted the estimated woody cover as well as the LC class assigned to the point. These data were then used to depict a histogram of the woody cover percentages across the entire Zagros area.

2.3. Results

2.3.1. Woody cover map

Figure 2.5 shows violin plots for the model performance metrics obtained during the iterative evaluations of the RF models for estimating woody cover. The results notably improve from the highest resolution at 10×10 m until 40×40 m, but then improvements slowly level off and remain approximately constant until they reach the coarsest spatial grain of 120×120 m. As the results hardly improved at resolutions coarser than 40 m, we prepared the prediction maps at 40 m spatial resolution, as a finer spatial grain was considered beneficial.

For the selected model with 40 m resolution, R^2 values range between 0.56 and 0.74, with a median value of 0.67. The RMSE values range between approximately 0.10 and 0.14, with a median of 0.12.
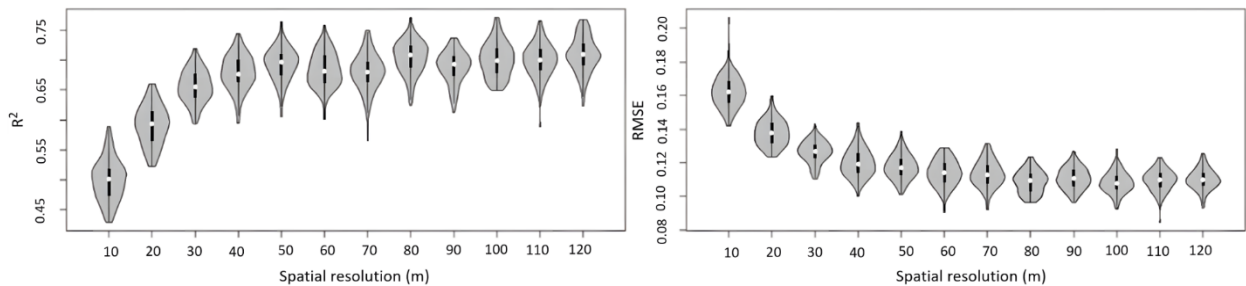
Figure 2.5 From left to right, the development of R^2 and RMSE with decreasing spatial grain for the RF models estimating woody cover are illustrated. The gray-shaded area in the violin plots shows the distribution of values, and the white point in each violin plot shows the median value.
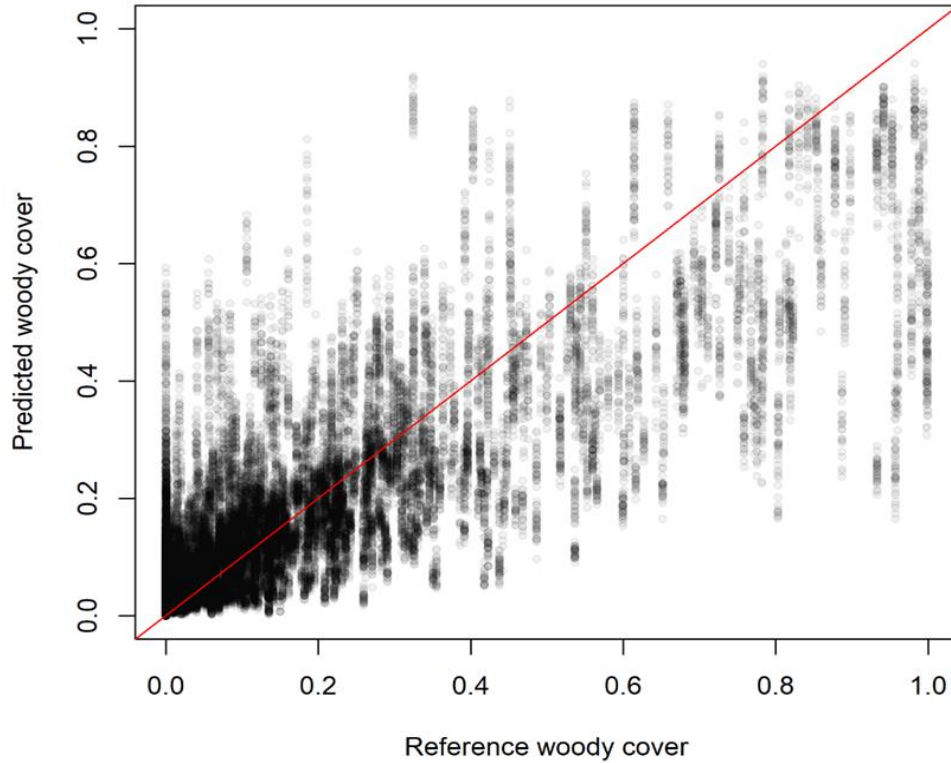
Figure 2.6 Scatter plot between observed and predicted woody cover estimates using the RF model at 40 m spatial grain. Results of all 100 model runs conducted in R

The corresponding scatter plot of the RF model with a 40-m pixel size indicates that the model works reasonably well but also that a quite notable amount of variation in the reference data cannot be explained. Particularly for higher cover values, the model only works moderately well (Figure 2.6). The tendency of RF to underestimate high and overestimate low values is also apparent.

The final woody cover map for the entire Zagros area is depicted in Figure 2.7. High woody cover values are particularly visible in the northern, more humid parts of Zagros and in the central mountain regions with higher elevations. This agrees very well with the existing knowledge of the cover distribution in the region.
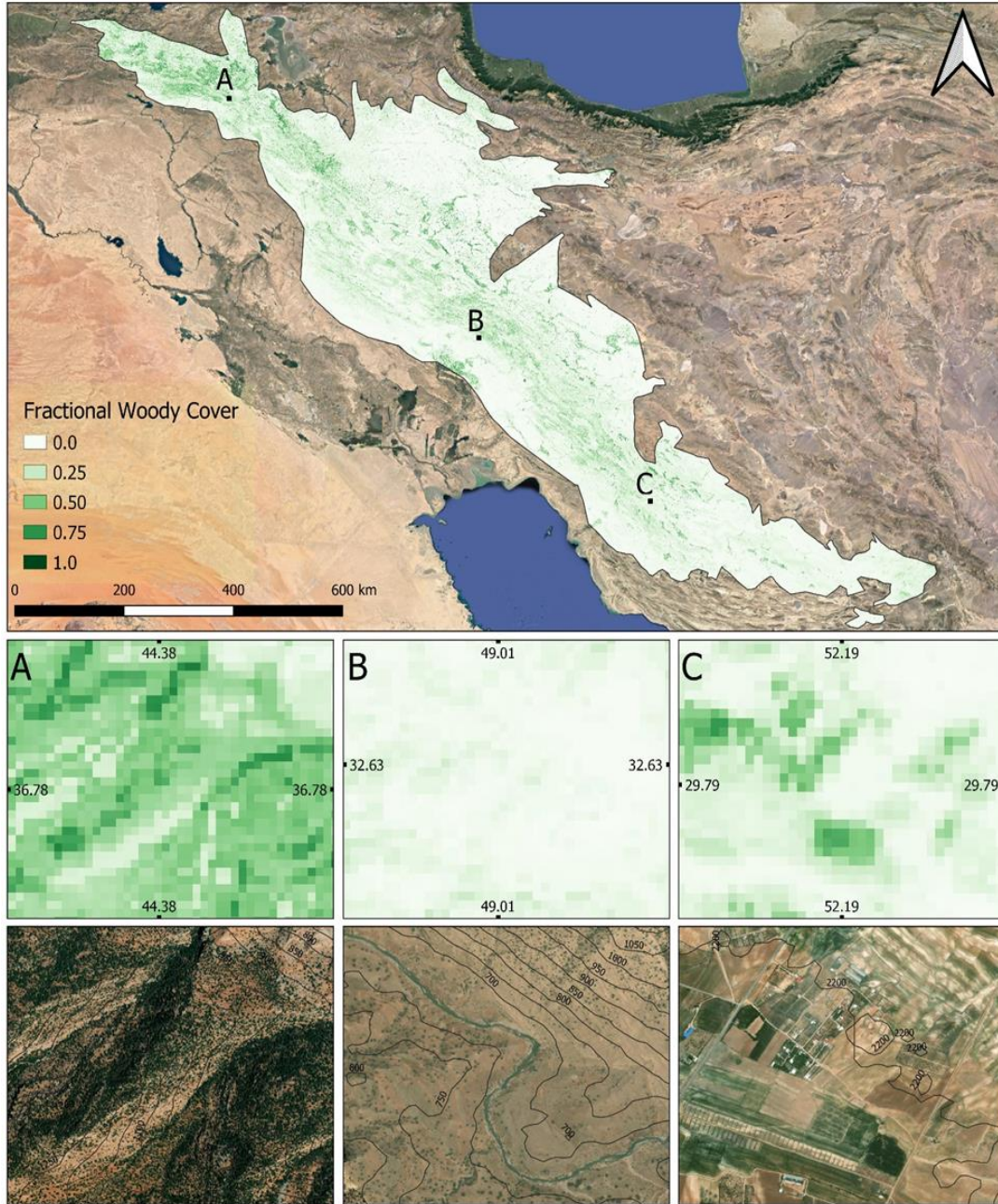
Figure 2.7 Map of woody cover estimates for the entire Zagros area. The three subsets A, B and C show two focus areas in topographically complex regions and one focus area with buildings and agricultural fields. The upper row shows the S2-based woody cover map and the bottom row the corresponding areas of VHR RGB imagery. Contour lines showing the elevation above sea level are shown on top of the RGB images.

The three focal areas of the woody cover map (Figure 2.7) show that the developed woody cover product is able to depict varied cover situations quite well, even though areas with over- and underestimated cover values are also clearly apparent. Judging from the displayed contour maps,

no obvious influence of topography on the woody cover estimates can be observed in the depicted focal area maps.

The selected predictors that were applied in the final RF models at each spatial grain are summarized in Table 2.1. The selected variables are overall very stable across the examined spatial grains. In almost all models, most S2 bands were selected except for the SWIR bands B10–B12 and the red-edge band B6. The B8a band is also only selected in one model, while for all other models, B8 (which includes the spectral region of B8a) was selected. Besides the original bands, the two examined indices, NDVI and RSR, as well as the threshold variable based on NDVI, were chosen in almost all models, whereby NDVI and the threshold variable were always among the first-ranked predictors. Additionally, two NDVI-based texture metrics (NDVI contrast and NDVI asimilarity) were frequently selected. All four bioclimatic variables were selected in almost all models, even though mostly at higher ranks.

Table 2.1 The VSURF selected predictors for woody cover estimation from the complete set of 40 predictors. The numbers represent the rank at which the corresponding variable was selected in the model of the corresponding grain size (columns).

Grain [m] Predictor	10	20	30	40	50	60	70	80	90	100	110	120
B2	6	5	6	6	6	5	6	6	6	6	6	6
B3	5	4	4	5	5	4	5	5	5	5	5	4
B4	2	2	3	3	3	3	2	2	3	2	2	3
B5	4	6		4	4		4	4	4	4	4	
B6			12									12
B7		11	11	13	13	12			13			11
B8	11			11	11		11	11	11	11	11	
B8a						10						
B12						11						
NDVI	1	1	1	1	1	1	1	1	1	1	1	1

thres	3	3	2	2	2	2	3	3	2	3	3	2
RSR	7	7	5	7	7		7	7	7	7	7	5
NDVI_contrast	9	8	7	9	9	7	9	9	9	9	9	7
NDVI_corr_1			13									13
NDVI_asm_1	15			14	14		15	15	13	15	14	
NDVI_texture55						14						
NDVI_entropy												
NDVI_var						13						
NDVI_ent_1						16						
B8_contrast			14									14
B8_ent_1	14	12					14	14		14	13	
B8_var	16						16	16		16	15	
bioclim 12	10	9	8	10	10	15	10	10	10	10	10	8
bioclim 15	8	10	10	8	8	9	8	8	8	8	8	10
bioclim 16	12		9	12	12	8	12	12	12	12	11	9
bioclim 17	13		13	15	15	9	13	13	14	13	12	13

2.3.2. LC map

Figure 2.8 displays a summary of the validation metrics for the LC classification. The highest sensitivity was gained by bare soil and built-up classes, with median values of both > 0.98. The lowest sensitivity values (0.85 and 0.92) were observed for the wooded area and agriculture classes, respectively. The highest specificity values were obtained for water, built-up classes, and

bare soil (all three > 0.99), and the lowest specificity values were obtained for rangeland, wooded area, agriculture, and plantation, respectively (approximately 0.98).

The corresponding trends are also mirrored in the balanced accuracies, which were again highest for the bare soil with a median value of 0.99, built-up and water with median values of more than 0.98, and lowest for the wooded area and agriculture with approximately 0.91 and 0.95, respectively. All metrics were comparably stable throughout the 100 iterations, which indicates that the number of training samples was sufficient. The LC classification model reached an overall accuracy and a kappa value of more than 0.94 and 0.93, respectively.
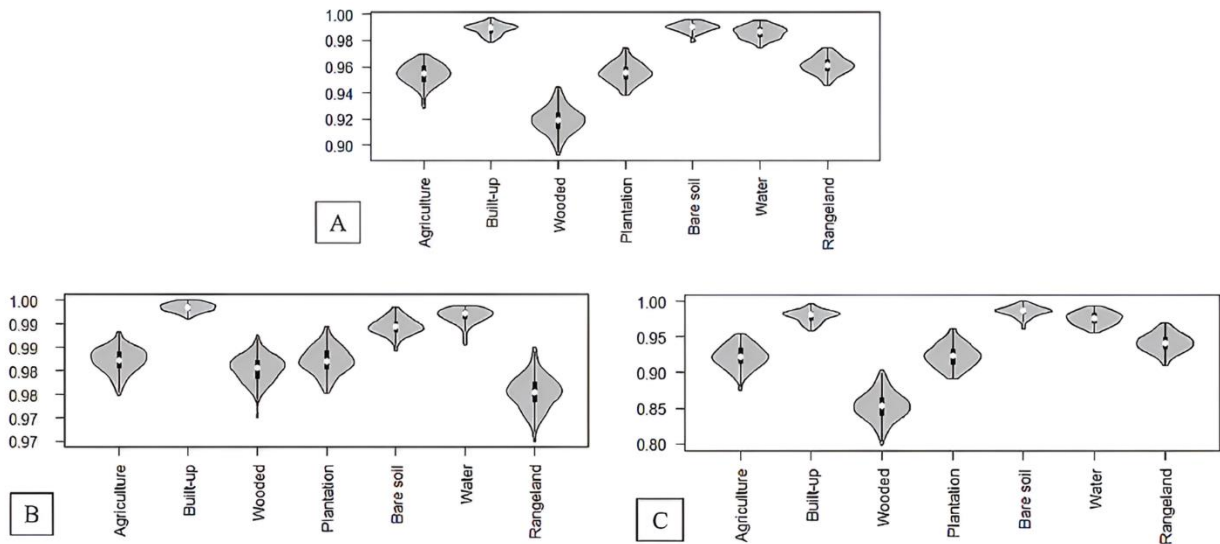
Figure 2.8 (A) Balanced accuracy; (B) specificity, and (C) sensitivity of the LC classes in the supervised classification

The final S2-based LC map for the entire study area and some focal area maps with corresponding high-resolution RGB imagery are shown in Figure 2.9. The dark-green belt of "wooded areas" reaching from the north-west to the south-east of the study area agrees very well with the fractional woody cover map (Figure 2.9). The huge agricultural areas in the north of Zagros are also clearly visible, while agricultural areas are more sparsely distributed in the southern parts of Zagros. The other land-cover classes mostly occur in smaller proportions, except for rangeland, which becomes more continuous in the southern parts of Zagros, where tree growth is more and more limited due to climatic conditions. Overall, the LC map agrees well with the known distribution of LC in the Zagros area.
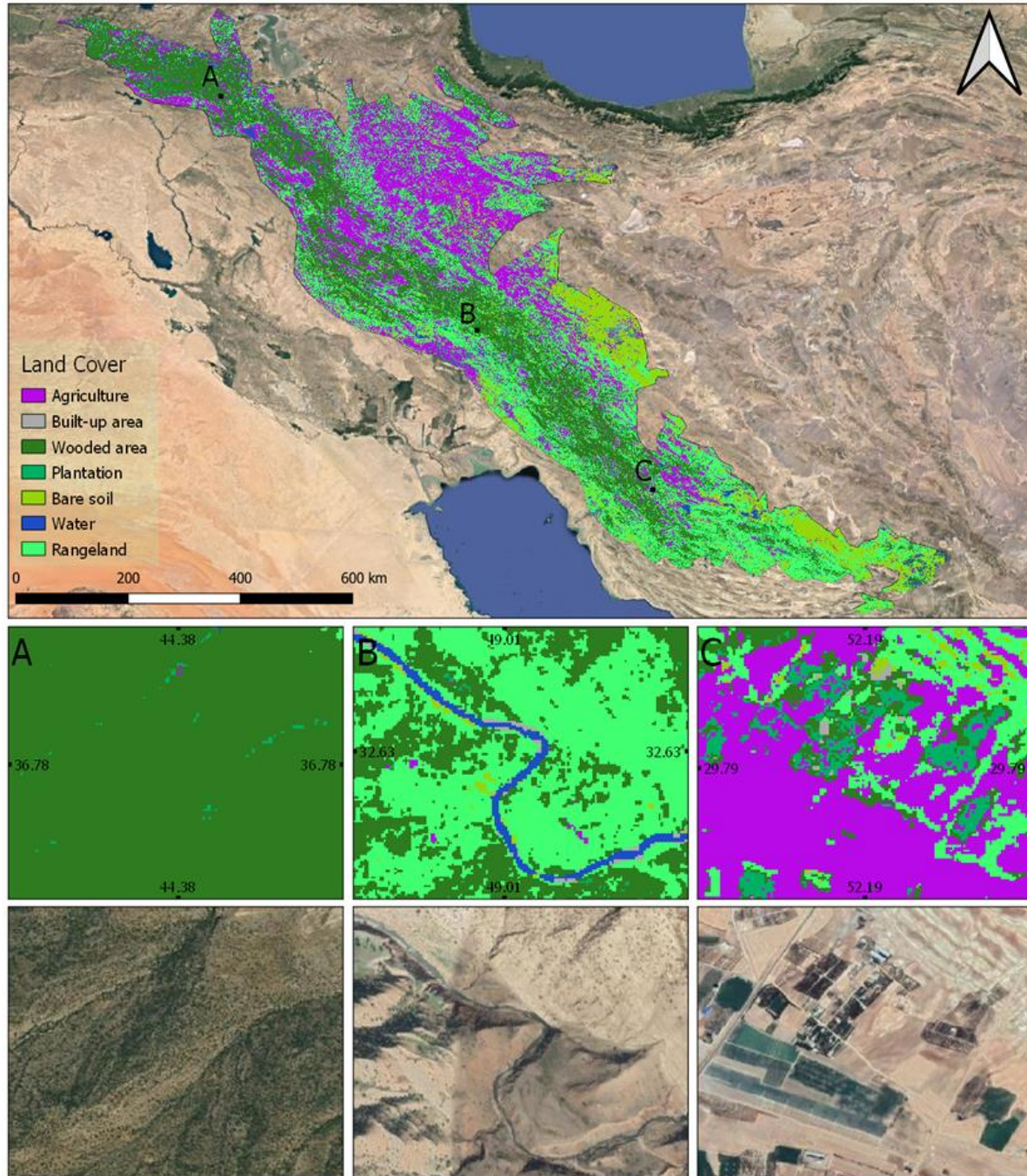
Figure 2.9 Map of LC estimates for the entire Zagros area. The panels A, B and C show focus areas of the S2-based LC map and below them, the corresponding areas of VHR RGB imagery (classes with non-green colors were masked out in the final woody cover product).

As shown in the focus area maps, discriminating the plantation or orchard class from the wooded areas was not always possible (see Figure 2.9 Panel C and additional graphs in the Supplementary Material I), and especially in areas with dense natural woody cover, some

confusion occurred. Some further confusion occurred between built-up areas and very bright bare soil or pebble areas (see Figure 2.9, panel B, along the river). Finally, the classes of bare soil, rangeland, and wooded areas expectedly showed some confusion. This is no surprise, as these three classes more or less form a continuum from bare soil to woodlands, with rangeland having higher fractions of herbaceous vegetation. A clear separation of the three classes is therefore challenging, even in the field.

2.3.3. Woody cover histogram
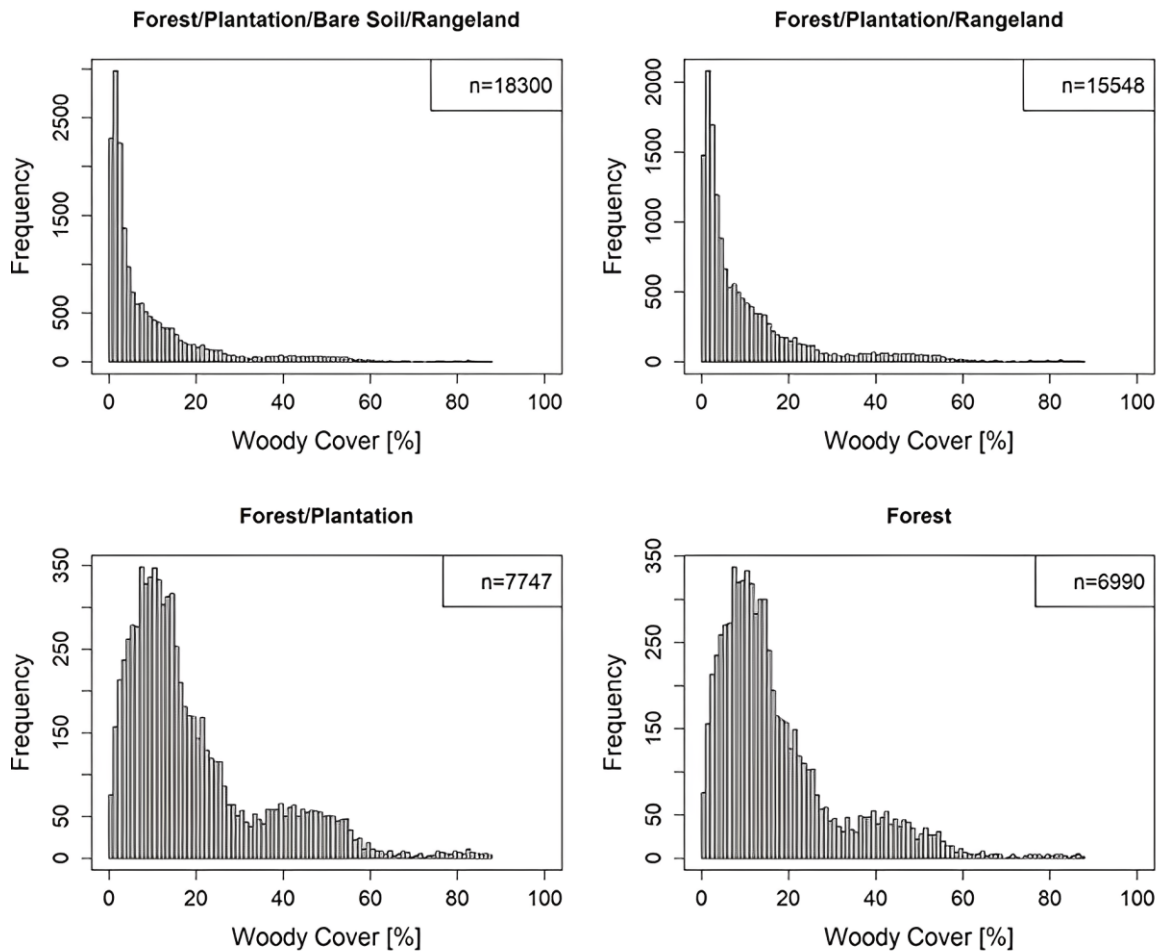
Figure 2.10 Histograms of woody cover estimates for n random points across the complete Zagros area and for different combinations of LC types as obtained from the LC classification.

According to the final woody cover map presented in this study, most areas classified as forests have a woody cover below approximately 60%, even though higher cover values exist in some areas (bottom right panel of Figure 2.10). The highest frequencies can be observed for areas with a cover of approximately 10%, which is FAO's minimum cover to fulfill the definition of a forest.

If woody cover estimates for bare soil, rangeland, and plantation areas are additionally considered in the histogram, the proportion of very low cover values increases notably (top panels in Figure 2.10).

2.4. Discussion

In this study, we suggest a fully RS-based workflow to estimate fractional woody cover across the entire Zagros Mountains. Our results demonstrate the capability of S2 images to estimate woody cover in the semi-arid Zagros Forest area using reference data from VHR satellite imagery from Google Earth and Bing instead of field measurements. Our methodology is practical when focusing on vast areas where field sampling can be very time-consuming and expensive. Recently published studies proved that VHR imagery can be used as a complement to field sampling (e.g., Anchang et al., 2020; Eskandari et al., 2020), whereas some studies solely relied on VHR imagery as a surrogate for field data (e.g., Kattenborn et al., 2019; Fassnacht et al., 2021; Ludwig et al., 2019). The latter studies argued that, for certain objectives, VHR imagery might even be more reliable than field data. For example, visual estimates of woody cover on the ground may be less accurate as the field observer is not sharing the bird's-eye perspective of the satellite data (Kattenborn et al., 2019). Visual comparisons of our resulting woody cover map showed very good agreement with the VHR data and seem to confirm the validity of this approach.

One challenge when working with extensive study areas is environmental variability. The Zagros area is considered a geographic entity, but the environmental and socio-political settings within Zagros vary widely. The Zagros area has varying rainfall patterns and crosses several climatic zones, from very hot and dry (in southern Zagros) to semi-arid and even cold climates (in northern Zagros) (Ashraf Vaghefi et al., 2019). Different dominant woody species may occur in each of these climatic zones, as exemplified by 1) the high mixture of *Q. libani* and *Q. infectoria* with *Q. brantii* in the northern part and their absence in the central and southern parts; and 2) the dominant Amygdalus *spp.* in the very southern part, occasionally in the absence of *Q. brantii*. Another significant source of variation is the traditional land-use practices outside the main urban centers, which range from the dominance of settled villages in the northern parts to different types of nomadic life in the central and southern parts, resulting in variable forest tenure and thus densities due to different silvopastoral systems. This might be one reason why our model was able to predict woody cover reasonably well, but still, a notable amount of unexplained variation remained. Given the comparably low woody cover in most parts of Zagros (Figures. 2.7 and 2.10), the obtained median RMSE value of 0.11 (11%) is comparably high and indicates that there is still room for improvement in the suggested workflow. Concerning the variability introduced by differing climatic conditions, we tried to at least partly account for the environmental gradients of the Zagros area by adding bioclimatic variables to our workflow. These turned out to be among the selected predictors in almost all RF models, which confirms the importance of considering information on environmental gradients in estimating woody cover fraction. Some earlier studies

focusing on woody cover estimation classified their study area into various bioclimatic zones and found a significant relationship between bioclimatic zones and woody cover density (e.g., Brandt et al., 2018; Sankaran et al., 2005). Thus, an alternative to our suggested approach could be to classify the entire study area into different climatic zones and then train separate zone-specific models.

Another source of variation in our workflow relates to the VHR (Bing and Google Images). Most Google satellite images for the Zagros area are more recent than the Bing Maps images (Lesiv et al., 2018). This was also reflected in the data used for our analysis (7000 Google Earth vs. 1000 Bing images). For most sub-regions, particularly in the central part of Zagros, no VHR imagery with an acquisition date after 2015 or 2016 was available. Hence, these older reference data might not have been fully representative of the current conditions mirrored in the S2 imagery and may have had a negative effect on our model performance. This issue could be addressed by collecting UAV data in areas with outdated VHR images; however, that would also lead to notably increased costs.

2.4.1. Effects of spatial grain on model performance

One objective of our study was to examine how the spatial grain of the analysis affects the quality of the model. We initially used S2 bands at 10 m pixel size and then additionally ran the model with down-sampled S2 data with pixel sizes from 20 to 120 m spatial resolution. Our results show a decrease in RMSE and an increase in R^2 from 10 to 60 m pixel size, followed by saturation and comparably stable results with only marginal fluctuations afterward. This model improvement at a coarser spatial grain matches our expectations and is in line with the findings of Korhonen et al. (2017), who reported better model performances when using nine S2 image pixels instead of one. Higginbottom et al. (2018) also estimated woody cover density using Landsat TM/ETM+ imagery at 30, 60, 90, and 120 m pixel sizes and suggested that the most accurate model was the model with the coarsest resolution ($R^2 = 0.8$, RMSE = 8.9, at the 120 m pixel scale) when solely using dry season images. They discussed that while the maps at 120 m were of the highest model accuracy, they were less suitable to detect smaller clumps and canopies of dryland vegetation. Accordingly, and as a compromise between model performance and the ability to depict finer spatial patterns, we used the 40-m model to produce our final map. The tendency of the models to perform better at coarser spatial grain may relate to at least two aspects: First, potential co-location errors between S2 and VHR imagery at the sub-pixel scale have less influence at coarser grain. Second, by increasing the spatial grain of the analysis, the number of extreme values in the reference data (very high and very low woody cover estimates) will decrease (see Supplementary Material I). The latter point may lead to reductions in RMSE, particularly if a model like RF is applied that tends to predict intermediate values. This phenomenon has, for example, been described for biomass estimation models trained with field plots of differing sizes and using several RS data types (e.g., Fassnacht et al., 2018; Hosseini et al., 2020) and is also related to the

inability of RF to predict out of the range of its reference values. It was consequently reported in many studies that RF tends to under-predict high and over-predict low values, which was also confirmed in our study (Figure 2.6).

2.4.2. Selected predictor variables

The spatial scale only had a minor influence on the selected predictor variables. According to the results of VSURF-based variable selection, the frequency and order in which predictor variables were selected remained fairly constant across all examined scales. One exception was band 8 (spectrally centered at 842 nm), which was repeatedly selected in models based on coarser grain data (> 70 m). It was also remarkably the case for two texture metrics based on the same band (B8_ent_1 and B8_var), which indicates that NIR-based texture information may become more relevant at coarser spatial grains. This seems logical, as spatial variation in reflectance in the NIR is likely to relate to varied woody cover situations in our study area. This variation may play less of a role at finer spatial grains, where the information in the individual pixel may be sufficient to describe the reference woody cover values extracted from the VHR images.

The most frequently selected predictor variables that were present in all RF models included NDVI, B4 (red band), thres, B3/green band, bio12 (annual precipitation), and B2/blue band. Hence, bands from the visual part of the spectrum were constantly selected. This partly agrees with Higginbottom et al. (2018), who reported B3 as the second-best individual S2 band (with R^2 = 0.66–0.70) for monitoring canopy properties in patchy, discontinuous woody vegetation in South Africa. Heckel et al., (2020) and Waśniewski et al. (2020) also reported that the bands from the visual domain notably contribute to estimating FC. In contrast to Higginbottom et al. (2018) and some studies in other forest ecosystems (e.g., Waśniewski et al., 2020; Heckel et al., 2020), we found the red edge bands (B5–B7) and also the bands located in the near-infrared (B8, B8a) to be of only intermediate importance for estimating woody cover. While this has also been reported by other earlier studies focusing on related variables such as leaf area index (LAI) (Meyer et al., 2019), it is very likely that this is also a consequence of NDVI being the most important predictor variable in all models. As NDVI captures the most important information contained in the red-edge bands, the additional, finer information from the red-edge bands may simply not be relevant when focusing on a straightforward target variable such as woody cover. The high importance of NDVI comes as no surprise, as it has been previously reported to be a highly significant predictor variable for estimating tree and woody canopy cover fractions in the Zagros region (Eskandari et al., 2020). It was interesting to see that our NDVI threshold predictor (named thres), a binary mask derived by applying a threshold of 0.17 to the NDVI, was among the most frequently selected predictor variables. The idea of this predictor was to imitate the approach with which the reference data was created, and we assumed that it would be particularly useful at coarser spatial resolutions. However, the predictor was relevant even at the finest spatial resolutions examined.

The two SWIR bands of S2 played almost no role in our study, and only B12 was selected once in the model at a 60 m spatial grain. This is not surprising, as the differentiation of the dark vegetation in front of the soil background is unlikely to depend on additional information on canopy structure or water content that is mostly contained in the SWIR bands. Furthermore, similar to the red-edge band, the most important information related to the SWIR bands (or at least Band 11) might have already been captured by the RSR index, which was also one of the most frequently selected predictors in all models. This index combines information from the RED, NIR, and SWIR regions and tends to decrease the effects of bright and pronounced soil background in situations with sparse canopy cover like our study area. This high relevance of the RSR index agrees well with the findings of several earlier studies focusing on similar target variables (e.g., Brown et al., 2000; Zhu et al., 2010).

Earlier studies proved that climatic variables are important for mapping woody vegetation and can improve RS models (e.g., Liu et al., 2017; Brandt et al., 2018). Therefore, to account for the potential influences of the large environmental gradient covered by the Zagros area on the relationship between RS data and woody cover, we also included selected bioclimatic variables (BIO12, BIO15, BIO16, and BIO17). The annual precipitation (BIO12) was selected in all models, while precipitation seasonality (Bio15) was selected in all models except the model with 40 m resolution. The precipitation of the wettest and driest quarters (BIO16 and BIO17) was also selected for all models except for the model with 20 m resolution. Even though the bioclimate variables had a notably lower spatial resolution as compared to the S2-based predictors, it was remarkable to observe that they were still selected in almost all models. We assume that the bioclimate variables were helpful to pre-stratify the feature space into coarse environmental regions, which may explain a part of the variability in the reference data that was collected across the entire Zagros area. Topography metrics were also explored in some preliminary analyses but were found to not increase the model's performance. The result of this analysis is shown in the Supplementary Material I. This was surprising but may partly be explained by the large environmental gradient of our study area. This gradient may challenge a stable relationship between topography and woody cover. For example, in the northern areas with more precipitation, a shaded slope may be disadvantageous (due to less light and hence photosynthetic activity), while in the southern areas with less precipitation, a shaded slope may be beneficial due to the reduced transpiration stress. A more detailed analysis would be required to understand how the patterns of differing woody cover values relate to environmental variables and land-use trajectories. Our woody cover map could be a good starting point to analyze this question in future studies, and corresponding findings may in turn be helpful to further improve the presented workflow by considering regional differences in the drivers of woody cover patterns.

2.4.3. Relevance of the created woody cover map

For environmental science and natural resource management, accurate and timely maps of woody cover are critical (Karlson et al., 2015). The Zagros Forests, which have a documented history of human settlements dating back beyond 5500 years, are one of Iran's most valuable cultural landscapes and play an important role in soil and water conservation. Climate change, population development, and people's reliance on these woodlands for their livelihoods (by harvesting wood and forest sub-products, turning woodlands into agricultural fields, and grazing areas) have all contributed to the decline of the woodland ecosystems in Zagros over the last 30 years (Jazirei and Ebrahimi, 2013). Despite the high environmental importance of these woodlands, they are currently not part of a national-scale protection plan. As a result, developing accurate maps of the Zagros Forests (cover, density, and distribution) is an important contribution to monitoring the area. Providing an accurate fractional woody cover map can therefore support forest managers in determining (1) the exact distribution of wooded areas in the vast Zagros region and (2) support the regular assessment of potential changes induced by, for example, changes in land-use practices and climate change (Eskandari et al., 2020).

Our woody cover product and the straightforward workflow developed here are particularly relevant for semi-arid and arid regions, as many existing large-scale tree and woody cover products based on satellite data have clear limitations for characterizing areas with sparse tree canopies (e.g., Brandt et al., 2016; Cunningham et al., 2019; Fagan 2020). To further illustrate this, we validated the Global Forest Change map (Hansen et al., 2000), a benchmark for many similar studies, using our reference dataset. The corresponding results show a severe underestimation of the woody cover across the entire Zagros Forest (Figure 2.7). This backs up prior findings of Bastin et al. (2017), Brandt et al. (2016), and Cunningham et al. (2019), who also reported that global forest and woody cover products are underestimating the woody cover in arid and semi-arid forests and woodlands. Our final woody cover map returned visually much more plausible estimates across the majority of the Zagros region compared with all available global products, including the GFC and a recently published map of the Zagros area (Ghorbanian et al., 2020).

2. Mapping fractional woody cover in an extensive semi-arid woodland area at different spatial grains with Sentinel-2 and very high-resolution data
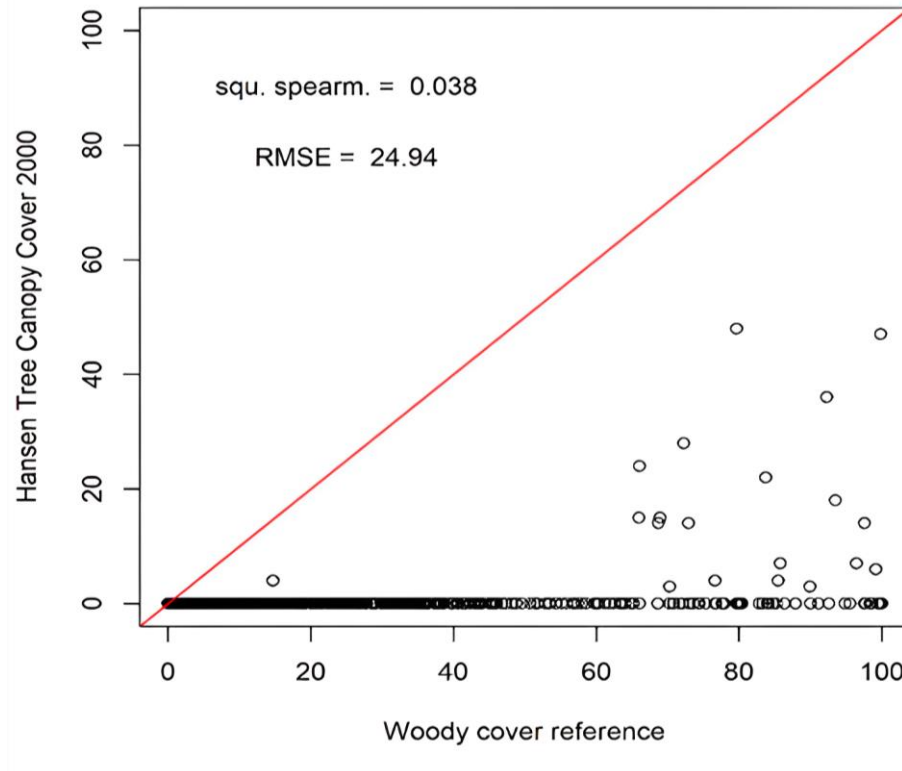
Figure 2.11 Validation graph of Hansen global FC product at 30 m resolution with our reference woody cover dataset. It is worth mentioning that the Hansen global FC product is estimated for trees with heights greater than 5 m. While these heights are not achieved in all areas of Zagros, there is still a large fraction of the area with notably higher trees.

In our product, we dealt with the problem of bright soil background by adding bare soil samples with corresponding zero woody cover reference values to our reference dataset and by including the RSR index as an input variable. Both measures improved the performance of our model. We also followed the suggestion by Symeonakis et al. (2018) and used S2 images of the dry/summer season, i.e., the time of maximum difference amongst the spectral signals amongst vegetation, crops, and grasses. In terms of additional RS data from active sensors, the application of S1 SAR data could be examined in the future. However, some studies have already shown that adding S1 data does not always improve the results (Heckel et al., 2020). In some preliminary analyses, the addition of S1 backscatter variables did not improve our models for estimating woody cover (results not shown here). One reason for this might be that the Zagros area is topographically complex, and the standard pre-processing of SAR data to account for terrain shadows, foreshortening, and related effects in GEE may not have been sufficient to obtain a signal that increases the information content already available in the S2 data. As discussed below, S1 data was, however, helpful in improving the differentiation of urban and bare soil areas in the land-cover classification. This may relate to the comparably extreme behavior or urban areas in the SAR signal (double-bounce effect), which may have led to a comparably clear signal despite the challenges discussed related to the pre-processing of the SAR data.

44

2.4.4. LC mapping

Studies on the status quo and changes in ecosystems and land-use systems in the Zagros region are partly constrained by the lack of reliable LC maps (Eskandari et al., 2020). Recently published LC maps for the entire country of Iran based on S1 and S2 data resulted in overall accuracy and kappa coefficients of 91.35% and 0.91, respectively (Ghorbanian et al., 2020). However, these maps showed a severe underestimation of forested areas in the Zagros region, mostly due to misclassification as rangelands. This may also relate to the definition of the classes of forest and rangeland. Most of the Zagros Forests are indeed used as rangeland by nomads and villagers living in the area. On the other hand, extensive temperate forest regions exist in the northern parts of Iran, and hence, in a national-scale LC map, the class forest may have been exclusively used for these ecosystems. Other products covering the entire Zagros area were not available, excluding global land-cover products, which are typically either available at a comparably coarse spatial grain or with only a few land-cover classes. Our LC product achieved high accuracies for the seven considered classes, and we deem it useful for masking out irrelevant LC classes from our woody cover product. The use of this map for other purposes may be limited due to the comparably sparse number of land-cover classes considered in the workflow. Furthermore, despite the overall high accuracy, we still observed some obvious misclassifications in our LC map. One of the major problems was the misclassification of orchards with natural woody cover. Particularly in areas where orchards are surrounded by forest stands, it is very challenging to discriminate between the two classes. One example is given in Supplementary Material I, where it is shown that very dense natural woodlands tend to be misclassified as plantation areas. One approach to improving related misclassifications in future studies may be to integrate spatial context into the analysis. In most cases, plantations and orchards occur in the immediate neighborhood of settlements and nearby roads. Hence, integrating a layer representing the distance to settlements and roads could be helpful to mitigate the over-classification of plantation areas. Further confusion occurred between the buildup class and bare soil. This is also a commonly occurring problem that has been discussed before (e.g., Piyoosh and Ghosh 2018). In the Zagros area, besides bare soil areas, areas covered with seasonally occurring herbaceous vegetation and crops (especially rainfed crops) can be confused with built-up areas. Combining optical and radar data can help mitigate this problem. While optical data is able to capture phenological characteristics of the vegetation, the backscatter behavior of SAR data can further contribute to reliably identifying built-up surfaces as the scattering behavior typically differs notably between vegetated and bare soil areas (Luti et al., 2021). Some earlier studies showed the potential of jointly using S1 and S2 data to extract built-up areas (e.g., Luti et al., 2021; Dong et al., 2020; Abdikan et al., 2016). However, in topographically complex areas such as the Zagros region, the pre-processing of SAR data to account for terrain shadows, foreshortening, and related effects is rather challenging. In our study, we addressed this issue by applying filters to the available S1 data catalog in GEE, and this

comparably straightforward approach resulted in reasonable SAR mosaics that contributed to improved separation of built-up and bare soil areas.

2.5. Conclusions

In this study, we proposed a workflow to map woody cover in an extensive semi-arid woodland region at comparably high spatial resolution using exclusively freely available datasets. The presented workflow, based on a combination of VHR images from Google Satellite, Bing, and S2 multispectral satellite data, implemented mostly in the GEE, resulted in a reliable woody cover product for the entire Zagros Forest area. An additional LC classification was used to mask out irrelevant LC classes. The woody cover product was compared to existing global FC datasets and proved to be of notably higher quality. The approach is particularly interesting because no costly field data is required, the work flow is straightforward to implement, and it could hence also be beneficial for estimating woody cover in other arid and semi-arid regions of the world.

Acknowledgements

2.6. Supplementary Material I

<u>Comparison of woody cover product with global FC maps</u>
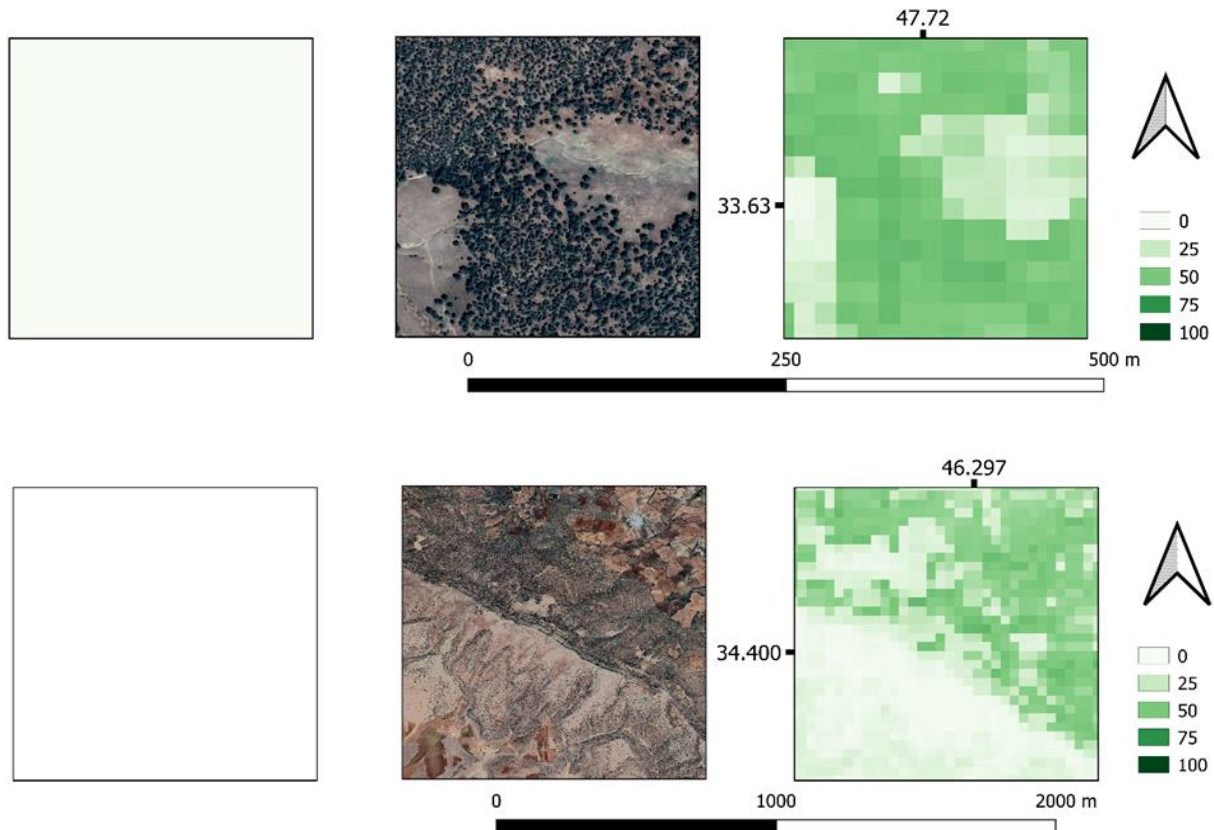
Figure 2.12 The left panels show the Hansen global FC product; the center panels show Google Satellite VHR imagery of the same area and the right panels show the predicted woody/canopy cover of our S2 based 40 m resolution model. All images are projected in the geographic coordinate system (EPSG 4326).

Figure 2.12 shows one exemplified site in the Zagros region where comparably high FC values can be observed, but the global FC product of Hansen fails to capture these areas adequately. It is important to say that the Hansen map only depicts forests with a minimum height of 5 m; however, at the same time, this minimum height is frequently reached by oak trees in the Zagros area, particularly in the comparably dense woodlands as shown here.
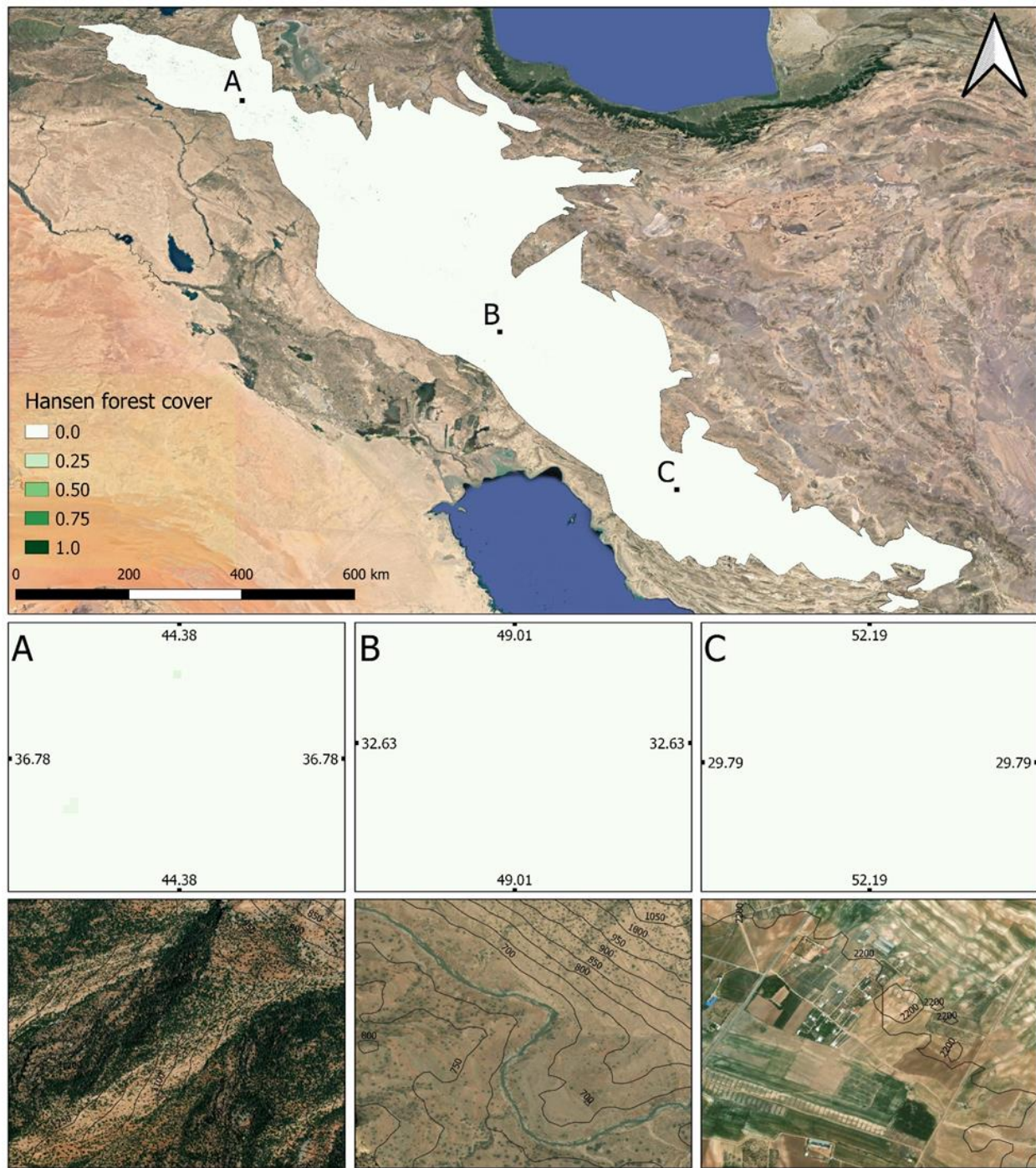
Figure 2.13 Map of Hansen global FC for the entire Zagros area. The three subsets A, B and C show two focus areas in topographically complex regions and one focus area with buildings and agricultural fields. The upper row shows the Hansen treecover2000 layer of FC map and the bottom row the corresponding areas of VHR RGB imagery. Contour lines showing the elevation above sea level are shown on top of the RGB images.

2. Mapping fractional woody cover in an extensive semi-arid woodland area at different spatial grains with Sentinel-2 and very high-resolution data

__List of all predictors used in the woody cover model__

Table 2.2 The predictors used in the study of woody cover.

Variable name	Description
"B2"	B2 (490 nm) band of S2 with 10 m resolution
"B3"	B3 (560 nm) band of S2 with 10 m resolution
"B4"	B4 (665 nm) band of S2 with 10 m resolution
"B8"	B8 (842 nm) band of S2 with 10 m resolution
"B5"	B5 (705 nm) band of S2 with 20 m resolution
"B6"	B6 (740 nm) band of S2 with 20 m resolution
"B7"	B7 (783 nm) band of S2 with 20 m resolution
"B8A"	B8a (865 nm) band of S2 with 20 m resolution
"B11"	B11 (1610 nm) band of S2 with 20 m resolution
"B12"	B12 (2190 nm) band of S2 with 20 m resolution
"B8_contrast"	Contrast metric of glcm function on NIR band with 3*3kernel size
"B8_var"	Variance metric of glcm function on NIR band with 3*3kernel size
"B8_ent"	Entropy metric of glcm function on NIR band with 3*3kernel size
"B8_corr"	Correlation metric of glcm function on NIR band with 3*3kernel size
"B8_asm"	Asimilarity metric of glcm function on NIR band with 3*3kernel size

2. Mapping fractional woody cover in an extensive semi-arid woodland area at different spatial grains with Sentinel-2 and very high-resolution data

"B8_contrast_1"	Contrast metric of glcm function on NIR band with 5*5 kernel size
"B8_var_1"	Variance metric of glcm function on NIR band with 5*5 kernel size
"B8_ent_1"	Entropy metric of glcm function on NIR band with 5*5 kernel size
"B8_corr_1"	Correlation metric of glcm function on NIR band with 5*5 kernel size
"B8_asm_1"	Asimilarity metric of glcm function on NIR band with 5*5 kernel size
"NDVI"	Normalized difference vegetation index
"ndvi_texture33"	Standard Deviation of NDVI band with 3*3 kernel size
"ndvi_texture55"	Standard Deviation of NDVI band with 5*5 kernel size
"nir_texture55"	Standard deviation of NIR band with 5*5 kernel size
"thres"	threshold of NDVI (Normalized difference vegetation index)
"NDVI_contrast"	Contrast metric of glcm function on NDVI band with 3*3 kernel size
"NDVI_var"	Variance metric of glcm function on NDVI band with 3*3 kernel size
"NDVI_ent"	Entropy metric of glcm function on NDVI band with 3*3 kernel size
"NDVI_corr"	Correlation metric of glcm function on NDVI band with 3*3 kernel size
"NDVI_asm"	Asimilarity metric of glcm function on NDVI band with 3*3 kernel size
"NDVI_contrast_1"	Contrast metric of glcm function on NDVI band with 5*5 kernel size
"NDVI_var_1"	Variance metric of glcm function on NDVI band with 5*5 kernel size
"NDVI_ent_1"	Entropy metric of glcm function on NDVI band with 5*5 kernel size

"NDVI_corr_1"	Correlation metric of glcm function on NDVI band with 5*5 kernel size
"NDVI_asm_1"	Asimilarity metric of glcm function on NDVI band with 5*5 kernel size
"bio12"	Annual Precipitation
"bio15"	Precipitation Seasonality (Coefficient of Variation) of Bioclim
"bio16"	Precipitation of Wettest Quarter of Bioclim
"bio17"	Precipitation of Driest Quarter of Bioclim
"rsr"	the reduced simple ratio index
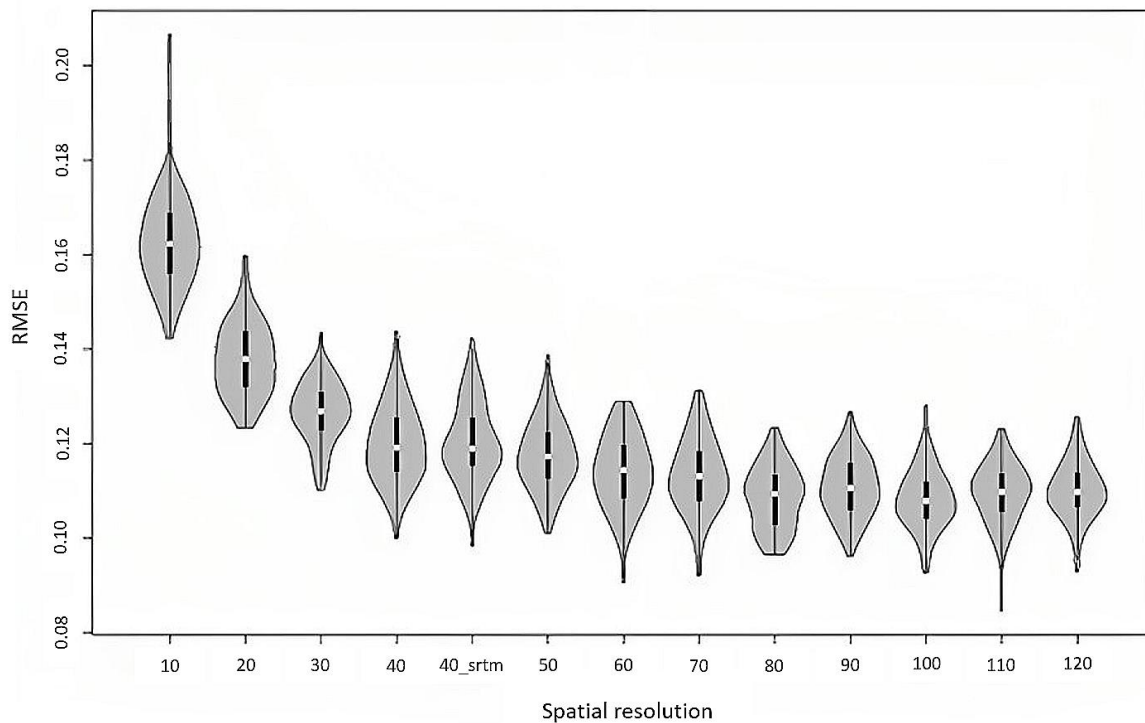
Figure 2.14 The development of RMSE with decreasing spatial grain for the RF models estimating woody cover are illustrated. The grey-shaded area in the violin plots shows the distribution of values, the white point in each violin plot shows the median value. Here we also added topographical variables (elevation and slope) called "40_srtm" using NASA SRTM Digital Elevation 30m data for the regression model with 40 spatial resolutions to check their effects on the model. As it can be seen, there are hardly any improvements in the model, so we did not use these variables in the final model.

51

2. Mapping fractional woody cover in an extensive semi-arid woodland area at different spatial grains with Sentinel-2 and very high-resolution data

<u>List of all predictors used in the LC model</u>

Table 2.3 The predictors used in the study of LC.

Variable name	Description
"1_NDVI"	NDVI index of S2 for spring
"1_SAVI"	SAVI index of S2 for spring
"1_NDTI"	NDTI index of S2 for spring
"0_EVI"	EVI index of S2 for fall
"slope"	Slope NASA SRTM Digital Elevation
"0_NDVI"	NDVI index of S2 for fall
"0_SAVI"	SAVI index of S2 for fall
"2_NDTI"	NDTI index of S2 for summer
"2_EVI"	EVI index of S2 for summer
"1_B8"	B8 band of S2 for spring
"elevation"	Elevation band of NASA SRTM Digital Elevation
"VH_1"	DESCENDING VH band for spring
"summer_gray_contrast"	Contrast metric of glcm function with 3*3 kernel size for summer
"spring_gray_contrast"	Contrast metric of glcm function with 3*3 kernel size for spring
"1_B12"	B12 band of S2 for spring
"VH_2"	VH band for summer (DESCENDING)
"1_B8A"	B8A band of S2 for spring
"1_B11"	B11 band of S2 for spring
"2_B8"	B8 band of S2 for summer
"2_RSR"	RSR index of S2 for summer
"0_RSR",	RSR index of S2 for fall
"1_B2"	B2 band of S2 for spring

VV_2",	VV band for summer (DESCENDING)
"2_B6"	B6 band of S2 for summer
"spring_gray_savg"	Sum Average metric of glcm function with 3*3 kernel size for spring

Validation of land-cover classification and examples for misclassifications

Table 2.4 Confusion matrix of LC classification – the confusion matrices of the 100 iterative validation runs were aggregated. Orange marked cells indicate higher amounts of confusion, for the two purple marked cells, additional examples are given below.

	Agriculture	Built-up	Wooded area	Plantation	Bare Soil	Water	Rangeland
Agriculture	26926	19	748	707	110	195	520
Built-up	4	28707	92	0	154	8	17
Wooded area	247	128	25639	1092	25	341	783
Plantation	1103	100	982	27919	0	104	4
Bare Soil	57	263	171	24	29512	47	440
Water	56	11	92	417	30	29288	0
Rangeland	833	95	2352	89	114	37	28198

The confusion matrix (Table 2.4) confirms the overall very-high accuracy of the land-cover classification. Confusions (marked in orange) are mostly observed for the different vegetation-related classes. An example for two typical confusions is depicted in Figure 2.15: Dense wooded areas are in some cases mis-classified as plantation areas (see also Figure 2.16) and very bright bare soil areas are in some cases confused as built-up. The latter problem was notably more pronounced in preliminary classification models that did not include SAR data.
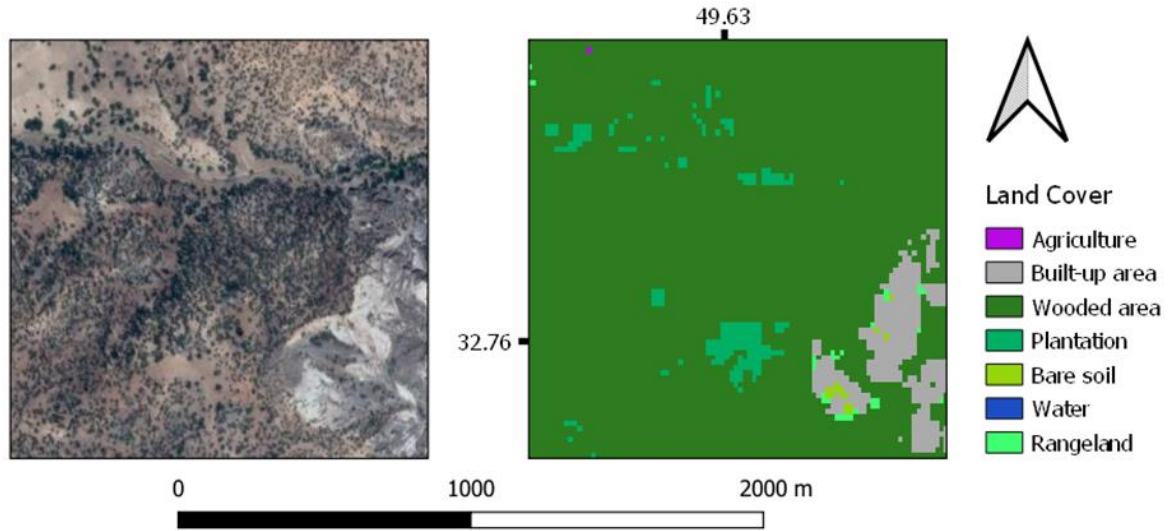
Figure 2.15 A wooded area example, that is miss-classified as plantation area and very bright bare soil area, that is miss-classified as built-up area

Figure 2.16 Two example photos of mixture of plantation/orchard and natural Zagros Forest in an area in Fars Province (taken in September 2019 by Elham Shafeian)

2. Mapping fractional woody cover in an extensive semi-arid woodland area at different spatial grains with Sentinel-2 and very high-resolution data
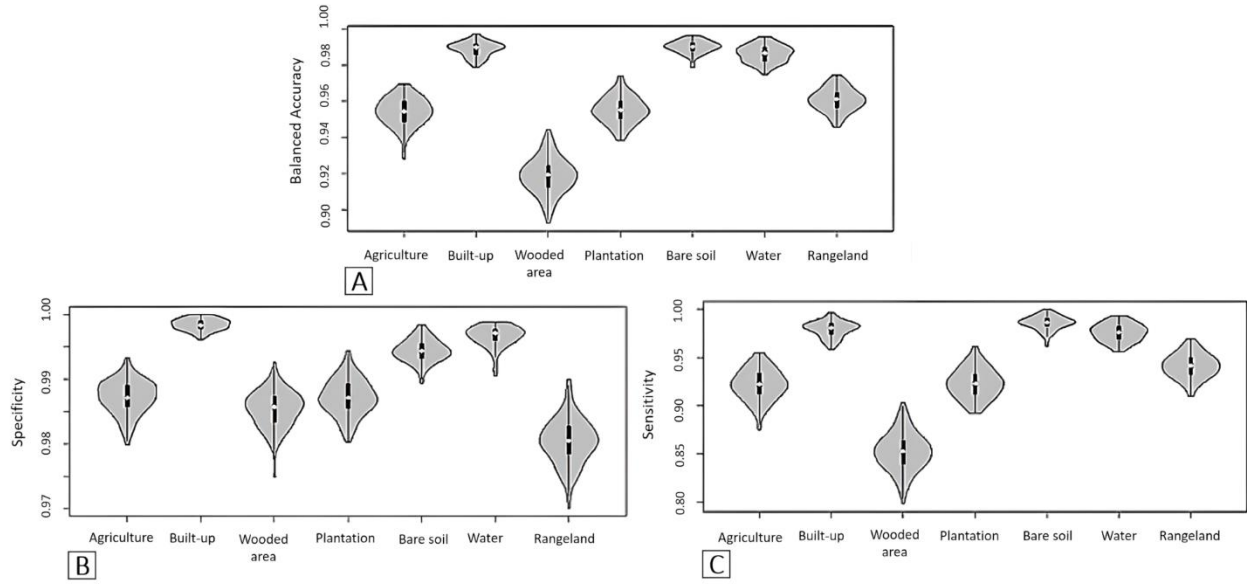
Figure 2.17 (A) Balanced accuracy; (B) specificity and (C) sensitivity of the LC classes in the supervised classification with topographical variables (elevation, slope) using NASA SRTM Digital Elevation 30m data, as it can be seen, there are hardly improvements in the landcover model, so we did not used these variables in the final model.

<u>Distribution of woody cover reference values for the examined spatial grains and correlations between the references datasets</u>

2. Mapping fractional woody cover in an extensive semi-arid woodland area at different spatial grains with Sentinel-2 and very high-resolution data
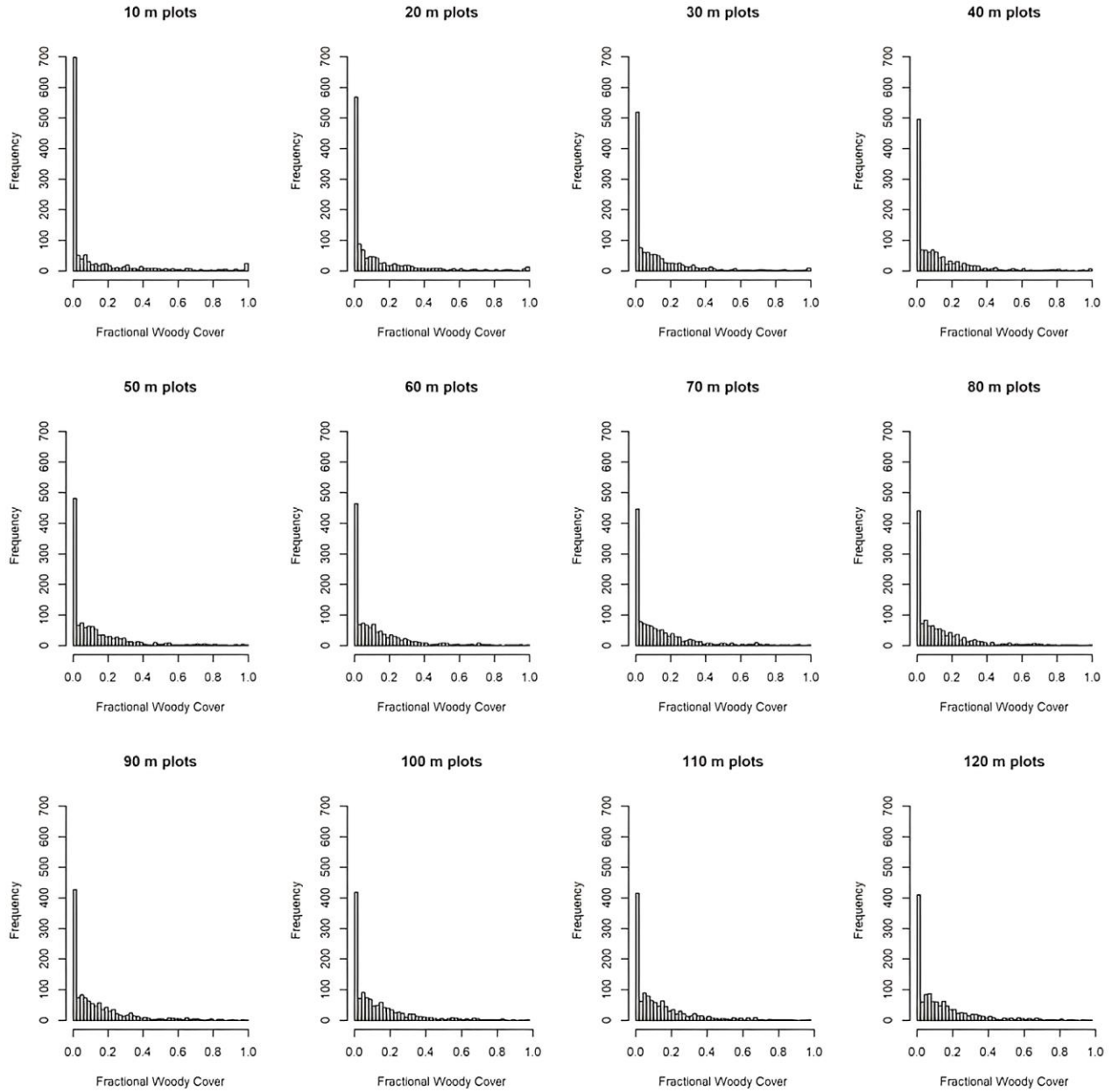
Figure 2.18 Histograms showing the woody cover reference datasets for the examined spatial grains. Extreme values (very high and very low cover values) become less frequent with increasing coarser spatial grains.

2. Mapping fractional woody cover in an extensive semi-arid woodland area at different spatial grains with Sentinel-2 and very high-resolution data
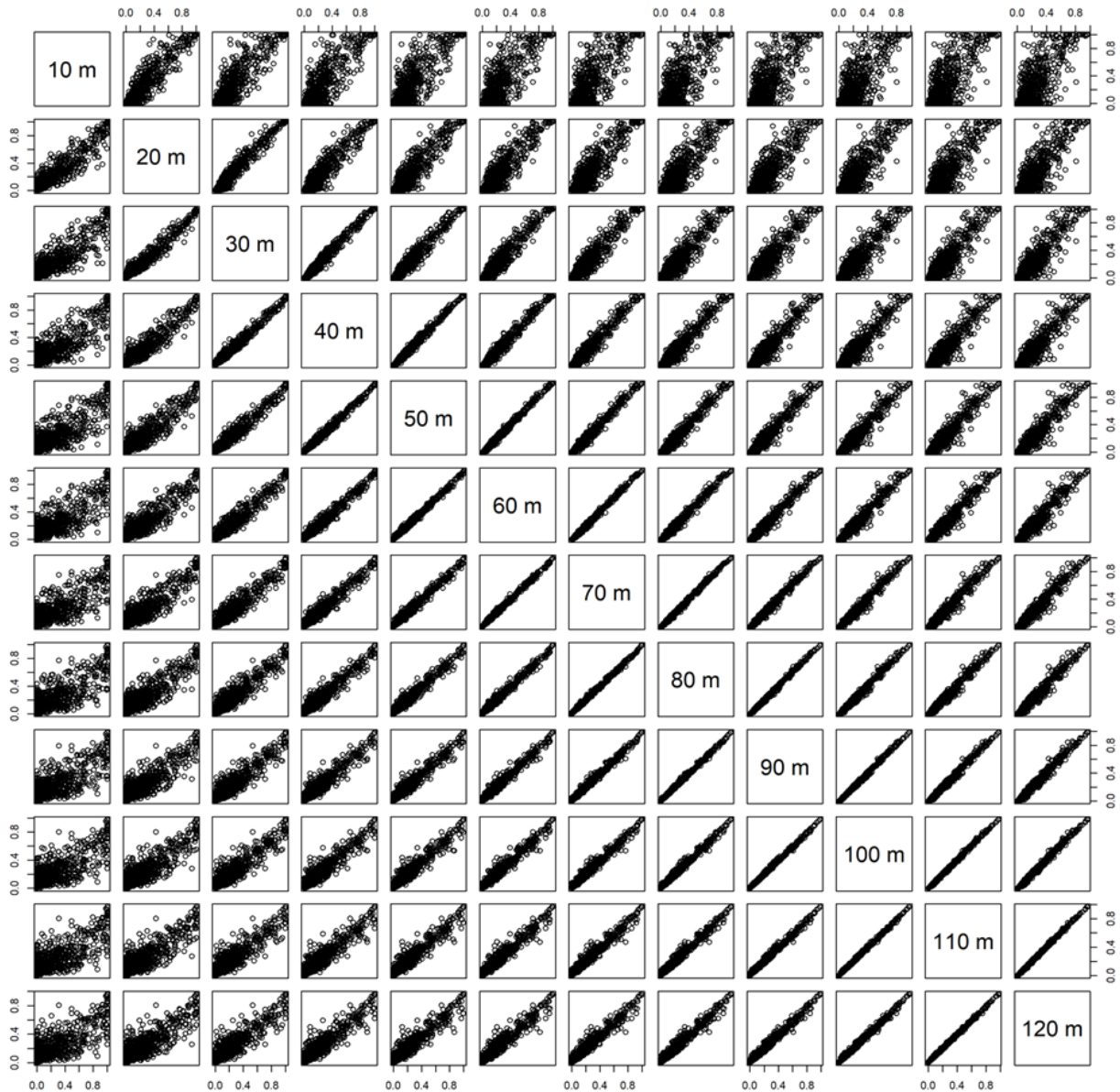
Figure 2.19 Scatterplots between all woody cover reference datasets for the examined spatial grains. As expected, the larger the grain difference, the less correlated the reference datasets applied for the different models are.

Reference images

The link to access the reference images used in the present study:

https://drive.google.com/drive/folders/1KjnVRMVRzrxp8KS1AqivGpUsjrhVFQ-x?usp=drive_link

2. Mapping fractional woody cover in an extensive semi-arid woodland area at different spatial grains with Sentinel-2 and very high-resolution data

Google Earth Engine Codes

for the Forest/woody cover product at 40 m spatial grain and at:

https://code.earthengine.google.com/d668f1c9e91b1c3c2be0b19678ec19ee

for the LC classification:

https://code.earthengine.google.com/f068d8006d0f81d01dcd1054081e1ec9

3. Detecting semi-arid forest decline using time series of Landsat data

Elham Shafeian, Fabian Ewald Fassnacht, Hooman Latifi

Abstract

Detecting forest decline is crucial for effective forest management in arid and semi-arid regions. RS using satellite image time series is a useful tool for identifying reduced photosynthetic activity caused by leaf loss and defoliation. However, current studies face limitations in detecting forest decline in sparse arid and semi-arid forests. In this study, three Landsat time-series-based approaches were used to distinguish non-declining and declining forest patches in the Zagros forests. The RF approach was the most accurate approach, with an overall accuracy and kappa value of almost 0.75 and 0.50, respectively followed by the anomaly detection approach with an overall accuracy and kappa value of 0.65 and 0.30, and the Sen's slope approach with an overall accuracy and kappa value of 0.64 and 0.30, respectively. The classification results were mostly unaffected by the Landsat acquisition times, indicating that rather environmental variables may have contributed to the separation of declining and non-declining areas and not the remotely sensed spectral signal of the trees. We conclude that identifying degraded and declining forest patches in arid and semi-arid regions using Landsat data is challenging. This difficulty arises from weak vegetation signals caused by limited canopy cover before a bright soil background, which makes it challenging to detect modest degradation signals. Additional environmental variables may be necessary to compensate for these limitations.

3.1. Introduction

Recent research highlights the rapid decline of arid and semi-arid forests worldwide, emphasizing the need for a better understanding of the causes of forest decline (e.g., Anderegg et al., 2012). While many studies have investigated deforestation in these regions (e.g., Hoyos et al., 2013; Waroux and Lambin 2012), forest decline has received relatively little attention (Waroux and Lambin 2012; Li et al., 2009). The decline of forests is often the result of degradation, which negatively impacts their functional and structural properties (Wang et al., 2020; Vásquez-Grandón et al. 2018). Forest decline can also decrease the regeneration capacity of a forest by reducing the number of available reproductive trees and altering micro-environmental conditions, in addition to the direct loss of trees (Cailleret et al., 2019). Moreover, forest decline can have long-term consequences for ecosystem services and regulatory services (Waroux and Lambin, 2012).

Forest decline is often caused by interacting biotic and abiotic factors (Hosseini et al., 2017). Among abiotic factors, droughts can have a particularly damaging effect on forests (Sulla-Menashe et al., 2014; Waroux and Lambin 2012). Arid and semi-arid ecosystems must deal with more frequent and severe droughts, which, in combination with other biotic stressors, can lead to significant forest decline (Sánchez-Pinillos et al., 2021). While forest decline occurs globally, arid and semi-arid ecosystems are particularly vulnerable, with an increasing tree mortality rate (David et al., 2022).

The Zagros forests in western Iran have been suffering from significant forest decline due to climatic extremes, wildfires, and overexploitation by local populations. Their low tree species diversity, dominated by a few oak species, in particular Brant's Oak (*Quercus brantii* Lindl.), makes them susceptible to various forest pathogens (Moradi et al., 2021; Goodarzi et al., 2016). Earlier studies conducted in the region often focused on deforestation but not forest decline (e.g., Moradi et al., 2021; Jahanbazy Goujani et al., 2020; Hosseini et al., 2017; Goodarzi et al., 2016). Understanding forest decline in the region is crucial for effective forest management and adaptation initiatives but is still lacking for larger continuous areas (Moradi et al., 2021).

Field data on forest decline is often limited due to cost, particularly in less accessible and extensive areas (Lausch et al., 2016, Diao et al., 2020, Shafeian et al., 2021) such as the Zagros forests. Studies performed by, for example, Wang et al. (2020) and Senf et al. (2020), indicate that RS is an alternative to assess forest decline in the field and over large regions. Comparing multitemporal satellite images enables the detection of changes in vegetation conditions in a particular area (Wang et al., 2020). Various studies have used VIs like NDVI (Jin et al., 2016) and normalized burn ratio (NBR) (Francini and Chirici, 2022) to detect forest decline. However, multispectral VIs are known to have limitations in monitoring biophysical and biochemical vegetation properties in semi-arid ecosystems (e.g., David et al., 2022). For instance, NDVI is sensitive to green components, not to woody components, and factors like moisture content and species composition can influence the relationship between biomass and NDVI. The EVI was developed to overcome the drawbacks associated with variable background reflectance and atmospheric interference in the

NDVI (David et al., 2022). The EVI provides more comprehensive information about changes in vegetation over time and space and is particularly suitable for assessing vegetation in arid and semi-arid ecosystems. Meanwhile, Bae et al. (2022) and Li et al. (2022) note that studies on forest decline commonly utilize VHR RS data, which can be costly and challenging to acquire for extensive areas.

As mentioned above, many RS studies in the context of forest monitoring have focused on deforestation rather than forest decline. The identification of deforestation (using optical RS) is based on the distinction of forest and non-forest land-cover types, such as open landscapes, bare soil, crops, and settlements (Hoekman et al., 2020). Among several types of RS data, multi-spectral optical images are the most cost-effective option for monitoring large forest areas. Time series of multispectral optical satellite data, such as Landsat and S2, have facilitated the development of various methodologies for mapping forest changes (Giannetti et al., 2020). In particular, the Landsat time series has been recognized as a valuable data source for tracking forest decline and disturbances due to their free accessibility, relatively high spatial resolution (30 m), long and consistent acquisition record, and accessibility (Dutrieux et al. 2015; Zhu et al. 2020; Diao et al. 2020; Senf et al. 2020; Giannetti et al. 2020; Rodman et al. 2021).

A variety of algorithms have been introduced for identifying forest disturbances throughout time, such as Continuous Change Detection and Classification (CCDC; Zhu and Woodcock, 2014), Landsat-based Trends in Disturbance and Recovery Detection (LandTrendr; Kennedy et al., 2010), and Breaks for Additive Season and Trend (BFAST; Verbesselt et al., 2010). Nevertheless, the majority of these algorithms are more advantageous for monitoring forest changes or deforestation than assessing forest decline or minor changes in forest status (Zhu et al., 2020). The difficulty of detecting subtle signals of degradation is a challenge for all algorithms, as spectral signals associated with tree mortality depend on various factors, including the number of canopy layers and FC (Hoekman et al., 2020).

This study seeks to assess the effectiveness of well-established methods like RF, anomaly detection, and Sen's slope analysis for identifying and mapping forest decline in the Zagros semi-arid forests.

3.2. Materials and Methods

3.2.1. Study area

The study area is located in the Chaharmahal and Bakhtiari provinces of Iran, in the Zagros semi-arid forests, with average rainfall of 250–800 mm and temperatures ranging from 9–25 °C (Attarod et al., 2016). The study area is located in the southwestern part of the province (Figure 3.1). The Zagros forests play an important role in preserving the unique vegetation and habitats indigenous to the region (Shafeian et al., 2021; Sagheb-Talebi et al., 2014). The most prominent and widespread tree species found in the area include Brant's oak (*Quercus brantii* Lindl.), which is partially mixed with *Quercus infectoria* G.Olivier, *Quercus libani* G.Olivier, wild pistachio

(*Pistacia atlantica* Desf.), and *Acer monspessulanum* L. In addition, one can commonly find *Crataegus spp.*, *Amygdalus spp.*, and *Pyrus spp.* in the area (Daneshmand Parsa et al., 2016; Erfanifard et al., 2014).
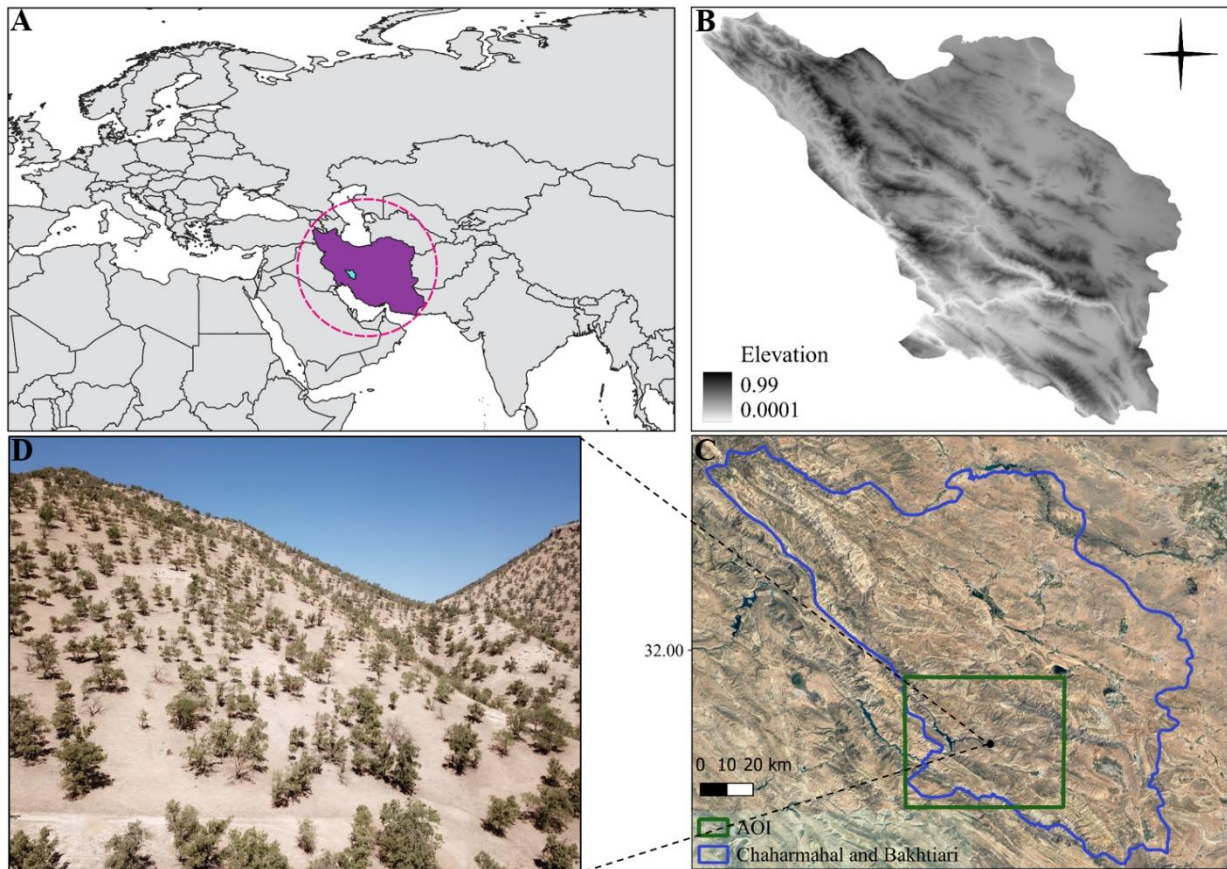
Figure 3.1 (A) Location of Iran; (B) Digital Elevation Model (DEM) of Chaharmahal and Bakhtiari Province; (C) Sampled area covered in the green square (AOI); (D) An example UAV image of the study region.

3.2.2. Reference data

So far, no official and regular forest inventories exist for the majority of the Zagros region. Therefore, we tried to maximize the number of field samples from which the state of the forest is known by merging various datasets collected between 2021 and 2022 in the region.

The first part of our reference data was collected during a field campaign in the spring of 2022, during which declining and non-declining areas were inventoried. After consultation with local experts to define the study area, a stratified random sampling approach was used to select areas for sampling. Two factors were considered to stratify the study area: Illumination Condition (IC) and FC. The IC for each pixel in the study area was calculated using NASA SRTM Digital Elevation imagery available on GEE (ID: USGS/SRTMGL1_003). Although IC is not directly related to forest decline, it was assumed that it could affect satellite signals. In addition, an existing FC map

for the area provided by Shafeian et al. (2021) was used. FC is known to significantly affect RS signals. The study area was divided into four classes each for IC and FC, resulting in a total of sixteen layers (combinations of IC and FC classes). To further account for accessibility, a 400-m buffer was applied around roads, and random points were generated within these buffers with a minimum distance of 100 m between each point. Nine random points were selected for each stratum, for a total of 144 candidate positions for field verification. Approximately half of these points were eventually visited and field recorded. During the field campaign, information on the condition of the forests was collected and classified into two general categories: "declining" and "non-declining". Overall, this process allowed the collection of reference data that can be used to validate and calibrate RS data to accurately assess forest decline in the study area.

The second source of reference data was a field campaign conducted in September 2021. The locations of the field surveys were determined by first stratifying the study area into two zones of declining and non-declining areas according to an EVI time series as observed for the last 36 years using Landsat data. To identify these zones, we applied an EVI anomaly approach based on data between 1986 and 2021. The resulting binary image indicated declining and non-declining areas. The field plot locations were chosen at random within the defined declining area. Plots in inaccessible areas were dropped and replaced with plots that were located closer to the roads. During the field campaign, we visited and recorded 43 sites. Any signs of deterioration, such as foliar deficiencies, branch mortality, or unusual leaf coloration, were documented (Figure 3.2 shows some examples of the decline signs).
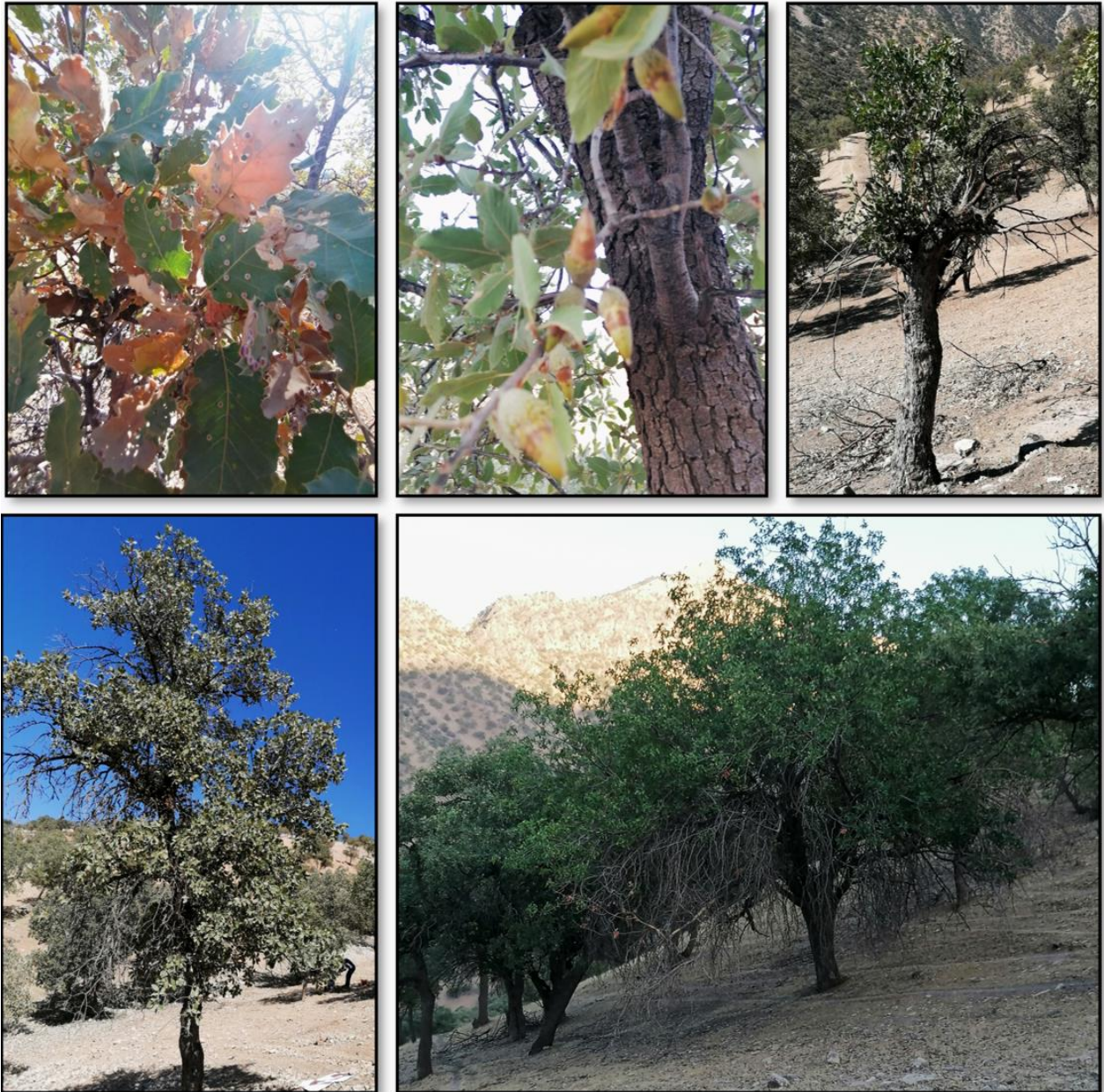
Figure 3.2 Example of declining trees in the study area. Images were taken by Elham Shafeian during the field campaign in September 2021. The exact reasons for the decline were often unknown. In some cases signs of the presence of damaging insects or pathogens were visible, but it was impossible to determine whether these were a consequence or the reason for the decline.

The third source of data is a set of additional GPS locations for declining and non-declining tree groups collected by local forest service officers in September 2022. All the reference points used in this study are jointly plotted in Figure 3.3. In total, we had positions for 461 declining and 422 non-declining plots.
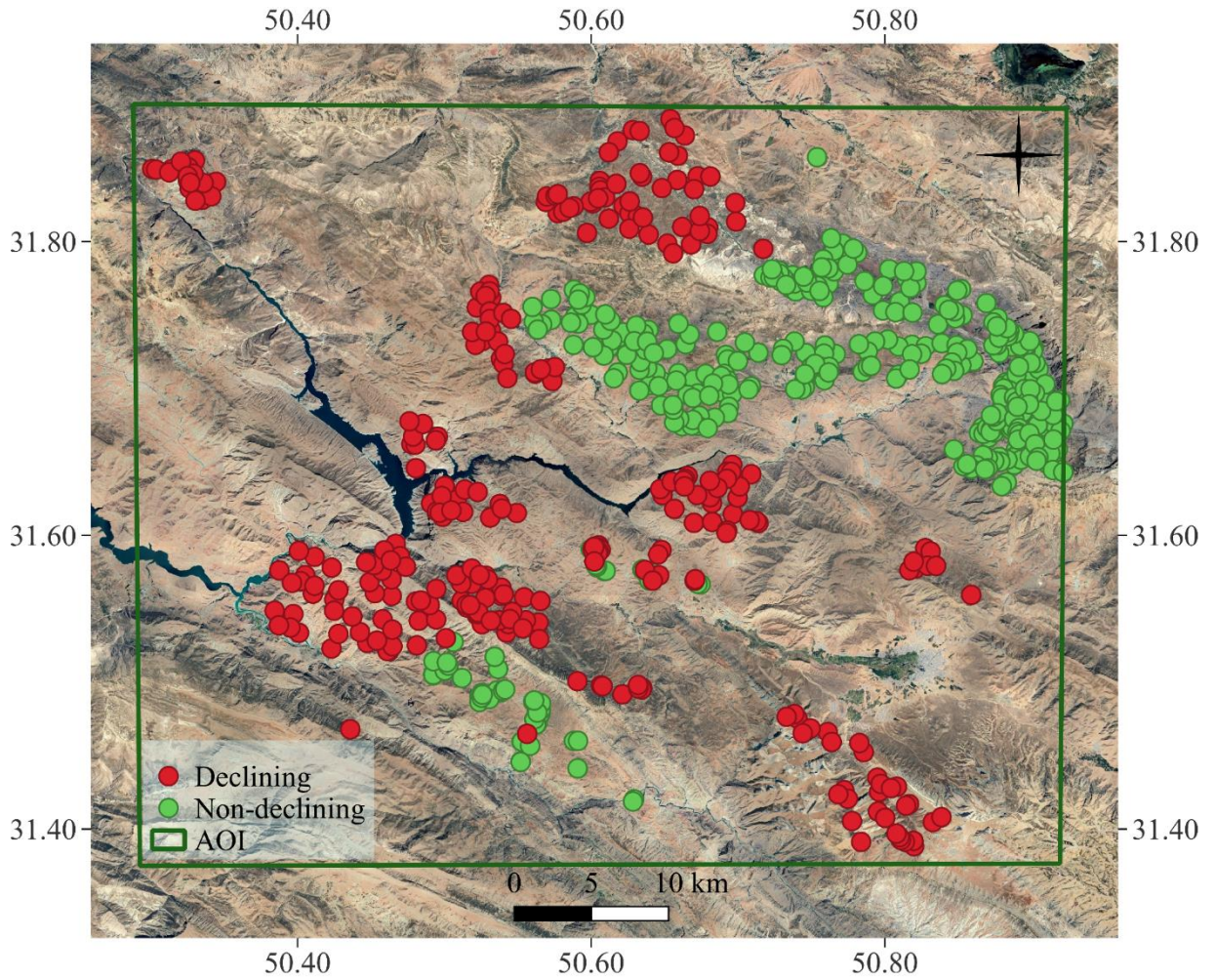
Figure 3.3 The reference points, declining areas in red and non-declining in green

3.2.3. Methodology

The workflow for the study is outlined in Figure 3.4 and further described below.
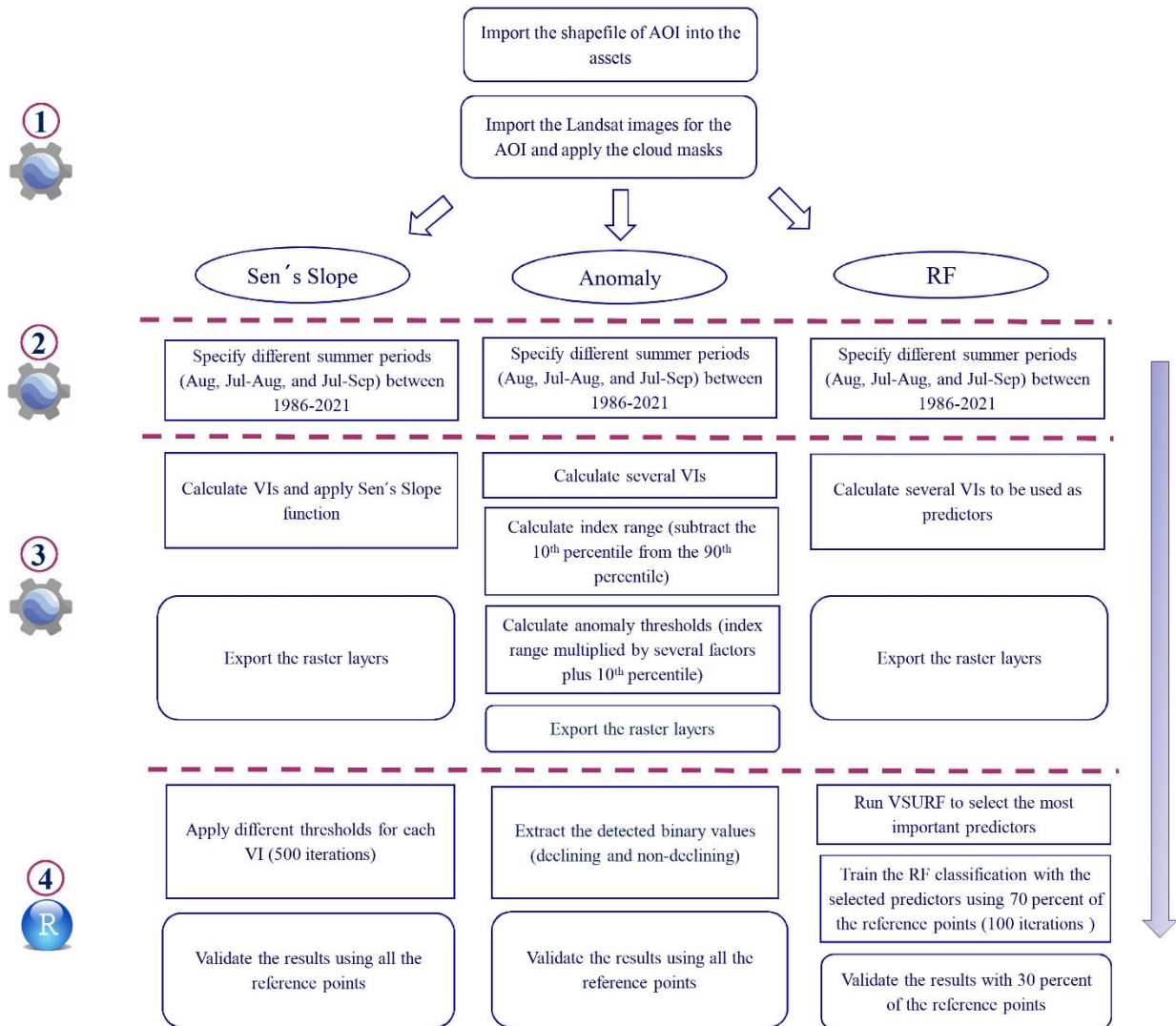
Figure 3.4 The workflow of the present study (steps 1, 2, and 3 were performed in GEE, and step 4 was performed in R.)

3.2.3.1. RS analysis

In this study, we looked at a variety of methodical approaches developed for analyzing time series and image stacks of optical Landsat images to see if we could distinguish between declining and non-declining forest regions. In the following, we will first describe the pre-processing steps and then introduce the tested methodical approaches.

3.2.3.1.1 Landsat time series and image processing

The GEE platform was used to process the Landsat image time series. The analysis employed the Landsat Surface Reflectance Tier 1 data from Landsat 4 Enhanced Thematic Mapper (ETM), Landsat 5 ETM, Landsat 7 ETM+, and Landsat 8 Operational Land Imager (OLI) (IDs,

respectively: LANDSAT/LT04/C01/T1; LANDSAT/LT05/C01/T1; LANDSAT/LE07/C01/T1; and LANDSAT/LC08/C02/T1_L2). We filtered the image collection to include all images that were available for the summer periods of 1986 to the summer periods of 2021. We examined three definitions for the summer periods to see if there was any effect on the results: (1) Landsat data from the months between July and the end of September, (2) July and the end of August, and (3) only August, i.e., the dry season, with the highest spectral signal differences between trees and other vegetation, crops, and grass, as suggested by Symeonakis et al. (2018). Then we calculated the annual median reflectance value for each pixel and band from the remaining cloud-free image stack, which resulted in a cloud-free, high-quality mosaic. In order to detect forest decline, a set of VIs was computed using these annual composites (Martin-Ortega et al., 2020). The examined VIs are summarized in Table 3.1. In the case of the RF classifications (see below), we did not use the annual mosaics but calculated a single mosaic using all Landsat data from the corresponding time periods.

Table 3.1 Equations of the used VIs

VI	Name	Equations	Reference
NDVI	Normalized Difference Vegetation Index	$(NIR - RED)/(NIR + RED)$	Rouse et al. (1974)
GNDVI	green NDVI	$(NIR - GREEN)/(NIR + GREEN)$	Gitelson et al. (1966)
kNDVI	Kernel NDVI	$\tanh((NIR - RED)^2 / 2\ sigma)$ $sigma = NIR + RED\ (0.5)$	Camps-Valls et al. (2021)
NRGI	Normalized Green-Red Vegetation index	$(GREEN - RED)/(GREEN + RED)$	Buce Saleh (2019)
EVI	Enhanced Vegetation Index	$2.5\ ((NIR - RED)/(NIR + C1 \times RED - 7.5 \times BLUE + 1))$	Liu and Huete (1995)
SR	Simple Ration	$(NIR)/(RED)$	Jordan (1969)
SLAVI	Specific Leaf Area Vegetation Index	$(NIR)/(RED + SWIR)$	Lymburner et al. (2000)
NDWI	Normalized Difference Water Index	$(GREEN - NIR)/(GREEN + NIR)$	Hardisky et al. (1983)
NDMI	Normalized Difference Moisture Index	$(NIR - SWIR)/(NIR + SWIR)$	United States Geological Survey
NDTI	Normalized Difference Tillage Index	$(SWIR1 - SWIR2) / (SWIR1 + SWIR2)$	Deventer et al. (1997)

NBR	Normalized Burn Ratio	(NIR- SWIR2)/(NIR + SWIR2)	United States Geological Survey
ARVI	Atmospherically Resistant Vegetation Index	(NIR-(2×RED)-BLUE)/(NIR+(2×RED) +BLUE)	Kaufman and Tanre (1992)
GCI	Green Chlorophyll Index	NIR / GREEN – 1	Gitelson et al. (2005)
GLI	Green Leaf Index	(GREEN-RED-BLUE)/(2× RED+GREEN+BLUE)	Gitelson et al. (2002)

3.2.3.2. Identifying forest decline

The datasets described in the previous section were used as inputs to the following approaches:

3.2.3.2.1 RF classification

The RF classifier (Breiman, 2001) was used to classify the study area into declining and non-declining classes. Previous studies (e.g., Belgiu and Dragut, 2016) successfully utilized the RF classifier for satellite data classification and forest disturbance analysis. In this study, several RF classifiers were trained with Landsat data covering various year intervals, and each classifier was validated using iterative splitting of the reference data (see below) into training and validation sets (with 100 repetitions) to distinguish between declining and non-declining areas throughout the study area. This was done using the randomForest package in R with the number of trees (ntree) set to 500 and the second parameter, mtry, set to default settings. In order to prevent the issue of having two different classes in one pixel (a few of the available field plots were located too close to each other), we built a function during the RF classification training to eliminate any duplicated reference pixels, resulting in the removal of 164 points. As a result, a total of 719 reference points remained. As inputs, we initially used the Landsat time series with images from summer 1986 to summer 2021 as well as from 2000–2021 and from 2010–2021 and examined the three input options described above: (1) images from July to the end of September; (2) images from July to the end of August; and (3) images from August. We examined several time periods since we did not have a clear idea of when the field-observed decline processes had started. According to local experts and previous literature, the decline accelerated after the year 2000 (e.g., Ghanbari Motlagh and Kiadaliri, 2021), but no detailed information exists. Since the RF was showing very stable results, we then examined even more time periods reaching further in the past (1986-1990, 1986-1999, 1991-1995, 1996-2000, 2001-2005, 2006-2010, 2011-2015, and 2016-20201).

We used all of the VIs listed in Table 3.1 as predictors, as well as the seven original bands of the Landsat data. Then, in addition to using all the predictors separately for each input period, we also applied the feature selection algorithm VSURF in R (Genuer et al., 2015). The first step in the

variable selection process with VSURF is to remove all non-essential, i.e. highly interrelated variables, from the dataset. The second step is to select all variables that are related to the response and help the model perform well. The third step refines the collection for prediction purposes by removing redundancy in the range of variables chosen in the second step (Genuer et al., 2015). Table 3.2 shows the predictor variables that were selected for each of the three input options. To obtain the final maps, we used all available reference data for classification. The result was a binary map of binary raster layers showing two classes (non-declining, and declining). To validate the RF model, the reference data set was repeatedly divided into 70% training samples and 30% validation samples (Shafeian et al., 2021). We obtained kappa and overall accuracy from the validation samples.

In addition to the Landsat series, we also applied an RF classification to S2 imagery captured between 2015 and 2021 using the same procedure (see Supplementary Material II). The spatial resolution of S2 imagery is higher than that of the Landsat series at 10 * 10 m, making it a good option for forest decline detection. However, these images have only been available since 2015, limiting the ability to perform time series analysis such as anomaly detection over a longer period.

3.2.3.2.2 Anomaly analysis

As a second approach, we applied a pixel-wise anomaly analysis using the VIs. For this purpose, we used the annual Landsat mosaics from 1986–2021. Again, we examined the three input options to define the summer period. Following the calculation of the VIs for each image collection as described above, a median value filter of a temporal moving window with a three-year interval was applied to the annual time series of the indices, that is, 1986–1989, 1987–1990,... 2018–2021. Then all these images were stacked into one single image time-series stack. This step was conducted to smooth the datasets and avoid the potential influence of particularly high or low values in an individual year, which may have been related to extraordinary weather conditions or a limited number of cloud-free sample pixels. For each pixel of this time series stack, the "all-time high" and "all-time low" values, defined as the 90th and 10th percentiles, respectively, were calculated. Then the 10th percentile was subtracted from the 90th percentile to check how widely the VI value of a given pixel varied over the whole time period. This range was then used to define an anomaly threshold. For example, the range was multiplied by 0.5, and the resulting value was added to the value of the 10th percentile of the VI time series. We then considered an area to be declining if the current VI value (see below) was below the 10th percentile plus the $0.5 \times$ range value. The corresponding areas were identified by applying the pixel-specific thresholds, resulting in a binary raster layer (zero or black = non-declining, and one or orange = declining) for each VI. We varied the factor with which the range was multiplied and examined the results for all factors from 0.15 to 0.9 with steps of 0.05. The current VI value for each pixel was obtained from a cloud-free mosaic image of the current status of the area calculated from Landsat images of the years 2018–2021. These calculations were performed for all indices given in Table 3.1.

3.2.3.2.3 Sen's Slope analysis

Sen's slope, or Theil-Sen's slope (Sen, 1968), is a non-parametric trend analysis that is resistant to outliers and rejects odd values without changing the slope (Correa-Díaz et al., 2019). We used this approach because it is useful to identify whether a regular time series has a statistically significant positive or negative trend. The Sen's slope can account for the magnitude of changes (Reygadas et al., 2019). Thus, after importing a cloud-free Landsat time series and calculating the aforementioned VIs (e.g., KNDVI, ARVI, etc.), the Sen's slope was calculated using the ee.Reducer.sensSlope() function available in GEE. With this algorithm, we could estimate the trend of changes in the region over the previous 36 years using mosaics of Landsat imagery. We again examined all three input options with respect to the summer period. The results were then exported as a raster layer for each summer period and VI (14 VIs and three summer periods gave a total of 42 single-band raster layers). To translate the Sen's slope results into a binary map that we could compare with our reference data, we defined a function to calculate 500 different threshold values for each VI (based on the range of Sen's slope values obtained for the VI) and determined the best threshold for detecting the declining areas (according to our reference data). We calculated the thresholds for each VI individually since each index had a different range of values. We ran this for each index separately over three summer seasons. Finally, the threshold with the highest overall accuracy was recorded (the results of the selected threshold for each index are summarized in Table 3.6 in Supplementary Material II).

3.2.3.3. Visualization of VIs time series

To guide the interpretation of the results, particularly with respect to the anomaly and Sen's slope analysis, we additionally visualized the VI time series from 1984-2022 for the two most accurate (according to overall accuracy) VIs using the pixels representing the reference data locations for declining and non-declining areas from the spring 2022 campaign. We calculated the median of all pixels coinciding with the corresponding reference plots.

3.3. Results

Figure 3.5 displays binary decline maps from all three approaches. To ensure that the analysis focused only on relevant LC types, we used an LC map to mask out irrelevant classes such as water, bare soil, and agriculture, using the LC map of Shafeian et al. (2021). This left only rangeland, forest, and plantations for further analysis, allowing for a more accurate and targeted assessment of the study area.

   Visual inspection revealed that certain areas in the southwest were consistently detected as declining zones in all approaches, but each approach contained some errors. RF performed better than the other two approaches. However, overall, the examined approaches performed moderately to poor, as also reflected in the noticeable differences between the maps.
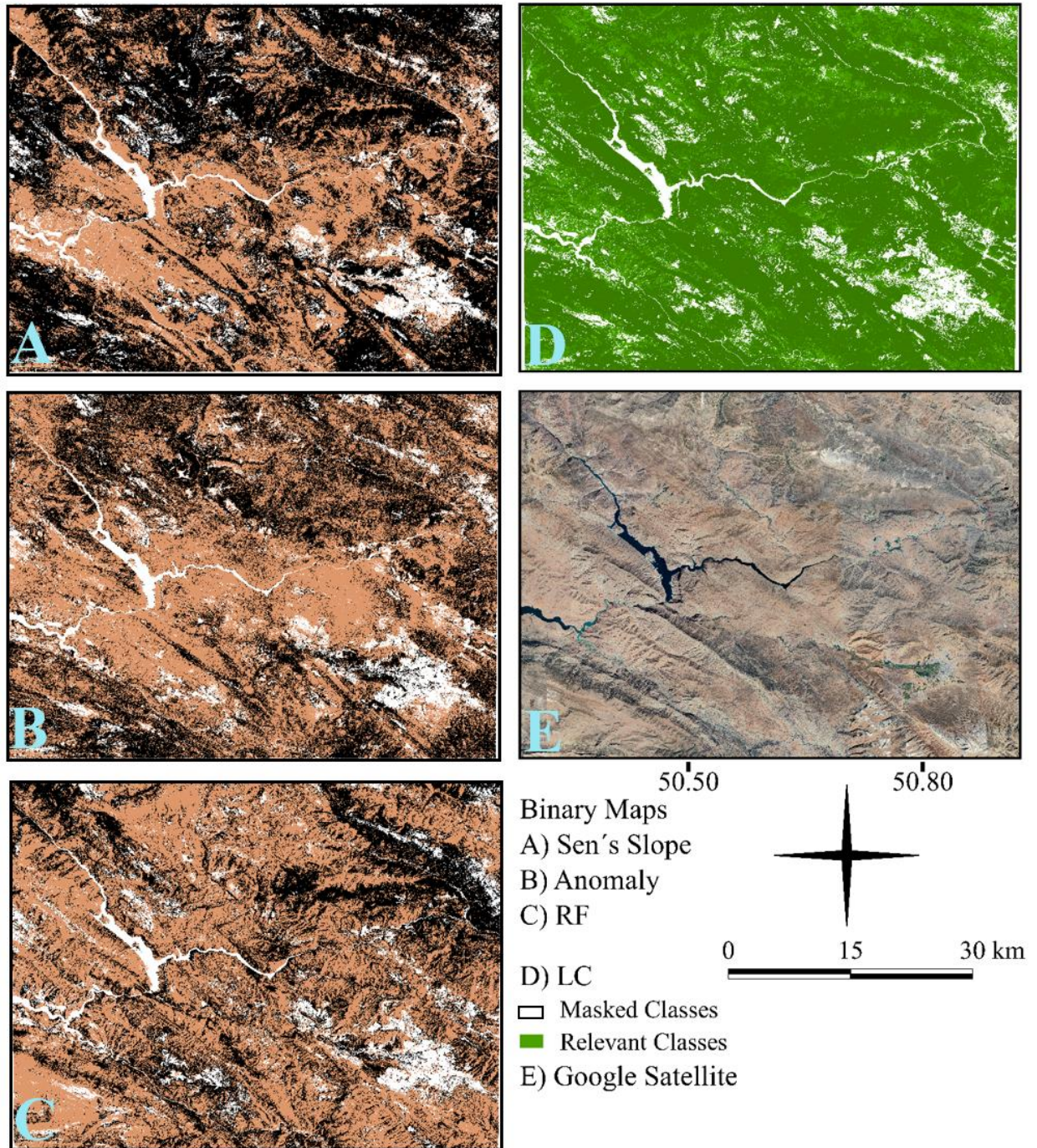
Figure 3.5 A) Sen's slope (NDMI index with threshold = 107.93 (August)); B) Anomaly (NRGI 20th percentile (July-August)), and C) RF (July-August) for 1986 to 2021(Declining forest areas are marked in orange, while non-declining areas are depicted in black); D) LC map (masked classes in white and the relevant classes in green); E) Google Earth view of the study area.

3.3.1. Validation and accuracy of forest decline detection

3.3.1.1. RF

The RF accuracy for different summer seasons was stable, with the median overall accuracy out of 100 iterations for splitting training and testing reference points ranging between 0.72 and 0.76 (Figure 3.6). The best accuracy was achieved using input datasets containing images taken between July 1 and the end of August for the years between 2000 and 2021 (overall accuracy = 0.76, kappa = 0.50). The user's accuracy for the non-declining class was approximately 0.80, whereas it was approximately 0.72 for the declining class. The producer's accuracies for the two classes were 0.78 and 0.72, respectively (see Figure 3.7). Images for the period between 1986 and 2021 had the second-highest median values for overall accuracy and kappa with 0.75 and 0.48, respectively (see Figure 3.6). The user´s and producer´s accuracies for the non-declining class of this analysis were around 0.76 and 0.77, respectively, and for the declining class, 0.70 and 0.69, respectively (see Figure 3.7).

More detailed RF results for the years 1986–2021, 2000–2021, and 2010–2021 for all the summer seasons are shown in Figure 3.13 in Supplementary Material II (i.e., specificity, F1 Score, etc.). The RF results for the years further in the past, including 1986–1999, 1990–1995, and 1996–2000, for the three examined summer periods and their comparison with other year interval results are shown in Figure 3.6. The highest accuracy was obtained for the input dataset with images from July 1 to the end of August for the years between 1996 and 2000 (overall accuracy = 0.76, kappa = 0.50). Also, the user´s accuracy of the non-declining class and the declining class for this analysis was almost 0.78 and 0.72, respectively, and the producer´s accuracy of the non-declining and declining classes was almost 0.80 and 0.71, respectively (Figure 3.7). The user´s accuracy of the non-declining class and the declining class for this analysis for other summer seasons (August and July-September) can be found in Figure 3.11 and Figure 3.12 in Supplementary Material II.
The RF results based on VSURF-selected predictors hardly improved accuracy and kappa values. The selected predictors are summarized in Table 3.2.

Table 3.2 The results of VSURF on RF for each season. The selected predictors of Landsat 8 images are written with a suffix (_LS8).

Landsat data for summer periods	Selected predictors
August **1986-2021**	B1 , B2 , B3_LS8, NDVI, B2_LS8, B3, NDWI, B5, NRGI, NDTI
August **2000-2021**	B2 , B1 , B3_LS8 , B3, NDMI, NDWI, B6, B1_LS8, NDTI
August **2010-2021**	B2, B1, B3_LS8, B3, B2_LS8, NDWI, B1_LS8, B6, B5
July- August **1986-2021**	B1, B2, B3_LS8, B3, NDVI, NDWI, NRGI, B5, B6, NDTI

July- August 2000-2021	B1, B2, B3, NRGI, NDTI, NDWI
July- August 2010-2021	B2, B1, B2_LS8, NDWI, B6, B5, NRGI, B1_LS8
July- September 1986-2021	B1, NDMI, B3, B2_LS8, NDWI, B6, NDTI
July- September 2000-2021	B2, B1, NDMI, B3, B2_LS8, NRGI, NDWI, NDTI
July- September 2010-2021	B2 , B1, NDMI, B3_LS8, B2_LS8, B3, B6, NDWI
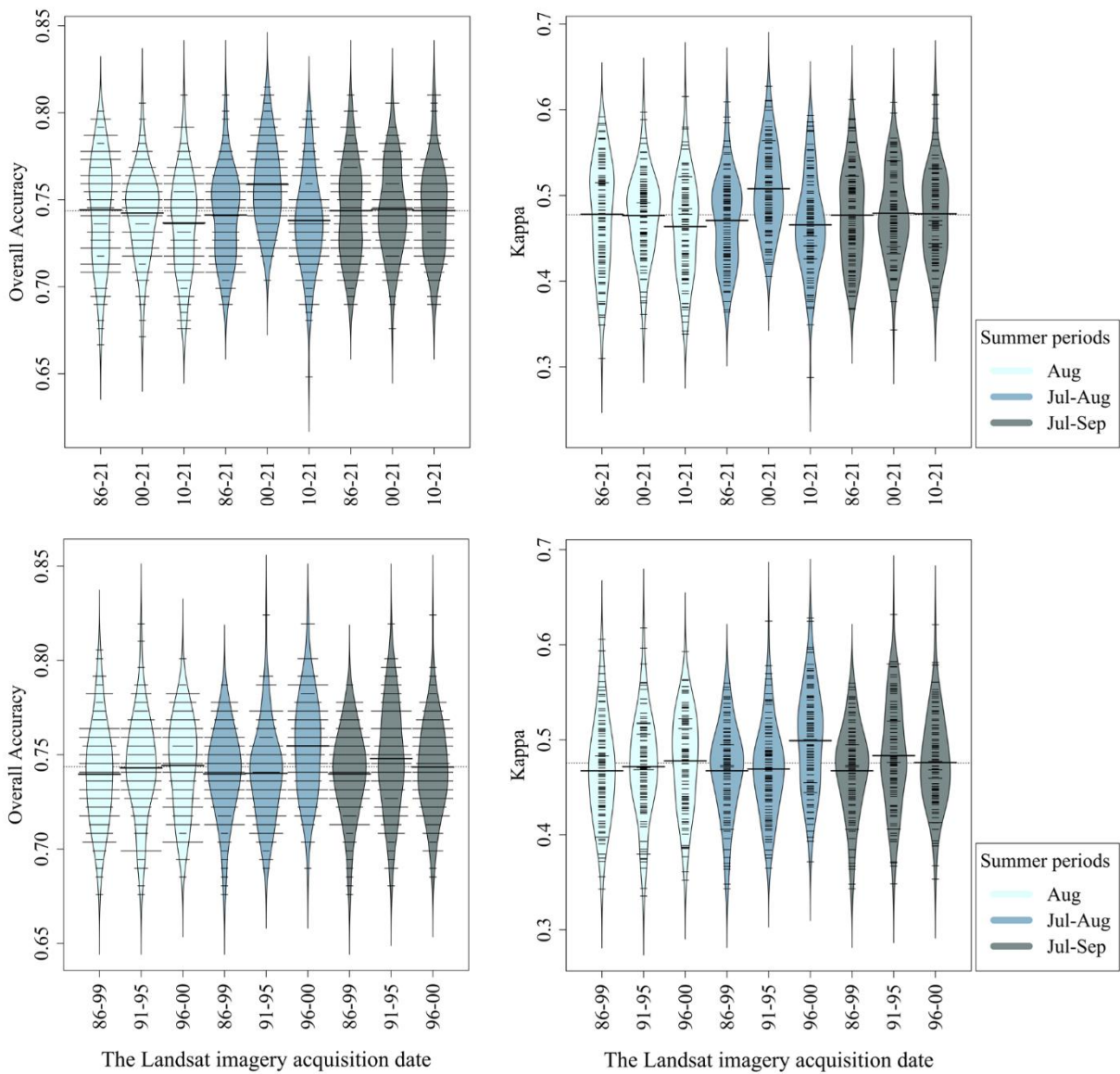
Figure 3.6 The upper row of the plot shows the overall accuracy and the kappa values of the RF classifications for the years 1986–2021 (86–21), 2000–2021 (00–21), and 2010–2021 (10–21) for the three

73

examined summer periods shown in different colors (August, July–August, and July–September). The lower row of the plot shows the same analysis for the years 1986–1999 (86–99), 1991–1995 (91–95), and 1996–2000 (96–00). The fine dashed lines indicate the overall mean across all bean plots.
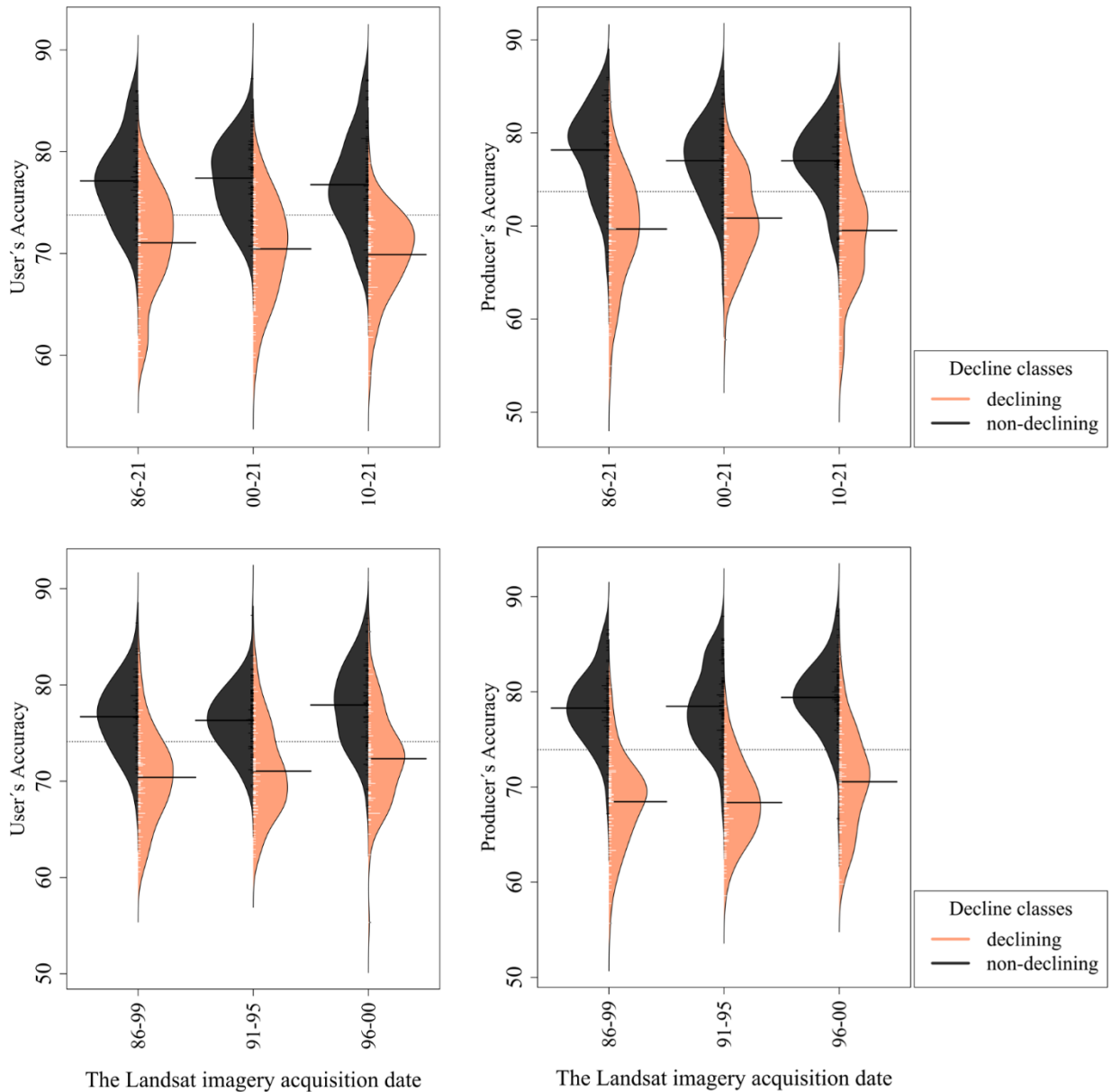
Figure 3.7 The upper row of the plot shows the user and producer accuracies for declining and non-declining classes of RF classifications for the years 1986–2021 (86–21), 2000–2021 (00–21), and 2010–2021 (10–21) for the July–August summer period. The lower row of the plot shows the same analysis for the years 1986–1999 (86–99), 1991–1995 (91–95), and 1996–2000 (96–00). The fine dashed lines show the overall mean across all bean plots.

3.3.1.2. Anomaly analysis

The best results for anomaly analysis were obtained when using the annual composite time series comprising images from July to August. In this configuration, the GLI (30th percentile) achieved a kappa value of 0.30 and an overall accuracy of 0.65. The user accuracies for the non-declining and declining classes were 0.61 and 0.69, respectively, while the producer accuracies for these classes were 0.71 and 0.59, respectively. In contrast, when using images from July and September, the NDWI (15th percentile) and the NDWI (20th percentile) had the lowest accuracy values, with kappa values and overall accuracy of -0.13 and 0.45, respectively. The Kappa values of anomaly analyses for three summer periods at different percentiles for all the VIs are shown in Figure 3.8, and the overall accuracies are shown in Figure 3.19, Supplementary Material II. Further details on the results can be found in Table 3.3. The detailed results of this analysis for user´s and producer´s accuracies for declining and non-declining classes can be found in Table 3.6, Supplementary Material II.
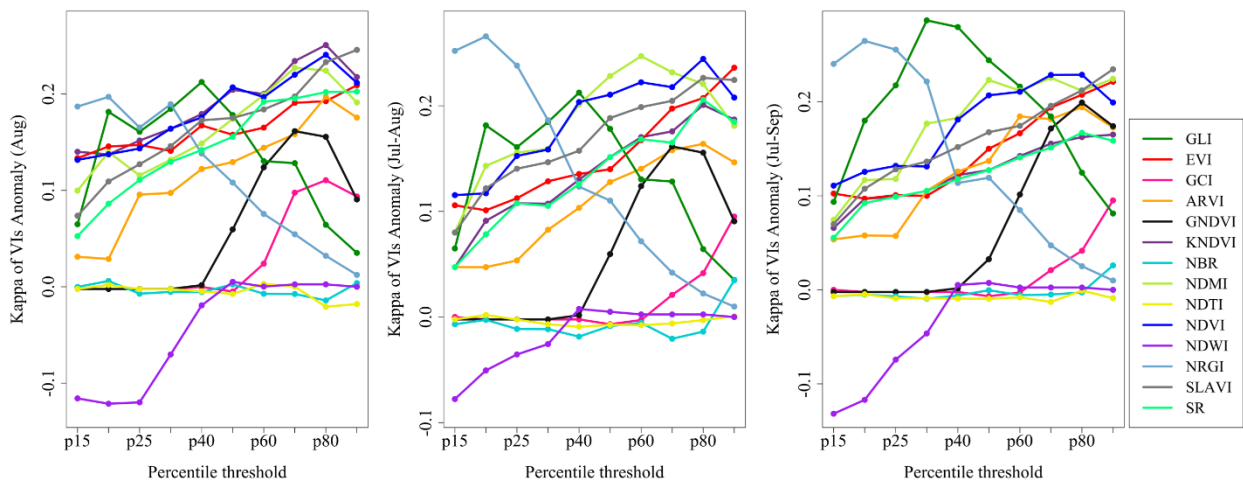
Figure 3.8 Kappa values of anomaly analysis at different percentiles for all the VIs of August (left panel), July to August (center panel), and July to September (right panel).

Table 3.3 A summary of the results (overall accuracy (in bold) and kappa value) of the anomaly approach for different VIs at different threshold percentiles (15–90) for July to August. The percentile (P) with the highest overall accuracy is marked with an asterisk, and the VI with the highest overall accuracy is underlined.

P VI	15	20	25	30	40	50	60	70	80	90
NDVI	**0.54**	**0.54**	**0.56**	**0.56**	**0.59**	**0.59**	**0.60**	**0.60**	**0.61**[*]	**0.60**
	0.11	0.11	0.15	0.15	0.20	0.21	0.22	0.21	0.24	0.20
GNDVI	**0.47**	**0.47**	**0.47**	**0.47**	**0.47**	**0.48**	**0.53**	**0.55**	**0.58**	**0.58**
	-0.002	-0.002	-0.002	-0.002	0	0.02	0.09	0.14	0.19	0.18

KNDVI	0.50	0.52	0.53	0.53	0.54	0.56	0.57	0.57	0.59	0.58
	0.04	0.09	0.10	0.10	0.13	0.15	0.17	0.17	0.20	0.18
NRGI	0.62*	0.63*	0.62*	0.60	0.57	0.57	0.55	0.54	0.53	0.52
	0.25	0.26	0.23	0.18	0.12	0.11	0.07	0.04	0.02	0.009
EVI	0.53	0.53	0.54	0.55	0.55	0.55	0.57	0.59	0.59	0.61*
	0.10	0.10	0.11	0.12	0.13	0.14	0.16	0.19	0.20	0.23
SR	0.50	0.52	0.53	0.53	0.54	0.56	0.57	0.57	0.59	0.58
	0.04	0.07	0.10	0.10	0.12	0.15	0.16	0.16	0.20	0.18
SLAVI	0.52	0.54	0.55	0.55	0.56	0.58	0.58	0.59	0.60	0.60
	0.07	0.12	0.14	0.14	0.15	0.18	0.19	0.20	0.22	0.22
NDWI	0.47	0.49	0.50	0.50	0.52	0.52	0.52	0.52	0.52	0.52
	-0.007	-0.005	-0.003	-0.002	0.007	0.004	0.002	0.002	0.002	0
NDMI	0.52	0.55	0.56	0.56	0.59	0.60	0.61*	0.61	0.60	0.59
	0.08	0.14	0.15	0.15	0.20	0.22	0.24	0.23	0.22	0.18
NDTI	0.47	0.47	0.47	0.47	0.47	0.47	0.47	0.47	0.47	0.48
	-0.002	-0.001	-0.002	-0.006	-0.009	-0.007	-0.007	-0.006	-0.002	0
NBR	0.47	0.47	0.47	0.47	0.46	0.47	0.47	0.46	0.47	0.50
	-0.006	-0.002	-0.01	-0.01	-0.002	-0.008	-0.005	-0.02	-0.01	0.03
ARVI	0.50	0.50	0.50	0.52	0.53	0.54	0.55	0.56	0.57	0.56
	0.04	0.04	0.05	0.08	0.10	0.12	0.14	0.15	0.16	0.14
GCI	0.47	0.47	0.47	0.47	0.47	0.47	0.47	0.49	0.50	0.53
	0	-0.002	-0.002	-0.002	-0.002	-0.006	-0.002	0.02	0.04	0.09
GLI	0.56	0.60	0.62*	<u>0.65*</u>	0.61	0.60	0.60	0.60	0.57	0.55
	0.14	0.22	0.26	0.30	0.22	0.19	0.19	0.12	0.07	0.05

3.3.1.3. Sen's Slope

The highest overall accuracy for Sen´s slope was achieved by GLI and NDMI for August, with approximately 0.64 (kappa = 0.53) and 0.63 (kappa = 0.56), respectively. The Kappa values of the Sen´s slope for all the VIs of three summer periods at different thresholds are shown in Figure 3.9; the overall accuracies are shown in Figure 3.20, Supplementary Material II. The lowest overall accuracy (0.39) was obtained by GCI and GNDVI for both August and July–August. Detailed information for the median overall accuracy and kappa values for each VI is shown in Table 3.4. The corresponding results for user´s and producer´s accuracies for declining and non-declining classes can be found in Table 3.7, Supplementary Material II.
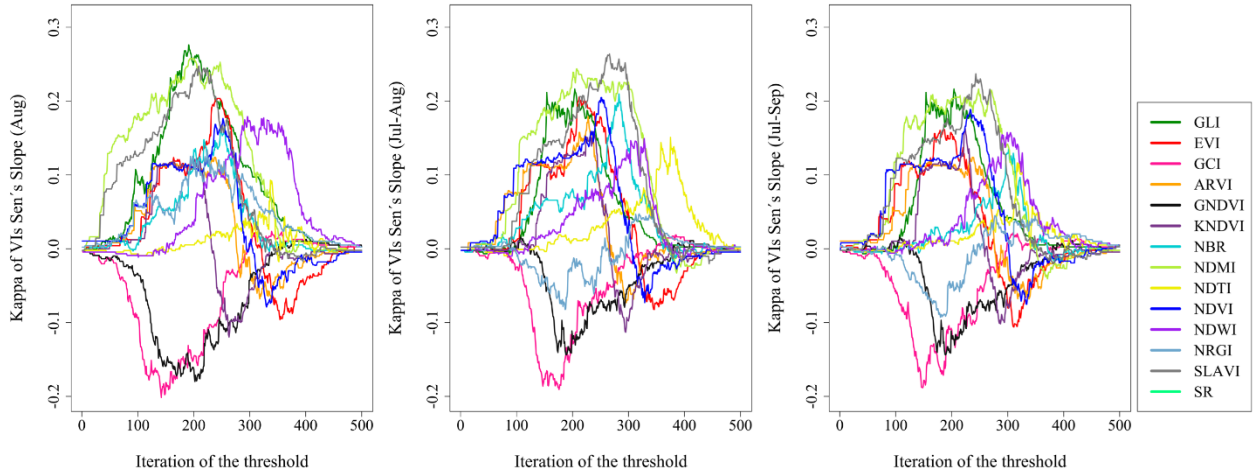
Figure 3.9 Kappa values of the Sen´s slope for all the VIs of August (left panel), July to August (center panel), and July to September (right panel).

Table 3.4 A summary of the most accurate results of Sen's slope for different VIs for August after trying 500 different VI-specific thresholds; the highest overall accuracies among all the VIs are marked with an asterisk sign.

VI	Overall Accuracy	Kappa
NDVI	0.51	0.01
GNDVI	0.47	-0.02
KNDVI	0.51	-0.004
NRGI	0.52	0.04
EVI	0.51	0.004
SR	0.51	0.48
SLAVI	0.52	0.06
NDWI	0.52	0.02

NDMI	0.55*	0.13
NDTI	0.49	0.002
NBR	0.52	0.009
ARVI	0.51	-0.01
GCI	0.47	-0.014
GLI	0.53	0.065

3.3.2. Time series of NDMI and GLI

NDMI and GLI were the best VI indicators of forest decline in the semi-arid forests studied. Figure 3.10 shows the time series (1984–2022) of Landsat-based NDMI and GLI values with median and standard deviation values for non-declining and declining reference points. Differences in VI over time for declining and non-declining regions were subtle, with no clear trend visible. GLI showed a downward trend after 2000, but it was visible in both declining and non-declining areas, making it hard to interpret. The trend also coincided with the launch of Landsat-7 and may relate to a technical artifact.
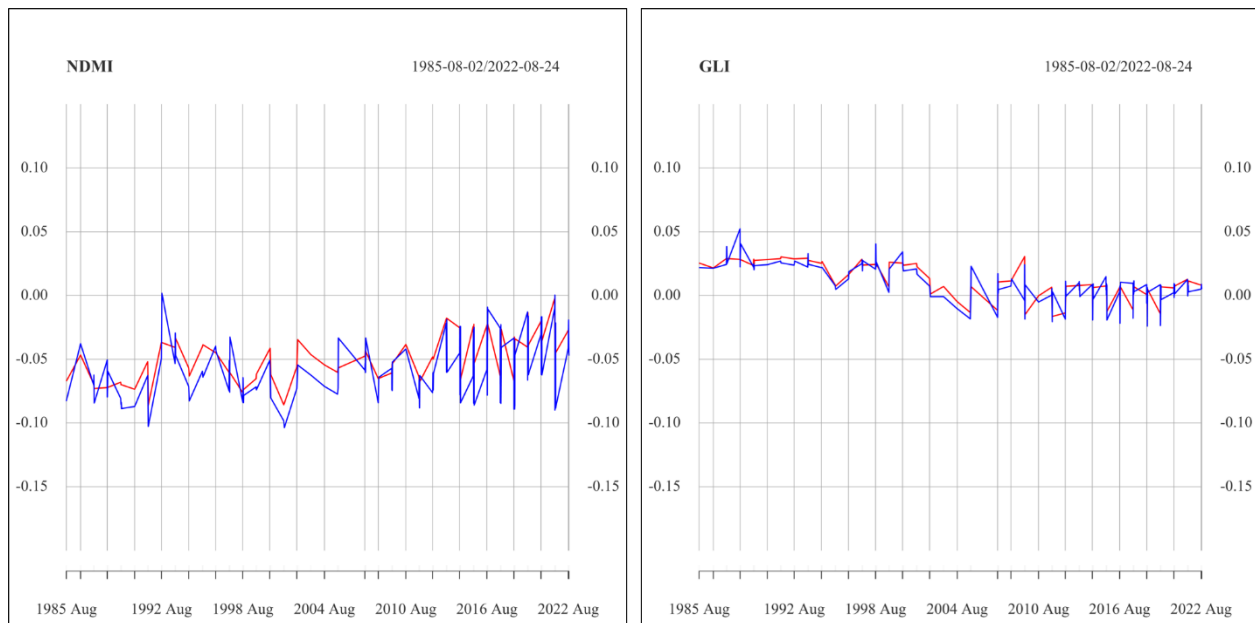
Figure 3.10 Time series of NDMI and GLI for August: The median of declining pixels (red) and non-declining pixels (blue) are depicted.

3.4. Discussion

In this study, we investigated whether well-established methods such as RF, anomaly detection, and Sen's slope analysis can detect and map forest decline in sparse and patchy semi-arid forests using the Landsat time series. In the following, we will discuss the technical results for the applied VIs and examined approaches, followed by a general discussion exploring challenges in detecting and mapping vegetation decline in mountainous semi-arid regions.

3.4.1. Spectral bands and VIs

Choosing appropriate RS indicators is critical for successfully detecting forest decline. In our study, the performance of VI-based approaches varied significantly depending on the VI used. This finding is consistent with previous studies on forest decline (Yu et al., 2021). Certain VIs, such as NDMI and GLI, appear to be more effective at detecting subtle spectral changes in semi-arid forests than other VIs. Such indices, which include a SWIR band, are more closely related to physiological variables such as hydraulic conductivity and water potential than greenness indices, particularly in arid and semi-arid regions (e.g., Moreno-Fernández et al., 2021; Marusig et al., 2020). However, the usefulness of NDMI has also been demonstrated in studies of ecosystem types other than arid and semi-arid regions. For example, Li et al. (2022) successfully used the NDMI to detect forest disturbance in a subtropical forest.

The NDMI is calculated using both NIR and SWIR bands. Both bands are known to be directly related to key vegetation properties, including the high NIR reflectance of parenchyma cells and the high sensitivity of the SWIR band to leaf water content. Hence, NIR and SWIR bands are frequently reported to be important predictors in studies examining vegetation dynamics using satellite data. For example, Meyer et al. (2019) found the NIR and SWIR bands as important variables for tracking changes in leaf area in satellite data time series. Similarly, Moreno-Fernández et al. (2021) found for Landsat time series data that forest decline was linked to the trend component of the spectral index series, with the wetness index NDMI exhibiting declines earlier than the greenness indices (EVI, and NDVI). Negative trends occurred earlier for wetness indices like NDMI than for greenness indices, indicating that the former may be better suited for detecting declines.

Gu et al. (2008) and Li et al. (2022) emphasized the significance of SWIR bands in identifying forest decline. Li et al. (2022) observed a decline in accuracy of up to 26 percent when excluding SWIR bands from their modified continuous monitoring of land disturbance approach. In our study, the SWIR bands and VIs that included SWIR bands were frequently chosen by the VSURF variable selection for various RF classifications, underscoring the importance of SWIR spectral bands in detecting semi-arid tree decline. Furthermore, the NDWI index, calculated from the green and NIR bands, was frequently selected but performed poorly in detecting anomalies during the July to August and July to September periods. Previous research, such as that by Das et al. (2023), has reported the relevance of NDWI in identifying declining and stressed forests.

In addition to NDMI and NDWI, GLI showed promising results in our study area, despite being rarely used in prior studies to detect forest decline. GLI has been utilized successfully for other vegetation monitoring purposes, such as detecting vegetation using aerial images (e.g., Eng et al., 2019). The GLI uses blue, green, and red bands. It was one of the best indices in anomaly and Sen´s slope approaches but was not selected by VSURF as an important variable for the RF classifications. However, all the bands that are required to calculate GLI were frequently selected by VSURF for the RF classifications in all summer periods. The selection of the green band partly agrees with Higginbottom et al. (2018), who reported the green band as the second-best individual band for monitoring canopy properties in sparse woody vegetation.

NDVI was only considered a medium-important index in anomaly and Sen's slope approaches and was not selected in any of the VSURF runs. Therefore, NDVI does not appear to be a reliable indicator of forest decline in arid and semi-arid vegetation, which is consistent with Madonsela et al. (2018) but contrasts with Camarero et al. (2015), who suggested that NDVI is a dependable indicator of drought-induced productivity decline.

It should be noted that leaf structure and vegetation type are also important to be considered when choosing the appropriate VIs. Only a few studies have investigated VIs for different leaf structures. Croft et al. (2014) evaluated several VIs to estimate leaf chlorophyll content in different leaf and canopy structures, including broadleaf and coniferous trees across a Canadian test site. They found that the canopy-scale relationship between spectral indices and foliar chlorophyll content was particularly strong for broadleaf samples compared to coniferous trees. However, in our study area, the tree species are mostly broad-leaved Brant oaks, so this was not an issue to consider. But, in heterogeneous forests with both types of leaf structure, this could be an important factor in selecting appropriate VIs.

3.4.2. The importance of acquisition time windows of satellite images

This study found that the best time window for detecting forest decline differed slightly depending on the approach used. The RF and anomaly approaches were more accurate in detecting declines in images captured from July to August, while Sen's slope was most accurate for images captured in August only. This may be due to the particularly dry conditions during these months, which lead to greater spectral differences between trees and other vegetation. This finding is supported by a study by Symeonakis et al. (2018). We observed that RF performed better for the predictors based on July and August images compared to Sen's slope, which worked slightly better for only August images. However, we did not find any explanation for this observation, and the performance differences were subtle.

3.4.3. Differences in performances between the examined approaches

In our study, RF outperformed other methods in terms of accuracy, which may be due to its use of multiple predictor variables. Although the overall performance was moderate, the balanced class-

specific accuracy suggests that RF was able to capture spectral information related to declining forest areas. Interestingly, we observed no notable differences in performance between RF models trained with Landsat data from different time periods (1986–2021, 2000–2021, and 2010–2021), despite the reference data being collected in 2021 and 2022. This observation was unexpected, as we expected that using more recent data would lead to better results. Results for different RF models with various additional year intervals are provided in Supplementary Material II. According to local experts, the widespread severe oak decline in the study area only emerged after 2010, which may indicate that the subtle spectral differences enabling to differentiate declining from non-declining areas in this study may not necessarily relate to changes in the spectral signal due to decline of the trees but rather to general differences in the site conditions on which declining and non-declining forest areas are located. This may very well relate to other environmental parameters such as differing soil conditions, co-occurring vegetation, topography, or a combination of both.

The anomaly detection and Sen's slope analysis approaches performed notably worse than RF in the study. A direct comparison between RF and the other two approaches (anomaly and Sen's slope) is not feasible due to the distinct methodologies employed in these analyses, in particular concerning the input data and the validation. RF, as a supervised classification method, a portion of the reference data (equal to 70% of all reference data) is directly utilized for model training. Contrarily, in the anomaly analysis and Sen's slope approach the reference data is only used for the validation and accuracy assessment; even though determining the optimal threshold based on the reference data is similar to applying the reference data as training data. Nevertheless, the better performance of RF is somewhat expected due to the notably increased number of predictors as compared to the other two tested approaches relying on a single VI.

Several earlier studies found Sen's slope approach useful for trend detection in vegetation degradation. For instance, Zhang et al. (2022) used three trend analyses, including Sen's slope and Mann-Kendall tests, to assess the changing trend and degradation of the environmental quality of the Loess Plateau in China. Sen's slope and Mann-Kendall analysis were observed to be robust and insensitive to outliers, and their combination was suggested to offer advantages over a simple linear regression. The Loess Plateau has experienced serious erosion processes, resulting in clearer spectral change signals in satellite imagery, which may explain the successful application of trend-analysis techniques in this area.

Our study found that anomaly detection and Sen's slope approach, which are based on temporal analysis, perform poorly. This suggests that we may not be able to detect a clear change in the spectral signal caused by forest decline. This though is also backed up by the visualization of the time series of the two most accurate VIs which showed similar signals for declining and non-declining areas, which makes a reliable separation with only one single VI's information difficult (Figure 3.10). The downward trend observed for GLI after 2000 may relate to the start of a general vegetation decline (reported in previous studies), but it could also be an artifact related to the launch date of Landsat 7 in 1999 with slightly deviating spectral properties. This supports the idea that, rather than spectral changes caused by forest decline, spectral differences due to differing

environmental conditions enable us to at least partly distinguish declining from non-declining areas in our semi-arid study area.

3.4.4. Environmental variables with a potential influence on forest decline

Earlier studies showed that topography is occasionally related to forest decline in the Zagros forests (Goodarzi et al. 2016). Adding topographic information to the RS predictors may be one way to improve the detection of declining areas. However, we utilized elevation, slope, and aspect data derived from a 30-m DEM (see Hawker et al., 2022 for more data details) for one of the RF classifications (1986-2021, July to August), and the results were not significantly improved (Supplementary Material II).

Differences in regional climatic conditions could be further important variables affecting forest decline. Multiple studies revealed an increase in forest decline worldwide associated with global warming and a more pronounced drought. Moreno-Fernandez et al. (2019) found that warmer conditions are directly linked to worse vegetation health in open, evergreen oak woodlands. Ahmadi et al. (2014) showed that climatic variables such as yearly precipitation, temperature, and moisture were strongly correlated with the risk of forest decline within Zagros forests. Similarly, Kooh Soltani et al. (2018) showed that these three elements were most crucial in the emergence of forest decline. Hence, one way to further improve the detection of declining oak stands may be to integrate climatic data. However, it is not fully clear whether our study area is large enough to span a sufficiently large climate gradient (independent from topography) to improve our results. The highly clustered occurrence pattern of declining areas in our reference dataset (Figure 3.4) suggests that the use of standard climatic datasets such as Bioclim at a spatial resolution of 1 km may lead to notably improved accuracy (Supplementary Material II), which is, however, mostly due to the spatial autocorrelation in our reference data. Thinning out the reference dataset could be accomplished but would likely lead to a too-small dataset to draw meaningful conclusions, whereas field inventory of larger sample sizes would entail a high level of logistics and financial means. Un-crewed aerial vehicles may contribute to making the corresponding effort more efficient (Latifi, 2023).

The influence of different soils and co-occurring vegetation communities on the observed decline processes remains unclear and requires further investigation. These variables could potentially lead to changes in the observed spectral signal. While we currently have limited information on these two variables for our study region, we plan to explore their influence in future work.

3.4.5. Technical challenges of detecting forest decline in semi-arid areas

Future work on detecting and mapping forest decline in arid and semi-arid areas could also benefit from technical improvements addressing some of the challenges that may have impacted the results of the present study. For example, in arid and semi-arid regions, detecting subtle decline processes is complicated by mixed pixels with bright soil backgrounds, as noted by Wang et al. (2022) and Maier et al. (2022). To address these challenges, we utilized blue bands and VIs that incorporated

the soil background, such as GLI and ARVI. However, it should be noted that even with this approach, the correction for the soil background is not entirely accurate, and more sophisticated approaches may be needed.

A further, often-neglected influential factor on the spectral signal is the influence of the cast shadows of trees. Depending on spatial resolution and acquisition geometries, tree shadows can negatively impact the quality of RS data and negatively affect vegetation monitoring through mixed pixels (Wang et al., 2022), particularly in low-density forests with potentially large shadow fractions. To address this issue, Larsen and Salberg (2010) proposed tree shadow removal approaches. Although not the focus of this study, developing an algorithm to quantify and correct the influence of shadows could be useful for monitoring Zagros' semi-arid forests via RS.

Other technical challenges that could have affected the identification and mapping of declining forest areas include the lack of correction factors to calculate VIs across different Landsat sensors. Landsat 4–7 and Landsat 8 have slight spectral band offsets, which can result in small changes in the spectral signal that are not related to underlying changes in the forest. Additionally, some spectral bands used in this study (red, NIR, and SWIR) are narrower for Landsat 8 than for Landsat 4–7. These challenges should be considered in future work to improve the accuracy of forest decline detection and mapping.

In an ideal scenario, satellite images would be acquired using identical technology and acquisition conditions, but this is not possible to achieve retrospectively. To address the differences between images in a time series, correction factors could be applied. However, in regions with limited information on the stability of the spectral signal over the last few decades, reference data or prior knowledge of spectrally stable areas would be necessary to successfully implement such corrections. Unfortunately, this was not feasible for our study due to the lack of corresponding information.

3.5. Conclusion

We evaluated three approaches in order to map declining forest areas in a semi-arid region using the Landsat time series from 1986 to 2021. These approaches were RF, anomaly detection, and Sen's slope analysis. RF outperformed the other two methods. Sen's slope and anomaly approaches produced unsatisfactory results, which did not result in maps that could serve as valuable input to forest managers. We found that VIs, including NIR and particularly SWIR, were helpful for all methods. Interestingly, the RF classification was not sensitive to the Landsat data's acquisition time periods, suggesting that its ability to distinguish declining from non-declining forest areas was likely due to general environmental differences rather than spectral changes caused by the decline process. Further research is required to identify the environmental factors that contribute to these variances. In conclusion, mapping forest decline in arid and semi-arid sparse cover forests using medium-resolution Landsat data is challenging, and technical improvements are needed to address issues with bright soil backgrounds and tree-cast shadows.

Acknowledgment

3.6. Supplementary Material II

<u>Additional Random Forest results</u>

RF using Landsat imagery
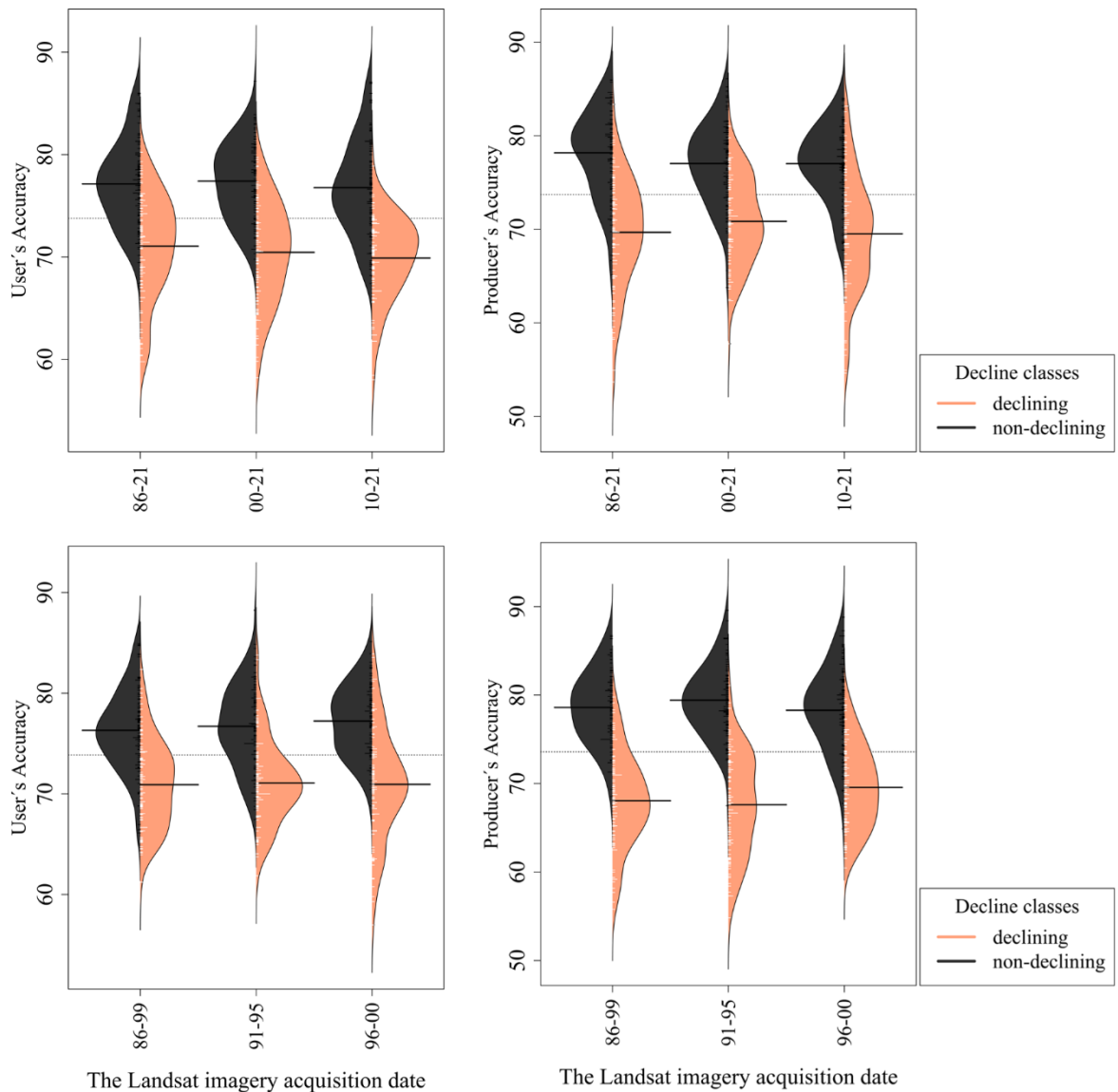
Figure 3.11 The upper row of the plot shows the user and producer accuracies for declining and non-declining classes of RF classifications for the years 1986–2021 (86–21), 2000–2021 (00–21), and 2010–2021 (10–21) for the August summer period. The lower row of the plot shows the same analysis for the

years 1986–1999 (86–99), 1991–1995 (91–95), and 1996–2000 (96–00). The fine dashed lines show the overall mean across all bean plots.
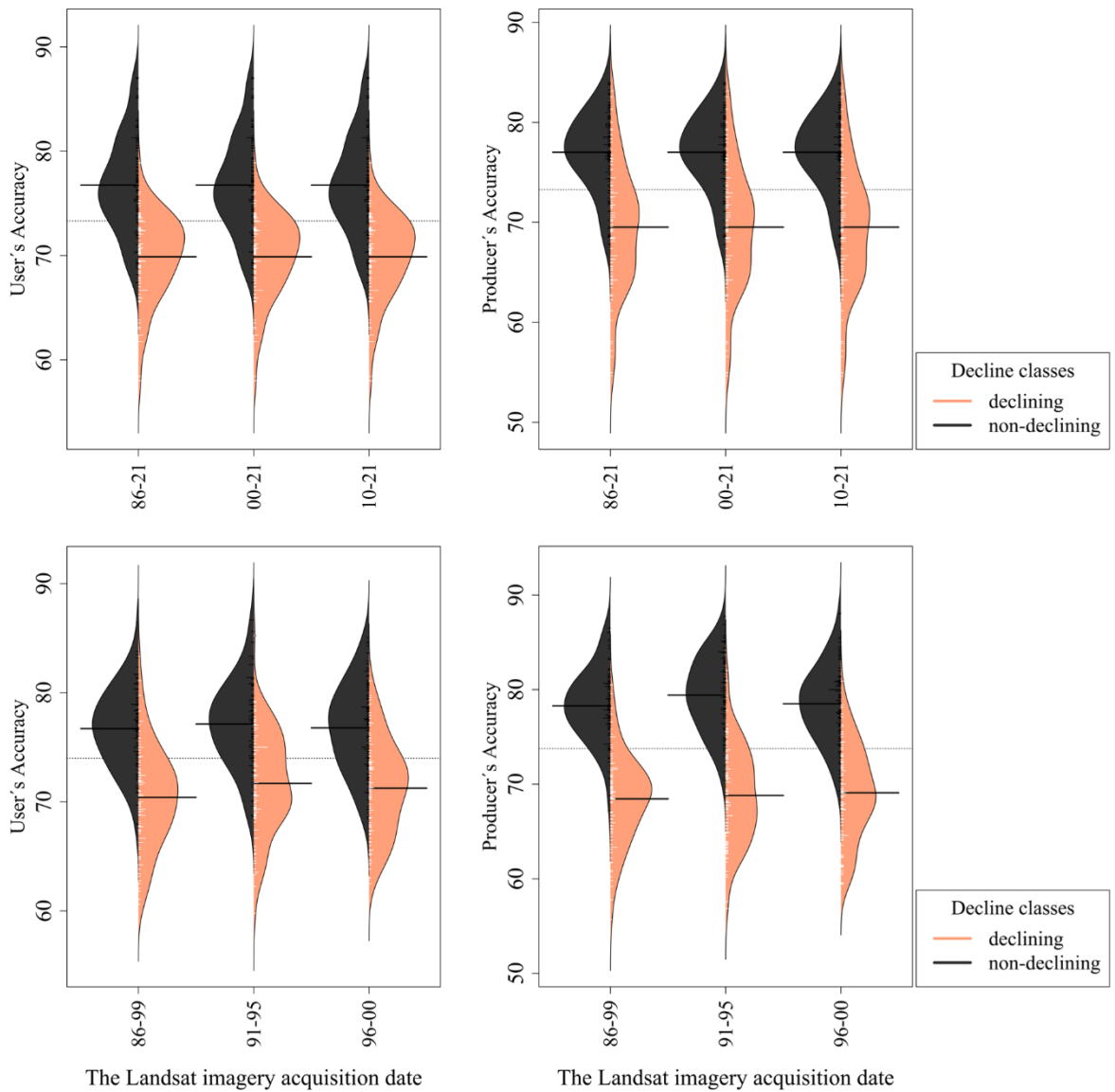
Figure 3.12 The upper row of the plot shows the user and producer accuracies for declining and non-declining classes of RF classifications for the years 1986–2021 (86–21), 2000–2021 (00–21), and 2010–2021 (10–21) for the July –September summer period. The lower row of the plot shows the same analysis for the years 1986–1999 (86–99), 1991–1995 (91–95), and 1996–2000 (96–00). The fine dashed lines show the overall mean across all bean plots.
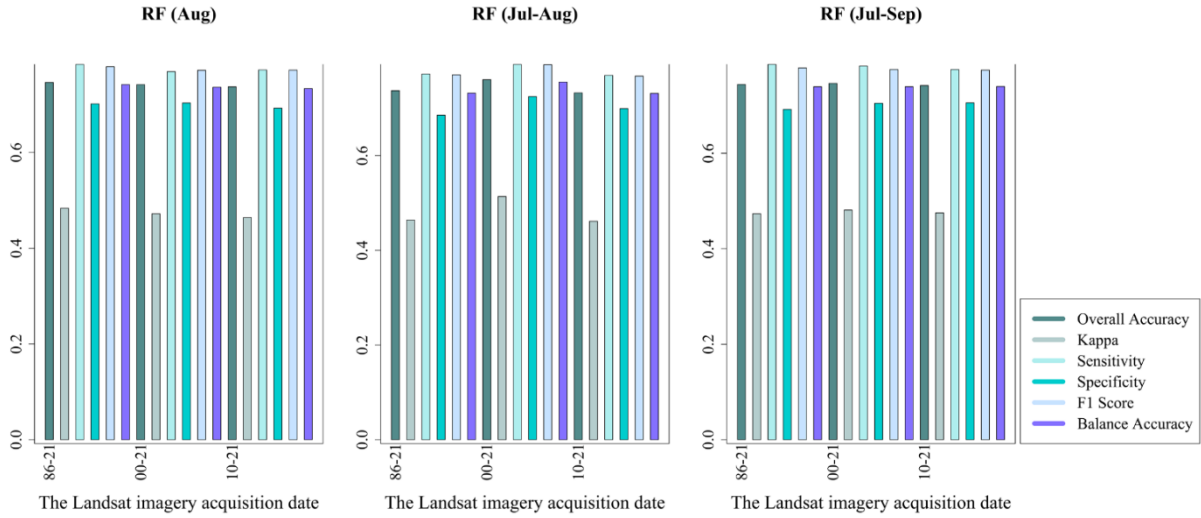
Figure 3.13 Results of the validation of the RF classifications for the years 1986–2021 (86), 2000–2021 (00), and 2010–2021 (10) for the summer seasons (August, July–August, and July–September), from left to right.
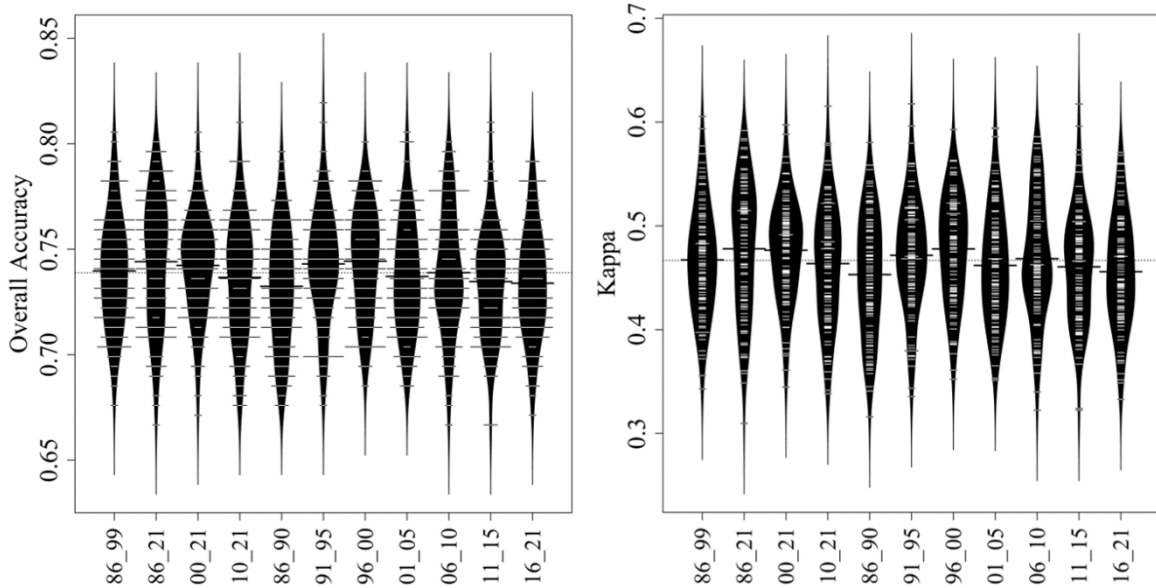
Figure 3.14 Overall accuracy and the kappa values of RF classifications for the years 1986-1999 (86-99), 1986-2021 (86-21), 2000-2021 (00-21), 2010-2021 (10-21), 1986-1990 (86-90), 1991-1995 (91-95), 1996-2000 (96-00), 2001-2025 (01-05), 2006-2010 (06-10), 2011-2015 (11-15), and 2016-2021 (16-21) for the month of August. The fine dashed lines indicate the overall mean across all bean plots.
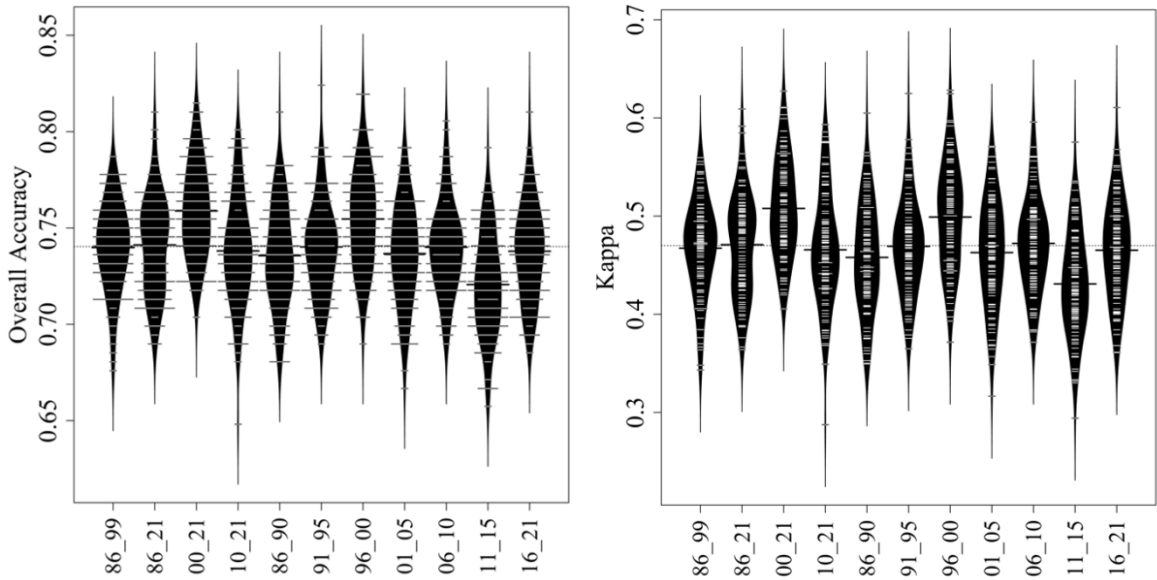
Figure 3.15 Overall accuracy and the kappa values of RF classifications for the years 1986-1999 (86-99), 1986-2021 (86-21), 2000-2021 (00-21), 2010-2021 (10-21), 1986-1990 (86-90), 1991-1995 (91-95), 1996-2000 (96-00), 2001-2025 (01-05), 2006-2010 (06-10), 2011-2015 (11-15), and 2016-2021 (16-21) for the months July to August. The fine dashed lines indicate the overall mean across all bean plots.
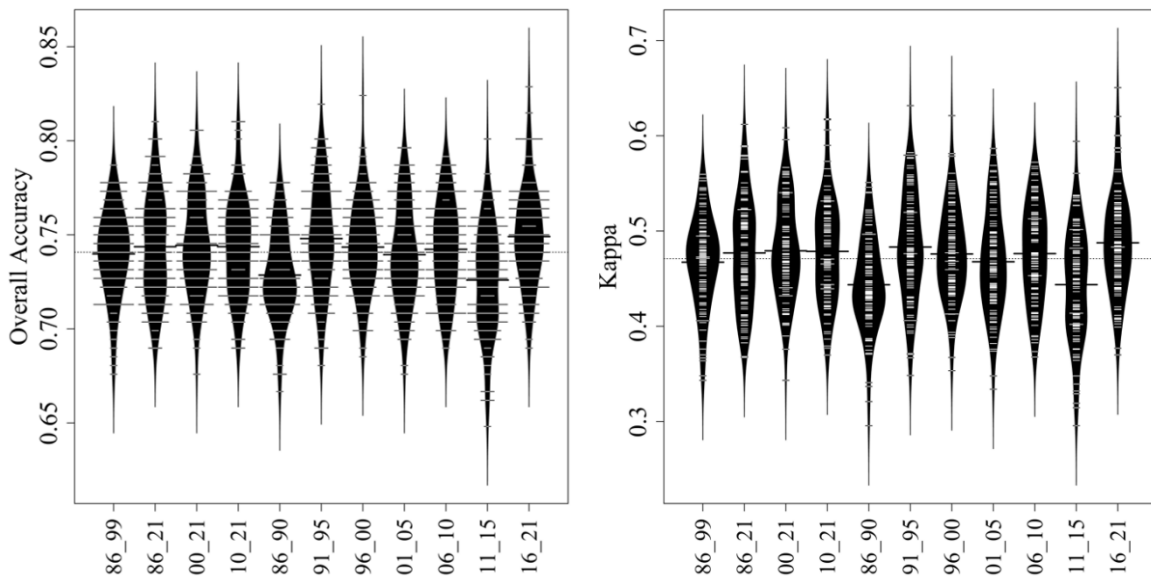
Figure 3.16 Overall accuracy and the kappa values of RF classifications for the years 1986-1999 (86-99), 1986-2021 (86-21), 2000-2021 (00-21), 2010-2021 (10-21), 1986-1990 (86-90), 1991-1995 (91-95), 1996-2000 (96-00), 2001-2025 (01-05), 2006-2010 (06-10), 2011-2015 (11-15), and 2016-2021 (16-21) for the months July to September. The fine dashed lines indicate the overall mean across all bean plots.
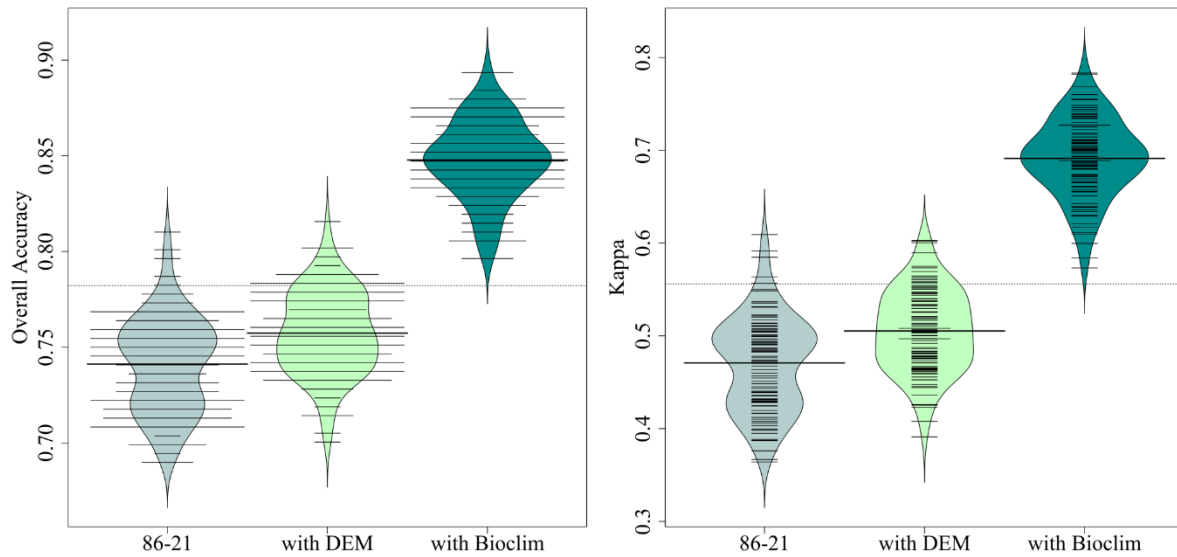
Figure 3.17 Overall accuracy and the kappa values of RF classifications for the years 1986–2021 (86–2021) for July to August months compared to the results with extra predictors using DEM (elevation, slope, and aspect) as well as Bicoclim variables (BIO01, BIO12, BIO15, and BIO17). The fine dashed lines indicate the overall mean across all bean plots.

So, according to Figure 3.17, the overall accuracy of the Landsat data for the 1986–2021 period was approximately 0.74 (kappa = 0.48). When incorporating DEM, the accuracy slightly increased, with an overall accuracy (OA) of 0.75 and a kappa of 0.50. Additionally, utilizing Bioclim data resulted in higher accuracy, reaching 0.84 with a corresponding kappa value of 0.69.

Table 3.5 A summary of the RF performance for different years at three different summer periods out of 100 iterations (gray rows: August, blue rows: July-August, purple rows: July-September), the highest overall accuracies of each summer period being marked with an asterisk sign.

Date – Period	Overall Accuracy	Kappa
1986-2021	0.747 *	0.484
2000-2021	0.745	0.483
2010-2021	0.74	0.47
1986-2021	0.745	0.48
2000-2021	0.756*	0.50

2010-2021	0.736	0.46
1986-2021	0.74	0.473
2000-2021	0.743	0.475
2010-2021	0.745*	0.472

RF classification using S2 imagery

We additionally ran the RF classification using S2 imagery between 2015 and 2021 for three different summer seasons. We calculated all of the VIs listed in Table 3.1 as predictors, as well as used the 10 original bands of the S2 images with 10 and 20 m spatial resolutions for a total of 24 bands in the images. In general, the overall accuracies and kappa values are lower than Landsat imagery, and this could be because the years of data availability for S2 are shorter and only available from 2015. Another potential issue could be that due to the sparse tree cover, the increased spatial resolution leads to higher variability in the spectral signal which further complicates the identification of the declining tree groups. The highest overall accuracy and kappa value were gained for the S2 images between July and September, with a median of 0.68 and 0.35, respectively. August images gained the second-highest overall accuracy and kappa value, with 0.675 and 0.335, respectively. Finally, the images between July and August with 0.664 and 0.32 had the lowest median overall accuracy and kappa value out of 100 iterations for splitting training and testing reference points.
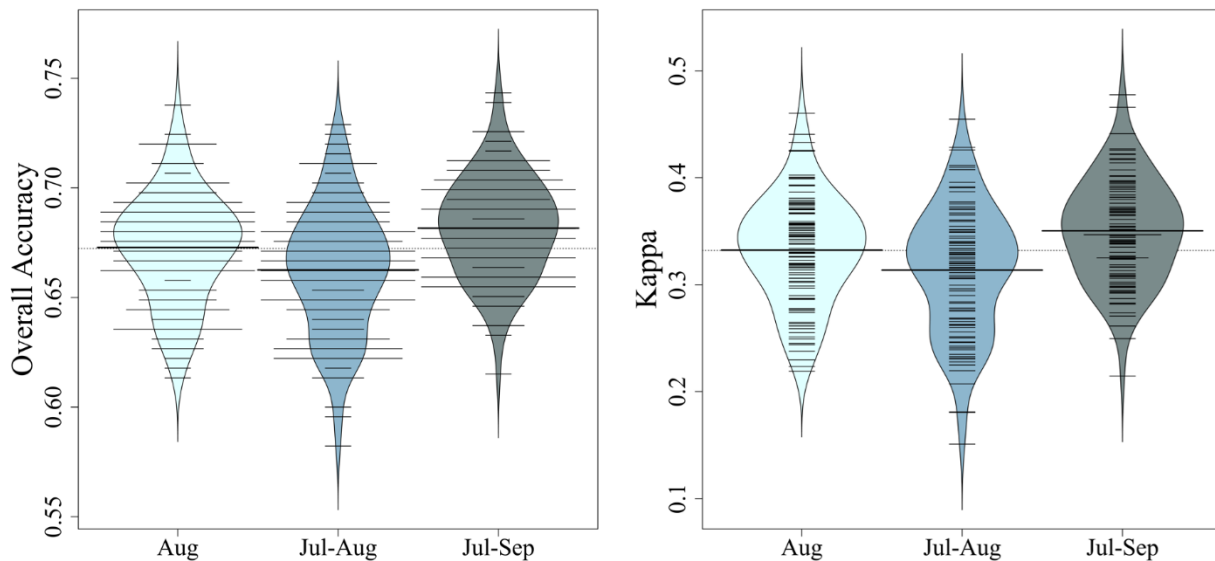
Figure 3.18 Overall accuracy and the kappa values of RF classifications using S2 imagery for the years 2015-2021 for the three examined summer periods. The fine dashed lines indicate the overall mean across all bean plots.

<u>Additional Anomaly results</u>
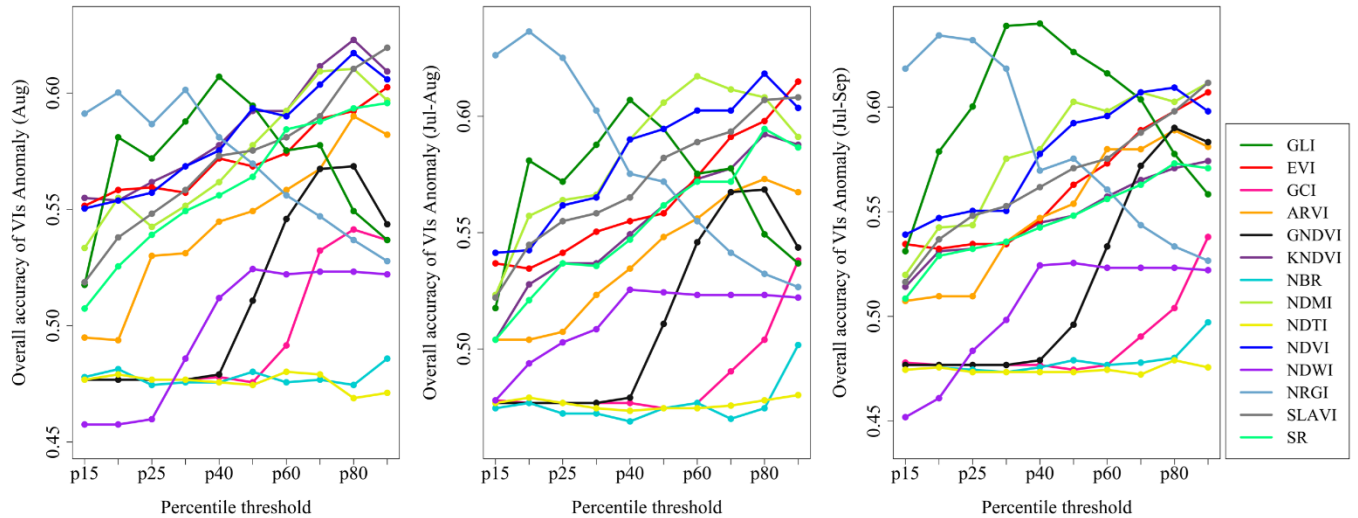
Figure 3.19 Overall accuracy of anomaly analysis at different percentiles for all the VIs of August (left panel), July to August (center panel), and July to September (right panel).

Table 3.6 The detailed user and producer accuracies for anomaly analysis for all VIs at different percentiles (Ps) for healthy or non-declining (H) classes in white columns and declining (D) classes in gray columns

Decline class																		
P	H	D	H	D	H	D	H	D	H	D	H	D	H	D	H	D	H	D
VI	15		20		25		30		40		50		60		70		80		90	
NDVI	0.51	0.89	0.51	0.87	0.52	0.88	0.52	0.86	0.54	0.83	0.54	0.80	0.55	0.75	0.56	0.69	0.58	0.68	0.58	0.62
	0.98	0.14	0.97	0.14	0.97	0.18	0.96	0.20	0.94	0.27	0.87	0.30	0.94	0.36	0.92	0.42	0.87	0.50	0.74	0.59
GNDVI	0.48	0	0.48	0	0.48	0	0.48	0	0.48	0.50	0.48	0.78	0.50	0.87	0.52	0.80	0.54	0.73	0.55	0.63
	0.99	0	0.99	0	0.99	0	0.99	0	0.99	0.002	0.99	0.03	0.98	0.12	0.94	0.20	0.86	0.33	0.67	0.50
KNDVI	0.49	0.89	0.50	0.94	0.51	0.93	0.51	0.90	0.51	0.90	0.52	0.83	0.53	0.78	0.53	0.73	0.55	0.71	0.55	0.66
	0.99	0.05	0.99	0.10	0.99	0.12	0.98	0.12	0.98	0.15	0.95	0.20	0.92	0.25	0.87	0.30	0.83	0.36	0.76	0.43
NRGI	0.60	0.64	0.65	0.63	0.66	0.61	0.66	0.58	0.68	0.55	0.84	0.55	0.97	0.54	1	0.53	1	0.53	1	0.52
	0.62	0.62	0.52	0.73	0.44	0.79	0.33	0.84	0.21	0.91	0.13	0.98	0.07	1	0.04	1	2	1	1	1
EVI	0.51	0.82	0.50	0.79	0.51	0.76	0.51	0.76	0.52	0.73	0.52	0.71	0.53	0.70	0.55	0.69	0.56	0.68	0.56	0.67
	0.96	0.14	0.96	0.14	0.94	0.17	0.93	0.20	0.91	0.23	0.88	0.23	0.85	0.32	0.82	0.38	0.77	0.44	0.71	0.52

SR	0.49	0.89	0.50	0.91	0.51	0.93	0.51	0.90	0.51	0.89	0.52	0.83	0.53	0.78	0.53	0.72	0.55	0.72	0.55	0.65
	0.99	0.05	0.99	0.09	0.99	0.12	0.98	0.12	0.98	0.15	0.95	0.20	0.92	0.25	0.87	0.30	0.84	0.37	0.76	0.43
SLAVI	0.50	0.87	0.51	0.09	0.52	0.89	0.52	0.89	0.52	0.82	0.53	0.82	0.54	0.77	0.54	0.73	0.56	0.70	0.57	0.67
	0.98	0.10	0.98	0.14	0.98	0.17	0.97	0.17	0.95	0.21	0.94	0.25	0.90	0.30	0.86	0.35	0.80	0.43	0.73	0.40
NDWI	0.35	0.50	0.34	0.51	0.31	0.51	0.27	0.51	0.80	0.52	1	0.52	1	0.52	1	0.52	1	0.52	-----	0.52
	0.11	0.81	0.06	0.89	0.03	0.93	0.01	0.96	0.94	1	0.04	1	0.02	1	0.02	1	0.02	1	0	1
NDMI	0.50	0.78	0.50	0.83	0.52	0.83	0.52	0.81	0.54	0.78	0.55	0.74	0.57	0.72	0.57	0.68	0.57	0.64	0.57	0.61
	0.96	0.12	0.96	0.19	0.95	0.20	0.94	0.22	0.91	0.30	0.86	0.37	0.82	0.43	0.75	0.48	0.68	0.68	0.54	0.60
NDTI	0.48	0	0.48	0.66	0.48	0.33	0.47	0	0.47	0.16	0.47	0.33	0.47	0.38	0.47	0.44	0.48	0.50	0.48	0.52
	1	0	1	0.04	0.99	0.02	0.99	0	0.99	0.02	0.98	0.06	0.98	0.01	0.97	0.02	0.96	0.03	0.95	0.04
NBR	0.47	0	0.47	0.40	0.47	0	0.47	0.14	0.47	0.16	0.47.5	0.43	0.47	0.48	0.47	0.43	0.47	0.48	0.49	0.60
	0.99	0	0.99	0.43	0.99	0	0.98	0.02	0.97	0.04	0.97	0.02	0.96	0.03	0.92	0.05	0.91	0.08	0.88	0.15
ARVI	0.49	0.89	0.49	0.89	0.49	0.90	0.50	0.91	0.50	0.89	0.51	0.80	0.52	0.80	0.53	0.74	0.53	0.68	0.53	0.63
	0.99	0.05	0.99	0.05	0.99	0.06	0.99	0.095	0.99	0.12	0.98	0.15	0.95	0.19	0.90	0.26	0.83	0.34	0.73	0.41
GCI	0.47	-----	0.48	0	0.48	0	0.48	0	0.48	0	0.48	0	0.48	0.43	0.48	0.68	0.49	0.62	0.51	0.61
	1	-0	1	0	0.99	0	0.99	0	0.99	0	0.99	0	0.99	0.65	0.97	0.04	0.92	0.12	0.79	0.30
GLI	0.52	0.73	0.56	0.74	0.58	0.73	0.61	0.69	0.62	0.60	0.63	0.59	0.70	0.58	0.71	0.55	0.75	0.54	0.78	0.53
	0.89	0.26	0.85	0.39	0.77	50	0.71	0.59	0.55	0.67	0.41	0.77	0.32	0.87	0.19	0.93	0.11	0.96	0.06	0.98

Additional Sen´s slope results
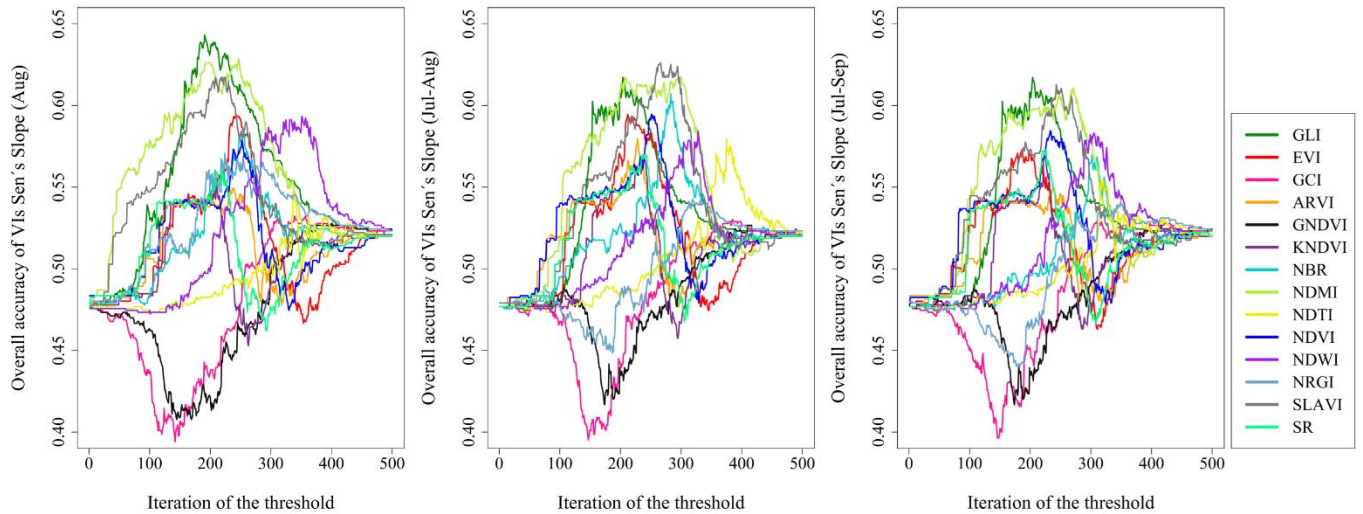
Figure 3.20 Overall accuracy of the Sen´s slope for all the VIs of three summer periods at different thresholds

Table 3.7 Shows the results of the range of Sen's slope threshold values for each index in parenthesis and the best thresholds in our study out of 500 different VI thresholds; the value in parentheses represents the range of values defined by the function for each VI.

VI	Threshold (Aug)	Threshold (Jul-Aug)	Threshold (Jul-Sep)
NDVI	(-398.2 to 618.8)	(-393.48 to 651.3)	(-397.6 to 687)

	113.37	130;132	106.6; 108.8
GNDVI	(67 to 460.7) 381.8; 382.6	(76.4 to 435.2) 370.5 to 374.8	(76.4 to 435.2) 370.5 to 374.8
KNDVI	(-1457 to 2588.6) 245.4	(-1846.5 to 2559) 245.9	-1867.8 to 2762 201.2
NRGI	-615.5 to -103.3 -386.6	(-676.25 to -162.2) -348.7; -330	-689.4 to -200.04 -348
EVI	(-304.9 to 319.3) -7.2; -3.45; -2.2; -0.95; 0.3; 1.5; 2.8	(-290.8 to 343.6) -22.5	(-279.3 to 428.4) -18.3;-16.9;-15.5
SR	-129.424 to 242.283 -129.4 to -79.51	(-157 to 246.7) -157 to -99.6	(-153.4 to 255.7) -153.4 to -101.8
SLAVI	(-471.7 to 832.7) 72; 95.5; 100.7; 108.6; 113.8	(-746 to 820.5) 85.8	(-581.33 to 826.9) 101.6
NDWI	(-461.3 to -67.6) -185.18	(-435.7 to -76.96) -200.6	(-466.8 to -66.6) -223
NDMI	-426.4 to 657.4 107.93	(-702.6 to 805.7) -79.95 to 201	(-613.3 to 891.5) 197.9; 200.9
NDTI	(-488 to 775.4) 362.7; 367.77	(-531.8 to 751.9) 430.3	(-668.3 to 968.9) 378.3
NBR	(-260.5 to 584.6) 169.67	(-258.3 to 530.3) -223.5	(-393 to 573.6) 190
ARVI	(-338.8 to 584.5) 97.85; 99.7; 101.5	(-353.3 to 699.9) 125.7	(-338.8 to 584.5) 97.8; 99.7; 101.5
GCI	(12.16 to 130.4) 92.2; 96.5	(13.9 to 120.9) 96; 96.3	(12.4 to 132.9) 86.8 ; 88.75
GLI	(-717.4 to 114.5) -400.65	(-849 to 166.1) -436	(-849.07 to 166.13) -436

Table 3.8 The detailed user and producer accuracies for Sen´s Slope analysis for all VIs at different for healthy or non-declining (H) classes in white columns and declining (D) classes in gray columns.

VI	User's Accuracy H - D		Producer's Accuracy H - D	
NDVI	0	0.52	0	0.99
GNDVI	1	0.52	0.002	1
KNDVI	0	0.52	0	0.99
NRGI	1	0.52	0.002	1

EVI	0	0.52	0	0.99
SR	0	0.52	0	0.99
SLAVI	0	0.52	0	0.99
NDWI	1	0.52	0.002	1
NDMI	0	0.52	0	0.99
NDTI	0	0.52	0	0.99
NBR	0	0.52	0	0.99
ARVI	0	0.52	0	0.99
GCI	1	0.52	0.002	1
GLI	1	0.52	0.002	1

Code availability

The GEE script examples for all approaches between 1986 and 2021 (the July to August summer period) are available at the following links:

Landsat composites used for RF classification:

https://code.earthengine.google.com/f6c031edd386262a516039388927b678

Anomaly analysis with the NDMI index:

https://code.earthengine.google.com/c84284b3c7e2aeea41677b6686e8093b

Sen´s slope with the NDMI index:

https://code.earthengine.google.com/ceced91e6bf5c932c1b022785c1e2f97

4. Unveiling the main drivers of tree decline in Zagros semi-arid Forests

Elham Shafeian, Michael Ewald, Hooman Latifi, Fabian Ewald Fassnacht

Abstract

Tree decline in semi-arid forest ecosystems causes severe socio-economic and environmental problems. This study investigates tree and forest decline in Iran's Zagros forests, considering environmental factors (e.g., topographic, soil, and climatic variables) and tree characteristics (e.g., DBH and tree height). We used field data from Chaharmahal-and-Bakhtiari (a study area covering 165 km²) and environmental data derived from freely available databases. Relationships between tree and forest decline and environmental data were analyzed using generalized additive models (GAMs). Our findings reveal that slope and the Bioclim-16 variable (precipitation of the wettest quarter) significantly influence tree decline across various decline classes (p-values: slope = 0.009, Bioclim-16 = 0.02). The best multivariate model for forest decline incorporated the explaining variables soil organic carbon (SOC) and silt, with SOC emerging as the key factor (p-value = 0.04). No significant correlation between tree or forest decline and tree characteristics was observed. Additionally, a spectral analysis of bare soil in declining and non-declining areas consistently demonstrated reduced reflectance values in declining regions across 10 S2 bands, with VNIR-3, SWIR-2, red, green, and blue bands consistently showing significant differences as unveiled by the Wilcoxon test in all seasons except winter. These reduced reflectance values may indicate that forests stocked on soils with larger grain size (a higher fraction of sand) and/or higher organic carbon content may be more prone to decline. This study contributes to our hitherto understanding of the main drivers of tree and forest decline in semi-arid forests, underscoring the potential utility of the spectral properties of bare soil in sparse semi-arid forests to predict the likelihood of tree decline.

4.1. Introduction

The dynamic response of trees to environmental variables over time demonstrates their ability to adapt to extreme events such as drought. This dynamic response is also called plasticity (Zheng et al., 2023). However, prolonged exposure to stressful situations causes trees to deteriorate. Particularly, a combination of biotic and abiotic factors can increase the stress level of trees and their subsequent deterioration (Hosseini et al., 2017). The occurrence of tree mortality and the consequent forest decline due to unfavorable climatic conditions has been reported in several ecosystem types (Andrus et al., 2023), but particularly in arid and semi-arid ecosystems (e.g., Ghanbari Motlagh and Kiadaliri, 2021; Walker et al., 2012; Mahdavi et al., 2015). This trend is expected to continue to accelerate in the next few decades (Etzold et al., 2019). Amongst other influences, climate warming may exacerbate drought stress and contribute to the decline of forests in water-limited arid and semi-arid regions hereafter semi-arid regions (Camarero, 2017). Therefore, these ecosystems are particularly susceptible to prolonged droughts (David et al., 2022), yet many semi-arid regions remain under-examined. Hence, it is crucial to identify factors that contribute to the decline of trees in such ecosystems.

The mountainous Zagros forests of western Iran are an example of a large semi-arid region that has received comparably little attention in the international literature. While some studies have addressed the subject of forest decline in the Zagros (Moradi et al., 2021; Jahanbazy Goujani et al., 2020; Hosseini et al., 2017), research on the forest decline in this ecosystem is still in its early stages. Most of the research in the Zagros area has focused on mapping and detecting forest decline (e.g., Ghasemi et al., 2023; Ghasemi et al., 2022; Karami et al., 2018) rather than understanding its drivers, which, along with comprehending the interconnections among the drivers, remains an open task (Moradi et al., 2021). Forest management, economic policies, and mitigation and adaptation initiatives can all benefit from a thorough understanding of forest decline (Anderegg et al., 2012).

Outside the Zagros area, a number of studies examined forest decline in (semi)-arid regions. For instance, Fensham and Fairfax (2007) showed in the Central Queensland savanna of Australia that areas with higher forest densities had reduced surface soil moisture availability. This led to an escalation in tree mortality as surface soil moisture decreased. Furthermore, the link between topography (i.e., elevation, slope, and aspect) and tree mortality or forest decline in semi-arid regions has been demonstrated in some previous studies, including studies in Zagros (e.g., Moradi et al., 2021; Jahanbazy Goujani et al., 2020; Hosseini et al., 2017). Topography influences irradiation and, therefore, soil moisture and drought conditions (Ewane et al., 2023). The effects of other environmental factors such as extreme climatic conditions and soil variables have been reported before; Zhang et al. (2023), in a study in semi-arid forests in China, identified climate and soil factors as the primary drivers of vegetation response to drought in their study area. In a study in the Wyoming Basin ecoregion of the United States, Assal et al. (2016) found that high elevation and northern slopes were related to increased drought-induced tree mortality. The study found that forest density may have increased on northern slopes during the wet 1990s, which may have

increased mortality risk during droughts. In terms of tree characteristics, they pointed out that most mortality occurred among the largest trees, but a significant number of small and medium-sized aspen trees also experienced mortality. Some studies have also focused on understanding the relationship between tree characteristics, such as tree height (e.g., Stovall et al., 2019), and tree mortality or forest decline in semi-arid regions.

While many studies discuss the main drivers of decline, there are also contrasting views even within similar ecosystem types. For example, in a (semi)-arid African savanna in South Africa, MacGregor and O'Connor (2002) conducted a study on *Colophospermum mopane* trees that were subjected to severe drought. The study found that trees growing in sandy or on fine-textured soils such as clay were not affected by dieback, as soil type and topography were not related to dieback. Instead, dieback was found to be associated with factors such as vegetation structure, soil quality, and soil chemical composition (i.e., high sodium content). These nuanced yet confounding results, especially in the semi-arid ecosystems, illustrate that the causes of forest and tree mortality due to environmental factors and tree characteristics are complex, difficult to predict, and site-specific, requiring local-level research (also noted by Sharwood, 2021; Bałazy et al., 2019).

As already briefly mentioned above, soil properties within forest ecosystems can serve as indicators of forest decline, and soils in declining forests may differ from those in healthy forests (e.g., Chaparro et al., 2018). However, conducting soil measurements in the field is both expensive and labor-intensive. Moreover, some study sites may remain inaccessible, such as those situated in steep or remote areas (Lausch et al., 2016; Diao et al., 2020). RS is a suitable method for monitoring forests (but also soil attributes) across extensive areas (Bałazy et al., 2019). Differences in spectral values have been shown to be associated with soil properties such as moisture (e.g., Welikhe et al., 2017; Fabre et al., 2015; Lobell and Asner, 2002), SOC (e.g., Esmizade et al., 2022; Shields et al., 1968), and texture (i.e., sand, silt, and clay content) (e.g., Bousbih et al., 2019). Chaparro et al. (2018) investigated the role of soil moisture in a forest decline event that occurred in 2012 in northeastern Spain, and concluded that in the presence of dry soils, the probability of observing a decline in deciduous forests increased. Another study conducted in the Central Zagros region by Esmizade et al. (2022) found a significant correlation between SOC content and reflectance values obtained from Landsat data. Generally, it has been observed that reflectance values in the visual and near-infrared regions decline with increasing grain size of the soil, soil moisture, and SOC. Thus, understanding whether there are spectral differences in the bare soil surrounding declining and non-declining forest patches may help us understand how soil properties affect forest decline. It should be noted, however, that predicting soil variables from RS is a challenging task because these methods only provide surface data and do not capture subsurface properties and states (e.g., Döpper et al., 2022). Still, satellite-based spectral analysis of bare soil areas in open semi-arid forests has so far not been related to forest decline processes but may help in identifying and mapping declining areas.

Detecting and mapping spatial patterns of forest decline is crucial, as it serves as a primary measure of comprehending tree mortality and predicting and regulating future forest development

(Etzold et al., 2019). This calls for enhancing data collection to attain an efficient and robust understanding of forest decline (Dorman et al., 2015). However, the limited availability of comprehensive datasets is a significant constraint in investigating forest decline in semi-arid regions. The collection of data on forest decline, including the identification of possible causes, is a tedious and time-consuming task due to the widespread nature of forest decline (Lausch et al., 2016; Diao et al., 2020; Shafeian et al., 2023). Furthermore, understanding tree and forest decline is complicated because tree mortality is unevenly distributed across numerous spatial scales and temporal variability occurs due to its gradual nature (Dorman et al., 2015). Additionally, multiple stress factors operating at different spatiotemporal scales hinder our understanding of forest decline (Camarero, 2017). There is no universally applicable answer to the question of which factors contribute significantly to forest decline processes (e.g., Bałazy et al., 2019), as the influence of diverse environmental factors on forest decline and tree mortality must be both individually and jointly assessed (Bałazy et al., 2019).

The primary objective of this study is to gain a deeper understanding of forest decline in the mountainous, semi-arid Zagros forests. We aim to gain a better understanding of the factors driving tree decline (individual trees) and forest decline (tree groups) by examining the relationships between different classes of decline and various environmental variables (i.e., topography and climate) as well as tree characteristics, including diameter at breast height (DBH) and tree height. The research also includes spectral analysis of bare soils in declining and non-declining tree groups using S2 imagery. Thus, this study seeks to answer two main questions: 1) what are the main drivers of tree and forest decline in the Zagros forests? 2) Is there a significant difference in the spectral values of bare soils between declining and non-declining tree groups using S2?

4.2. Material and Methods

4.2.1. Study area

The Zagros forests, which make up roughly 44% of Iran's total FC, play a pivotal role with respect to several key ecosystem services, including water supply, soil conservation, and climate change mitigation, as well as the overall socioeconomic stability of the region (Sagheb Talebi et al., 2014). Precipitation in the complete Zagros region generally demonstrates a declining pattern both from north to south and from west to east. The majority of the annual rainfall is concentrated during the winter season, with an average ranging from 400 to 800 mm, constituting about 70% of the total annual precipitation (Sagheb Talebi et al., 2014). Climatic data obtained from the Zagros region reveals an annual average temperature range spanning from 9 to 25 °C, with variations influenced by both latitude and altitude (Sagheb Talebi et al., 2014). The geographical scope of our research is centered in the southern sector of the central zone of Zagros forests, specifically situated within the Chaharmahal and Bakhtiari Province. The most dominant and widespread tree species include Brant's oak (*Quercus brantii* var. persica), which is partially mixed with *Quercus infectoria*

G.Olivier, *Quercus libani* G.Olivier, wild pistachio (*Pistacia atlantica* Desf.), and *Acer monspessulanum* L. In addition, *Crataegus* spp., *Amygdalus* spp., and *Pyrus* spp. occur frequently (Erfanifard et al., 2014). Leaves of Brant's oaks appear and reach full growth at different times in the Zagros region, ranging from early March to late May (Hesami et al., 2016; Mardani and Youssefi, 2005). Conversely, leaves begin to fall starting in early November and are usually completely shed by December (Mardani and Youssefi, 2005). Figure 4.1 shows the location of our study area as well as the distribution of sampled sites.
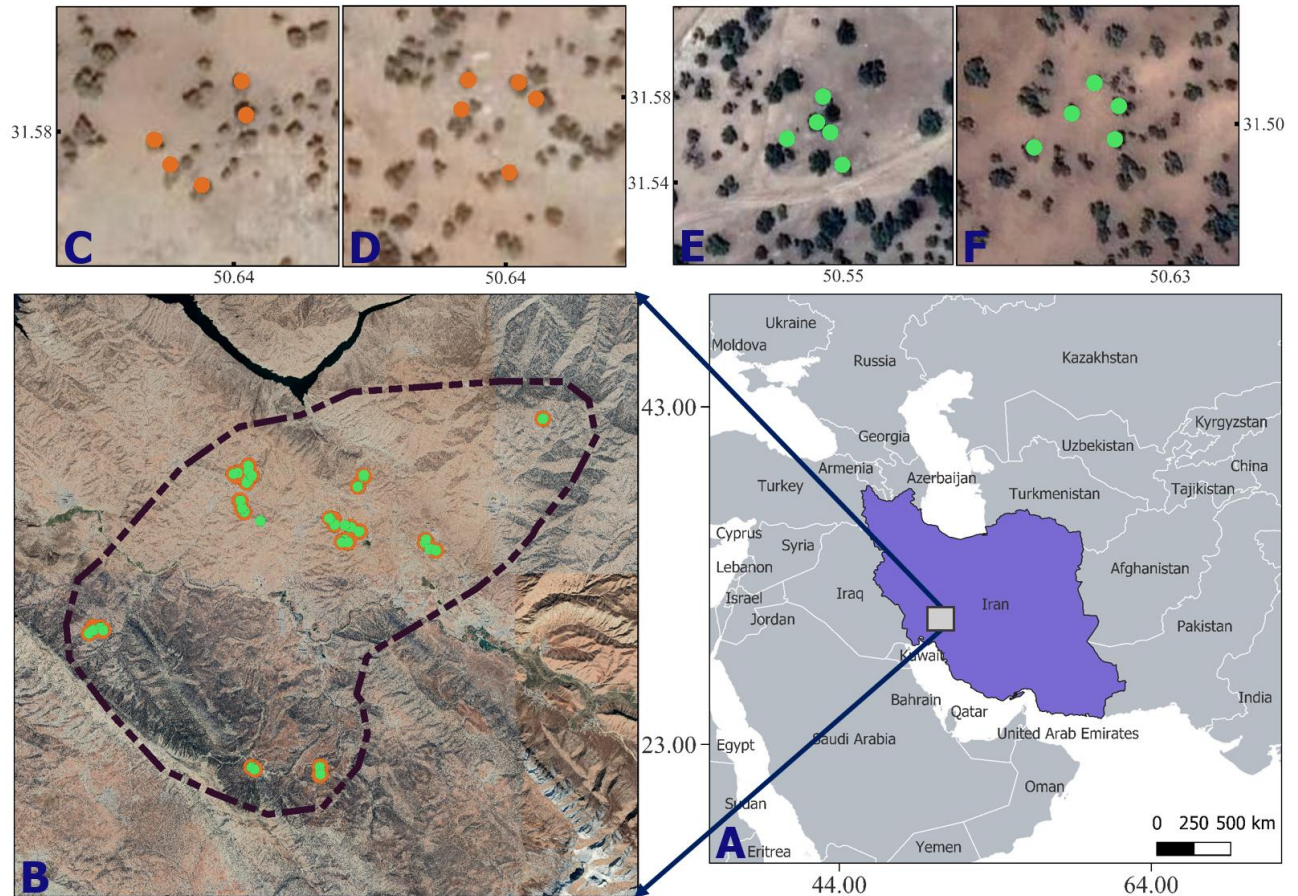
Figure 4.1 From the right bottom to the right top: A) The location of Iran; B) The study area covered with Google satellite imagery; C-D) A close-up of two declining tree groups (the orange points are the declining sampled trees); E-F) A close-up of two non-declining tree groups (the green points are the non-declining sampled trees).

4.2.2. Reference data

4.2.2.1. Sample plots and individual trees

A field campaign was conducted during the summer of 2021 to gather reference data. The sites for the field surveys were chosen by dividing the study area into declining and non-declining zones

based on Landsat imagery observations from the past 36 years (Shafeian et al., 2023). To determine these zones, we utilized an EVI anomaly approach, utilizing data from 1986 to 2021 (refer to Shafeian et al., 2023 for more information). Field plot locations were chosen at random within the identified areas of decline, which are characterized by notably reduced EVI values compared to historic values. We ensured to survey all major illumination, aspect, and slope configurations. We investigated 43 plots consisting of five individual trees (hereafter called tree groups), resulting in a total of 215 individual trees sampled. For the analysis, we used 190 (90 declining and 100 non-declining) individual trees, for which the exact locations were identifiable in the unmanned aerial vehicle (UAV) imagery collected during the field survey. Differential GPS was utilized to record the central positions of the field plots (Figure 4.1). A DJI® Mavic Pro equipped with an RGB camera was employed for the drone surveys that captured aerial snapshots of every plot. The high-resolution UAV data was acquired and used to evaluate the crown condition of the trees and to match the field data with the high-resolution Google Maps satellite imagery that was used as base maps in QGIS. Detailed records of the site's general conditions were also collected, including individual trees. The declining sampled trees were further subdivided into four classes: non-declining (class = 0), slightly declining (class = 1), moderately declining (class = 2), and severely declining (class = 3). This classification was determined using approximate percentage ranges of the damage (detailed descriptions provided in Table 4.1) and tree group decline levels (i.e., non-declining and declining). To classify the overall decline level of tree groups, a systematic approach was implemented. If more than 60 percent of the trees within a tree group were defined as "declining," we categorized the entire group as "declining", which was otherwise categorized as "non-declining". Additionally, we took into account the condition of the surrounding regions in the field to make informed classifications. This method allowed for a comprehensive assessment of tree group health while considering both the majority condition within the group and the broader environmental context. The tree groups, divided into declining and non-declining, amounted to n = 43.

Table 4.1 The detailed description of the individual tree decline classes

	Tree decline Category	Damage Percentage Range	Description
	0. **Healthy or non-declining**	0-5%	Trees in this category were in excellent health, with very minimal or no visible damage.
	1. **Slightly declining**	5-30%	Trees in this category had some visible damage or stress but were generally healthy. This may include a few dead branches or minor insect damage.

	2. **Moderately declining**	30-50%	Trees in this category were experiencing significant stress and damage. They had extensive insect infestations, multiple dead branches, or signs of disease.
	3. **Severely declining**	More than 50%	Trees in this category were in critical condition and at risk of declining further or dying. They had extensive damage and significant dieback, and they may show clear visible signs of disease.
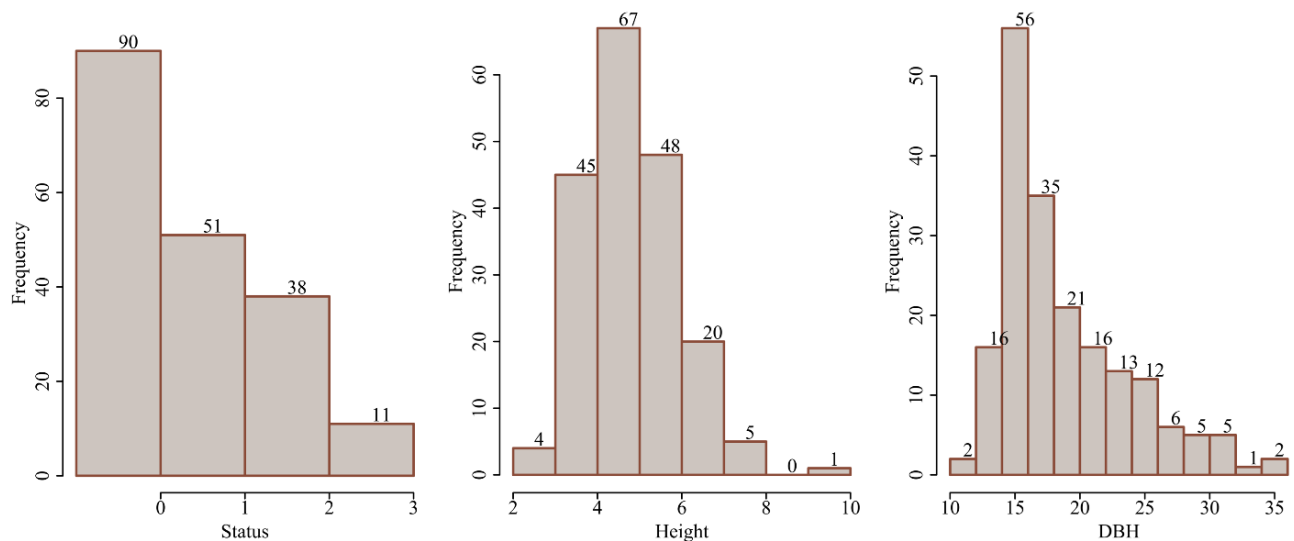
Figure 4.2 Histograms providing information on the individual trees analyzed in this study, from left to right: frequencies (the number of trees) of different tree decline classes (status); frequencies of the approximate tree height (H) in m; DBH in cm.

4.2.2.2. Reference data over bare soil areas

A second reference dataset was obtained by visually interpreting Google satellite imagery in QGIS. We identified areas that were predominantly covered with bare soil and were located close to declining and non-declining tree groups. These areas were analyzed to determine if there were any differences in the spectral properties of the bare soil inside or near declining and non-declining tree groups. These reference points were established in S2 pixels, which we assumed to be free of vegetation (0% tree cover) based on visually interpreting Google satellite imagery. A total of 486 reference points were collected, consisting of 256 areas located near declining and 230 areas near non-declining tree groups.

4.2.3. RS data

4.2.3.1. S2

The multispectral data of S2 has been found to be valuable in identifying forest decline by comparing the spectra of declining forests to those of healthy ones over time (Pontius et al., 2020). S2 comprises two polar-orbiting satellites, resulting in a 5-day revisit time. The Multispectral Imager (MSI) provides 13 spectral bands with pixel sizes ranging from 10 to 60 m. We excluded three bands with a resolution of 60 m and utilized the remaining 10 bands in our study. Our objective was to analyze the spectral properties of bare soil in declining and non-declining tree groups. Processing of the S2 imagery was conducted through the GEE platform, importing the Harmonized S2 MSI: Multispectral Instrument, Level-2A (ID: "COPERNICUS/S2_SR_HARMONIZED") dataset. To ensure data quality, we filtered the image collection to include cloud-free or less cloudy (0–5%) composite images available between 2020 and 2022. The study considered four distinct seasons: winter (January to the end of March), spring (April to the end of June), summer (July to the end of September), and autumn (October to the end of December). For each month, a 15-day median image was exported, resulting in two images per month. This division was achieved by dividing the image acquisition dates into two intervals: the 1st to the 15th day of the month and the 16th to the last day of the month (a total of 72 exported images). See Supplementary Material III for the link to GEE scripts for importing and downloading S2 images.

4.2.4. Environmental variables

An overview of the variables utilized to investigate their relationship with declining and non-declining trees and tree groups is presented in Table 4.2. Detailed descriptions of these relevant variables are provided below.

4.2.4.1. Topography

We used the Global FABDEM (Forest and Buildings Removed from Copernicus DEM), one of the most recent DEM products available as a project on GEE (Hawker et al., 2022), to investigate the effect of topography. After importing the DEM dataset, we calculated the slope and aspect using its elevation band, and the result of each calculated variable was exported separately as a single raster layer using QGIS. We additionally calculated a hillshade image, setting the sun's elevation at 56.4° and azimuth at 144.1°. These settings matched the acquisition time of a PlanetScope image acquired close to the date of our field campaign, mid-September 2021, which was used for a plausibility check and confirmed the validity of the obtained shadowing patterns.

4.2.4.2. Topographic Wetness Index

The compound topographic index (CTI), also referred to as the topographic wetness index (TWI), serves as a potential drought indicator related to tree and forest decline in our analysis. Beven and Kirkby (1979) introduced the concept of this index. TWI values range from -3 to 30, and the TWI is computed using factors like slope steepness and direction to estimate the accumulation of water flow. Elevated TWI values commonly signify wetter conditions, whereas lower TWI values are indicative of drier conditions and steeper slopes (Winzeler et al., 2022). The TWI serves as an objective measure of site moisture (Winzeler et al., 2022; Kopecký and Cizkova, 2010), aiding in the detection of stressed trees and forest decline. First, we imported the image collection of the "MERIT/Hydro/v1_0_1" global hydrology dataset into GEE to obtain upstream data (Yamazaki et al., 2019). The flow accumulation area and elevation bands of the upstream drainage area were chosen. Then the TWI equation given below was employed to derive a raster layer. Supplementary Material III includes a GEE script link for TWI estimation.

TWI = upstream drainage area (flow accumulation area) × pixel size or resolution
/ (slope radians) × $\log_{10}$ (4.1)

4.2.4.3. Climate

Prolonged exposure to extreme conditions (warmer and drier) can lead to partial canopy dieback and tree mortality (Andrus et al., 2023), particularly in semi-arid ecosystems. As temperature and precipitation are considered important climatic variables in tree and forest decline (e.g., Andrus et al., 2023; Shiravand and Hosseini, 2020), we also included selected bioclimatic variables from the Bioclim dataset (Hijmans et al., 2005). We included temperature data (i.e., bioclim-1 = annual mean temperature, bioclim-4 = temperature seasonality (standard deviation 100), bioclim-7 = temperature annual range, and bioclim-10 = temperature annual range) as well as precipitation data (i.e., bioclim-12 = annual precipitation, bioclim-15 = seasonality of precipitation (coefficient of variation), bioclim-16 = precipitation of the wettest quarter, and bioclim-17 = precipitation of the driest quarter) to account for potential influences of climatic gradients on tree decline (Shafeian et al., 2021). The data were acquired in GEE ("WORLDCLIM/V1/BIO"), and each variable or band was exported separately as a single raster layer. See Supplementary Material III for the link to GEE scripts for importing and downloading Bioclim variables (ca. 1 to 2 km).

4.2.4.4. Soil

Soil properties, including moisture levels and soil texture (i.e., clay, sand, and silt content), significantly impact the drought susceptibility of forests (Ewane et al., 2023). In warmer and drier climates marked by reduced soil moisture, lower humidity, and greater heat stress, trees may struggle to reach the critical physiological thresholds needed for survival (Andrus et al., 2023). Soil variables were extracted from SoilGrids data, an initiative led by the World Soil Information Center (ISRIC), which is available on GEE at a spatial resolution of 250 m. SoilGrids offers maps for ten

discrete soil properties. To gain more comprehensive insights into this dataset, please refer to Poggio et al. (2021).

4.2.4.5. Tree density

The term tree density or FC refers to the proportion of land covered by the vertical projection of the tree canopy relative to the total area (Gonsamo et al., 2013). Andrus et al. (2023) posit that reducing FC can potentially increase resource availability, promoting the vigor and growth of surviving trees. Similarly, the study confirms the inverse correlation, wherein high forest density may limit resource availability and decrease tree vigor and growth. We compared the FC of declining versus non-declining trees and tree groups in the study area, as it is considered a major contributing factor to forest decline (e.g., Ghanbari Motlagh and Kiadaliri, 2021; Hosseini et al., 2017). Our data was obtained from an FC map available for the entire Zagros region (Shafeian et al., 2021).

4.2.4.6. Illumination

Illumination is a significant resource for plants that influences their recruitment and growth. It can also play a vital role in forest survival (Matsuo et al., 2021). The illumination condition (IC) ranges from 0 to 1 and represents poorly lit and well-illuminated zones, respectively, and it is determined by the incidence angle. The following equation was used to determine IC:

$$IC = \cos(z) \times \cos(s) \times \sin(z) \times \sin(s) \times \cos(a - o) \qquad (4.2)$$

where z is the solar zenith angle (incident angle for a horizontal surface, provided by the sensor metadata), s is the terrain slope calculated from the DEM, a is the solar azimuth angle (provided by the sensor metadata), and o is the terrain aspect. A GEE script was applied to use the DEM and metadata of the solar angels in the image to determine the IC at the pixel level and add it as a new band (Martín-Ortega et al., 2020). Pixels with high median IC values (bright pixels) are placed in the sun's direction and receive more light (Martn-Ortega et al., 2020). The link for the corresponding GEE scripts can be found in Supplementary Material III.

Table 4.2 List of environmental variables with their sources

Variable	Source
Topography	DEM (30-m) (Hawker et al., 2022)
TWI	MERIT Hydro (Yamazaki et al., 2019)
Climate	Data Long-term means of precipitation and temperature of Worldclim (Hijmans et al., 2005)
Soil	SoilGrids data from World Soil Information (ISRIC) (Poggio et al., 2021)
FC	Fractional woody cover map (Shafeian et al., 2021)
IC	DEM (30-m) (Hawker et al., 2022)

4.2.5. Tree characteristics

Tree decline can be notably influenced by tree characteristics (i.e., DBH, height, and crown size). Several studies have shown that differences in DBH (e.g., Akkuzu et al., 2009; Schroeder, 2010; Eriksson et al., 2005) and tree height (e.g., Tymi'nska-Czaba'nska et al., 2022; Stovall et al., 2019) can lead to different tree mortality rates. Therefore, we also investigated potential links between field-measured DBH, tree height, and the decline of individual trees and tree groups.

4.2.6. Methodology

4.2.6.1. Distribution of the environmental variables

The density plots, also referred to as kernel density estimation (KDE) plots, illustrate the distribution of environmental variables within distinct groups, namely declining and non-declining individual trees (Figure 4.4). The density plots depict the distribution of the same environmental variables across different tree groups (Figure 4.5). We employed the Terra package in R (Hijmans et al., 2023) to retrieve raster and spatial data values at these reference points.

4.2.6.2. Statistical analysis

In total, we fitted four GAM models. In the first two models, we used four tree decline classes at the individual tree level (four classes of decline: healthy, slightly declining, moderately declining, and severely declining) as response variables fitted one model using the environmental variables as predictors and one model using the tree characteristics. We fitted two more models using the same sets of predictors but the decline classes at the tree group level (two classes of decline: declining and non-declining) as response variables. Tree group decline status was included as a binary response variable, and tree decline at the individual tree level was included as an ordered categorical response variable in the respective models. Environmental variables were included in the models as predictors (i.e., individual smooth terms). For the models including individual tree decline classes as a response variable, we additionally included the tree group ID as a random factor in the model as individual trees from one tree group were not considered independent replications. Some variables were omitted from the analysis due to noticeable inter-correlations (more than 80%) among variables, specifically elevation and several bioclimatic variables such as bioclimate-01, bioclimate-04, bioclimate-07, bioclimate-10, bioclimate-12, and bioclimate-15. Therefore, from the bioclimatic variables, we retained bioclimate-16 for the analysis. This resemblance in correlation patterns is visualized in Figure 4.9 (Supplementary Material III), which depicts correlation plots for both the reference data and the remaining environmental variables. For a more comprehensive view, correlation plots for all environmental variables, including the excluded ones, are available in Supplementary Material III. We set an upper limit on the number of environmental predictors (n = 3) and tree characteristics predictors (n = 2) in the GAM models and explored models with all possible variable combinations. This is because when dealing with numerous

predictor variables, hidden relationships among some of them may lead to redundancy, which could affect the accuracy and interpretability of GAM models as well as increase the computation time. Final models were selected based on the lowest Akaike Information Criterion (AIC) value, indicating the best fit.

Model residuals were checked for spatial autocorrelation by calculating Morans' I values. The residuals of the models with tree group status as a response variable were significantly auto-correlated for both environmental predictors as well as tree characteristics. Therefore, we refitted these models, including the center coordinates of the tree groups as an additional smooth term to account for the spatial autocorrelation. The GAM models with individual tree decline levels as a response variable were only significantly auto-correlated when using tree characteristics as a predictor. Therefore, we refitted these models as well, including the coordinates of each individual tree as an additional smooth term to account for the spatial autocorrelation. We applied the GAM models using the mgcv package (Wood, 2023) available in R software (version 4.2.1) (R Core Team, 2022) using restricted maximum likelihood for smoothing parameter estimation. The dimensions of the individual smooth terms were restricted to a maximum value of three to avoid too-wiggly spline fits (overfitting).

In an additional experiment, we compared the spectral values of bare soils near two tree groups (declining and non-declining), during the 2020–2022 timespan to analyze the main bands using the Wilcoxon statistical test. The methodological flowchart is depicted in Figure 4.3. Reference point classes were captured for both declining and non-declining bare soil. Values were then extracted through the terra package in R (Hijmans et al., 2023), using S2 imagery. Subsequently, a Wilcoxon test using the wilcox.test function of the stats package in R (R Core Team, 2022) was conducted to determine significant statistical differences between the two classes of decline at various S2 spectral bands.
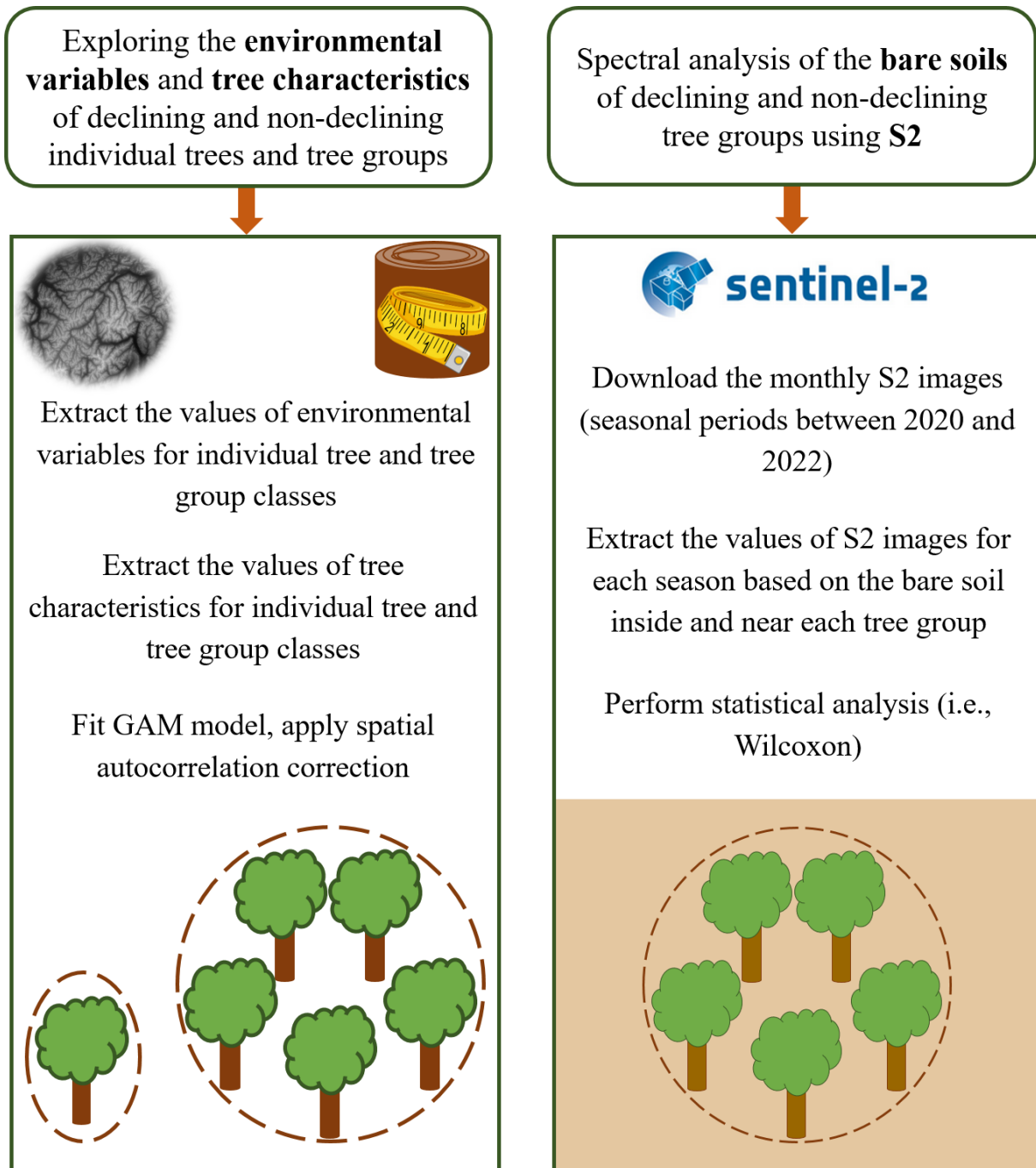
Figure 4.3   Study workflow: The left side displays the GAM model formation for comparing potential decline drivers at individual tree and tree group levels. The right side demonstrates the RS analysis on the bare soils of two declining and non-declining tree groups.

4.3. Results

4.3.1. Distribution of the environmental variables

4.3.1.1. Distribution of environmental variables for declining and non-declining individual trees

Figure 4.4 illustrates the distribution of environmental factors among the non-declining and declining individual trees in two groups: those that are healthy (non-declining) and those that are declining (slightly, moderately, and severely declining). The distributions indicate differences in several environmental predictors between groups. Most apparent were differences in slope and aspect distribution between trees that are declining and those that are not declining. Mostly declining trees were spread over the medium slope. Differences in the shape of the distributions were less pronounced for the remaining variables but visible for bioclimate-04, soil texture, soil water content, and IC. For the temperature variable bioclimate-04 (bio-04), the frequency of declining trees increases with higher bioclimate-04 values. In relation to soil attributes, areas with declining trees were predominantly located in regions featuring moderate clay, sand, and silt content. However, the maximum occurrence of trees not experiencing a decline was observed in areas with a higher sand content. Nonetheless, as the clay content increased, there was a slight decline in the frequency of non-declining trees.
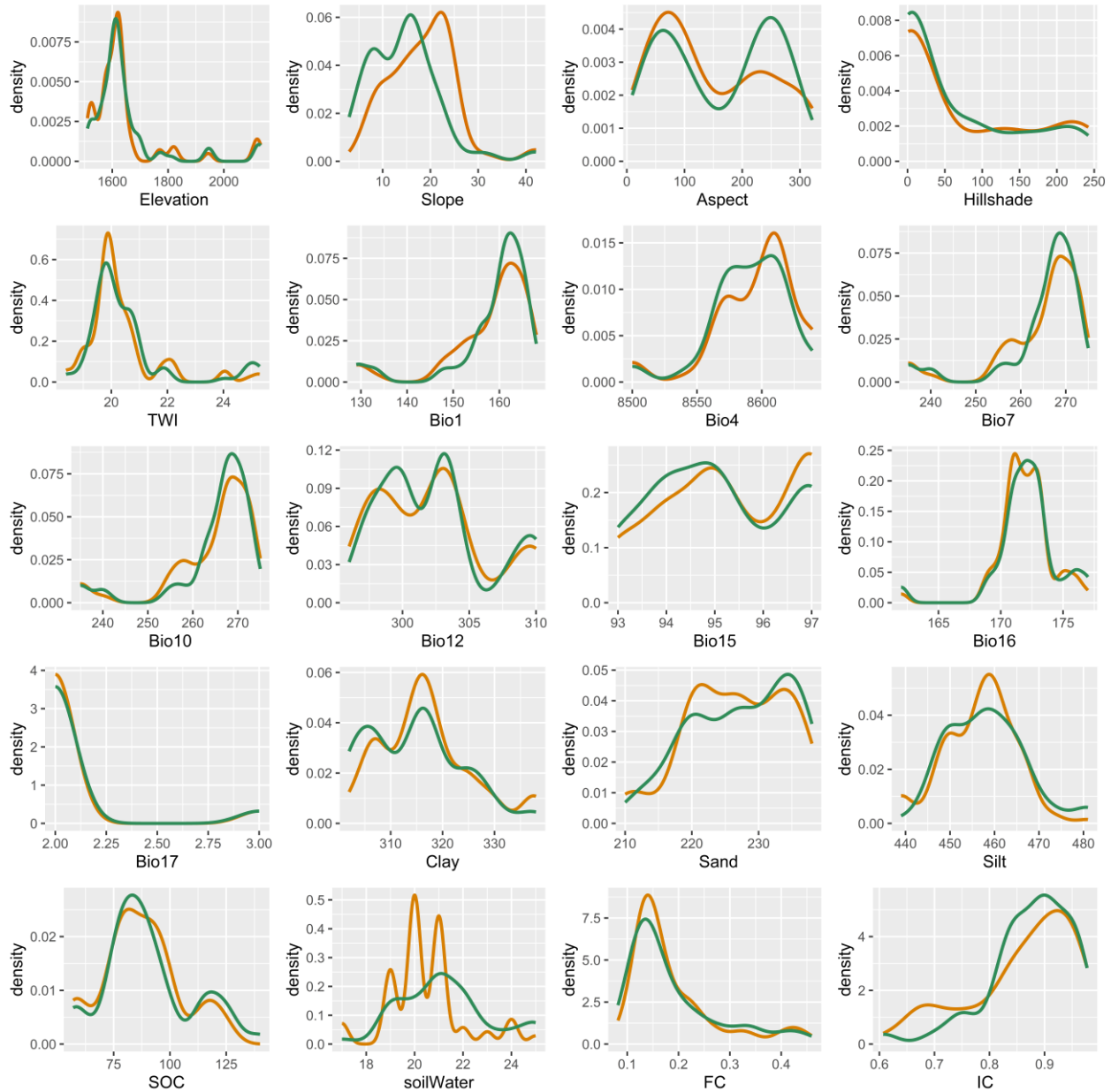
Figure 4.4 Density plots of environmental variables for declining (in orange) and non-declining (in green) individual trees (topographic, climate, and soil variables as well as FC and IC).

4.3.1.2. Distribution of environmental variables for declining and non-declining tree groups

Figure 4.5 depicts the distribution of environmental variables between declining and non-declining tree groups. Differences could be observed regarding topography, climate variables, soil factors, and FC among the two classes. Declining tree groups were found at lower elevations (less than 1700 m) and on subtle slopes. The frequency of the non-declining tree groups was higher in the areas with higher TWI (values >20). Declining tree groups were more frequently present on soils

with high sand content and less frequently associated with soils with high silt content. Declining tree groups showed greater soil water content fluctuations, with higher density in lower water content areas. Additionally, increasing illumination was linked to the higher density of declining tree groups.
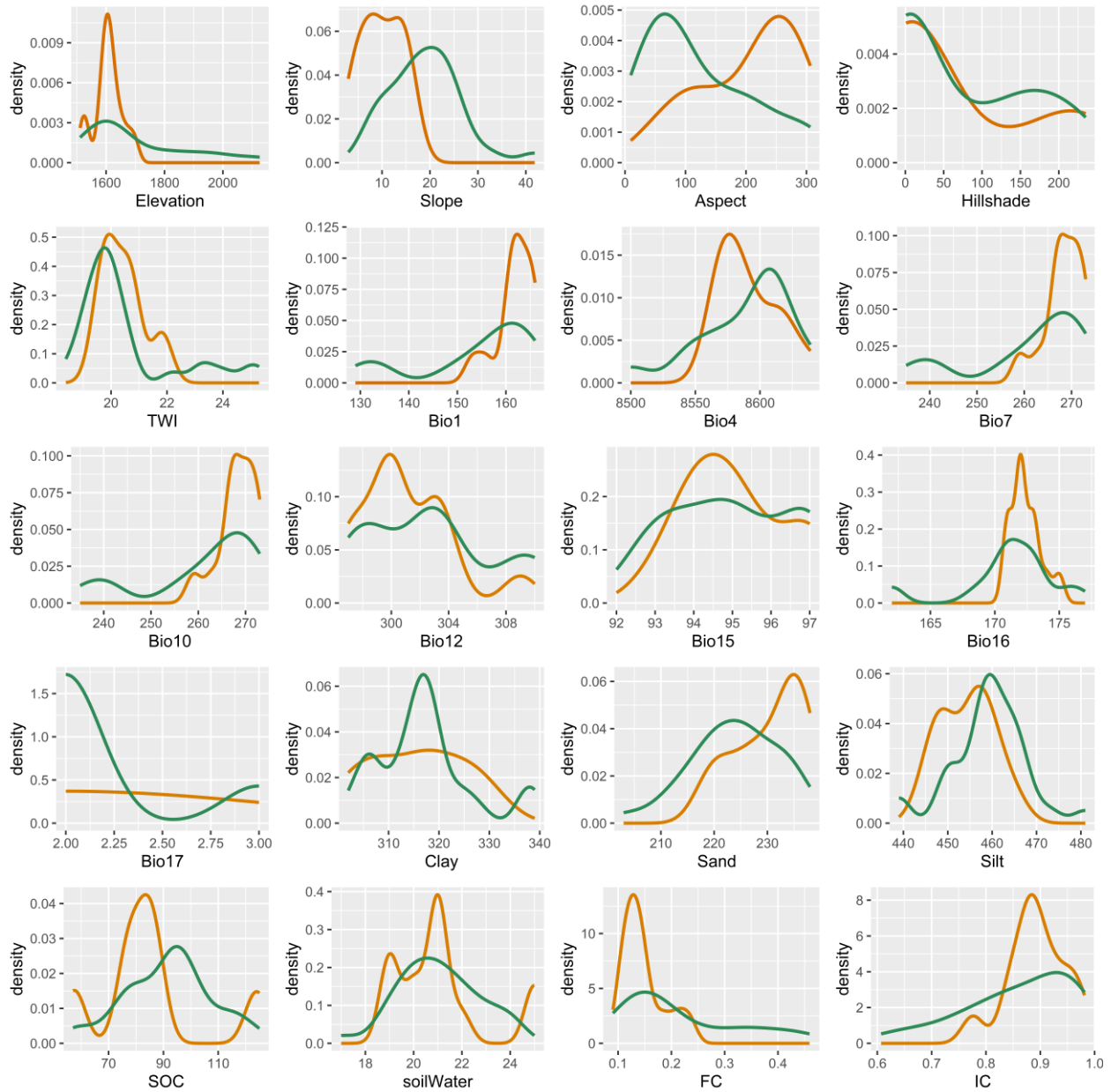
Figure 4.5 Density plots of environmental variables of declining (in orange) and non-declining (in green) tree groups (topographical, climate, and soil variables as well as FC and IC).

4.3.2. GAM

4.3.2.1. GAM for individual tree decline

The most optimal GAM with the lowest AIC value of 411.7040, used for modeling the categorical response variables representing individual tree decline classes, included the slope, TWI, and bioclimate-16 as predictors. This model explained approximately 18% of the variance in the data, based on a sample size of n = 190.

Interestingly, the analysis revealed that the lowest level of individual tree decline was observed in areas with medium to steep slopes. When considering the response curve of the precipitation in the wettest quarter of the year (bioclimate-16), there was an initially inverse relationship, particularly for precipitation levels lower than 170 mm (Figure 4.6). However, afterward, it showed a nearly linear positive relationship between precipitation and the individual tree decline classes. This suggests that in areas with lower precipitation, individual tree decline tends to increase, but beyond a certain threshold, higher precipitation is associated with a decrease in individual tree decline. The results for all non-significant variables as well as the top five best models are provided in Supplementary Material III.

Table 4.3 The outcomes of the best GAM models: environmental variables as predictors using individual tree decline classes as response variables (the significant variables are bold and denoted with asterisks).

Variable	Effective degrees of freedom	p-value
Slope	2.080e+00	**0.009***
TWI	8.747e-05	0.8
Bioclimate-16	1.467e+00	**0.02***

Table 4.4. The outcomes of the best GAM models: tree characteristics as predictors using individual tree classes as response variables

Variable	Effective degrees of freedom	p-value
DBH	1.644e-01	0.2
H	1.411e-04	0.8
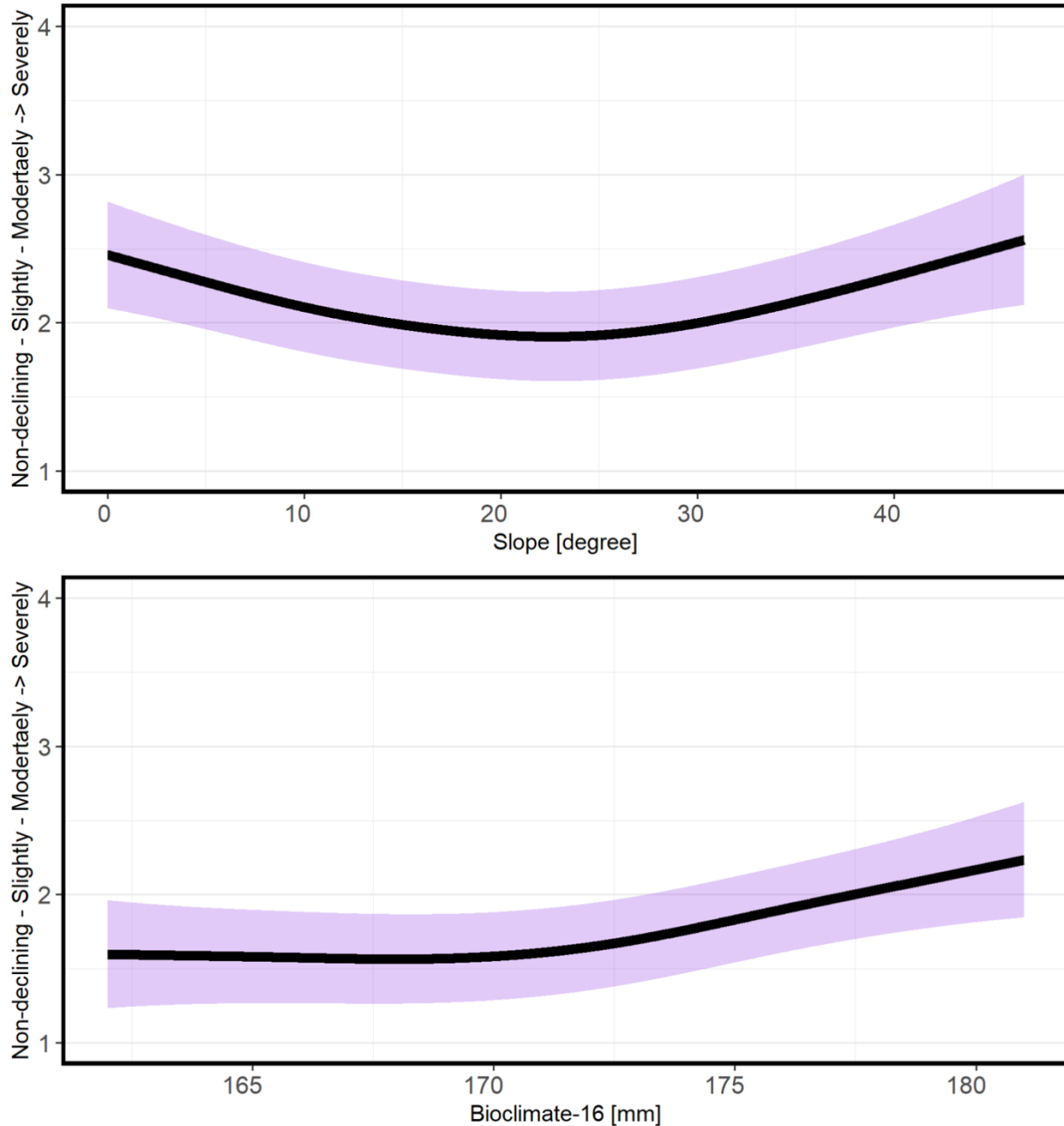
Figure 4.6   The selected significant variables from top to bottom (slope and bioclimate-16) of the best GAM model across different individual tree decline categorical classes. Low values of the y-axis (response) indicate lower tree decline.

4.3.2.2. GAM for tree group decline

The analysis conducted at the tree group level revealed that the most effective predictors were a combination of slope, SOC, and soil silt content. This combination was indicated by the model with the lowest AIC value of 45.59, which accounted for 51% of the total variance. Notably, only the effect of SOC was found to be statistically significant (with a p-value of 0.04), while the other

variables were considered insignificant, with p-values of 0.16 for slope and 0.97 for silt. This suggests that declining tree groups were primarily associated with soils containing lower and higher organic carbon contents. So, the lowest decline levels were found in areas where the soil had medium values of SOC.

Regarding models concerning tree characteristics, the GAM provided no significant results. The model's ability to explain the variance was relatively modest, at approximately 6%. The results for all non-significant variables as well as the top five best models are provided in Supplementary Material III.

Table 4.5 The outcomes of the best GAM models: environmental variables as predictors using tree group classes (the significant variables are bold and denoted with asterisks.)

Variables	Degree of freedom	p-value
Slope	6.424e-01	0.1
SOC	8.442e-01	**0.04***
Silt	6.780e-06	0.9

Table 4.6 The outcomes of the best GAM model: tree characteristics as predictors using tree group classes

Variables	Degree of freedom	p-value
DBH	1.5	0.5
H	0.00014	0.5
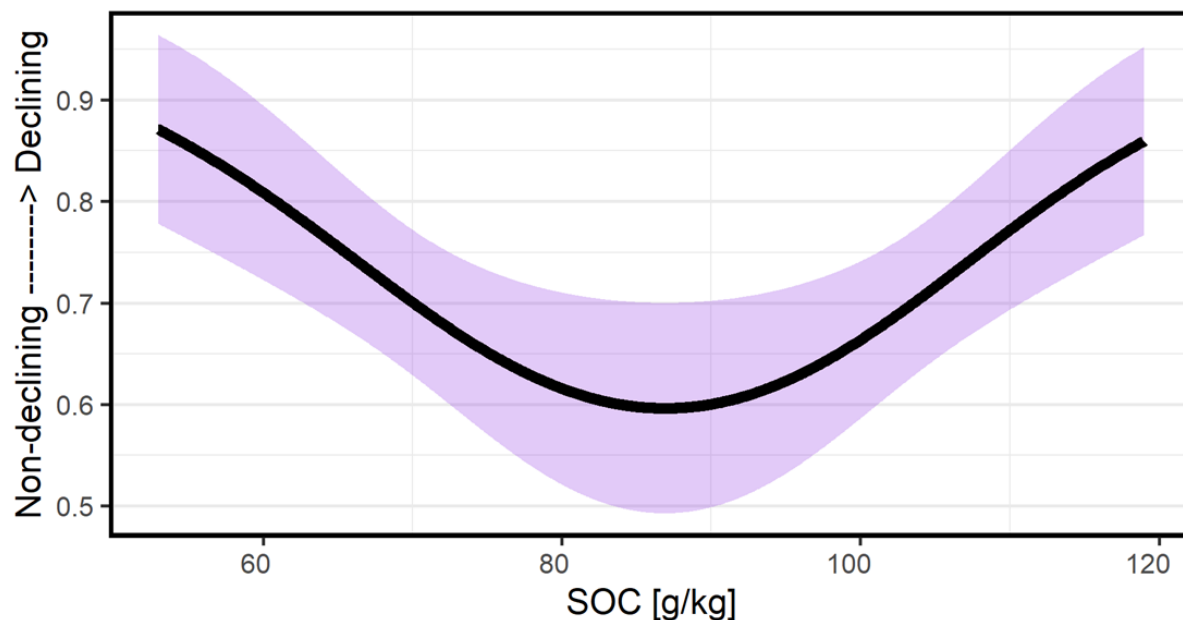
Figure 4.7 The selected significant variable (SOC) of the best GAM model across different tree group decline binary classes. Low values of the y-axis (response) indicate a low level of tree decline.

4.3.3. Spectral analysis of S2 data over bare soil areas

The bean plots (Figure 4.8) show the S2 bands of bare soil pixels next to declining and non-declining regions during four seasons from 2020 to 2022. Figure 4.8 shows differences in the spectral values of bare soil between the non-declining and declining tree groups. Throughout all seasons, except for winter, which showed some fluctuations, soil areas within or near non-declining tree groups consistently exhibited higher spectral values in almost all S2 bands. The distinction was particularly noticeable in the visible near-infrared bands (i.e., VNIR-1 and VNIR-2). Table 4.7 presents the statistical results of the Wilcoxon tests comparing two groups of bare soils. The tests were conducted based on the variations observed in the 10 S2 bands.
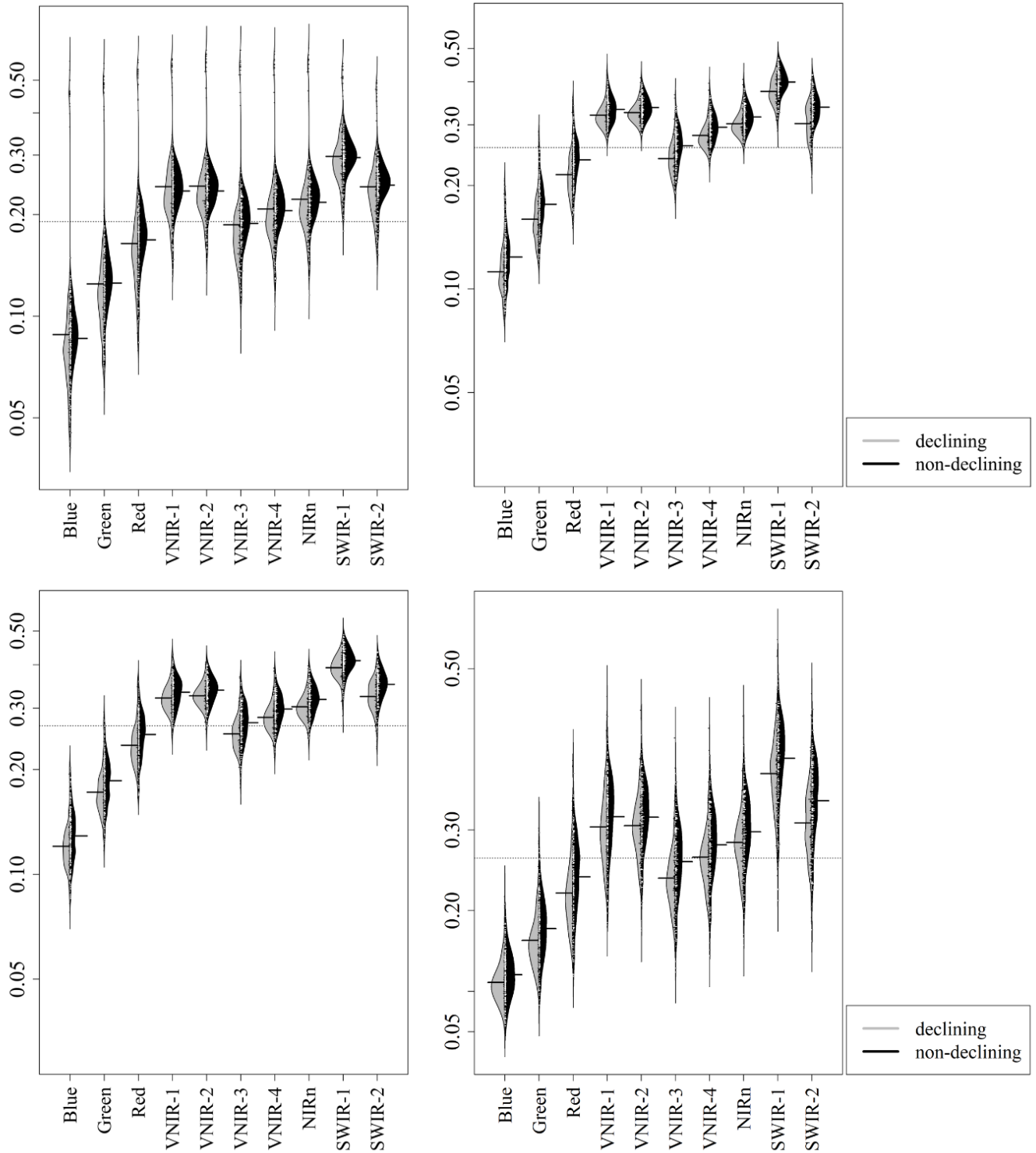
Figure 4.8 Spectral values of the bare soil over declining and non-declining areas using S2 bands during the winter (top left), spring (top right), summer (bottom left), and fall (bottom right) seasons of three consecutive years (2020–2022).

Table 4.7 Wilcoxon test results for two groups of bare soils based on used S2 band differences (significant results are denoted with asterisks).

Season Band	winter	spring	summer	fall
Blue	0.019*	4.447462e-08*	5.396698e-05*	1.495838e-04*
Green	0.009 *	3.808531e-09*	1.790776e-06*	1.479342e-05*
Red	0.007*	2.502013e-10*	7.480984e-07*	2.425030e-06*
VNIR-1	0.66	2.952863e-06*	1.030380e-04*	8.593128e-04*
VNIR-2	0.37	4.005048e-07*	2.125996e-06*	5.251821e-04*
VNIR-3	0.002*	6.937863e-12*	1.151809e-09*	9.022430e-08*
VNIR-4	0.03*	9.064574e-11*	7.494382e-09*	5.892351e-06*
NIRn	0.09	1.279199e-09*	3.121966e-08*	5.748596e-05*
SWIR-1	0.18	1.867500e-12*	5.117691e-09*	8.259254e-07*
SWIR-2	0.01*	3.388447e-18*	3.857722e-14*	9.044554e-10*

Table 4.7 shows that the VNIR-3, SWIR-2, red, green, and blue bands were significantly different in all seasons. Notably, all 10 bands were also significantly different in the summer and fall seasons. In winter, only half of the analyzed S2 bands showed statistical significance when comparing the two bare soil groups located within and near declining and non-declining tree groups. In addition, the observed p-values for winter were generally higher compared to other seasons.

4.4. Discussion

4.4.1. Environmental variables

4.4.1.1. Topography

The importance of topography on tree and forest decline has been mentioned in several earlier studies (Ewane et al., 2023; Najafifar et al., 2019; Assal et al., 2016). For example, Ewane et al. (2023) found that topographic convergence, associated with increased precipitation, is a crucial predictor of ecosystem productivity and plant responses to drought. The authors pointed out that trees on steeper slopes are more likely to suffer from drought because of drainage and stronger winds. On the other hand, trees in valleys are better at handling drought since they receive extra water from the valley sides.

Among topographical factors in our study, slope was found to be strongly associated with individual tree decline classes (the highest tree decline was observed in the medium slope values). Furthermore, it was selected as an influencing factor in both best-performing GAM models. The GAM results showed that slope values were significantly different between declining and non-declining tree groups, with a p-value of 0.009. Our results thus corroborate previous research (Ewane et al., 2023; Solaymani and Jabbari, 2015) in different ecosystem types. In the semi-arid Wyoming Basin ecoregion, Assal et al. (2016) determined that high elevation and northern slopes significantly reduced tree mortality during droughts. Also, Solaymani and Jabbari (2015), in a study on Zagros forests, found that soil erosion and degradation were observed on sloped terrains. They also noted that the negative impacts of soil erosion became more noticeable on steeper slopes, indicating a strong connection between slope steepness and the severity of oak dieback.

In a study in semi-arid Zagros forests, Hosseini et al. (2017) found that higher elevations show the greatest rates of tree mortality and crown decline. This is somehow in contrast with our density plot (Figure 4.4 and Figure 4.5), which suggests that declining tree groups are found in the lower elevations (maximum frequency at 1600 m). At the level of individual trees, no differences were visible along the elevation gradient. Due to the strong correlation between elevation and climate variables (i.e., temperature), elevation was later excluded from our GAM model analysis.

In another study in the Zagros region, Nourinejad and Rostami (2014) already identified slope as having a significant correlation with oak decline, while no correlation was found for elevation. They stated that slope in combination with aspect controls the solar irradiation and hence affects the water availability and transpiration of the trees, which was in line with Parvaneh et al. (2015), who similarly underscored the importance of slope in explaining the prevalence of declining trees. In our analysis, aspect was also a selected variable among the best models (third best) of tree groups. However, it was not statistically significant in any of the selected models.

As another topographical variable, hillshade did not show a statistically significant connection with the different levels of individual tree or tree group decline in our study. However, it was among the fourth and fifth best models in the GAM models of individual tree and tree group classes of decline, respectively. These outcomes are partly in line with the findings of Najafifar et al. (2019) in a part of Zagros forests. They found that forest dieback was more common in areas with less shading, emphasizing the significant impact of hillshade on the drying conditions of oak trees, which was even more influential than the aspect of the terrain.

TWI is an additional parameter indicating soil moisture conditions. TWI can contribute to explaining tree and forest decline, yet it is often overlooked in the literature. To our knowledge, no study has examined the influence of TWI on tree decline, specifically in arid and semi-arid regions. This index is closely correlated with multiple soil properties, including horizon depth, silt percentage, and SOC. Our results suggested that TWI was not among the significant variables, but it was one of the selected predictors in the best GAM model aiming to differentiate individual tree decline classes. Remarkably, the frequencies of the individual tree decline classes and particularly declining tree groups were higher when the TWI was lower (Figure 4.4 and Figure 4.5). Thus, this

observation supports the idea that tree decline is more likely to occur in dry regions in Zagros, but this needs to be further examined since the results were not statistically significant.

4.4.1.2. Climatic variables

Shiravand and Hosseini (2020) identified climate factors related to oak tree dieback in a part of the central Zagros region. They found humidity, temperature, and precipitation to be the primary variables with a substantial impact on tree dieback. This is also in line with our results, in which the precipitation variable was selected in all of the best GAM models as an influential variable among four classes of individual tree decline, as well as in the fourth best GAM model as an influential variable among two tree group decline classes. Moreover, bioclimate-16 showed significant differences among the four tree decline classes (p-value = 0.02). The relationship between decline levels and precipitation was initially slightly negative but then turned into a positive relationship once precipitation increased to higher levels (Figure 4.6). While this may seem counter-intuitive at first, it may be related to higher use intensities in regions with higher precipitation, as humans may settle preferably in areas where more water is available. However, this hypothesis has to be verified with additional investigations. Alternatively, higher elevations (that are also characterized by higher precipitation) may be strongly affected by climate change and therefore show a stronger occurrence of decline. It is also worth considering that the spatial resolution of the Bioclim variables is quite coarse, covering roughly 1 to 2 km per grid cell. This means that all trees within a single tree group (and, in some cases, even in multiple tree groups) are likely to have the same Bioclim values. Therefore, the results presented here should not be over-interpreted given the relatively small overall study area of less than 165 km^2.

4.4.1.3. Soil

Soil is another important factor that needs to be considered to understand forest and tree decline, especially in arid and semi-arid areas. When analyzing tree group decline classes using GAM, we found that SOC emerged as one of the most important variables, particularly among tree groups (being selected and significant in all up to the fifth-best models) and even in the individual tree decline classes (being among the variables selected in the third-best model). In tree groups of decline, SOC was statistically significant, with a p-value of 0.04. Notably, higher SOC values were observed in the non-declining class in comparison to the declining classes (Figure 4.5). This could be because the presence of SOC contributes to enhancing soil structure, which, in turn, increases the soil's water-holding capacity, as suggested by Zhao et al. in 2022b. A fairly similar trend was observed for soil moisture, although no statistically significant differences were identified in comparisons among the declining groups.

In a study in the semi-arid forests of China, Zhang et al. (2023) pinpointed climate and soil factors as the dominant and constraining factors influencing how vegetation responds to drought. In the tree group analysis, silt content was among the selected variables of the best GAM model, while it was influential in the second-best class at the individual tree decline level. However, it was

not significant. Also, clay content was among the influencing factors of the best GAM model for different tree groups of decline (as one selected predictor of the third-best model, p-value = 0.9). Also, for the tree group classes of decline, clay was selected in the third-best model as an influencing variable but not statistically significant (p-value = 0.9) (for more information, see Table 4.8 and Table 4.9 in Supplementary Material III).

Moreover, from the visual inspection of the soil texture results (i.e., clay, silt, and sand, see Figure 4.5), the declining tree groups were mainly found in areas with higher amounts of sand. This could be because sandy soils are not able to hold enough water, increasing the likelihood of soil drought in a region like Zagros. In contrast, fine soils containing a higher proportion of silt and clay have a higher capacity to hold water (Giap et al., 2021). The results indicated that the non-declining trees were more frequently found in areas with relatively higher amounts of silt (Figure 4.4 and Figure 4.5) which would confirm the assumption that trees in the Zagros region survive better on soils with better water-holding capacity (e.g., Žížala et al., 2019). It is important to acknowledge that the spatial resolution of the soil dataset used in our study, with a pixel size of approximately 250 m, is coarser than the scale of other predictor variables in our study. This difference in resolution could potentially limit the interpretability of our results and should be taken into consideration. Furthermore, it is worth noting that the digital soil mapping product used may not have undergone evaluation specifically for the Zagros area. The validation of digital soil mapping products is crucial (e.g., Döpper et al., 2022) due to potential variations in soil properties influenced by topography, geology, and vegetation. Thus, future research should include a focus on local soil characterization and validation to prevent potential inaccuracies in the analysis. This could involve field surveys, soil sampling, and laboratory analyses to create a reliable soil dataset tailored to the Zagros region. These efforts would improve the accuracy and usefulness of soil data for forest and tree decline analysis research.

4.4.1.4. Tree density

Reduced growth rates in trees facing competition from neighboring trees (i.e., on a 5-m neighborhood scale) can jeopardize the survival of trees in arid and semi-arid ecosystems (Dohn et al., 2017). Tymi'nska-Czaba'nska et al. (2022) found that the probability of tree mortality is notably impacted by stand density. However, this observation confirms the patterns seen in denser forests, where light plays a central role as a limiting factor for tree growth, sparking active competition among trees for sunlight (e.g., Dormann et al., 2020). Hosseini et al. (2017) surprisingly observed increased tree mortality rates in regions of the patchy semi-arid Zagros area characterized by higher tree density and shallow soils. This occurred despite the trees being widely spaced with ample access to light, making the presence of competition in this context unexpected. Even if we did not find any significant results, the visual interpretation (Figure 4.5) of the density plots for forest density was different for our study. We found more declining tree groups at lower forest densities in the individual tree decline classes as well as in the tree groups (12–17% cover). The cause of this may be attributed to either the decline itself, which leads to a reduction in tree cover, or to

119

higher stress levels caused by reduced shading from neighboring trees or by more challenging site conditions. The importance of site conditions in oak tree decline was also emphasized in previous studies (e.g., Haavik et al., 2015). Therefore, competition does not seem to be a significant factor in our study area, as contrary to previous studies on tree competition in other ecosystems or regions (e.g., Ozendaal et al., 2020; Dohn et al., 2017; Hosseini et al., 2017).

4.4.1.5. Illumination

Illumination, as a combination of topography and sun position, may affect the decline of forests and trees by influencing irradiation and possibly evapotranspiration rates. Illumination is often disregarded in literature. To our knowledge, no study has investigated the impact of illumination as a contributing factor to tree decline, particularly in arid and semi-arid regions. We examined this factor in our analysis, but it was not statistically significant in the overall analysis. However, we observed a higher prevalence of the declining tree group classes in well-illuminated areas, potentially due to higher drought and water scarcity resulting from increased illumination and decreased shading. Also, IC was selected as an important predictor in some of the best GAM models but was not statistically significant. Given that illumination is an integrated variable that combines slope, aspect, and sun position, it may further increase its significance if other topographical variables are not integrated into the model.

4.4.2. Tree characteristics

There was no significant difference in tree height as well as DBH (i.e., tree age) between declining and non-declining individual trees or tree groups. However, in our analysis before examining the spatial autocorrelation, the DBH showed significance in the GAM models (p-value = 0.0008) fitted for tree group decline classes. In general, both tree height and DBH had low p-values. However, the p-value of DBH was always lower, showing more significance compared to tree height. Additional, more detailed information on site conditions or forest growth rates (i.e., tree ring analysis) would be required to fully understand this result.

In contrast to our research, tree heights, and DBH have been identified as significant factors in studying forest decline (e.g., Tymi'nska-Czaba'nska et al., 2022; Etzold et al., 2019; Schroeder, 2010; Akkuzu et al., 2009). Etzold et al. (2019) found that older and larger trees (larger DBH) experienced an increase in mortality in Swiss forests, while smaller trees (smaller DBH) tended to have lower mortality rates. The findings of Etzold et al. (2019) align with Shifley et al. (2006), who demonstrated that the most valuable risk factors for predicting oak mortality at the stand level in the temperate forests of the Missouri Ozark Highlands were typically related to the crown class and diameter of individual oaks. Oaks with a DBH greater than 25 cm, including the black and scarlet oak species, exhibited increased mortality rates. Additionally, Assal et al. (2016) conducted a study within the semi-arid Wyoming Basin ecoregion, indicating that a greater number of larger trees (DBH > 20 cm) experienced higher mortality rates. However, a significant number of small and medium-sized trees also showed signs of mortality. In semi-arid Zagros forests, the literature

indicates widespread documentation of severely declining or dead Persian oak trees belonging to different size classes. A wide range of tree sizes was examined (DBH from around 5 to 75 cm). However, among these classes, the highest occurrence of such incidents was found in trees within the DBH range of 15–25 cm (the highest dead trees). This observation was reported by Hosseini et al. (2017), who emphasized the significance of DBH in Persian oak mortality dynamics. Furthermore, Colangelo et al. (2017) showed that smaller trees in partly similar Mediterranean areas with dry summers grow slower and are at a higher risk of mortality than larger trees. They concluded that there is a negative correlation between the size of the tree, whether in height or diameter, and the probability of tree mortality. The study highlights the complex interplay of factors affecting tree survival, noting that in arid regions, forest areas with fewer trees tend to experience higher mortality rates. Meanwhile, a study on Mediterranean oak forests found that declining trees had reduced height and radial growth rates compared to their non-declining counterparts (Ripullone et al., 2020).

Baguskas et al. (2014) noted that taller trees intercept more fog than smaller trees in south-central California, featuring a Mediterranean climate, which counteracts drought stress and improves survival rates. They pointed out that the increased vulnerability of trees could be due to their smaller root-to-shoot ratio in contrast to larger trees, which may limit their access to deeper soil water reserves. These findings suggest that tree characteristics, particularly tree height, are not reliable indicators across multiple sites and ecosystems since the findings in the literature are highly variable (Sherwood et al., 2021).

4.4.3. Spectral analysis of bare soil using S2

We observed higher values across almost all the S2 bands for every season within non-declining regions compared to the declining ones (see Figure 4.8). This observation poses a challenge in the interpretation given the expected correlation between higher soil moisture and reduced reflectance across all wavelengths (Loshelder and Coffman, 2023; Tian and Philpot, 2015). However, it is important to acknowledge that soil reflectance is influenced not solely by soil moisture but also by variables such as soil texture (sand, silt, and clay), soil surface roughness, and organic matter content. These factors are intricate variables that are interconnected (Žížala et al., 2019). As such, the complex relationship between soil texture type, water content, and spectral reflectance remains unresolved, as emphasized by Tian and Philpot (2015). In our case, we presume that soil moisture in the upper part of the soil will be very low, particularly during spring, summer, and parts of autumn. Hence, the observed higher reflection values of non-declining areas within this temporal range are most likely related to finer grain sizes. This would be plausible since finer grain sizes may indicate a better water-holding capacity in these areas and would also corroborate our results related to the soil variables from the SoilGrids dataset, where we observed higher sand fractions for the declining forest patches. The partly reversed trend observed for winter, on the other hand, may at least partly relate to increased surface soil moisture, given that more precipitation is expected for these months.

4.5. Conclusion

In this study, we examined a range of factors that may contribute to the decline of semi-arid Zagros forests, including environmental variables and the characteristics of trees at both individual and group levels. Our findings reveal several important insights: 1) Environmental factors, such as slope and precipitation (measured using bioclimate-16), were found to be related to the decline, particularly at individual tree levels. 2) Within the context of forest decline among tree groups, soil variables, specifically SOC, emerged as an important factor, followed by soil silt and clay content. 3) DBH and tree height were not related to tree decline. 4) Additionally, we performed a spectral analysis on bare soil in areas where forest decline was observed and compared them to areas without signs of decline. Our analysis consistently demonstrated decreased spectral values in all 10 S2 bands utilized in bare soils within areas experiencing decline compared to non-declining areas. The VNIR-3, SWIR-2, red, green, and blue bands of S2 demonstrated significant differences (performed by the Wilcoxon test) between the two groups of bare soil across all seasons. We hypothesize that these differences in reflectance values are related to differing dominant grain sizes in the soils, which are known to also determine the water-holding capacity of the soils.

This study enhances our comprehension of the intricacies related to the decline of trees and forests in the semi-arid Zagros region. It highlights the significant role played by environmental factors as well as introduces the spectral analysis of bare soil for decline assessment in semi-arid regions, which may contribute to a better understanding of the spatial variability of forest decline in the region. While the selected variables were consistent with general expectations and previous research, it remained difficult to get a clear picture of the direct drivers based on observed relationships between environmental factors and tree decline, stressing the need for further research. For future studies, we recommend exploring the use of a higher-resolution DEM, such as TanDEM-X at 12 m, to enhance the quality of topographical variables that have been shown to play a very important role in tree and forest decline. Additionally, when dealing with a relatively small study area like ours (approximately 165 km^2), it is recommended to obtain more refined soil and climate data, possibly connected with additional field surveys, which may enable a more comprehensive understanding of tree decline. Moreover, expanding field sampling to other Zagros sub-regions can provide a more comprehensive understanding of forest decline in the entire Zagros.

Acknowledgment

4.6. Supplementary Materials III

The covariation between the examined environmental variables

In order to uncover the relationships or correlation between the examined environmental variables, we created correlation plots using the corrplot function in R (Figure 4.9) for both response variables (individual tree and tree group decline classes). Notably, we observed that FC and IC exhibited a negative correlation of approximately 43% among tree groups and 53% among individual tree classes. Bioclimate-16 and aspect also displayed relatively high negative correlations, standing at 78% and 46% among tree groups and individual tree classes, respectively. Hillshade and IC showcased a positive correlation exceeding 80% in both correlation plots, which is not surprising since both variables are derived from DEM. Furthermore, hillshade and soil water content demonstrated a substantial negative correlation of -65% and -39 among individual tree and tree group classes, respectively. Among the soil variables included in both correlation plots, clay, and sand stood out with the most prominent positive and negative correlations with precipitation (bioclimate–16), exceeding 50% in magnitude, respectively.
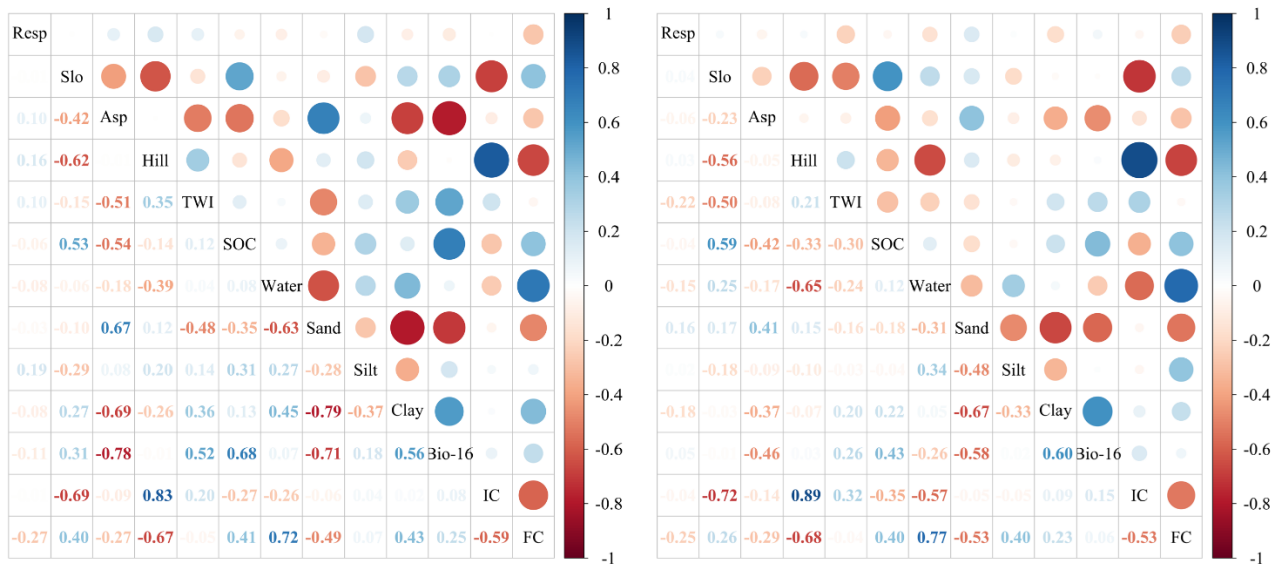
Figure 4.9 Correlation plots (from left to right) of tree groups and individual tree decline to environmental factors (including the response variables (resp), slope (slo), aspect (Asp), hill shading (hill), TWI, SOC, soil-water content (water), sand, silt, clay, bioclimate-16 (bio-16), IC, and FC).

<u>Distribution of the examined variables based on declining and non-declining individual trees</u>

The box plots compare the values of several variables across different individual tree decline classes (the non-declining class is called "healthy", the slightly declining class is called "low", the moderately declining class is called "moderate" and the severely declining class is called "severe."
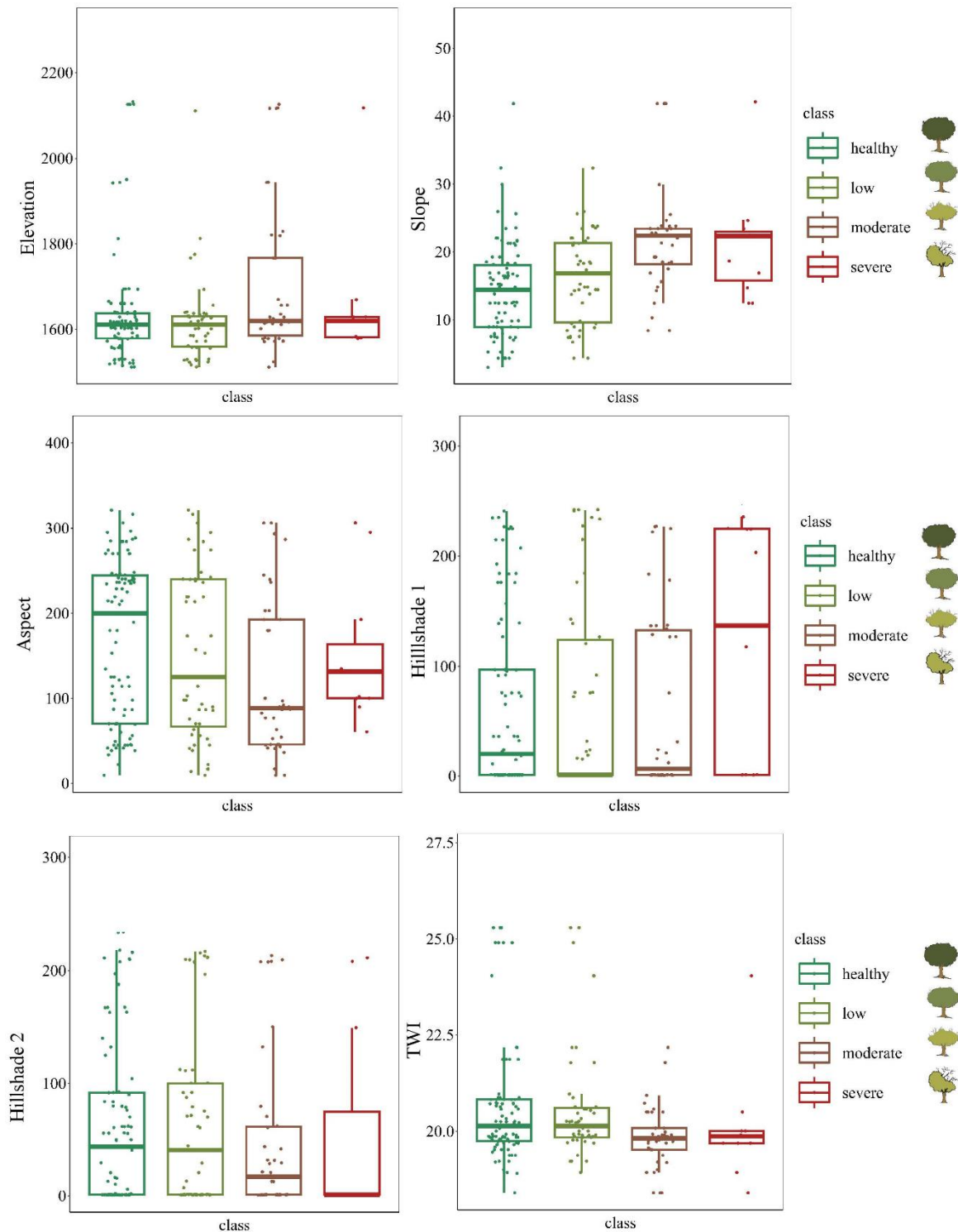
Figure 4.10 Boxplots: comparing values of topographical variables across different individual tree decline classes (The settings of the calculated hill-shading (i.e., Sun's elevation and azimuth) were taken from the PlanetScope images of September (hillshade 1) and February (hillshade 2)
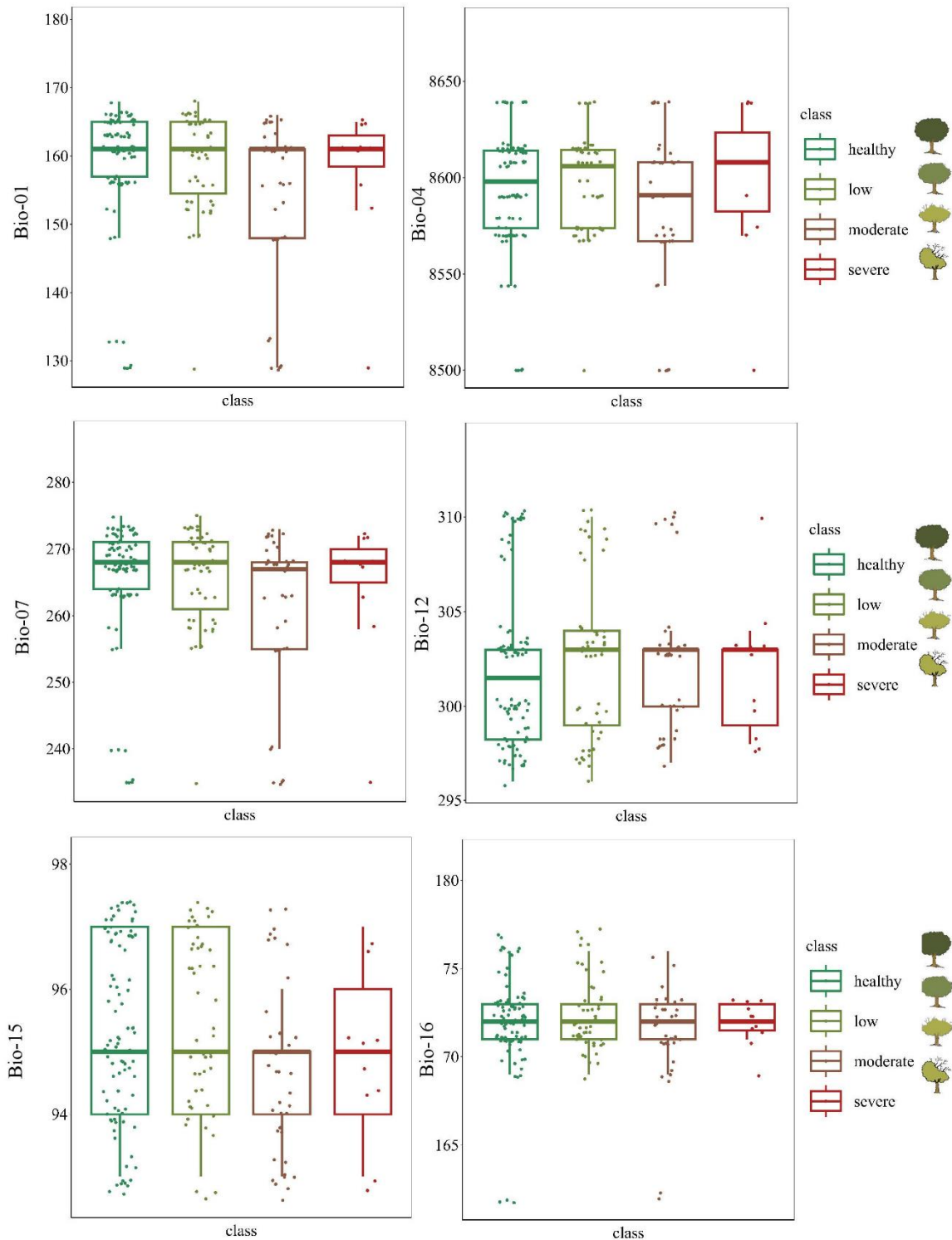
Figure 4.11 Boxplots: comparing values of climatic variables across different individual tree decline classes (since the results of bioclimate-07 (bio-07) and -10 were very similar, we only showed the bioclimate-07)
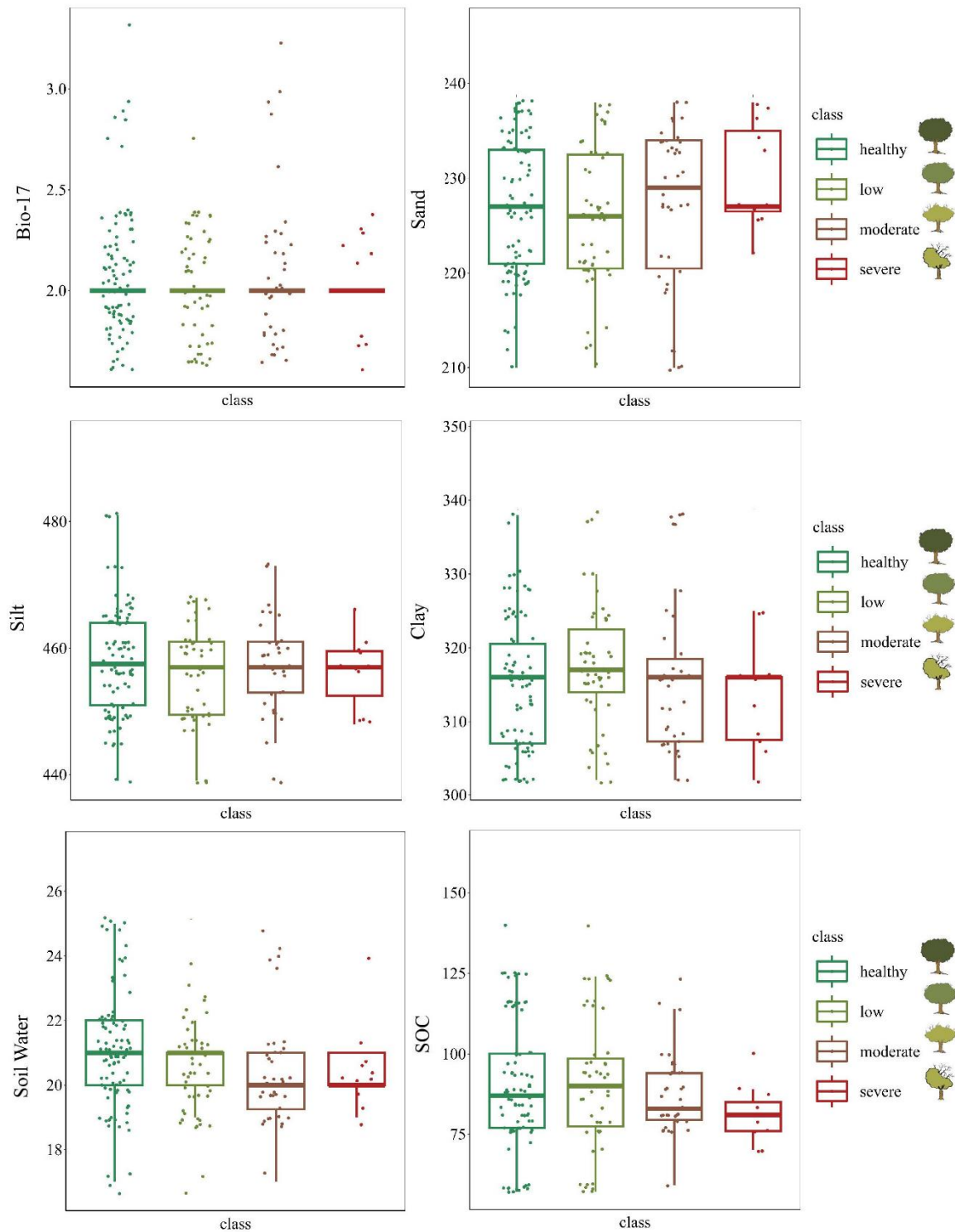
Figure 4.12 Boxplots: comparing values of climatic variable (i.e. Bioclimate-17) and soil variables across different individual tree decline classes
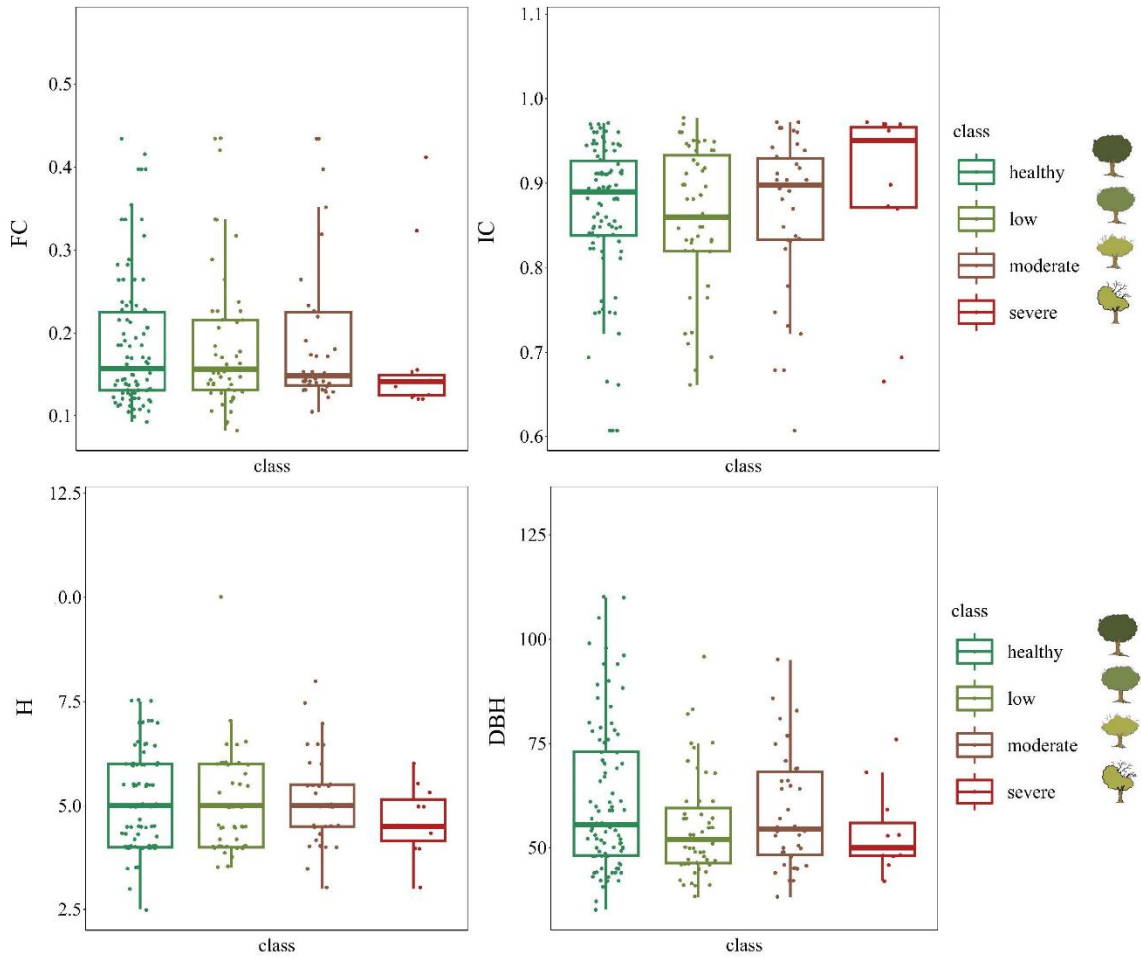
Figure 4.13 Boxplots: comparing values of FC, IC, H, and DBH across different individual tree decline classes

Statistical analysis

GAM

Some of the results of the best GAM models for non-significant variables are shown in Figure 4.14 and Figure 4.15.
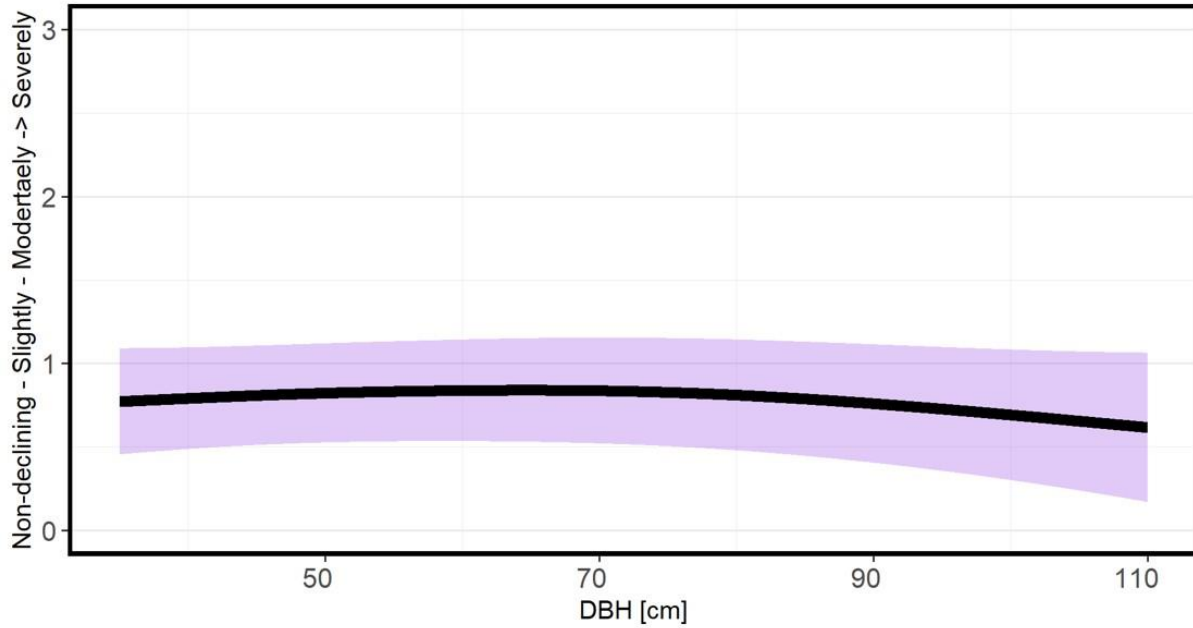
Figure 4.14 The selected non-significant variable (DBH) of the best GAM model across different individual tree decline categorical classes. The lower y-axis (response) values indicate a lower level of decline.
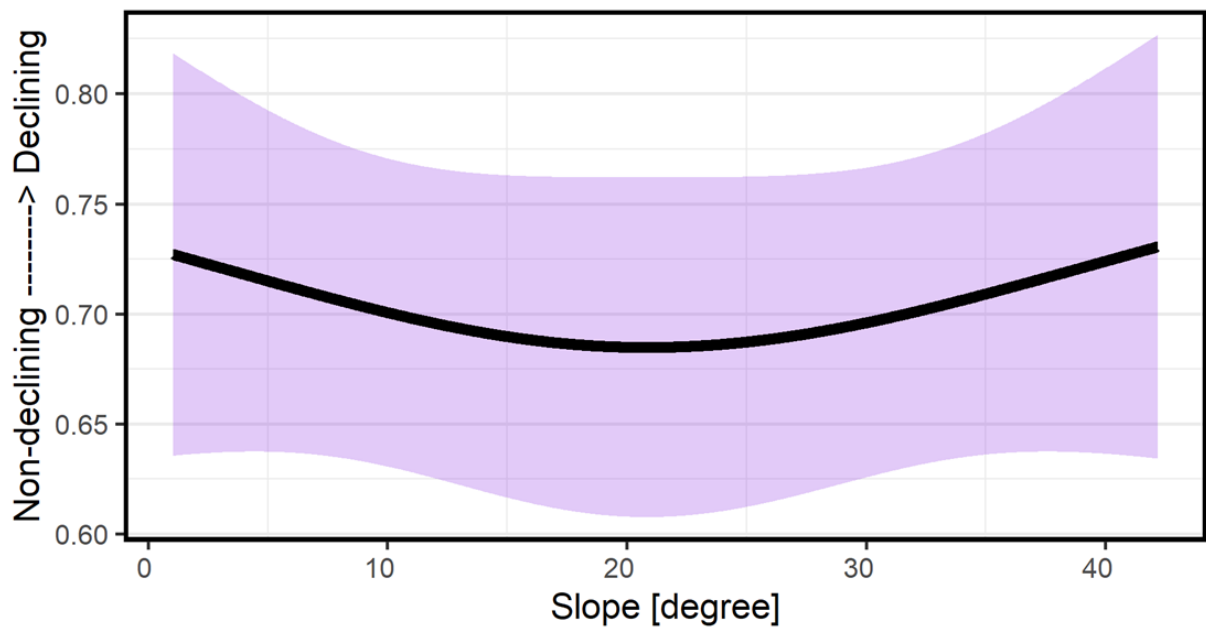
Figure 4.15 The selected non-significant variable (slope) of the best GAM model across different tree group binary classes. The lower y-axis (response) values indicate a lower level of decline.

Detailed information on the best GAM models (the first five) with the lowest AIC is shown in Table 4.8

Table 4.8 The outcomes of the five best GAM models: environmental variables as predictors using individual tree classes (the significant variables are bold and denoted with asterisks).

Model Number	AIC	Variable	Effective degrees of freedom	p-value
1	AIC: 411.7040	Slope	2.080e+00	**0.009***
		TWI	8.747e-05	0.8
		Bioclimate-16	1.467e+00	**0.02***
2	AIC: 411.7044	Slope	2.080e+00	**0.009***
		Silt	1.268e-04	0.6
		Bioclimate-16	1.467e+00	**0.02 ***
3	AIC: 411.7047	Slope	2.080e+00	**0.009***
		SOC	1.461e-04	0.8
		Bioclimate-16	1.467e+00	0.02
4	AIC: 411.7049	Slope	2.080e+00	**0.009***
		Hillshade	1.909e-04	0.8
		Bioclimate-16	1.467e+00	**0.02 ***
5	AIC: 411.7054	Slope	2.080e+00	**0.009***
		Aspect	1.834e-04	0.4
		Bioclimate-16	1.467e+00	**0.02 ***

Table 4.9 The outcomes of the five best GAM models: environmental variables as predictors using tree group classes (the significant variables are bold and denoted with asterisks).

Model Number	AIC	Variable	Effective degrees of freedom	p-value
1	AIC: 45.59518	Slope	6.424e-01	0.1
		SOC	8.443e-01	**0.04***
		Silt	6.780e-06	0.9
2	AIC: AIC: 45.59518	Slope	6.424e-01	0.1
		Aspect	9.852e-06	0.6
		SOC	8.443e-01	**0.04 ***
3	AIC: AIC: 45.59519	Slope	6.424e-01	0.1
		SOC	8.443e-01	**0.04***
		Clay	9.341e-06	0.9
4	AIC: 45.5952	Slope	6.424e-01	0.1
		SOC	8.443e-01	**0.04***
		Bioclimate-16	1.493e-05	0.6
5	AIC: 45.59521	Slope	6.424e-01	0.1

		Hillshade	9.959e-06	0.4
		SOC	8.443e-01	**0.04***

GEE scripts

S2 data

https://code.earthengine.google.com/9129c63509509d1563530d32cbe5d215

Bioclim data

https://code.earthengine.google.com/993713a946f36488f05e9a1d48c8f6da

TWI

https://code.earthengine.google.com/30338b1d044e39068acf0861c9000fc4

IC

https://code.earthengine.google.com/cef723b924827d7f73cb25b92ae07186

5. Synthesis and outlook

5.1. Synthesis

5.1.1. Research summary

Forest decline is a global phenomenon, also affecting trees in fragile arid and semi-arid ecosystems. Thus, it is essential to improve methods that enable the detection, mapping, and understanding of this phenomenon, especially in arid and semi-arid areas where RS faces limitations due to very bright soil backgrounds and cast shadow effects. This thesis established a baseline in remote sensing-assisted forest decline studies by 1) presenting a workflow to estimate FC employing purely remotely sensed data (devoid of field data) as a preliminary step to detect forest decline, 2) documenting the challenges of global FC products in arid and semi-arid regions, in which they serve as input for several environmental studies without being properly validated, 3) examining various time-series methods on Landsat images to identify forest decline and discussing the obstacles related to detecting and mapping forest decline in arid and semi-arid forests, and 4) conducting a driver analysis to examine the causes of forest decline in a specific area of the Zagros forests in order to gain greater insight into the contributing factors. As part of the driver analysis, the spectral values of the bare soil within both declining and non-declining tree groups were analyzed using S2 imagery.

5.1.2. Research questions

5.1.2.1. Is it possible to use S2 and VHR imagery to map FC for the vast semi-arid Zagros forests? How does the spatial grain of the S2 in the analysis affect the model quality?

In the second chapter of this thesis, the capability of S2 imagery to map FC in the extensive Zagros region using RF regression was evaluated. The result of this chapter demonstrated the unreliability of global FC products in arid and semi-arid areas. For example, Hansen's global FC product showed an enormous underestimation of the FC of the Zagros region. This is only one example that shows that the accurate quantification of woody cover from satellite imagery over arid and semi-arid ecosystems with sparse vegetation cover (Soleimannejad et al., 2018; Yang et al., 2012) and often limited amounts of field reference data (Bai, 2010) remains a challenge. For instance, Fagan (2020) indicates that the use of the current global FC product for estimating the afforestation potential in arid and semi-arid areas may lead to a significant overestimation as the true FC is substantially underestimated. Through their study in arid areas with VHR imagery, Bastin et al. (2017)

demonstrated that the global tree cover products might show 40–47% lower FC than the actual cover of global drylands. The findings of the first study (Chapter 2) were also consistent with prior research (Fagan, 2020; Smith et al., 2019; Bastin et al., 2017) on underestimation of the global FC data (i.e., Hansen Global FC and TanDEM-X) in arid and semi-arid areas like Zagros. Before this background, the first study presented a workflow that combines VHR images from Google Satellite and Bing Map with S2 satellite data to create a reliable FC map for the vast semi-arid Zagros forests. This workflow is particularly valuable because it does not necessitate expensive in-situ data collection. It is straightforward and not time-consuming to implement and can prove beneficial for estimating FC in other semi-arid areas.

Another objective of the second chapter was to examine how the spatial grain of the analysis affects the quality of the FC model. The S2 bands at 10 m pixel size were initially used, followed by model runs with downscaled S2 data with pixel sizes ranging from 20 to 120 m in spatial resolution. The results showed a decrease in RMSE and an increase in R^2 from 10 to 60 m pixel sizes. This model improvement at a coarser spatial grain matches our expectations and is in line with the findings of previous studies that discussed that coarser resolution resulted in the highest model accuracy in FC mapping (e.g., Korhonen et al., 2017 in boreal forests, and Higginbottom et al., 2018 in semi-arid forests). The tendency of the models to perform better at coarser spatial grain may relate to at least two aspects: First, potential co-location errors between S2 and VHR imagery at the sub-pixel scale have less influence at coarser grain. Second, by increasing the spatial grain of the analysis, the number of extreme values in the reference data (very high and very low woody cover estimates) will decrease.

According to the results of VSURF-based variable selection, the most frequently selected predictor variables included NDVI, bioclimate-12 (annual precipitation), and bands from the visual part of the spectrum. This is partially in line with findings by Higginbottom et al. (2018), who identified B3 as the second-best individual S2 band for monitoring canopy properties in patchy woody vegetation in South Africa. Heckel et al. (2020) and Waśniewski et al. (2020) reported that the bands within the visible spectrum significantly aid in estimating FC. The RSR index was one of the important predictors in all the models. This alignment with previous studies that investigated comparable target variables (e.g., Brown et al., 2000; Zhu et al., 2010) highlights the significance of the RSR index. Earlier studies proved that climatic variables are important for mapping woody vegetation and can improve RS models (e.g., Liu et al., 2017; Brandt et al., 2018). Based on the results of this study, the precipitation variables (bioclimate-12, -15, -16) appeared in almost all models.

Thus, the first study holds importance in its ability to detect and map FC, a crucial aspect for assessing forest ecosystem health, as described by Wang and Cochrane (2005). Additionally, this study highlights the existing issues with global FC products, which serve as input for multiple environmental studies but lack proper validation.

5.1.2.2. Are established trend analysis approaches (i.e., RF, anomaly detection, and Sen's slope) that have been successfully used to identify and map forest disturbances and decline in other ecosystems also suitable for semi-arid areas?

The second study (Chapter 3) sought to examine whether established approaches that have been successfully used to detect and map forest decline in other ecosystems are also suitable for arid and semi-arid areas. More precisely, RF classification, anomaly detection, and Sen's slope were examined for detecting and mapping forest decline in the Zagros forests. In this research, the RF model demonstrated superior accuracy compared to the other approaches. Interestingly, no notable differences in performance were observed among RF models trained with Landsat data from different time periods (i.e., 1986–2021, 2000–2021, and 2010–2021 years), despite the reference data being collected in 2021 and 2022. This observation was unexpected, as it was expected that utilizing more recent data would lead to better results. According to local experts and the previous literature (e.g., Yaghmaei et al., 2021), the widespread decline of oak in the study area only arose after 2010. This suggests that the subtle spectral differences that were utilized to differentiate between declining and non-declining areas in this study may not relate to changes in the spectral signal caused by the forest decline but rather to general differences in site conditions. This may be related to environmental factors such as varying soil conditions, topography, or their combination.

The anomaly detection and Sen's slope approaches performed notably worse than RF in the study and only achieved marginally better results than a random classification. However, a direct comparison between RF and the other two approaches is infeasible because these analyses employ distinct methodologies, particularly those involving input data and validation. For model training, RF utilizes a supervised classification method that involves a portion of the reference data (70% of all reference data). However, in both the anomaly analysis and Sen's slope approach, reference data only serves the purpose of validation and accuracy assessment. Therefore, the better performance of RF is somewhat anticipated owing to the significantly higher number of predictors in comparison to the other two tested approaches that rely on a single VI.

Moreover, in the third Chapter, the results showed that the type of VI matters a lot for tree decline analysis. In all the applied time series approaches, NDMI performed better than other VIs like NDVI and GNDVI, which was in line with the results of Francini and Chirici (2022). NDMI is a proxy of vegetation water content and was suggested by some recent studies as a wetness index to monitor forest decline, particularly in arid and semi-arid regions (e.g., Moreno-Fernández et al., 2021; Marusig et al., 2020). The NDMI is calculated using both NIR and SWIR bands, both of which are known to be directly related to key vegetation properties and are frequently reported to be important predictors in studies examining vegetation dynamics using satellite data (e.g., Meyer et al., 2019). Further studies by Li et al. (2022), Gu et al. (2008), and Wang et al. (2007) also highlighted the high relevance of SWIR bands for detecting forest decline. The results of the second study further highlight the challenges of RS-based products in arid and semi-arid regions. Some forest decline processes may lead to structural changes below the tree canopy, which are challenging to detect from above. Furthermore, biomass losses may not always correspond

135

accurately with changes in the canopy cover (Gao et al., 2020). In arid and semi-arid regions, these challenges can be exacerbated by the fact that the spectral signal relating to tree cover is heavily influenced by the formation of mixed pixels with bright soil backgrounds (Wang et al., 2022; Maier et al., 2022). The issue of bright soil backgrounds was addressed to some extent by utilizing blue bands along with VIs such as GLI and ARVI. Since the blue band can be informative for discriminating between soil and vegetation. However, it is evident that the corresponding correction is not flawless. Therefore, detecting forest decline in mountainous and semi-arid regions via medium-resolution RS poses multiple challenges, which have been spcifically addressed in only a limited portion of the existing literature (e.g., Wang et al., 2022; Maier et al., 2022).

This study advances forest decline detection through RS in sparsely forested mountainous ecosystems. It addresses challenges and offers recommendations for overcoming them, emphasizing the importance of identifying decline hotspots and prioritizing conservation efforts, as highlighted in Moradi et al. (2021).

5.1.2.3. What are the main drivers of forest and tree decline in Zagros forests? Is there a notable or significant difference in the spectral values of bare soils between declining and non-declining tree groups using S2?

The third study of this thesis (Chapter 4) focused on the analysis of a number of potential drivers of tree decline in part of the Zagros region. Among the examined topographical variables, a strong association between slope and individual tree decline classes (i.e., non-declining, slightly declining, moderately declining, and severely declining) was observed, with the highest tree decline occurring in areas with medium slope values. Additionally, slope consistently emerged as an influential factor in all the GAM models. Thus, a significant difference was observed in slope values between declining and non-declining individual trees (with a p-value of 0.009). These findings align with previous research (e.g., Ewane et al., 2023; Parvaneh et al., 2015; Solaymani and Jabbari, 2015) on various ecosystem types. In the semi-arid Wyoming Basin ecoregion, Assal et al. (2016) demonstrated that high elevations and northern slopes had a notable effect on tree mortality during droughts. In another study conducted in the Zagros area, Nourinejad and Rostami (2014) found a significant correlation between slope and oak decline. They pointed out that slope, in conjunction with aspect, plays a crucial role in controlling solar irradiation and, consequently, impacts water availability and tree transpiration.

The results of Chapter 4 showed that aspect was also an influential variable among the best models (third best) of tree group classes (i.e., declining and non-declining). However, it was not statistically significant in any of the selected models. Moreover, hillshade did not exhibit a statistically significant association with the various levels of decline. However, it was among the fourth and fifth best models in the GAM models of individual tree and tree group classes of decline, respectively. These results partially align with the findings of Najafifar et al. (2019) in Zagros forests, who indicated that forest dieback was more prevalent in areas with less shading, underscoring the substantial influence of hillshade on the drying conditions for oak trees. TWI was

another topographical factor that did not emerge as a statistically significant variable. However, it was included as one of the selected predictors in the best GAM designed to distinguish between individual tree decline classes. Interestingly, the frequencies of tree decline classes were higher in areas where the TWI was lower. This observation indicates a higher likelihood of tree decline in the drier regions of the Zagros area, although further investigation is necessary in the future.

Concerning the climatic variables, Shiravand and Hosseini (2020) found temperature and precipitation to be the primary variables with a substantial impact on tree dieback. This is also in line with the results of Chapter 4, where the precipitation (of the wettest quarter) was selected in a number of the best GAM models as an influential variable among classes of individual trees (p-value = 0.02) and tree group decline. According to the GAM results, the relationship between decline levels and precipitation (bioclimate-16) initially shows a slight negative correlation. However, this correlation becomes positive as precipitation levels increase. While this may initially appear counter-intuitive, it could be attributed to higher human settlement and activity in areas with greater precipitation, as people may naturally prefer regions with more water availability. Alternatively, higher elevations (that are also characterized by higher precipitation) may be strongly affected by climate change and therefore show a stronger occurrence of decline.

Moreover, soil variables, particularly SOC, emerged as the primary influential factors in forest decline. This finding suggests that the primary factor contributing to tree decline is the availability of water after the vegetation season. Moreover, tree decline appears to be mitigated when soil conditions enhance their capacity to retain water, thus highlighting the critical role of soil properties in this context. In tree groups, SOC was statistically significant, with a p-value of 0.04. Notably, higher SOC values were observed in the non-declining class in comparison to the declining classes. This could be because the presence of SOC contributes to enhancing soil structure, which, in turn, increases the soil's water-holding capacity (Zhao et al., 2022b). In a study in the arid and semi-arid forests of China, Zhang et al. (2023) pinpointed climate and soil factors as the dominant and constraining factors influencing how vegetation responds to drought. The results of the third study of this thesis show that silt was among the selected variables of the best GAM models, both at individual tree and tree group classes of decline. However, it did not attain a significant result. Also, clay was among the influencing factors of the best GAM model for different tree groups of decline (as one selected predictor of the third-best model).

Additionally, the declining tree groups were primarily located in areas with higher sand content based on soil texture analysis (i.e., clay, silt, and sand). This may be due to sandy soils' inadequate water retention capabilities, resulting in increased susceptibility to soil drought in the Zagros region. Conversely, soils with a higher proportion of silt and clay have a greater capacity to retain water, as indicated by previous research (e.g., Giap et al., 2021). The study found that non-declining trees were located in areas with higher levels of silt, supporting the hypothesis that trees in the Zagros region thrive on soils with good water retention (Žížala et al., 2019).

Moreover, FC was examined in this study, where the analysis did not reveal any statistically significant results. However, when visually interpreting the density plots for FC in the study area,

clear differences were noticed compared to previous research conducted in the Zagros region. In a study by Hosseini et al. (2017), higher FC was associated with increased tree mortality, even though the trees in those areas had ample access to light. The examination of the results from Chapter 4 showed that more declining trees were found in areas with lower forest densities, covering 12–17% of the area. This suggests that competition might not be a significant factor in the study area, in contrast to findings in previous studies on tree competition (e.g. Ozendaal et al., 2020; Dohn et al., 2017; Hosseini et al., 2017).

The IC, as another examined factor, was not statistically significant among different decline classes. However, it was selected as an important predictor in some of the best GAM models, where a higher prevalence of the declining tree group classes in well-illuminated areas was observed. This could be potentially due to higher drought and water scarcity resulting from increased illumination and decreased shading in these areas. Given that illumination is an integrated variable that combines slope, aspect, and sun position, it may further increase its significance if other topographical variables are not integrated into the model.

When looking at tree characteristics, we did not find any significant differences in tree height or DBH (which indicates a tree's age) between declining and non-declining individual trees or tree groups. However, it is worth noting that, before correcting for spatial autocorrelation, the DBH showed significance in GAM fitted for tree group decline classes (p-value = 0.0008), which suggests that more research is needed to confirm these observations.

Taking into account the results of Chapter 4 in this thesis and these observations, it becomes clear that tree characteristics, especially tree height, lack consistent reliability as indicators across various sites and ecosystems due to the considerable variability found in the literature (Sherwood et al., 2021).

In addition to the decline driver analysis, Chapter 4 included a spectral analysis which was performed on bare soil in areas where forest decline was observed and compared to areas without signs of decline. Consistently, decreased spectral values were demonstrated in ten S2 bands utilized in bare soils within areas experiencing decline compared to non-declining areas. The VNIR-3, SWIR-2, red, green, and blue bands of S2 showed significant differences (as confirmed by the Wilcoxon test) between the two groups of bare soil across all seasons. It is hypothesized that these differences in reflectance values are mostly linked to variations in the dominant grain sizes in the soils, which also affect soil water-holding capacity. This observation poses a challenge in the interpretation given the simultaneously expected correlation between higher soil moisture and reduced reflectance across all wavelengths (Loshelder and Coffman, 2023; Tian and Philpot, 2015). However, it is important to acknowledge that soil reflectance is influenced not solely by soil moisture, but also by variables such as texture, surface roughness, and SOC, among others. These factors are complex, diverse, and interconnected (Žížala et al., 2019).

Chapter 4´s findings show that improved soil water retention helps alleviate tree decline. Despite some remaining gaps, this research aligns with expectations and previous studies, enhancing our understanding of the complex link between environmental factors and tree decline.

This study may contribute to effective mitigation strategies, forest sustainability, and policymaking (Anderegg et al., 2012).

5.2. Outlook

This thesis delves into RS applications in semi-arid regions to study forest decline. Yet there is still a broad spectrum of factors potentially affecting decline that still remains unexplored. This underscores the need for additional research. In this concluding section, we identify avenues to enhance our understanding of the challenges facing Zagros forests.

When studying arid and semi-arid areas and their forest decline through RS, future research should explore technical improvements to overcome potential challenges that might affect study results. An often-overlooked factor is the impact of tree shadows on spectral signals, which can negatively affect data quality and influence vegetation monitoring. In low-density forests, this issue can introduce signal biases and affect interpretation. To address this, researchers have proposed shadow removal algorithms, such as those by Larsen and Salberg (2010). Therefore, introducing algorithms to measure and correct cast shadow effects could enhance the accuracy of mapping and characterizing sparse arid and semi-arid forests using RS, as highlighted by Ghasemi et al. (2023). Another technical issue is that Landsat archives exhibit spectral band offsets between Landsat 4-7 and 8, causing minor spectral discrepancies unrelated to actual forest changes. Landsat 8's red, NIR, and SWIR bands are narrower than their 4–7 counterparts (Maier et al., 2022). Ideally, all satellite images should use consistent technology and acquisition conditions, including uniform solar positioning. Since retroactive standardization is impractical, one solution to mitigate these variations in the time series analysis is applying correction factors through radiometric calibration, geometric correction, atmospheric correction, and data fusion.

Monitoring forest decline in arid and semi-arid ecosystems through multispectral VIs is currently limited (David et al., 2022). Some studies have reported weak connections between NDVI and the canopy in arid and semi-arid forests (David et al., 2022). Also, VIs like the NDMI and the GLI are more proficient in detecting subtle shifts in spectral patterns within arid and semi-arid forests than other indices. Studies indicate that NDMI has proven effective in forest decline detection in arid and semi-arid regions, as notified by Francini and Chirici (2022) as well as in the third chapter of this thesis. Therefore, there is a need for refining specific vegetation indices tailored for the Zagros region. This issue received only limited attention in previous literature (e.g., Fakhri et al., 2022).

Based on the results of the third study, slope, precipitation, and SOC were among the most important variables in individual tree and forest decline occurrences. However, there are still opportunities for improving related driver analyses. For future studies, one option worth considering is the adoption of higher-resolution DEMs, such as those derived from TanDEM-X data. These approaches can significantly enhance the quality of topographical variables. Furthermore, forthcoming research endeavors could extend their field sampling efforts to

encompass additional sub-regions within the Zagros, thereby cultivating a more comprehensive comprehension of forest decline across the entire Zagros region.

Additionally, when dealing with a relatively small study area (i.e., 165 km^2), it would be worthwhile to consider obtaining more refined soil and climate data. Access to in-situ soil and climate data can enhance the accuracy of assessing tree decline. This significance becomes evident in cases like the third study, where the data used had a limited spatial resolution.

As a final remark, our field campaigns have underscored the critical necessity of addressing the management-related challenges facing the Zagros region. Issues such as illegal logging, unsustainable forest-based agriculture, and overgrazing are likely to be among the primary contributors to forest decline in this region but could not adequately be accounted for in this thesis. To combat these threats effectively, it is imperative to reduce the local people´s reliance on forests. This goal can be accomplished through an approach that prioritizes social and economic development. This multifaceted strategy encompasses the establishment of alternative income sources, enhancing educational opportunities, and launching campaigns or joint projects to increase international awareness.

Bibliography

Abdikan, S., Sanli, F. B., Ustuner, M., & Calò, F. (2016). Land cover mapping using sentinel-1 SAR data, The International Archives of the Photogrammetry. *XXIII ISPRS Congress*, *XLI-B7*.

Abdollahnejad, A., Panagiotidis, D., & Bílek, L. (2019). An Integrated GIS and Remote Sensing Approach for Monitoring Harvested Areas from Very High-Resolution, Low-Cost Satellite Images. *Remote Sensing*, *11*(21), 2539. https://doi.org/10.3390/rs11212539

Ahmadi Sani, N., Darvishsefat, A. A., Zobieri, M., & Farzaneh, A. (2007). Potentiality of aster images for forest density mapping in Zagros forests of Iran, case study: Marivan forests. *IRANIAN JOURNAL OF NATURAL RESOURCES*, *61*(3), 603–614.

Ahmadi, R., Kiadaliri, H., Mataji, A., & Kafaki, S. (2014). Oak Forest decline zonation using AHP model and GIS technique in Zagros forests of Ilam province. *Journal of Biodiversity and Environmental Sciences*, *4*(3), 141–150.

Akkuzu, E., Sariyildiz, T., Kucuk, M., & Duman, A. (2009). Ips typographus (L.) and Thanasimus formicarius (L.) populations influenced by aspect and slope position in Artvin-Hatila Valley National Park, Turkey. *Afr. J. Biotechnol*, *8*, 877–882.

Alibakhshi, S., Hovi, A., & Rautiainen, M. (2019). Temporal dynamics of albedo and climate in the sparse forests of Zagros. *Science of The Total Environment*, *663*, 596–609. https://doi.org/10.1016/j.scitotenv.2019.01.253

Anchang, J. Y., Prihodko, L., Ji, W., Kumar, S. S., Ross, C., Yu, Q., Lind, B., Sarr, M. A., Diouf, A., & Hanan, N. P. (2020). Toward Operational Mapping of Woody Canopy Cover in Tropical Savannas Using Google Earth Engine. *Frontiers in Environmental-Science*, *8*(4).

Anderegg, W. R. L., Kane, J. M., & Anderegg, L. D. L. (2012). Consequences of widespread tree mortality triggered by drought and temperature stress. *Nature Climate Change*, *3*. https://doi.org/10.1038/NCLIMATE163.

Andersen, H., McGaughey, R. J., & Reutebuch, S. E. (2005). Estimating forest canopy fuel parameters using LIDAR data. *Remote Sensing of Environment*, *94*, 441–449. https://doi.org/10.1016/j.rse.2004.10.013

Andrews, C. M., D'Amato, A. W., Fraver, S., Palik, B., Battaglia, M. A., & Bradford, J. B. (2020). Low stand density moderates growth declines during hot droughts in semi-arid forests. *J Appl Ecol*, *57*, 1089–1102. https://doi.org/10.1111/1365-2664.13615

Andrus, R. A., Peach, L. R., Cinquini, A. R., Mills, B., Yusi, J. T., Buhl, C., Fischer, M., Goodrich, B. A., Hulbert, J. M., Holz, A., Meddens, A. J. H., Moffett, K. B., Ramirez, A., & Adams, H. D. (2023). Canary in the Forest? – Tree mortality and canopy dieback of western redcedar linked to drier and warmer summer conditions. *Stress Biology*. https://doi.org/10.1101/2023.01.11.522134

Arsalani, M., Pourtahmasi, K., Azizi, G., Bräuning, A., & Mohammadi, H. J. D. (2018). Tree-ring based December–February precipitation reconstruction in the southern Zagros Mountains, Iran. *Dendrochronologia*, *49*, 45–56. https://doi.org/10.1016/j.dendro.2018.03.002

Ashraf Vaghefi, S., Keykhai, M., Jahanbakhshi, F., Sheikholeslami, J., Ahmadi, A., Yang, H., & Abbaspour, K. C. (2019). The future of extreme climate in Iran. *Scientific Reports*, *9*, 1464.

Assal, T. J., Anderson, P. J., & Sibold, J. (2016). Spatial and temporal trends of drought effects in a heterogeneous semi-arid forest ecosystem. *Forest Ecology, and Management*, *365*, 137–151.

https://doi.org/10.1016/j.foreco.2016.01.017

Attarod, P., Rostami, F., Dolatshahi, A., Sadeghi, S. M. M., Amiri, G. Z., & Bayramzadeh, V. (2016). Do changes in meteorological parameters and evapotranspiration affect declining oak forests of Iran? *J. For. Sci*, *62*, 553–561. https://doi.org/10.17221/83/2016-JFS

Bae, S., Müller, J., Förster, B., Hilmers, T., Hochrein, S., Jacobs, M., Leroy, B. M., Pretzsch, H., Weisser, W. W., & Mitesser, O. (2022). Tracking the temporal dynamics of insect defoliation by high-resolution radar satellite data. *Methods in Ecology and Evolution*, *13*(1), 121–132. https://doi.org/10.1111/2041-210X.13726

Baguskas, S. A., Peterson, S. H., Bookhagen, B., & Still, C. J. (2014). Evaluating spatial patterns of drought-induced tree mortality in a coastal California pine forest. *Ecol. Manage*, *315*, 43–53. https://doi.org/10.1016/j.foreco.2013.12.020

Bai, L. (2010). Comparison and Validation of Five Global Land Cover Products over the African Continent, Degree-thesis in Physical Geography and Ecosystem Analysis. *Lund University*. http://lup.lub.lu.se/luur/download?func=downloadFile&recordOId=1969905&fileOId=1969934

Bałazy, R., Zasadab, M., Ciesielskia, M., Waraksaa, P., & Zawiła-Niedźwieckic, T. (2019). Forest dieback processes in the Central European Mountains in the context of terrain topography and selected stand attributes. *Forest Ecology and Management*, *435*, 106–119. https://doi.org/10.1016/j.foreco.2018.12.052

Baret, F., Hagolle, O., Geiger, B., Bicheron, P., & Miras, B. (2007). LAI, fAPAR and fCover CYCLOPS global products derived from VEGETATION Part 1: Principles of the algorithm. *Remote Sensing of Environment*, *110*, 275–286. https://doi.org/10.1016/j.rse.2007.02.018

Bastin, J. F., Berrahmouni, N., Grainger, A., Maniatis, D., Mollicone, D., Moore, R., Patriarca, C., Picard, N., Sparrow, B., Abraham, E. M., Aloui, K., Atesoglu, A., Attorre, F., Bassüllü, Ç., Bey, A., Garzuglia, M., García-Montero, L. G., Groot, N., Guerin, G., & Castro, R. (2017). The extent of forest in dryland biomes. *Science*, *356*, 6338, 635–638. https://doi.org/10.1126/science.aam6527

Baumann, M., Ozdogan, M., Kuemmerle, T., Wendland, K. J., Esipova, E., & Radeloff, V. C. (2012). Using the Landsat record to detect forest-cover changes during and after the collapse of the Soviet Union in the temperate zone of European Russia. *Remote Sensing of Environment*, *124*, 174–184. https://doi.org/10.1016/j.rse.2012.05.001

Beck, H. E., Zimmermann, N. E., McVicar, T. R., Vergopolan, N., Berg, A., & Wood, E. F. (2018). Present and future Köppen-Geiger climate classification maps at 1-km resolution". *Nature Scientific Data*. https://doi.org/10.1038/sdata.2018.214

Belgiu, M., & Dragut, L. (2016). Random forest in remote sensing: A review of applications and future directions. *ISPRS Journal of Photogrammetry and Remote Sensing*, *114*, 24–31. https://doi.org/10.1016/j.isprsjprs.2016.01.011

Beven, K. J., & Kirkby, M. J. (1979). A physically based, variable contributing area model of basin hydrology. *Hydrological Sciences Bulletin*, *24*(1), 43–69. https://doi.org/10.1080/02626667909491834

Bivand, R., Rundel, C., Pebesma, E., Stuetz, R., Hufthammer, K. O., Giraudoux, P., Davis, M., & Santilli, S. (2018). *rgeos: Interface to Geometry Engine - Open Source ('GEOS')* (0.4-2) [Computer software]. https://CRAN.R-project.org/package=rgeos

Bousbih, S., Zribi, M., Pelletier, C., Gorrab, A., Lili-Chabaan, Z., Baghdadi, N., Aissa, N. B., & Mougenot, B. (2019). Soil Texture Estimation Using Radar and Optical Data from Sentinel-1 and Sentinel-2. *Remote Sens*, *11*, 1520. https://doi.org/10.3390/rs11131520

Brandt, M., Hiernaux, P., Rasmussen, K., Mbow, C., Kergoat, L., Tagesson, T., Ibrahim, Y. Z., Wélé, A., Tucker, C. J., & Fensholt, R. (2016). Assessing woody vegetation trends in Sahelian drylands using MODIS based seasonal metrics. *Remote Sensing of Environment*, *183*, 215–225. https://doi.org/10.1016/j.rse.2016.05.027

Brandt, M., Rasmussen, K., Hiernaux, P., Herrmann, S., Tucker, C. J., Tong, X., Tian, F., Mertz, O., Kergoat, L., Mbow, C., David, J. L., Melocik, K. A., Dendoncker, M., Vincke, C., & Fensholt, R. (2018). Reduction of tree cover in West African woodlands and promotion in semi-arid farmlands. *Nature Geoscience*, *11*, 328–333. https://doi.org/10.1038/s41561-018-0092-x

Breiman, L. (2001). Random forests. *Machine Learning*, *ue 1, Vol 45:5–32*. https://link.springer.com/article/10.1023/A:1010933404324.

Briglia, N., Williams, K., Wu, D., Li, Y., Tao, S., Corke, F., Montanaro, G., Petrozza, A., Amato, D., Cellini, F., Doonan, J. H., Yang, W., & Nuzzo, V. (2020). Image-Based Assessment of Drought Response in Grapevines, Front. *Plant Sci*, *11*(595). https://doi.org/10.3389/fpls.2020.00595

Brown, L., Chen, J. M., Leblanc, S. G., & Cihlar, J. (2000). A Shortwave Infrared Modification to the Simple Ratio for LAI Retrieval in Boreal Forests: An Image and Model Analysis, Remote Sens. *Environ*, *71*, 16–25.

Bucini, G., Saatchi, S., Hanan, N., Boone, R. B., & Smit, I. (2009). Woody cover and heterogeneity in the savannas of the Kruger National Park, South Africa. *2009 IEEE International Geoscience and Remote Sensing Symposium*, *4*, IV–334. https://doi.org/10.1109/IGARSS.2009.5417381

Caballero, C. B., Biggs, T. W., Vergopolan, N., West, T. A. P., & Ruhoff, A. (2023). Transformation of Brazil's biomes: The dynamics and fate of agriculture and pasture expansion into native vegetation. *Science of the Total Environment*, *896*, 166323. https://doi.org/10.1016/j.scitotenv.2023.166323

Cailleret, M., Dakos, V., Jansen, S., Robert, E. M. R., Aakala, T., Amoroso, M. M., Antos, J. A., Bigler, C., Bugmann, H., Caccianaga, M., Camarero, J.-J., Cherubini, P., Coyea, M. R., Čufar, K., Das, A. J., Davi, H., Gea-Izquierdo, G., Gillner, S., Haavik, L. J., … Martínez-Vilalta, J. (2019). Early-Warning Signals of Individual Tree Mortality Based on Annual Radial Growth. *Frontiers in Plant Science*, *9*. https://doi.org/10.3389/fpls.2018.01964

Camarero, J. J. (2017). The Multiple Factors Explaining Decline in Mountain Forests: Historical Logging and Warming-Related Drought Stress is Causing Silver-Fir Dieback in the Aragón Pyrenees. *High Mountain Conservation in a Changing World*, *apter 6*, 131–154. https://doi.org/10.1007/978-3-319-55982-7_6

Camarero, J. J., Franquesa, M., & Sangüesa-Barreda, G. (2015). Timing of Drought Triggers Distinct Growth Responses in Holm Oak: Implications to Predict Warming-Induced Forest Defoliation and Growth Decline. *Forests*, *6*, 1576–1597. https://doi.org/10.3390/f6051576

Camps-Valls, G., Campos-Taberner, M., Moreno-Martínez, Á., Walther, S., Duveiller, G., Cescatti, A., Mahecha, M. D., Muñoz-Marí, J., García-Haro, F. J., Guanter, L., Jung, M., Gamon, J. A., Reichstein, M., & Running, S. W. (2021). A unified vegetation index for quantifying the terrestrial biosphere, Sci. *Adv*, *7*, 7447.

Chaparro, D., Piles, M., Martínez-Vilalta, J., Vall-llossera, M., Vayreda, J., Banqué-Casanovas, M., & Camps, A. (2018). Modelling forest decline using smos soil moisture and vegetation optical depth. *IGARSS - IEEE International Geoscience and Remote Sensing Symposium*. https://doi.org/10.1109/IGARSS.2018.8518107

Ciesla, W. M., & Donaubauer, E. (1994). *Decline and dieback of trees and forests: A global overview*.

Clatterbuck, W. K. (2006). *Dieback and Decline of Trees* (Issue SP686). University of Tennessee Extension.

Coburn, C. A., & Roberts, A. C. B. (2004). A multiscale texture analysis procedure for improved forest stand classification. *INT. J. Remote Sensing*, *25*(20), 4287–4308. https://doi.org/10.1080/0143116042000192367

Colangelo, M., Camarero, J. J., Borghetti, M., Gazol, A., Gentilesca, T., & Ripullone, F. (2017). Size matters a lot: Drought-Affected Italian Oaks Are Smaller and Show Lower Growth Prior to Tree Death. *Front. Plant Sci*, *8*(135). https://doi.org/10.3389/fpls.2017.00135

Corcoran, J., Knight, J., Pelletier, K., Rampi, L., & Wang, Y. (2015). The Effects of Point or Polygon Based Training Data on RandomForest Classification Accuracy of Wetlands. *Remote Sens*, *7*, 4002–4025. https://doi.org/10.3390/rs70404002

Correa-Díaz, A., Silva, L. C. R., Horwath, W. R., Gómez-Guerrero, A., Vargas-Hernández, J., Villanueva-Díaz, J., Velázquez-Martínez, A., & Suárez-Espinoza, J. (2019). Linking remote sensing and dendrochronology to quantify climate-induced shifts in high-elevation forests over space and time. *Journal of Geophysical Research: Biogeosciences*, *124*, 166–183. https://doi.org/10.1029/2018jg004687

Cunningham, D., Cunningham, P., & Fagan, M. E. (2019). Identifying biases in global tree cover products: A case study in Costa Rica. *Forests*, *10*(10), 853. https://doi.org/10.3390/f10100853

Daneshmand Parsa, R., Mirzaei, R., & Bihamtai Toosi, N. (2016). Predicting the changes of Chaharmahal and Bakhtiari Province forests using landscape metrics and Markov chain model (1994-2035. *The 2nd International Earth Surface Ecology Conference, 25th-30th October*.

Darvishi Booloorani, A., Ranjbareslamloo, S., Mirzaie, S., Bahrami, H. A., Mirzapour, F., Abbaszadeh, T., & N. (2020). Spectral behavior of Persian oak under compound stress of water deficit and dust storm. *Int J Appl Earth Obs Geoinformation*, *88*(102082). https://doi.org/10.1016/j.jag.2020.102082

Darvishsefat, A., & Saroei, S. (2003). Evaluation of the potential of Landsat ETM+ for forest density mapping in Zagros forests of Iran. *International GIS and Remote Sensing Symposium*. https://doi.org/10.1109/IGARSS.2003.1294498

Das, A. C., Shahriar, S. A., Chowdhury, M., Hossain, M., L., M., S., T., Md.K., A., R., & Salam, M. A. (2023). Assessment of remote sensing-based indices for drought monitoring in the north-western region of Bangladesh. *Heliyon*, *9*(e13016).

David, R. M., Rosser, N. J., & Donoghue, D. N. M. (2022). Remote sensing for monitoring tropical dryland forests: A review of current research, knowledge gaps and future directions for Southern Africa, Environ. *Res. Commun*, *4*, 042001.

Deka, J., Tripathi, O. P., & Khan, M. L. (2012). Implementation of Forest Canopy Density Model to Monitor Tropical Deforestation. *Journal of the Indian Society of Remote Sensing*, *41*, 2.

Delgado-Aguilar, M. J., Hinojosa, L., & Schmitt, C. B. (2019). Combining remote sensing techniques and participatory mapping to understand the relations between forest degradation and ecosystem services in a tropical rainforest. *Applied Geography*, *104*, 65–74. https://doi.org/10.1016/j.apgeog.2019.02.003

Deventer, A. P., Ward, A. D., Gowda, P. H., & Lyon, J. G. (1997). Using Thematic Mapper data to identify contrasting soil plains and tillage practices. *Photogrammetric Engineering & Remote Sensing*, *63*(1), 87–93.

Deur, M., Gašparović, M., Balenović, I., (2020). Tree Species Classification in Mixed Deciduous Forests Using Very High Spatial Resolution Satellite Imagery and Machine Learning Methods. *Remote Sens*, *12*, 3926. https://doi.org/10.3390/rs12233926

Diao, J., Feng, T., Li, M., Zhu, Z., Liu, L., Biging, G., Zheng, G., Shen, W., Wang, H., Wang, J., & Ji, B. (2020). Use of vegetation change tracker, spatial analysis, and random forest regression to assess the evolution of plantation stand age in Southeast China. *Annals of Forest Science*, *77*, 27. https://doi.org/10.1007/s13595-020-0924-x

Dobrowski, S. Z., Safford, H. D., Cheng, Y. B., & Ustin, S. L. (2008). Mapping mountain vegetation using species distribution modeling, image-based texture analysis, and object-based classification. *Applied Vegetation Science*, *11*, 499-508,. https://doi.org/10.3170/2008-7-18560

Dohn, J., Augustine, D. J., Hanan, N. P., Ratnam, J., & Sankaran, M. (2017). Spatial vegetation patterns and neighborhood competition among woody plants in an East African savanna. *Ecology, Ecology*, *98*(2), 478–488. https://doi.org/10.1002/ecy.1659

Dong, D., Wang, C., Yan, J., He, Q., Zeng, J., & Weia, Z. (2020). Combining Sentinel-1 and Sentinel-2 image time series for invasive Spartina alterniflora mapping on Google Earth Engine: A case study in Zhangjiang Estuary. *Journal of Applied Remote Sensing*, *14*(4).

Döpper, V., Roch, A. D., Berger, K., Gränzig, T., a, V., J., K., B., F., & M. (2022). Estimating soil moisture content under grassland with hyperspectral data using radiative transfer modelling and machine learning. *International Journal of Applied Earth Observations and Geoinformation*, *110*, 102817.

Dorman, M., Svoray, T., Perevolotski, A., Moshe, Y., & Sarris, D. (2015). What determines tree mortality in dry environments? A multi-perspective approach. *Ecological Applications*, *25*(4), 1054–1071. https://doi.org/10.1890/14-0698.1

Dormann, C. F., Bagnara, M., Boch, S., Hinderling, J., Janeiro Otero, A., Schäfer, D., Schall, P., & Hartig, F. (2020). Plant species richness increases with light availability, but not variability, in temperate forests understory. *BMC Ecology*, *20*(43). https://doi.org/DOI: 0.1186/s12898-020-00311-9.

Dutrieux, L. P., Verbesselt, J., Kooistra, L., & Herold, M. (2015). Monitoring forest cover loss using multiple data streams, a case study of a tropical dry forest in Bolivia. *ISPRS Journal of Photogrammetry and Remote Sensing*, *107*, 112–125. https://doi.org/10.1016/j.isprsjprs.2015.03.015

Eng, L. S., Ismail, R., Hashim, W., & Baharum, A. (2019). The use of VARI, GLI, and VIgreen formulas in detecting vegetation in aerial images. *International Journal of Technology*, *10*(7), 1385–1394. https://doi.org/10.14716/ijtech.v10i7.3275

Erfanifar, Y., Khodaei, Z., & Fallah Shamsi, R. (2014). A robust approach to generate canopy cover maps using UltraCam-D derived orthoimagery classified by support vector machines in Zagros woodlands, West Iran. *European Journal of Remote Sensing*, *47*(1), 773–792. https://doi.org/10.5721/EuJRS2014474

Eskandari, S., Jaafari, M. R., Oliva, P., Ghorbanzadeh, O., & Blaschke, T. (2020). Mapping Land Cover and Tree Canopy Cover in Zagros Forests of Iran: Application of Sentinel-2, Google Earth, and Field Data. *Remote Sens*, *12*. https://doi.org/10.3390/rs12121912

Esmizade, S., Landi, A., & Mateenfar, H. R. (2022). Using satellite imagery and spectral data to estimate the amount of soil organic carbon in central Zagros forests in Khoozestan. *J. Env. Sci. Tech*, *24*(1).

Estiarte, M., & Penuelas, J. (2015). Alteration of the phenology of leaf senescence and fall in winter deciduous species by climate change: Effects on nutrient proficiency. *Global Change Biology*, *21*, 1005–1017. https://doi.org/10.1111/gcb.12804

Estoque, R. C., Dasgupta, R., Winkler, K., Avitabile, V., Johnson, B. A., Myint, S. W., Gao, Y., Ooba, M., Murayama, Y., & Lasco, R. D. (2022). Spatiotemporal pattern of global forest change over the past 60 years and the forest transition theory, Environ. *Res. Lett*, *17*, 084022.

https://doi.org/10.1088/1748-9326/ac7df5

Etzold, S., Zieminska, K., Rohner, B., Bottero, A., Bose, A. K., Ruehr, N. K., Zingg, A., & Rigling, A. (2021). One Century of Forest Monitoring Data in Switzerland Reveals Species and Site-Specific Trends of Climate-Induced Tree Mortality, Front. *Plant Sci*, *10*(307). https://doi.org/10.3389/fpls.2019.00307

Ewane, E. B., Mohan, M., Bajaj, S., Galgamuwa, G. A. P., Watt, M. S., Arachchige, P. P., Hudak, A. T., Richardson, G., Ajithkumar, N., & Srinivasan, S. (2023). Climate-Change-Driven Droughts and Tree Mortality: Assessing the Potential of UAV-Derived Early Warning Metrics. *Remote Sens*, *15*(2627), 15102627. https://doi.org/10.3390/rs15102627

Fabre, S., Briottet, X., & Lesaignoux, A. (2015). Estimation of Soil Moisture Content from the Spectral Reflectance of Bare Soils in the 0.4–2.5 μm Domain. *Sensors*, *15*, 3263–3281. https://doi.org/10.3390/s150203262

Fadaei, H., Sakai, T., Yoshimura, T., & Kazuyuki, M. (2010). Estimation of tree density with high-resolution imagery in the Zarbin forest of north iran (cupressus sempervirence var. Horzontalis. *International Archives of the Photogrammetry, Remote Sensing and Spatial Information Science*, *XXXVIII, Part 8*, 679–684.

Fagan, M. E. (2020a). A lesson unlearned? Underestimating tree cover in drylands biases global restoration maps. *Global Change Biology*, *26: 9*, 4679–4690. https://doi.org/10.1111/gcb.15187

Farella, M. M., Barnes, M. L., Breshears, D. D., Mitchell, J., Leeuwen, W. J. D., & Gallery, R. E. (2022). Evaluation of vegetation indices and imaging spectroscopy to estimate foliar nitrogen across disparate biomes. *Ecosphere*, *13*, 3992. https://doi.org/10.1002/ecs2.3992

Farr, T. G., Rosen, P. A., Caro, E., Crippen, R., Duren, R., & Hensley, S. (2007). The shuttle radar topography mission. *Reviews of Geophysics*, *45*, 2004. https://doi.org/10.1029/2005RG000183

Fassnacht, F. E., Latifi, H., & Hartig, F. (2018). Using synthetic data to evaluate the benefits of large field plots for forest biomass estimation with LiDAR. *Remote Sensing of Environment*, *213*, 115–128. https://doi.org/10.1016/j.rse.2018.05.007

Fassnacht, F.E., Schmidt-Riese, E., Kattenborn, T., Hernández, J., (2021). Explaining Sentinel 2-based dNBR and RdNBR variability with reference data from the bird´s eye (UAS) perspective. Int. J. Appl. Earth Obs. Geoinf, 95(102262). https://doi.org/10.1016/j.jag.2020.102262

Fensham, R. J., & Fairfax, R. J. (2007). Drought-related tree death of savanna eucalypts: Species susceptibility, soil conditions, and root architecture. *Journal of Vegetation Science*, *18*, 71–80. https://doi.org/10.1111/j.1654-1103.2007.tb02517.x

Forest Canopy Density Stratification Using Biophysical Modeling. (2003). *Journal of the Indian Society of Remote Sensing*, *31*(4).

Francini, S., & Chirici, G. (2022). A Sentinel-2 derived dataset of forest disturbances occurred in Italy between 2017 and 2020. *Data in Brief*, *42*(108297).

Friedl, M. A., McIver, D. K. H., J.C.F., Z., Muchoney, X. Y. D. S., A.H., W., C.E., G., S., S., A., C., A., B., A., G., F., S., & C. (2002). Global land cover mapping from MODIS: algorithms and early results. *Remote Sensing of Environment*, *83*, 287–302. https://doi.org/10.1016/S0034-4257 (02)00078-0

Gao, Q., Zribi, M., Escorihuela, M. J., & Baghdadi, N. (2017). Synergetic Use of Sentinel-1 and Sentinel-2 Data for Soil Moisture Mapping at 100 m Resolution. *Sensors*, *17*. https://doi.org/10.3390/s17091966

Gao, Y., Skutschi, S., Paneque-G´alvez, J., Ghilardi, A., (2020). Remote sensing of forest degradation: A review, Environ. *Res. Lett*, *15*, 103001. https://doi.org/10.1088/1748-9326/abaad7

García Criado, M., Myers-Smith, I. H., Bjorkman, A. D., Lehmann, C. E. R., & Stevens, N. (2020). Woody plant encroachment intensifies under climate change across tundra and savanna biomes. *Global Ecology and Biogeography*, *29*(5), 925–943. https://doi.org/10.1111/geb.13072

Genuer, R., Poggi, J. M., & Tuleau-Malot, C. (2015). VSURF: An R package for variable selection using random forests. *The R J*, *7*(2). https://doi.org/10.32614/RJ-2015-018

Ghanbari Motlagh, M., & Kiadaliri, M. (2021). Zoning of areas with susceptibility to oak decline in western Iran. *Quaestiones Geographicae*, *40*(1), 76–83. https://doi.org/10.2478/quageo-2021-0006

Ghasemi, M., Latifi, H., & Pourhashemi, M. A. (2022). Novel Method for Detecting and Delineating Coppice Trees in UAV Images to Monitor Tree Decline. *Remote Sens*, *14*(5910). https://doi.org/10.3390/rs14235910

Ghasemi, M., Latifi, H., & Pourhashemi, M. A. (2023). Integrating UAV and freely available space borne data to describe tree decline across semi-arid mountainous forests. *Environmental Modeling & Assessment*. https://doi.org/10.1007/s10666-023-09911-3

Ghorbanian, A., Kakooei, M., Amani, M., Mahdavi, S., Mohammadzadeh, A., & Hasanloud, M. (2020). Improved land cover map of Iran using Sentinel imagery within Google Earth Engine and a novel automatic workflow for land cover classification using migrated training samples. *ISPRS Journal of Photogrammetry and Remote Sensing*, *167*, 276-288 276-288. https://doi.org/10.1016/j.isprsjprs.2020.07.013

Giannetti, F., Pegna, R., Francini, S., McRoberts, R. E., Travaglini, D., Marchetti, M., Mugnozza, G. S., & Chirici, G. (2020). A New Method for Automated Clearcut Disturbance Detection in Mediterranean Coppice Forests Using Landsat Time Series. *Remote Sens*, *12*, 3720. https://doi.org/10.3390/rs12223720

Giap, G. E., Rudiyanto, S., & M.S. (2021). Infiltration into Sand, Silt, and Clay at Field. *Capacity Journal of Advanced Research in Fluid Mechanics and Thermal Sciences*, *84*(2), 159–166. https://doi.org/10.37934/arfmts.84.2.159166

Gislason, P. B., A., J., & Sveinsson, J. R. (2006). Random Forests for land cover classification. *Pattern Recognition Letters*, *27*, 294–300. https://doi.org/10.1016/j.patrec.2005.08.011

Gitelson, A. A., Kaufman, Y. J., Stark, R., & Rundquist, D. (2002). Novel algorithms for remote estimation of vegetation fraction. *Remote Sens. Environ*, *80*, 76–87. https://doi.org/10.1016/S0034-4257 (01)00289-9

Gitelson, A. A., Merzyak, M. N., & Lichtenthaler, H. K. (1996). Detection of red-edge position and chlorophyll content by reflectance measurements near 700 nm. *J. Plant Physiol*, *148*(3⁄4), 501–508. https://doi.org/10.1016/S0176-1617 (96)80285-9

Gitelson, A. A., Vina, A., Ciganda, V., Rundquist, D. C., & Arkebauer, T. J. (2005). Remote estimation of canopy chlorophyll content in crops. *Geophysical Research Letters*, *32*, 08403. https://doi.org/10.1029/2005GL022688

Gonsamo, A., D'Odorico, P., & Pellikka, P. (2013). Measuring fractional forest canopy element cover and openness—Definitions and methodologies revisited. *Oikos*, *122*, 1283–1291. https://doi.org/10.1111/j.1600-0706.2013.00369.x

Goodarzi, N., Zargaran, M. R., Banj Shafiei, A., & Tavakoli, M. (2016). The effect of geographical directions and location on the dispersion of Oak decline, Shurab forest area. *Lorestan Province, Forest Research and Development*, *2*(3).

Griffiths, P., & Hostert, P. (2015). Forest cover dynamics during massive ownership changes – Annual disturbance mapping using annual Landsat time-series. In C. Kuenzer, S. Dech, & W. (Eds.),

Remote Sensing Time Series, Revealing Land Surface Dynamics (pp. 307–322). Wagner, Springer.

Gu, Y., Hunt, E., Wardlow, B., Basara, J. B., Brown, J. F., & Verdin, J. P. (2008). Evaluation of MODIS NDVI and NDWI for vegetation drought monitoring using Oklahoma Mesonet soil moisture data, Geophys.Res. *Lett*, *35*, 22401.

Haavik, L. J., Billings, S. A., Guldin, J. M., & Stephen, F. M. (2015). Emergent insects, pathogens, and drought shape changing patterns in oak decline in North America and Europe. *Forest Ecol Manage*, *354*, 190–205. https://doi.org/10.1016/j.foreco.2015.06.019

Hansen, M. C., DeFries, R. S., Townshend, J. R. G., & Sohlberg, R. (2000). Global land cover classification at 1 km spatial resolution using a classification tree approach. *Int. J. Remote Sens*, *21*(6), 1331–1364. https://doi.org/10.1080/014311600210209

Hardisky, M. A., Klemas, V., & Smart, R. M. (1983). The influences of soil salinity, growth form, and leaf moisture on the spectral reflectance of Spartina alterniflora canopies. *Photogrammetric Engineering and Remote Sensing*, *49*, 77–83.

Hawker, L., Uhe, P., Paulo, L., Sosa, J., Savage, J., Sampson, C., & Neal, J. (2022). A 30m global map of elevation with forests and buildings removed. *Environmental Research Letters*, *17*(2). https://doi.org/10.1088/1748-9326/ac4d4f

He, Y., Zhang, X., Shi, Y., Xu, X., Li, L., & Wu, J.-L. (2021). Premature senescnce leaf 50 promotes heat stress tolerance in rice (Oryza sativa L. *Rice*, *N Y), 14*, 53. https://doi.org/10.1186/s12284-021-00493-w

Heckel, K., Urban, M., Schratz, P., Mahecha, M. D., & Schmullius, C. (2020). Predicting forest cover in distinct ecosystems: The potential of multi-source sentinel-1 and -2 data fusion. *Remote Sens*, *12*(302). https://doi.org/10.3390/rs12020302

Hesami, S. M., & Davazdahemami, S. (2016). Phenology of Persian Oak(Quercus bratii lindl.) in three different sites in Fars province. *Iran, Journal of Zagros Forests Researches*, *3*(1).

Higginbottom, T. P., Symeonakis, E., Meyer, H., & Linden, S. (2018). Mapping fractional woody cover in semi-arid savannahs using multi-seasonal composites from Landsat data. *ISPRS J. Photogramm. Remote Sens*, *139*, 88–102. https://doi.org/10.1016/j.isprsjprs.2018.02.010

Hijmans, R. J., Bivand, R., Pebesma, E., & Sumner, M. D. (2023). *terra: Spatial Data Analysis* (1.7-55) [Computer software]. https://cran.r-project.org/web/packages/terra/index.html

Hijmans, R. J., Cameron, S. E., Parra, J. L., Jones, P. G., & Jarvis, A. (2005). Very High Resolution Interpolated Climate Surfaces for Global Land Areas. *International Journal of Climatology*, *25*, 1965–1978. https://doi.org/10.1002/joc.1276

Hoekman, D., Kooij, B., Quiñones, M., Vellekoop, S., Carolita, I., Budhiman, S., Arief, R., & Roswintiarti, O. (2020). Wide-Area Near-Real-Time Monitoring of Tropical, Forest Degradation and Deforestation Using Sentinel-1. *Remote Sens*, *12*, 3263. https://doi.org/10.3390/rs12193263

Hosseini, A., Hosseini, S. M., & Linares, J. C. (2017). Factors and stand conditions associated with Persian oak decline. *Instituto Nacional de Investigación y Tecnología Agraria y Alimentaria O, 26(3), 13 ,. https://doi.org/10.5424/fs/2017263-11298*

Hosseini, Z., Latifi, H., Naghavi, H., Bakhtiarvand Bakhtiari, S., & Fassnacht, F. E. (2020). Influence of plot and sample sizes on aboveground biomass estimations in plantation forests using very high-resolution stereo satellite imagery, Forestry. *An International Journal of Forest Research*, *94*(2), 278–291. https://doi.org/10.1093/forestry/cpaa028

Hoyos, L. E., Cingolani, A. M., Zak, M. R., Vaieretti, M. V., Gorla, D. E., & Cabido, M. R. (2013). Deforestation and precipitation patterns in the arid Chaco forests of central Argentina. *Applied*

Vegetation Science, *16*, 260–271. https://doi.org/10.1111/j.1654-109X.2012.01218.x

Huang, C., Song, K., Ki, S., Townshend, J. R. G., Davis, P., Masek, J. G., & Goward, S. N. (2008). Use of a dark object concept and support vector machines to automate forest cover change analysis. *Remote Sensing of Environment*, *112*, 970–985. https://doi.org/10.1016/j.rse.2007.07.023

Iverson, L. R., Graham, R. L., & Cook, E. A. (1989). Applications of satellite remote sensing to forested ecosystems. *Landscape Ecology*, *3*(2), 131–143. https://doi.org/10.1007/BF00131175

Jahanbazy Goujani, H., Iranmanesh, Y., Talebi, M., Shirmardi, H. A., A., M., M., P., & Habibi, M. (2020). Effect of physiographic factors on the absorption of essential nutritional elements of the leaf in Brant`s oak (Quercus brantii Lindl.) forests of Helen, Chaharmahal & Bakhtiari province, affected by the decline, Nutrient habitats. *Functional Ecology*, *15*, 423–434.

Jazirei, M. H., & Ebrahimi Rostaghi, M. (2013). *Zagros Forestry*. University of Tehran press (UTP).

Jin, Y., Sung, S., Lee, D. K., Biging, G. S., & Jeong, S. (2016). Mapping Deforestation in North Korea Using Phenology-Based Multi-Index and Random Forest. *Remote Sens*, *8*, 997. https://doi.org/10.3390/rs8120997

Jongman, R. H. G., Skidmore, A. K., Mücher, C. A., Bunce, R. G. H., & Metzger, M. J. (2017). Global Terrestrial Ecosystem Observations: Why, Where, What and How? In M. Walters & R. J. Sholes (Eds.), *2017. The GEO Handbook on Biodiversity Observation Networks* (pp. 978-3-319-27286-3 330). Springer.

Jordan, C. F. (1969). Derivation of leaf area index from quality of light on the forest floor Ecology. *Ecology*, *50*(4), 663–666. https://doi.org/10.2307/1936256

Joshi, C., Leeuw, J., Skidmore, A. K., Duren, I. C., & Oosten, H. (2006). Remotely sensed estimation of forest canopy density: A comparison of the performance of four methods. *International Journal of Applied Earth Observation and Geo-Information*, *8*, 84–95. https://doi.org/10.1016/j.jag.2005.08.004

Karlson, M., Ostwald, M., Reese, H., Sanou, J., Tankoano, B., & Mattsson, E. (2015). Mapping Tree Canopy Cover and Aboveground Biomass in Sudano-Sahelian Woodlands Using Landsat 8 and Random Forest. *Remote Sens*, *7*, 10017–10041. https://doi.org/10.3390/rs70810017

Kattenborn, T., Lopatin, J., Förster, M., Braun, A. C., & Fassnacht, F. E. (2019). UAV data as an alternative to field sampling to map woody invasive species based on combined Sentinel-1 and Sentinel-2 data. *Remote Sens. Environ*, *227*, 61–73. https://doi.org/10.1016/j.rse.2019.03.025

Kaufman, Y. J., & Tanre, D. (1992). Atmospherically resistant vegetation index (ARVI) for eos-modis. *IEEE Transactions on Geoscience and Remote Sensing*, *30*(2), 261–270. https://doi.org/10.1109/36.134076

Kennedy, R. E., Yang, Z., & Cohen, W. B. (2010). Detecting trends in forest disturbance and recovery using yearly Landsat time series: 1. *LandTrendr - Temporal Segmentation Algorithms, Remote Sensing of Environment*, *114*, 2897–2910. https://doi.org/10.1016/j.rse.2010.07.008

Kennedy, R. E., Yang, Z., Gorelick, N., Braaten, J., Cavalcante, L., Cohen, W. B. H., & S. (2018). Implementation of the LandTrendr Algorithm on Google Earth Engine. *Remote Sens*, *10*(691). https://doi.org/10.3390/rs10050691

Khabazi, M. (2020). Satellite data as indicators of oak forests canopy cover change (Case study Kamfirouze oak forests. *Journal of Wildlife and Biodiversity*, *4*(1), 66-72,. https://doi.org/10.22120/jwb.2019.119131.1106

Kooh Soltani, S., Alesheikh, A. A., Ghermezcheshmeh, B., & Mehri, S. (2018). An evaluation of the potential Oak declines Forest of the Zagros using GIS, RS, and FAHP methods. *Iranian Journal of*

Ecohydrology, *5*(2), 713–725.

Kopecký, K., & Cizkova, S. (2010). Using topographic wetness index in vegetation ecology: Does the algorithm matter? *Applied Vegetation Science*, *13*, 450–459. https://doi.org/10.1111/j.1654-109X.

Korhonen, L., Packalen, P., Hadi, P., P., R., & M. (2017). Comparison of Sentinel-2 and Landsat 8 in the estimation of boreal forest canopy cover and leaf area index. *Remote Sens. Environ*, *195*, 259–274. https://doi.org/10.1016/j.rse.2017.03.021

Kuemmerle, T., Chaskovskyy, O., Knorn, J., Radeloff, V. C., Kruhlov, I., Keeton, W. S., & Hostert, P. (2009). Forest cover change and illegal logging in the Ukrainian Carpathians in the transition period from 1988 to 2007. *Remote Sensing of Environment*, *113*, 1194–1207. https://doi.org/10.1016/j.rse.2009.02.006

Kuenzer, C., Dech, S., & Wagner, W. (2015). Remote Sensing Time Series Revealing Land Surface Dynamics: Status Quo and the Pathway Ahead. In C. Kuenzer, S. Dech, & W. (Eds.), *Remote Sensing Time Series, Revealing Land Surface Dynamics* (pp. 1–24). Wagner, Springer.

Kuuluvainen, T., Angelstam, P., Frelich, L., Jõgiste, K., Koivula, M., Kubota, Y., Lafleur, B., & Macdonald, E. (2021). Natural Disturbance-Based Forest Management: Moving Beyond Retention and Continuous-Cover Forestry. *Front. For. Glob. Change*, *4*(629020). https://doi.org/10.3389/ffgc.2021.629020

Lanfri, S. (2010). *Vegetation analysis using remote sensing, Emergency Early Warning and Response Space Applications* [Master thesis,]. Argentinian Spatial Agency (CONAE) Cordoba National University (UNC.

Larsen, S. Ø., & Salberg, A.-B. (2010). Vehicle detection and roadside tree shadow removal in high-resolution satellite images, The International Archives of the Photogrammetry. *Remote Sensing and Spatial Information Sciences*, 4 7.

Latifi, H. (2023). Potentials, and pitfalls of applying consumer-grade unmanned aerial vehicles for the inventory of Zagros forests. *Iranian Journal of Forest and Poplar Research*, *30*(3), 299–307.

Latifi, H., Fassnacht, F. E., Hartig, F., Bergere, C., Hernández, J., Corvalán, P., & Kochc, B. (2015). Stratified aboveground forest biomass estimation by remote sensing data. *International Journal of Applied Earth Observation and Geoinformation*, *38*, 229–241. https://doi.org/10.1016/j.jag.2015.01.016

Lausch, A., Erasmi, S., King, D. J., Magdon, P., & Heurich, M. (2016). Understanding Forest Health with Remote Sensing -Part I. *A Review of Spectral Traits, Processes, and Remote-Sensing Characteristics, Remote Sens*, *8*(12), 1029. https://doi.org/10.3390/rs8121029

Lee, A. C., & Lucas, R. M. (2007). A LiDAR-derived canopy density model for tree stem and crown mapping in Australian forests. *Remote Sensing of Environment*, *111*, 493–518. https://doi.org/10.1016/j.rse.2007.04.018

Lesiv, M., See, L., Laso Bayas, J. C., Sturn, T., Schepaschenko, D., Karner, M., Moorthy, I., McCallum, F., & S. (2018). Characterizing the Spatial and Temporal Availability of Very High-Resolution Satellite Imagery in Google Earth and Microsoft Bing Maps as a Source of Reference Data. *Land*, *7*, 118. https://doi.org/10.3390/land7040118

Li, M., Huang, C., Zhu, Z., Wen, W., Xu, D., & Liu, A. (2009). Use of remote sensing coupled with a vegetation change tracker model to assess rates of forest change and fragmentation in. *International Journal of Remote Sensing*, *30*(24), 6559–6574. https://doi.org/10.1080/01431160903241999

Li, X., Chen, Y., Jian, S., Wan, C., Weng, S., & Rao, D. (2022). Methods for Mapping Forest Disturbance and Degradation from Optical Earth Observation Data. *A Review, Sustainability*, *14*, 10312.

Liao, Z., Dijk, A. I. J. M., He, B., Larraondo, P. R., & Scarth, P. F. (2020). Vegetation cover, height and biomass at 25-m resolution across Australia derived from multiple sites, airborne and satellite observations. *International Journal of Applied Earth Observation and Geoinformation*, *93*, 1022092. https://doi.org/10.1016/j.jag.2020.102209

Lillesand, T. M., Kiefer, R. W., & Chipman, J. W. (2008). Earth Resource Satellites Operating in the Optical Spectrum. In T. M. Lillesand, R. W. Kiefer, & J. W. Chipman (Eds.), *Remote Sensing and Image Interpretation* (6th ed., pp. 392–481). Wiley.

Lima, T. A., Beuchle, R., Langner, A., Grecchi, R. C., Griess, V. C., & Achard, F. (2019). Comparing Sentinel-2 MSI and Landsat 8 OLI Imagery for Monitoring Selective Logging in the Brazilian Amazon. *Remote Sens*, *11*, 961. https://doi.org/10.3390/rs11080961

Liu, H. Q., & A.R, Heute. (1995). A feedback-based modification of the NDV I to minimize canopy background and atmospheric noise. *IEEE Transactions on Geoscience and Remote Sensing*, *33*(457), 465.

Liu, X., Liu, H., Qiu, S., Wu, X., Tian, Y., & Hao, Q. (2017). An Improved Estimation of Regional Fractional Woody/Herbaceous Cover Using Combined Satellite. *Data and High-Quality Training Samples Remote Sens*, *9*, 32.

Lobell, D. B., & Asner, G. P. (2002). Moisture effects on soil reflectance, *Soil Sci. Soc. Am. J*, 66, 722–727. https://doi.org/10.2136/sssaj2002.7220

López, G., J., J. P. M., D., L. M., & Higuera, A. P. (2016). Monitoring changes of forest canopy density in a temperate forest using high-resolution aerial digital photograph. *Investigations Geográficas, Boletín, num.*

Loshelder, J. I., & Coffman, R. A. (2023). Soil Moisture Content from Spectral Reflectance Using Visible, Near-Infrared, and Short-Wave Infrared Light. *J. Irrig. Drain Eng*, *149*(6), 04023010. https://doi.org/10.1061/jidedh.ireng-10055

Ludwig, M., Morgenthal, T., Detsch, F., Higginbottom, T. P., Valdes, M. L., Nauß, T., & Meyer, H. (2019a). Machine learning and multi-sensor-based modeling of woody vegetation in the Molopo Area. *South Africa, Remote Sensing of Environment*, *222*, 195–203. https://doi.org/10.1016/j.rse.2018.12.019

Luti, T., Fioravante, P.D., Marinosci, I., Strollo, A., Riitano, N., Falanga, V., Mariani, L., Congedo, L., Munafò, M., Land Consumption Monitoring with SAR Data and Multispectral Indices. (2021). *Remote Sens*, *13*. https://doi.org/10.3390/rs13081586

Lymburner, L., Beggs, P. J., & Jacobson, C. R. (2000). Estimation of canopy-average surface-specific leaf area using Landsat TM. *Data Photogrammetric Engineering and Remote Sensing*, *66*, 183–191.

Macgregor, S.D., O'Connor, T.G., (2002). Patch dieback of Colophospermum mopane in a dysfunctional semi-arid African savanna. Austral Ecology, 27, 385–395. https://doi.org/10.1046/j.1442-9993.2002.01192.x

Madonsela, S., Cho, M. A., Ramoelo, A., Mutanga, O., & Naidoo, L. (2018). Estimating tree species diversity in the savannah using NDVI and woody canopy cover. *Int J Appl Earth Obs Geoinformation*, *66*, 106–115. https://doi.org/10.1016/j.jag.2017.11.005

Mahdavi, A., Mirzaer Zadeh, Niknezhad, M., & Karami, O. (2015). Assessment and prediction of oak tree decline using logistic regression model (Case study: Bivareh forest, Malekshahi-Ilam) (in Persian. *Iranian Journal of Forest and Range Protection Research*, *13*(1), 20–33. https://doi.org/10.22092/ijfrpr.2015.102389

Mahdavi, A., Mirzayi, J., & Karami, O. (2014). Status of Dead Trees in Zagros Forests (case study: Forests of Beyore district of Ilam province. *Journal of Forest Sustainable Development*, *1*(4), 329–340.

Maier, P., Fassnacht, F. E., & Schmidtlein, S. (2022). *Detection and Explanation of Vegetation Degradation Patterns on the Tibetan Plateau via Historic and Current Satellite Data*.

Makinde, E. O., & Salami, A. T. (2013, November 4). Remote sensing of vegetation stress and indicators, 2013. *Proceedings of Global Geospatial Conference 2013 Addis Ababa*.

Malagnoux, M., Sène, E. H., & Atzmon, N. (2007). Forests, trees, and water in arid lands: A delicate balance. *Unasylva*, *58*(229), 24–29.

Mardani, F., & Youssefi, B. (2005). Phenology of Quercus brantii Lindl. In the forests of Kurdistan province. *Iranian Journal of Forest and Poplar Research*, *13*(3), 252–277.

Martín-Ortega, P., García-Montero, L. G., & Sibelet, N. (2020). Temporal Patterns in Illumination Conditions and Its Effect on Vegetation Indices Using Landsat on Google Earth Engine. *Remote Sens*, *12*(211). https://doi.org/10.3390/rs12020211

Marusig, D., Petruzzellis, F., Tomasella, M., Napolitano, R., Altobelli, A., & Nardini, A. (2020). Correlation of Field-Measured and Remotely Sensed Plant Water Status as a Tool to Monitor the Risk of Drought-Induced Forest Decline. *Forests*, *11*, 77. https://doi.org/10.3390/f11010077

Masaitis, G., Mozgeris, G., & Augustaitis, A. (2013). Spectral reflectance properties of healthy and stressed coniferous trees. *iForest - Biogeosciences and Forestry*, *1*, 30–36. https://doi.org/10.3832/ifor0709-006

Matsuo, T., Martínez-Ramos, M., Bongers, F., Sande, M. T., & Poorter, L. (2021). Forest structure drives changes in light heterogeneity during tropical secondary forest succession. *J Ecol*, *109*, 2871–2884. https://doi.org/10.1111/1365-2745.13680

Meiforth, J. J., Buddenbaum, H., Hill, J., & Shepherd, J. (2020). Monitoring of Canopy Stress Symptoms in New Zealand Kauri Trees Analysed with AISA Hyperspectral Data. *Remote Sens*, *12*, 926. https://doi.org/10.3390/rs12060926

Mellor, A., S., B., Haywood, A., & Jones. (2015). Exploring issues of training data imbalance and mislabeling on random forest performance for large area land cover classification using the ensemble margin. *ISPRS Journal of Photogrammetry and Remote Sensing*, *105*, 155–168. https://doi.org/10.1016/j.isprsjprs.2015.03.014

Meyer, L. H., Heurich, M., Beudert, B., Premier, J., & Pflugmacher, D. (2019). Comparison of Landsat-8 and Sentinel-2 Data for Estimation of Leaf Area Index in Temperate Forests. *Remote Sens*, *11*(1160).

Mirzaeizadeh, V., Niknejad, M., & Hojjati, S. M. (2015). Estimation of Forest Canopy Density using FCD. *Ecology of Iranian Forests*, *3*(5).

Moradi, M. J., Kiadaliri, H., Babaie Kafaky, S., & Bakhoda, H. (2021). Detection of high potential areas of Persian oak forests declines in Zagros, Iran, using topics method. *Cerne*, *v. 27*, 102640,. https://doi.org/10.1590/01047760202127012640

Moreno-Fernández, D., Ledo, A., Martin-Benito, D., Canellas, A., & Gea-Izquierdo, G. (2019). Negative synergistic effects of land-use legacies and climate drive widespread oak decline in evergreen Mediterranean open woodlands. *Forest Ecology, and Management*, *432*, 884–894. https://doi.org/10.1016/j.foreco.2018.10.023

Moreno-Fernández, D., Viana-Soto, A., Camarero, J. J., Zavala, M. A., Tijerín, J., & García, M. (2021). Using spectral indices as early warning signals of forest dieback: The case of drought-prone Pinus pinaster forests. *Science of the Total Environment*, *793*, 148578. https://doi.org/10.1016/j.scitotenv.2021.148578

Nagelkirk, R. L., & Dahlin, K. M. (2020). Woody Cover Fractions in African Savannas from Landsat and

High-Resolution Imagery. *Remote Sens*, *12*, 813. https://doi.org/10.3390/rs12050813

Najafifar, A., Hosseinzadeh, J., & Karamshahi, K. (2019). The role of hillshade, aspect, and toposhape in the woodland dieback of arid and semi-arid ecosystems: A case study in Zagros woodlands of Ilam province. *Iran, Journal of Landscape Ecology*, *12*(2), 79–91. https://doi.org/10.2478/jlecol-2019-0011

Nourinejad, J., & Rostami, A. (2014). Investigation of oak decline and its relation to physiographic factors in the forests of West of Iran (case study: Ilam Province. *Journal of Biodiversity and Environmental Sciences (JBES*, *5: (2*, 201–207.

Parvaneh, E., Etemad, V., Marvie Mohajer, M., R., Z. A., H., G., & Attarod, P. (2015). The relationships between the rate of oak trees decline and forest types, soil characteristics, and topographic conditions in Ghalaje Forests of Kermanshah, west of Iran. *Iranian Journal of Forest*, *8*(3), 263–275.

Pasquarella, V. J., Arevalo, P., Bratley, K. H., Bullock, E. L., Gorelick, N., Yang, Z., & Kennedy, R. (2022). Demystifying LandTrendr and CCDC temporal segmentation. *International Journal of Applied Earth Observations and Geoinformation*, *110*, 102806.

Peñuelas, J., & Sardans, J. (2021). Global Change and Forest Disturbances in the Mediterranean Basin: Breakthroughs, Knowledge Gaps, and Recommendations. *Forests*, *12*, 603. https://doi.org/10.3390/f12050603.

Piyoosh, A. K., & Ghosh, S. K. (2018). Development of a modified bare soil and urban index for Landsat 8 satellite data. *Geocarto International*, *33*(4), 423–442. https://doi.org/10.1080/10106049.2016.1273401

Poggio, L., Sousa, L. M., Batjes, N. H., Heuvelink, G. B. M., Kempen, B., Ribeiro, E., & Rossite, D. (2021). SoilGrids 2.0: Producing soil information for the globe with quantified spatial uncertainty. *Soil*, *7*, 217–240. https://doi.org/10.5194/soil-7-217-2021

Pontius, J., Schaberg, P., & Hanavan, R. (2020). Remote Sensing for Early, Detailed, and Accurate Detection of Forest Disturbance and Decline for Protection of Biodiversity. In J. A. Cavender-Bares, J. A. Gamon, & P. A. Townsend (Eds.), *Remote Sensing of Plant Biodiversity* (pp. 121–154). Springer.

Pourmoghadam, K., Pourmoghadam, K., Khosropour, E., & Haidari, H. (2013). Identifying forest types associated with physiological factors in middle Zagros forests in Iran. *International Journal of Advanced Biological and Biomedical Research*, *1*(8), 830–834.

R: The R Project for Statistical Computing. (2023). *https://www.r-project.org/*

Rahimi, S. H., Sharifia, Z., & Mastrolonardo, G. (2020). Comparative Study of the Effects of Wildfire and Cultivation on Topsoil Properties in the Zagros Forest, Iran. *Eurasian Soil Science*, *53*(11), 1655–1668. https://doi.org/10.1134/S1064229320110113

Rautiainen, M., & Heiskanen, J. (2013). Seasonal Contribution of Understory Vegetation to the Reflectance of a Boreal Landscape at Different Spatial Scales. *IEEE Geoscience and Remote Sensing Letters*, *10*(4), 923. https://doi.org/10.1109/LGRS.2013.2247560

Rautiainen, M., Mõttus, M., Heiskanen, J., Akujärvi, A., Majasalmi, T., & Stenberg, P. (2011). Seasonal reflectance dynamics of common understory types in a northern European boreal forest. *Remote Sensing of Environment*, *115*, 3020–3028. https://doi.org/10.1016/j.rse.2011.06.005

Rikimaru, A., Roy, P., & Miyatake, S. (2002). Tropical forest cover density mapping. *Tropical Ecology*, *43*(1), 39–47.

Ripullone, F., Camarero, J. J., Colangelo, M., & Voltas, J. (2020). Variation in the access to deep soil water

pools explains tree-to-tree differences in drought-triggered dieback of Mediterranean oaks. *Tree Physiology*, *40*, 591–604. https://doi.org/10.1093/treephys/tpaa026

Rodman, K. C., Andrus, R. A., Veblen, T. T., & Hart, S. J. (2021). Disturbance Detection in Landsat Time Series is influenced by Tree Mortality Agent and Severity, Not by Prior Disturbance. *Remote Sensing of Environment*, *254*, 112244. https://doi.org/10.1016/j.rse.2020.112244

Rouse, J. W., Haas, R. H., Schell, J. A., Deering, D. W., & others. (1974). Monitoring vegetation systems in the Great Plains with ERTS. *NASA Spec. Publ*, *351*(1), 309.

Sáenz-Romero, C., Mendoza-Maya, E., Gómez-Pineda, E., Blanco-García, A., Endara-Agramont, A. R., Lindig-Cisneros, R., López-Upton, J., Trejo-Ramírez, O., Wehenkel, C., Cibrián-Tovar, D., Flores-López, C., Plascencia-González, A., & Vargas-Hernández, J. J. (2020). Recent evidence of Mexican temperate forest decline and the need for ex situ conservation, assisted migration, and translocation of species ensembles as adaptive management to face projected climatic change impacts in a megadiverse country, Can. *J. For. Res*, *50*, 843–854.

Sagheb Talebi, K., Sajedi, T., & Pourhashemi, M. (2014). *Forests of Iran: A Treasure from the Past, a Hope for the Future* (Vol. 10). Springer Netherlands. https://doi.org/10.1007/978-94-007-7371-4

Sánchez-Pinillos, D. 'Orangeville, L., B., Y., C., P., W., J., T., A.R., K., & D. (2021). Sequential droughts: A silent trigger of boreal forest mortality. *Global Change Biology*, *00*, 1–15. https://doi.org/10.1111/gcb.15913

Sankaran, M., Hanan, N. P., Scholes, R. J., Ratnam, J., Augustine, D. J., Cade, B. S., Gignoux, J., Higgins, S. I., Le Roux, X., Ludwig, F., Ardo, J., Banyikwa, F., Bronn, A., Bucini, G., Caylor, K. K., Coughenour, M. B., Diouf, A., Ekaya, W., Feral, C. J., … Zambatis, N. (2005). Determinants of woody cover in African savannas. *Nature*, *438*(7069), 846–849. https://doi.org/10.1038/nature04070

Sasaki, N., & Putz, F. E. (2009). Critical need for new definitions of "forest" and "forest degradation" in global climate change agreements. *Conservation Letters*, *2*, 226–232. https://doi.org/10.1111/j.1755-263X.2009.00067.x

Schlerf, M., & Atzberger, C. (2006). Inversion of a forest reflectance model to estimate structural canopy variables from hyperspectral remote sensing data. *Remote Sensing of Environment*, *100*, 281–294. https://doi.org/10.1016/j.rse.2005.10.006

Schroeder, L. M. (2010). Colonization of storm gaps by the spruce bark beetle: Influence of gap and landscape characteristics. *Agric. For. Entomol*, *12*, 29–39. https://doi.org/10.1111/j.1461-9563.2009.00447.x

Senf, C., Buras, A., Zang, C. S., Rammig, A., & Seidl, R. (2020). Excess forest mortality is consistently linked to drought across Europe. *Nature Communications*, *11*, 6200. https://doi.org/10.1038/s41467-020-19924-1

Shafeian, E., Fassnacht, F. E., & Latifi, H. (2021). Mapping fractional woody cover in an extensive semi-arid woodland area at different spatial grains with Sentinel-2 and very high-resolution data. *International Journal of Applied Earth Observation and Geoinformation*, *105*, 102621. https://doi.org/10.1016/j.jag.2021.102621

Shafeian, E., Fassnacht, F. E., & Latifi, H. (2023). Detecting forest decline in semi-arid forests using a time series of Landsat data. *European Journal of Remote Sensing*, *56*(1), 2260549,. https://doi.org/10.1080/22797254.2023.2260549

Shahvali Kouhshour, A., Pir Bavaghar, M., & Fatehi, P. (2012). Forest cover density mapping in sparse and semi dense forests using forest canopy density model (Case study: Marivan forests. *Journal of*

Applied RS & GIS Techniques in Natural Resource Science, *3*(3).

Sharwood, L. N. (2021). *Modeling Environmental Factors Related to Drought-Induced Tree Mortality Based on Lidar and Hyperspectral Imagery, master of science thesis*. Portland State University. https://doi.org/10.15760/etd.7745.

Shields, J. A., Paul, E. A., Arnaud, R. Js., & Head, W. K. (1968). Spectrophotometric measurement of soil color and its relationship to moisture and organic matter, Can. *J. Soil Sci*, *48*, 271–280.

Shifley, S. R., Fan, Z., Kabrick, J. M., & Jensen, R. G. (2006). Oak mortality risk factors and mortality estimation. *For. Ecol. Manage*, *229*, 16–26. https://doi.org/10.1016/j.foreco.2006.03.033

Shiravand, H., & Hosseini, S. A. (2020). A new evaluation of the influence of climate change on Zagros oak forest dieback in Iran. *Theoretical and Applied Climatology*, *141*, 685–697. https://doi.org/10.1007/s00704-020-03226-z

Simula, M. (2009). Towards defining forest degradation, Comparative analysis of existing definitions. In *For. Res. Assessment Working Paper 154*. FAO.

Smith, W. K., Dannenberg, M. P., Yan, D., Herrmann, S., Barnes, M. L., Barron-Gafford, G. A., Biederman, J. A., Ferrenberg, S., Fox, A. M., Hudson, A., Knowles, J. F., MacBean, N., Moore, D. J. P., Nagler, P. L., Reed, S. C., Rutherford, W. A., Scott, R. L., Wang, X., & Yang, J. (2019). Remote sensing of dryland ecosystem structure and function: Progress, challenges, and opportunities. *Remote Sensing of Environment*, *233*(July), 111401. https://doi.org/10.1016/j.rse.2019.111401

Solaymani, H. R., & Jabbari, S. (2015). Impacts and vulnerabilities of climate change and socio-economic challenges on Oak forest deterioration – west of Iran, XIV WORLD FORESTRY CONGRESS, Durban. *South Africa*.

Soleimannejad, L., Bonyad, A. E., & Naghdi, R. (2018). Remote sensing-assisted mapping of quantitative attributes in Zagros open forests of Iran. *Caspian J. Environ. Sci*, *16*(3), 215–230.

Stovall, A. E. L., Shugart, H., & Yang, X. (2019). Tree height explains mortality risk during an intense drought. *NATURE COMMUNICATIONS*, *10*(4385). https://doi.org/10.1038/s41467-019-12380-6

Sulla-Menashe, D., Kennedy, R., E., Y., Z., B., J., K., O.N., F., & M.A. (2014). Detecting forest disturbance in the Pacific Northwest from MODIS time series using temporal segmentation. *Remote Sensing of Environment*, *151*, 114–123. https://doi.org/10.1016/j.rse.2013.07.042

Symeonakis, E., Higginbottom, T. P., Petroulaki, K., & Rabe, A. (2018). Optimisation of Savannah Land Cover Characterisation with Optical and SAR Data. *Remote Sens*, *10*, 499. https://doi.org/10.3390/rs10040499

Tejaswi, G. (2007). Manual on deforestation, degradation, and fragmentation using remote sensing and GIS, "Strengthening monitoring, assessment, and reporting on sustainable forest management in Asia." In *Forestry Department, Food and Agriculture Organization of the United Nations*.

Tian, J., & Philpot, W. D. (2015). Relationship between surface soil water content, evaporation rate, and water absorption band depths in SWIR reflectance spectra. *Remote Sensing of Environment*, *169*, 280–289. https://doi.org/10.1016/j.rse.2015.08.007

Turner, W., Rondinini, C., Pettorelli, N., Mora, B., Leidner, A. K., Szantoi, Z., Buchanan, G., Dech, S., Dwyer, J., Herold, M., Koh, L. P., Leimgruber, P., Taubeneck, H., Wegmann, M., Wikelski, M., & Woodcock, C. (2015). Free and open-access satellite data are key. *Biological Conservation*, *182*, 173–176. https://doi.org/10.1016/j.biocon.2014.11.048

Twery, M. J., & Weiskittel, A. R. (2013). Forest-Management Modelling. In J. Wainwright, M. Mulligan, J. Wiley, & Sons (Eds.), *Environmental Modelling* (pp. 379–398).

Vásquez-Grandón, A., Donoso, P. J., & Gerding, V. (2018). Forest Degradation: When Is a Forest

Degraded? *Forests*, *9*, 726. https://doi.org/10.3390/f9110726

Verbesselt, J., Hyndman, R., Zeileis, A., & Culvenor, D. (2010). Phenological change detection while accounting for abrupt and gradual trends in satellite image time series. *Remote Sensing of Environment*, *114*(12), 2970–2980. https://doi.org/10.1016/j.rse.2010.08.003

Verhoef, W. (1984). Light scattering by leaf layers with application to canopy reflectance modeling: The SAIL model. *Remote Sensing of Environment*, *16*, 125–141. https://doi.org/10.1016/0034-4257(84)90057-9

Villegas, J. C., Dominguez, F., Barron-Gafford, G. A., Adams, H. D., Guardiola-Claramonte, M., Sommer, E. D., Selvey, A. W., Espeleta, J. F., Zou, C. B., Breshears, D. D., & Huxman, T. E. (2015). Sensitivity of regional evapotranspiration partitioning to variation in woody plant cover: Insights from experimental dryland tree mosaics. *Global Ecology and Biogeography*, *24*(9), 1040–1048. https://doi.org/10.1111/geb.12349

Wagenseil, H., & Samimi, C. (2007). Woody vegetation cover in Namibian savannahs. *erdkunde*, *10*(3112), 325–334. https://doi.org/10.3112/erdkunde.2007.04.03

Walker, J. J., Beurs, K. M., Wynne, R. H., & Gao, F. (2012). Evaluation of Landsat and MODIS data fusion products for analysis of dryland forest phenology. *Remote Sensing of Environment*, *17*, 381–393. https://doi.org/10.1016/j.rse.2011.10.014

Wang, C., Qi, J., & Cochrane, M. (2005). Assessment of tropical forest degradation with canopy fractional cover from Landsat ETM+ and IKONOS imagery. *Earth Interactions*, *9*(22), 1–18. https://doi.org/10.1175/EI133.1

Wang, H., Muller, J. D., Tatarinov, F., Yakir, D., & Rotenberg, E. (2022). Disentangling Soil, Shade, and Tree Canopy Contributions to Mixed Satellite Vegetation Indices in a Sparse Dry Forest. *Remote Sens*, *14*, 3681.

Wang, Z., Lyu, L., Liu, W., Liang, H., Huang, J., & Zhang, Q. B. (2020). Topographic patterns of forest decline as detected from tree rings and NDVI. *Catena*, *198*, 105011.

Waroux, Y., & Lambin, E. F. (2012). Monitoring degradation in arid and semi-arid forests and woodlands: The case of the argan woodlands (Morocco. *Applied Geography*, *32*, 777 786.

Waśniewski, A., Hosciło, A., Zagajewski, B., & Moukétou-Tarazewicz, D. (2020). Assessment of Sentinel-2 Satellite Images and Random Forest Classifier for Rainforest Mapping in Gabon. *Forests*, *11*, 941. https://doi.org/10.3390/f11090941

Watts, L. M., & Laffan, S.W. (2014). Effectiveness of the BFAST algorithm for detecting vegetation response patterns in a semi-arid region. *Remote Sensing of Environment*, *154*, 234–245. https://doi.org/10.1016/j.rse.2014.08.023

Welikhe, P., Essamuah–Quansah, J., Fall, S., & McElhenney, W. (2017). Estimation of Soil Moisture Percentage Using LANDSAT-based Moisture Stress Index. *J Remote Sensing & GIS*, *6*(2). https://doi.org/10.4172/2469-4134.1000200

Windrim, L., Carnegie, A. J., Webster, M., & Bryson, M. (2020). Tree Detection and Health Monitoring in Multi-Spectral Aerial Imagery and Photogrammetric Point Clouds using Machine Learning, DOI 10.1109/JSTARS.2020.2995391. *IEEE Journal of Selected Topics in Applied Earth Observations and Remote Sensing*.

Wingate, V. R., Kuhn, N. J., Phinn, S. R., & Waal, C. (2019). Mapping trends in woody cover throughout Namibian savanna with MODIS seasonal phenological metrics and field inventory data. *Biogeosciences Discuss*. https://doi.org/10.5194/bg-2019-28

Winzeler, H. E., Owens, P. R., Read, Q. D., Libohova, Z., Ashworth, A., & Sauer, T. (2022). Topographic

Wetness Index as a Proxy for Soil Moisture in a Hillslope Catena. *Flow Algorithms and Map Generalization, Land*, *11*. https://doi.org/10.3390/land11112018

Wood, E. M., Pidgeon, A. M., Radeloff, V. C., & Keuler, N. S. (2012). Image texture as a remotely sensed measure of vegetation structure. *Remote Sensing of Environment*, *121*, 516–526. https://doi.org/10.1016/j.rse.2012.01.003

Xie, Y., Sha, Z., & Yu, M. (2008). Remote sensing imagery in vegetation mapping: A review. *Journal of Plant Ecology*, *1*(1), 9–23. https://doi.org/10.1093/jpe/rtm005

Yamazaki, D., Ikeshima, D., Sosa, J., Bates, P. D., Allen, G. H., & Pavelsky, T. M. (2019). MERIT Hydro: A High-Resolution Global Hydrography Map Based on Latest Topography Dataset. *Water Resources Research*, *55*, 5053–5507. https://doi.org/10.1029/2019wr024873

Yang, J., Weisberg, P. J., & Bristow, N. A. (2012). Landsat remote sensing approaches for monitoring long-term tree cover dynamics in semi-arid woodlands: Comparison of vegetation indices and spectral mixture analysis. *Remote Sensing of Environment*, *119*, 62–71. https://doi.org/10.1016/j.rse.2011.12.004

Yang, L., Jia, K., Liang, S., Wei, X., Yao, Y., & Zhang, X. (2017). A robust algorithm for estimating surface fractional vegetation cover from Landsat data. *Remote Sensing*, *9*(8), 1–20. https://doi.org/10.3390/rs9080857

Yang, X., & Crews, K. A. (2019). Fractional woody cover mapping of Texas savanna at Landsat scale. *Land*, *8*(1). https://doi.org/10.3390/land8010009

Yang, X., Li, R., Jablonski, A., Stovall, A., Kim, J., Yi, K., Ma5, Y., Beverly, D., Phillips, R., Novick, K., Xu, X., & Lerdau, M. (2023). Leaf angle as a leaf and canopy trait: Rejuvenating its role in ecology with new technology. *Ecology Letters*, *26*, 1005–1020. https://doi.org/10.1111/ele.14215

Yao, Y., Liang, S., Cao, B., Liu, S., Yu, G., & Jia, K. (2018). Satellite detection of water stress effects on terrestrial latent heat flux with MODIS shortwave infrared reflectance data. *Journal of Geophysical Research: Atmospheres*, *123*(11), 410-11,430. https://doi.org/10.1029/2018jd029011

Ye, W., Li, X., Chen, X., & Zhang, G. (2014). A spectral index for highlighting forest cover from remotely sensed imagery. *Proc. SPIE 9260, Land Surface Remote Sensing II, 92601L*. https://doi.org/10.1117/12.2068775

Yu, T., Liu, P., Zhang, Q., Ren, Y., & Yao, J. (2021). Detecting Forest Degradation in the Three-North Forest Shelterbelt in China from Multi-Scale Satellite Images. *Remote Sens*, *13*, 1131.

Zandler, H., Brenning, A., & Samimi, C. (2015). Quantifying dwarf shrub biomass in an arid environment: Comparing empirical methods in a high dimensional setting. *Remote Sensing of Environment*, *158*, 140–155. https://doi.org/10.1016/j.rse.2014.11.007

Zhang, J., Ding, J., Hou, X., & Wu, P. (2023). Quantifying drought response sensitivity and spatial and temporal heterogeneity of vegetation in arid and semi-arid regions. *International Journal of Remote Sensing*, *44*(5), 1665–1683. https://doi.org/10.1080/01431161.2023.2182651

Zhang, J., Yang, G., Yang, L., Li, Z., Gao, M., Yu, C., Gong, E., Long, H., & Hu, H. (2022). Dynamic Monitoring of Environmental Quality in the Loess Plateau from 2000 to 2020 Using the Google Earth Engine Platform and the Remote Sensing Ecological Index. *Remote Sens*, *14*, 5094. https://doi.org/10.3390/rs14205094

Zhang, M., Huang, H., Li, Z., Hackman, K. O., Liu, C., Andriamiarisoa, R. L., Raherivelo, T. A. N. A., Li, Y., & Gong, P. (2020). Automatic High-Resolution Land Cover Production in Madagascar Using Sentinel-2 Time Series, Tile-Based Image Classification, and Google Earth Engine. *Remote Sens*, *12*, 3663. https://doi.org/10.3390/rs12213663

Zhang, W., Brandt, M., Wang, Q., Prishchepov, A. V., Tucker, C. J., Li, Y., Lyu, H., & Fensholt, R. (2019). From woody cover to woody canopies: How Sentinel-1 and Sentinel-2 data advance the mapping of woody plants in savannas. *Remote Sensing of Environment*, *234*, 111465. https://doi.org/10.1016/j.rse.2019.111465

Zhao, W., Zhao, H., Wang, H., & Y, H. (2022). Research progress on the relationship between leaf senescence and quality, yield, and stress resistance in horticultural plants. *Front. Plant Sci*, *13*(1044500). https://doi.org/10.3389/fpls.2022.1044500

Zhao, X., Zhang, W., Feng, Y., Mo, Q., Su, Y., Njoroge, B., Qu, C., X., G., & X, L. (2022). Soil organic carbon primarily control the soil moisture characteristic during forest restoration in subtropical China. *Front. Ecol. Evol*, *10*(1003532). https://doi.org/10.3389/fevo.2022.1003532

Zheng, T., Martínez-Vilalta, J., García-Valdés, R., Gazol, A., Camarero, J. J., Mu, C., & Mencuccini, M. (2023). Growth plasticity of conifers did not avoid declining resilience to soil and atmospheric droughts during the 20th century. *Forest Ecosystems*, *10*, 100107. https://doi.org/10.1016/j.fecs.2023.100107

Zhu, G., Ju1, W., Chen, J. M., Zhou, Y., Li, X., & Xu, X. (2010). Comparison of Forest Leaf Area Index Retrieval Based on Simple Ratio and Reduced Simple Ratio. *18th International Conference on Geoinformatics*. https://doi.org/10.1109/geoinformatics.2010.5568204

Zhu, Z., & Woodcock, C. E. (2014). Continuous change detection and classification of land cover using all available Landsat data. *Remote Sens. Environ*, *144*, 152–171. https://doi.org/10.1016/j.rse.2014.01.011

Zhu, Z., Zhang, J., Yang, Z., Aljaddani, A. H., Cohen, W. B., Qiu, S., & Zhou, C. (2020). Continuous monitoring of land disturbance based on Landsat time series. *Remote Sens. Environ*, *238*, 111116. https://doi.org/10.1016/j.rse.2019.03.009

Žížala, D., Juřicová, A., Zádorová, T., Zelenková, K., & Minařík, R. (2019). Mapping soil degradation using remote sensing data and ancillary data: South-East Moravia, Czech Republic. *European Journal of Remote Sensing*, *52:sup1*, 108–122. https://doi.org/10.1080/22797254.2018.1482524

Acknowledgments

I wish to convey my heartfelt appreciation to all those who have stood by me during my doctoral studies. Foremost, my deepest gratitude goes to my first supervisor, Prof. Dr. Sebastian Schmidtlein, for his invaluable guidance, unwavering encouragement, and continuous support. His sharp inquiries and constructive feedback have been instrumental in shaping my research, and I am also thankful for the fantastic workspace he provided at the institute with a breathtaking view (figure below). I also extend my sincere thanks to Prof. Dr. Stephan Hinz and Prof. Dr. Florian Wittmann for their thorough review of this thesis and their presence on my Ph.D. committee. I am appreciative of their interest and valuable input.

A very special thanks go to my supervisor, Prof. Dr. Fabian Ewald Fassnacht, who worked with me closely more than anyone else during the whole period and was responsible for most of my learning process. He has consistently served as an unwavering source of inspiration, countless enjoyable moments, and, let's be honest, a few challenging times that I would not have been able to overcome without his support. He provided me with motivating and critical feedback and even supported me mentally during my doctoral studies as well as the Corona crisis. I am deeply grateful to him for changing my life. Similarly, I must thank my co-supervisor, Prof. Dr. Hooman Latifi, for his quick and valuable assistance in delineating ideas, writing papers and organizing our field campaigns in Zagros forests. This journey to earning my doctorate would not have been the same without his support.

I would like to express my gratitude to Dr. Ethan Householder for his unwavering friendliness and warm welcome and for generously allowing me to utilize the Dendro lab at the Floodplain Institute in Rastatt up to this point.

I extend my gratitude to the individuals at the Institute of Geography and Geoecology (IFGG), including Rita Seith and Petra Kajtazi-Zizmann, for their invaluable administrative support. I would also like to express my appreciation to Reiner Gebhardt, who consistently assisted me with technical issues, always wearing a smile! Furthermore, I wish to thank the following respected individuals: Prof. Dr. Caroline Kramer, Prof. Dr. Javier Lopatin, Dr. Christoph Mager, Dr. Florian Hogewind, Dr. Christophe Neff, Dr. Michael Ewald, Dr. Johannes Senn, Dr. Anne Lewerentz, Dr. Tamalika Chapparty, Dr. Jesse Kalwij, Dr. Yhasmin Mendes de Moura, Dr.Teja Kattenborn, Dr. Jeff Gafna, Rocio Araya López, Ulrike Märkel, Jannika Schäfer, Felix Schiefer, Pia Labenski, and Christopher Schiller. Their generosity in sharing their valuable time and providing feedback has been instrumental in my journey.

I would like to express my gratitude to the German Academic Exchange Service (DAAD), particularly the DAAD office in Tehran and Section ST33, Middle East, for granting me a scholarship that extended for over four years and for helping with my family's visits to Iran. My appreciation goes out to the Graduate School for Climate and Environment (GRACE), especially

Acknowledgements

The spectacular view of my workplace at IFGG (October 2023)

Abbreviations and acronyms

AIC	Akaike information criterion
BFAST	The Breaks for Additive Seasonal and Trend
BIO1	Annual Mean Temperature
BIO4	Temperature Seasonality
BIO7	Temperature Annual Range
BIO10	Mean Temperature of Warmest Quarter
BIO12	Annual Precipitation
BIO15	Precipitation Seasonality
BIO16	Precipitation of Wettest Quarter
BIO17	Precipitation of Driest Quarter
CCDC	The Continuous Change Detection and Classification
cm	Centimeter
DBH	Diameter at breast height
DEM	Digital Elevation Model
ES	Ecosystem Services
FC	Forest Cover
GAM	Generalized Additive Model
GEE	Google Earth Engine
GLCM	Gray-level co-occurrence texture metrics
KDE	Kernel Density Estimation
km^2	Square Kilometer
IC	Illumination Condition
LandTrendr	Landsat-based detection of Trends in Disturbance and Recovery
LC	Land Cover
m	Meter
nm	Nanometer
NIR	Near infrared
R^2	Coefficient of determination
RF	Random Forest
RMSE	Root Mean Square Error
RS	Remote Sensing
SOC	Soil Organic Carbon
S2	Sentinel-2
SWIR	Short-wave infrared
TWI	Topographic Wetness Index
VHR	Very High Resolution
VI	Vegetation Index
VIs	Vegetation Indices
VNIR	Visible Near infrared
VSURF	Variable Selection Using Random Forests

Additional abbreviations of the used VIs are provided in Table 3.1.